Multi-scale Modelling of Bacteria Transport and Growth in Periodic Porous Media



Maha Alhajri
Somerville College
University of Oxford

Thesis submitted for
Doctor of Philosophy
Trinity 2023

This thesis is dedicated to my beloved parents, who have meant so much to me and continue to do so. Even though they are no longer in this world, their memories guide my life.

Acknowledgements

My most profound appreciation goes to Professor Philip Maini and Professor Alain Goriely, my advisors, for their time, effort, and understanding in helping me succeed in my studies. Their vast wisdom and wealth of experience have inspired me throughout my studies. Finally, I want to express my gratitude to everyone at the University of Oxford, particularly Mrs Charlotte Turner. Thanks to their generosity and encouragement, my time spent studying and living in the UK has been truly rewarding. In addition, I'd like to thank Dr Andrew Montgomery and Dr Jane Sedwick for their emotional support throughout my research. Finally, I want to give a special thanks to my sister; without her unwavering emotional and financial support over the past few years, finishing my studies would have been impossible.

Abstract

Understanding bacterial transport through porous media is crucial for determining the efficiency of bioremediation strategies. Specifically, chemotaxis – the movement of bacteria in response to chemical gradients – plays a crucial role by directing bacteria towards higher chemical concentrations. Therefore, understanding the behaviour of chemotactic bacteria in porous media can help design more effective bioremediation strategies by facilitating the movement of bacteria towards subsurface contaminant sites. There have been many laboratory studies of bacterial transport in the subsurface environment using various methods and techniques. Unfortunately, the existing mathematical models, cannot aid in resolving the inconsistencies between mathematical simulations and experimental data. In particular, when using the upscaled Keller-Segel model derived using gas kinetic theory.

In this thesis we aim to is to develop effective media models of bacterial chemotactic transport in porous media. Our method of upscaling throughout the thesis uses asymptotic homogenisation. This method is especially useful when dealing with highly heterogeneous systems since it captures the whole system's behaviour without accounting for the physical heterogeneity; another objective is to understand the theoretical limitations of the upscaling procedure, thus providing a framework for further uses of the asymptotic homogenisation on more refined models.

To achieve these objectives, we gave a detailed outline of a simple Keller-Segel model in a periodic microstructure and providing an argument of the model's limitations and validity. First, we established the model's validity at the pore scale. Second, we identified the varying timescales of the different processes governing the transport model. Through the second step, we identified three different limiting cases of the transport model. Then we applied the homogenisation method to derive three effective forms of the Keller-Segel model according to the advective flow strength. Finally, applying the effective models on two case studies, we validated the effective models through direct comparison using the results from performing the exact simulations or by comparing the predictions of the effective model against experimental data.

In all the effective models derived using asymptotic homogenisation, we found that the upscaled chemotaxis process is affected by the attractant's upscaled diffusive process regardless of any flow dispersion effects. These findings differ from the upscaled model developed using the average volume method, where the chemotaxis flow contributes to the dispersion parameter. Nevertheless, both methods yielded the same simulation results, thus showing the robustness of the two upscaling methods. However, the homogenised models in this thesis are easier to simulate and carry out extensive numerical investigations. Finally, using numerical simulations we showed that the order of the relative error between the homogenised model and the exact solution of the bacterial density is $\sqrt{\varepsilon}$, which is the same order as the error in the homogenised substrate gradient. However, the error analysis did not include limiting case of dominant additive timescales.

The insight gained in this thesis has significant implications for the development of experimental studies concerning chemotactic transport, where it can guide the development of experimental protocols to achieve better control of the different factors that may affect chemotactic transport. Furthermore, it supports the application of asymptotic homogenisation to develop different mathematical models. For instance, to develop an effective Keller-Segel model under different assumptions that overcome some of the limitations imposed in this thesis or apply asymptotic homogenisation to other mathematical approaches that deal with different bias transport processes in porous media.

Contents

1 Introduction **1**
- 1.1 Bacterial Transport in Bulk Aqueous Solution . . . 2
- 1.2 Bacterial Transport in Porous Media . . . 4
  - 1.2.1 Bacterial Random Motility in Porous Media . . . 4
  - 1.2.2 Chemotaxis Migration in Porous Media . . . 6
  - 1.2.3 Mathematical Modelling and Computations . . . 8
- 1.3 Outline of Thesis . . . 10
- 1.4 Statement of Originality . . . 11

2 Keller-Segel Model Incorporating Confinement, Flow and Metabolic Rates **12**
- 2.1 Domain of the Model . . . 13
- 2.2 Validity of the Continuum Models in Porous Media . . . 14
- 2.3 Description of the Mathematical Model . . . 16
  - 2.3.1 Advection Flux . . . 17
  - 2.3.2 Chemotactic Flux . . . 18
  - 2.3.3 Model Kinetics . . . 20
    - 2.3.3.1 Saturated Monod Kinetics . . . 20
    - 2.3.3.2 Kinetics of Inhibition . . . 22
    - 2.3.3.3 The Net Generation and Consumption Rate . . . 23
  - 2.3.4 Solid-Aqueous Interface . . . 24
- 2.4 The Mathematical Model . . . 24
- 2.5 The Mathematical Model Time Scales . . . 25
- 2.6 Non-dimensionalisation . . . 26
  - 2.6.1 Dimensionless Stokes Equations . . . 27
  - 2.6.2 Dimensionless Keller-Segel Model . . . 28
- 2.7 Concluding Remarks . . . 29

3 Asymptotic Homogenisation Method **31**
- 3.1 Preliminaries . . . 32
- 3.2 Darcy Velocity . . . 34
- 3.3 Microscopic Description of the Model . . . 38

3.4 Chemotactic Transport in a Diffusion Regime . . . 41
3.4.1 The Homogenised Model . . . 42
3.4.2 The Formal Asymptotic Expansion . . . 44
3.5 Chemotactic Transport in an Advection-Diffusion Regime . . . 49
3.5.1 The Homogenised Model . . . 50
3.5.2 The Formal Asymptotic Homogenisation . . . 51
3.6 Chemotactic Migration in an Advection-Dispersion Regime . . . 56
3.6.1 The Homogenised Model . . . 57
3.6.2 Formal Asymptotic . . . 59
3.7 Concluding Remarks . . . 71

4 Travelling Chemotactic Waves in a Periodic Porous Medium 73
4.1 Background Studies . . . 73
4.2 Mathematical Model . . . 74
4.3 Changing Variables for Numerical Simulations . . . 76
4.4 Numerical Investigations . . . 80
4.4.1 Immobile Aqueous Phase . . . 80
4.4.1.1 The Homogenised Model . . . 81
4.4.1.2 Effective Diffusion Tensors . . . 82
4.4.1.3 Effects of Growth Kinetics . . . 82
4.4.1.4 Effects of Chemotaxis Drift . . . 85
4.4.1.5 Initial Substrate Concentration Effects . . . 86
4.4.2 Mobile Aqueous Phase . . . 88
4.4.2.1 Advection–Diffusion Regime . . . 89
4.4.2.2 Advection–Dispersion Regimes . . . 90
4.4.3 Model Validation . . . 94
4.5 Concluding Remarks . . . 97

5 The Transverse Chemotactic Migration in a Porous Microfluidic Device 98
5.1 Overview of the Experimental Study . . . 99
5.2 The Mathematical Model . . . 101
5.2.1 Very Thin Porous Medium (VTPM) . . . 101
5.2.2 Laminar Flow in VTPM . . . 102
5.2.3 The Keller-Segel Model in VTPM . . . 103
5.2.4 Non-dimensionalisation . . . 104
5.2.5 Revisiting the Periodic Homogenisation Method . . . 106
5.3 Depth-Averaged Flow . . . 108
5.3.1 Formal Asymptotic Expansion of Brinkman Equations . . . 109
5.3.2 Local Depth-Averaged Flow . . . 111
5.4 Depth-Averaged Keller–Segel Model . . . 111
5.4.1 The Depth-Averaged Homogenised Keller-Segel Model . . . 112

5.4.2 The Classical Homogenised Keller-Segel Model 113
5.5 Numerical Investigations 115
5.5.1 Effective Dispersion Tensors 115
5.5.2 Effective Mixing Boundary Layer 117
5.6 Comparison Against Experimental Data 119
5.6.1 Testing the Classical Homogenised Model 119
5.6.2 Testing the Homogenised Depth-Averaged Model 121
5.7 Discussion and Conclusions 128

6 Conclusions **130**
6.1 Review of the Thesis 130
6.2 Future Work 132

List of Figures

1.1 A zone contaminated by DNAPL showing the source of the contamination (gray) and plume (yellow). At the pore scale, the dissolved contaminant resides in the aqueous phase (adopted and modified from Pak et al. [148]). 2

2.1 A schematic plot of the rectangular region domain $\Omega^* = [0, L_{x_1^*}] \times [-L_{x_2^*}/2, L_{x_2^*}/2]$. For the solid phase, Ω_s^*, we consider two porous configurations: a square array of solid circular inclusions and a hexagonal array of solid circular inclusions. The aqueous phase, the saturated porous structure, of the domain is denoted by Ω_f^*. See text for further details. Notice that the periodic porous media are not restricted to the given two microstructures. 14

2.2 Plots of the magnitude of chemotactic velocity, $\|\mathbf{v}_c^*\|$ [cm s^{-1}] of *E.coli* bacteria under a chemoattractant gradient in 1D using Eq.(2.3.12). The values of the gradient, $\|\nabla^* s^*\|$ [mM cm^{-1}], vary from 0 to 20 [mM cm^{-1}], and the chemoattractant concentration $\|s^*\|$ [mM] varies from 0 to 1 [mM]. The magnitude of chemotactic velocity defined in Eq.(2.3.12) is plotted in (a), and in (b) we plotted $\|\mathbf{v}_c^*\|$ when $\xi^* < 1$. For these simulations we assumed the following values of the parameters, $v_s = 22$ [µm s^{-1}], $\chi_0^* = 4 \times 10^{-5}$ [cm^2 s^{-1}], $K_d^* = 0.125$ [mM] [5]. . 21

2.3 Plots of the magnitude of chemotactic velocity, $\|\mathbf{v}_c^*\|$ [cm s^{-1}] with the same parameter values used in Figure 2.2. Here we used the chemotactic velocity defined using the receptor law in Eq.(2.3.16). The chemotactic velocity plotted exceeds the bacteria swimming speed in (a), but in (b) when satisfying the conditions $\xi^* < 1$, the magnitude of chemotactic velocity remains in an acceptable range as in Figure 2.2. 21

3.1 Conceptual illustration of the asymptotic homogenisation approach (dimensionless). For more details, please refer to text. 33

3.2 The three limiting cases we upscale in this chapter. 41

4.1 Schematic sketch of the porous domain investigated in this chapter. Where the domain length is $L^*_{x_1} = 6.25$ [cm] and width is $L^*_{x_2} = 0.65$ [cm]. The microstructure consisting of square arrays of circular inclusions, where the dimension of the representative volume element is $l_{y_1^*} = l_{y_2^*} = 250$ [µm]. 76
4.2 Schematic illustration adapted from [10] showing in (a) the standard homogenisation in a fixed domain Ω_ε and in (b) the rescaled homogenisation process with a constant periodicity cell and increasing domain $\widehat{\Omega}_\varepsilon = \varepsilon^{-1}\Omega_\varepsilon$. 79
4.3 Schematic sketch of the domain using the new reference frame $\widehat{\Omega}_\varepsilon$ where $\widehat{\Gamma}_s = \varepsilon^{-1}\Gamma_s$ and $\widehat{\Gamma} = \varepsilon^{-1}\Gamma$. The domain consists of $M \times N = 30 \times 25$ periodic unit cells $\widehat{Y}_\varepsilon$, where each cell is a translation of the unit cell Y^0; 80
4.4 Schematic sketch showing the initial bacteria concentrations injected into $\widehat{\Omega}_{in}$. (a) represents the case study when we assume an immobile aqueous phase, and (b) the case study when we assume a mobile aqueous phase. The dimensionless length and diameter of the initial injections is set as 20. 81
4.5 Plots showing the simulation results for the model in Eqs.(4.4.1) assuming the absence of growth/decay kinetics with the relevant parameters in Table 4.2. In (a) we give a one-dimensional (1D) bacteria traveling wave solution (solid lines) and the substrate fronts (dashed lines) plotted at $\tau = 0,\ 800,\ 1200,\ 2000,\ 2800$. In (b) we plotted the profiles of the chemotactic velocity given in Eq.(4.4.3) at $\tau = 800,\ 1200,\ 2000,\ 2800$. The plot in (c) shows the time evolution of 1D bacterial traveling bands and in (d) the plot shows the time evolution of 1D substrate fronts. The dashed lines in (c) and (d) corresponds to the travelling waves plotted in (a) at $\tau = 0,\ 800,\ 1200,\ 2000,\ 2800$. 83
4.6 Results of the simulations of the same model in Figure 4.5 for $\delta = 0.4$. In (a) we show the one-dimensional (1D) bacteria bands (solid lines) and the substrate fronts (dashed lines) plotted at $\tau = 0,\ 100,\ 300,\ 500,\ 700$. In (b) we plotted the profiles of the chemotactic velocity at $\tau = 100,\ 300,\ 500,\ 700$ for the same chemotactic velocity used in Figure 4.5. In (c) we plotted the time evolution of 1D bacterial traveling wave solutions (bands) and in (d) we plotted the time evolution of 1D substrate fronts. The dashed lines in (c) and (d) corresponds to the travelling waves plotted in (a) at $\tau = 100,\ 300,\ 500,\ 700$. 84

4.7 Simulation plots of the full model given in Eqs.(4.4.1) with the growth/decay kinetics for the parameters given in Table 4.2, where $\delta = 0.04$. The plots in (a) show the bacterial chemotactic bands (solid lines) and substrate fronts (dashed lines) plotted at $\tau = 0,\ 800,\ 1200,\ 2000,\ 2800$, (b) chemotactic velocity plotted at $\tau = 800,\ 1200,\ 2000,\ 2800$. In (c) and (d) plots show the time evolution of the 1D bacterial waves and 1D substrate fronts, respectively. The dashed lines in (c) and (d) corresponds with the bacterial bands and substrate waves in (a). 86

4.8 Using the parameter values in Table 4.2, in (a) we show the simulation results of the effective chemotactic model in Eqs.(4.4.1) in the absence of any metabolic rates, and in (b) we show the propagating Fisher–Kolmogorov–Petrovsky–Piskunov equation (F-KPP) waves obtained when $\chi_0 = 0$ in Eqs.(4.4.1). 87

4.9 Plots showing the chemotactic bacterial bands for the full chemotactic model Eqs.(4.4.1), including the growth/decay kinetics assuming the parameter values in Table 4.2. (a) Wave speeds for the three initial concentrations plotted for the same time interval. The wave speeds in (a) were plotted by tracking the position of position of the band peak against time τ. In (b) we plotted the travelling bacterial bands when $s^*_{in} = 28.3$ [mgL^{-1}], (c) when $s^*_{in} = 10$ [mgL^{-1}], and (d) when $s^*_{in} = 5$ [mgL^{-1}]. 87

4.10 Plots showing the simulation results of the model described in Section 4.4.2 of the chemotactic bacterial waves (solid lines) and the substrate (dashed lines) in stagnant flow (a) when no growth/decay kinetics were considered and (b) when growth/decay kinetics were considered at $\tau = 0,\ 800,\ 1000,\ 1200$. The plots in (c) and (d) are repeated simulation results when $\widehat{\mathrm{Pe}} = 0.02$ at $\tau = 0,\ 800,\ 1000,\ 1200$. Note that the parameters given in Table 4.2 were used. 89

4.11 Numerical simulations for the full effective model in Eqs.(4.3.8) and Eqs.(4.3.10) when (a) $\widehat{\mathrm{Pe}} = 0.02$ and (b) $\widehat{\mathrm{Pe}} = 0.1$ at $\tau = 450,\ 750$. Note that the plots here are 2D visualisation of the bacteria bands given in Figure 4.10(c) and (d). 90

4.12 Semi-log plots for the eigenvalues of the dispersion tensors of the substrate, the bacteria, and the chemotactic drift. The x-axis is the logarithmic scale of the Péclet number and y-axis is the linear scale of the bacterial dispersion tensors components. 91

4.13 Plots showing the numerical simulations of the model described in Eqs.(4.4.30). The Plots show the effect of the effective diffusion tensor (left) and dispersion tensor (right) on the growth expansion of the population. The dispersion tensor is computed for $\widehat{\mathrm{Pe}} = 5$. 93

4.14 Schematic sketch showing (a) the subdomain $\widehat{\Omega}'_\varepsilon$ with microstructure consisting of $N = 250$ circular inclusion, where in (b) we give a closer look at the microstructure of the subdomain. The homogenised subdomain is shown in (c) and (d). 94
4.15 Plots of the simulation results showing the location of the peaks for both the exact and effective travelling waves using the parameter values listed in Table 4.2. The density peaks obtained from the chemotactic model simulation and the density peaks obtained from the F-KPP model simulation are plotted for the same time steps in (a) and (b), respectively. 95
4.16 Relative errors in the density peaks and speed, plotted for the same time steps for different initial substrate concentrations. 96

5.1 Schematic illustration of the T-sensor, where (a) shows the top view of the device in the $x_1^* x_2^*$-plane with the main channel dimensions with length of $L_{x_1^*} = 8.3$ [cm] and width of $L_{x_2^*} = 0.6$ [cm], note that the height of the channel $H^* = 13$ [μm] is much smaller that its width. In (b) we show a cross section illustrating the microstructure of the main channel and zoomed-in view in (c). The two-dimensional periodic cell is shown in (d) with dimensions of $l_{y_1^*} = 425.7$ [μm] and $l_{y_2^*} = 246$ [μm]. 100
5.2 An illustration showing the effect of the shallow channel on the flow. In (a) we plot a rectangular duct channel (not proportional to the real domain measurements); (b) shows the uniform axial flow (the axial flow in the main channel), and (c) the parabolic flow between the two parallel plates in the z^*-direction. Note that the cylindrical pillars are omitted for clarity and the horizontal velocity profile in (b) represents the homogenised/averaged velocity profile. 102
5.3 Schematic plots showing 3D (a) $\boldsymbol{Y}$ periodic unit, (b) $\boldsymbol{Y^0}$ aqueous phase, and (c) $\boldsymbol{\Sigma}^0$ solid phase. 107
5.4 Schematic plots showing the simplified 2D (a) Y periodic unit, (b) Y^0 aqueous phase, and (c) Σ^0 solid phase with boundaries defining the aqueous-solid interface $\partial\Sigma^0$. 107
5.5 Log-log plots for eigenvalues of the dispersion tensors for the chemoattractant, bacteria ($D^{*\star} = D_b^*$) and the chemotactic drift ($\varepsilon^{-1} = 195$). The vertical lines mark the orders ε^{-1} and ε^{-2}. The effective tensors were obtained by solving (5.4.16) defined on the periodic unit cell shown in Figure 5.4. While the zero order flow approximation in (5.4.16) is derived from the homogenisation of the 2D Stokes equation in porous media, as demonstrated in Section 3.2. 116

5.6 Numerical results of the homogenised model in the 2D domain: (a) dimensional spatial distribution of the chemoattractant concentration $\mathcal{S}^*$ under different flow velocities and (b) spatial concentration of the chemoattractant gradient $\|\nabla^*\mathcal{S}^*\| = \sqrt{\left(\partial\mathcal{S}^*/\partial x_1^*\right)^2 + \left(\partial\mathcal{S}^*/\partial x_2^*\right)^2}$. The plots were obtained by solving (5.4.16) defined on the periodic unit cell shown in Figure 5.4. The zero order flow approximation in (5.4.16) is derived by upscaling the 2D Stokes equation in porous media, as demonstrated in Section 3.2. 118
5.7 (a) Illustration of the non-dimensional mixing boundary layer. (b) Full width at half maximum of the Gaussian probability density curve FWHM. Using direct numerical simulations, we computed FWHM using a MATLAB function [143] ((FWHM) $= 2\sqrt{2\ln 2}\,\sigma \sim 2.355\sigma$). 119
5.8 Plots of the boundary layer width at transient locations represented with indices $i = 2 \cdots 195$, such that $x_1(i) \leftarrow i$. Here we are solving (5.4.16) defined on the periodic unit cell shown in Figure 5.4. where the zero order flow approximation in (5.4.16) is derived by upscaling the 2D Stokes equation in porous media, as demonstrated in Section 3.2. Red curves denote the width of boundary layers computed assuming the original model defined in a 2D non-porous domain, whereas blue curves denote boundary layers using the homogenised model. 120
5.9 Plots with the predicted tracer profiles using the homogenised classical model in (5.4.14)-(5.4.19) modified to consider the transport of the tracer alone. The profiles were plotted against the experimental data from Long and Ford [122]. In these simulations we assumed both the superficial velocity, $\langle \mathbf{v}_0^* \rangle_{Y^0} = V_{avg}^*$, and interstitial linear velocity, $\langle \mathbf{v}_0^* \rangle_{Y^0} = \phi^{-1} V_{avg}^*$. 122
5.10 Plots with the predicted bacteria profiles for the non-chemotactic test (control test) using the classical model in (5.4.14)-(5.4.19) modified to consider the transport of the bacteria alone. The bacterial density was scaled by the initial injected density and plotted against the experimental data from Long and Ford [122]. As in Figure 5.9, we assumed both the superficial velocity, $\langle \mathbf{v}_0^* \rangle_{Y^0} = V_{avg}^*$, and interstitial linear velocity, $\langle \mathbf{v}_0^* \rangle_{Y^0} = \phi^{-1} V_{avg}^*$. 123
5.11 Plots of the predicted chemotactic bacterial population profiles using the classical model in (5.4.14)-(5.4.19), the bacterial density was scaled by the initial injected density and plotted against the experimental data from Long and Ford [122]. As before, in the simulations we assumed both the superficial velocity, $\langle \mathbf{v}_0^* \rangle_{Y^0} = V_{avg}^*$, and interstitial linear velocity, $\langle \mathbf{v}_0^* \rangle_{Y^0} = \phi^{-1} V_{avg}^*$. 124

5.12 Plots comparing the predicted tracer profiles obtained from simulating the homogenised classical model in (5.4.14)-(5.4.19) and the depth-averaged model in (5.4.7)-(5.4.12) after being modified to account for the tracer transport only. The tracer profiles are plotted against the experimental tracer data from Long and Ford [122] while assuming $\langle \mathbf{v}_0^* \rangle_{Y^0} = \langle \bar{\mathbf{v}}_0^* \rangle_{Y^0} = \phi^{-1} V_{avg}^*$. 125
5.13 Repeated tests comparing the predicted control profiles against the experimental control data from Long and Ford [122]. Here we conducted simulations of the classical model in (5.4.14)-(5.4.19) and the depth-averaged model in (5.4.7)-(5.4.12) after being modified to account for the transport of the bacterial density in the control test only. In the simulations we assumed that $\langle \mathbf{v}_0^* \rangle_{Y^0} = \langle \bar{\mathbf{v}}_0^* \rangle_{Y^0} = \phi^{-1} V_{avg}^*$. 126
5.14 Plots comparing the chemotactic test data from Long and Ford [122] against the predictions obtained from the simulations of the classical model in (5.4.14)-(5.4.19) and the depth-averaged model in (5.4.7)-(5.4.12). Here we are assuming $\langle \mathbf{v}_0^* \rangle_{Y^0} = \langle \bar{\mathbf{v}}_0^* \rangle_{Y^0} = \phi^{-1} V_{avg}^*$. 127

Chapter 1

Introduction

Over the past decades, organic pollutants have been discarded irresponsibly [142]. In the United States alone, it is estimated that conventional decontamination techniques will cost $1 trillion [142, 49]. Often, the key contributors to the spread of organic contamination in soil and groundwater is the unintentional release and improper disposal of solvents and petroleum-based products into the soil. These organic compounds often form non-aqueous phase liquids (NAPLs) that acts as long-term sources of contamination [216]. While large NAPL pools can be removed, residual amounts often remain lodged in the soil. Even under flowing water, these trapped NAPLs may stay immobile, acting as small, scattered sources of contamination that gradually dissolve into groundwater. The natural flow of the groundwater forms a contaminated plume downstream of the NAPL source which is difficult to eliminate (see Figure 1.1). Recognising the high cost and impracticality of fully removing all trapped contaminants, researchers have explored the role of the microbial communities in subsurface environments and how they can be used to develop safe alternatives to physicochemical remediation strategies, such as pump-and-treat methods [128, 104, 149].

Bioremediation is an alternative remediation strategy where removing pollutants involves bacterial populations. It is an environmentally friendly and cost-effective method for treating contamination and can be applied to various contaminants, including NAPLs [187]. Studies have shown that bacterial populations migrate chemotactically toward contaminants [85, 110, 147, 149, 152, 151, 215]. Others provided experimental evidence of chemotaxis's role in the biodegradation of different pollutants [130, 205, 171]. However, only some laboratory studies mimicking subsurface environments investigated if microbial motility and chemotaxis migration can occur in heterogeneous media. [144, 77, 122, 66, 111]. As a result, experimental data sets are limited, and there is still much to be done to explore how confinement at the pore scale alters bacterial motility and chemotaxis.

This chapter provides general background on bacterial transport in porous media. First, we start with the well-demonstrated and characterised microbial transport processes in an aqueous system: random motility and chemotaxis. The former allows

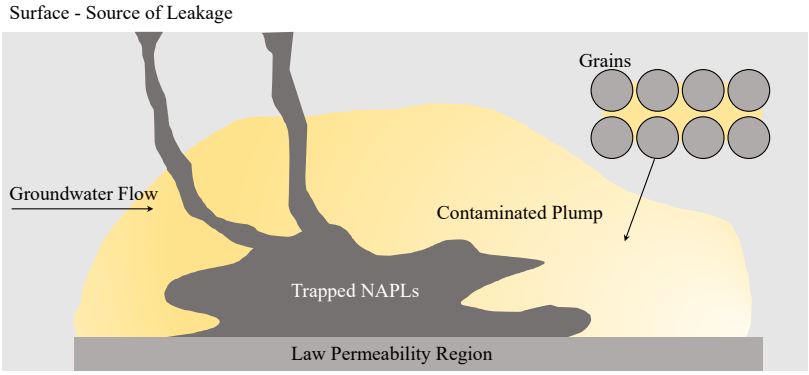


Figure 1.1: *A zone contaminated by DNAPL showing the source of the contamination (gray) and plume (yellow). At the pore scale, the dissolved contaminant resides in the aqueous phase (adopted and modified from Pak et al. [148]).*

bacteria to move independently of chemical signals, whereas the latter allows motile bacteria to detect chemical gradients in their environment. Next, we set the stage to discuss the current thesis's justification, relevance, and limitations by reviewing some pertinent laboratory and mathematical studies on random motility and chemotactic migration in porous media. Finally, the chapter concludes with an outline of the remaining chapters of the thesis. Note that more specific background reviews regarding the mathematical model developed in this thesis and the computational case studies are presented within each main research chapter.

1.1 Bacterial Transport in Bulk Aqueous Solution

Motility is a critical strategy for bacteria to navigate their environments. Berg and Brown [31] were the first to quantify the swimming behaviour of a single bacterial cell in an isotropic solution using a three-dimensional microscope. The behaviour is regarded as a three-dimensional random walk consisting of constant runs interrupted by brief reorientations. The swimming pattern of an individual cell consists of a series of runs and tumbles. Like diffusion, the ultimate macroscopic consequence of all random motility is the uniform distribution of cells within a medium. This behaviour is quantified at the level of the individual cell by the linear run speed, the duration of the run, and the turn angle between two successive runs. Later, Lovely and Dahlquist [126] linked the individual behaviour with the macroscopic transport

parameter describing the motility at the population scale, μ_0^* as

$$\mu_0^* = \frac{v_s^2 \tau}{3(1 - \langle \cos\theta \rangle)}, \tag{1.1.1}$$

where v_s is the experimentally measured bacterial swimming speed, τ is the mean run time, $\langle \cos\theta \rangle$ is the bacterial directional persistence and θ is the turn angle distributions. This definition is reduced to the commonly used equation for bulk diffusion for a bacterial cell with no random walk bias [65],

$$\mu_0^* = \frac{v_s^2 \tau}{3}. \tag{1.1.2}$$

The parameters in Eq.(1.1.1) are measured using either a three-dimensional tracking microscope [31, 197] or a three-dimensional defocused particle tracking methodology [208]. Other experimental techniques can directly quantify the diffusive-like macroscopic parameter, such as capillary assays [3, 175] and stopped-flow diffusion chamber [80, 5]. The parameters obtained with all the different approaches are consistent [116, 5]. In general, the average run length of bacteria is longer than the diffusion length of chemical solutes, and thus, the random motility is one order of magnitude slower than dissolved chemicals in the aqueous phase.

Chemotaxis is the biased random movement of bacteria in response to a chemical concentration gradients in their environment. The process is controlled by specialised proteins called chemoreceptors located at the surface of the bacterium's cell body. When attached to certain substances in the environment, these receptors initiate a signalling cascade within the bacterium that eventually regulates flagellar rotation. The direction and velocity of the chemotactic movement is regulated by the bacterium's ability to compare the fraction-bound receptors at different times as it swims across certain concentration gradients [166, 32]. This results in an extended bacterial run length to either approach or flee the increasing chemical gradient.

There are two common chemotactic strategies: the metabolism–independent and the metabolism–dependent mechanisms. The former is the strategy by which the bacterium reacts to the concentration of attractant chemicals in its local surroundings and is independent of the current metabolism state of the bacteria. The latter is where the bacteria react to metabolites created during the nutrient breakdown rather than directly detecting it [69, 74]. However, studies often adopt the convention that views chemotaxis as being attracted by the nutritional preferences of bacteria. The correlation between the chemotactic and metabolic preferences of the bacteria was the main strategy adopted by many early studies [4, 188, 134] and later when studying the chemotactic migration towards environmental pollutants in the bioremediation field [105, 152, 151, 86, 109].

In a static bulk medium, a single bacterium chemotaxis is quantified as a biased random walk style [66]. At the population level, the chemotactic migration of bacteria

is described following a convective-like transport coefficient [16, 166, 44]. For instance, in a shallow chemoattractant gradient, the chemotactic velocity is given by

$$\mathbf{v}_c^* = \frac{\chi_0^*}{3} \frac{K_d^*}{(K_d^* + s^*)^2} \nabla^* s^*, \tag{1.1.3}$$

where χ_0^* is the chemotactic sensitivity coefficient, K_d^* is the attractant receptor dissociation coefficient, and s^* is the chemoattractant concentration and ∇^* is the gradient.

1.2 Bacterial Transport in Porous Media

In general, observing bacterial activities in field studies can be challenging due to the complexity of the environment. The subsurface environment is often highly heterogeneous, with a wide range of different types of soil and rock and varying levels of porosity and permeability. Also, the flow dynamics in subsurface environments can be complex, with varying flow rates and directions. On the other hand, laboratory studies operate on much shorter time and spatial scales than most field studies, making it easier to control and isolate a single process to study. Bacterial motility and chemotaxis are often studied at various lengths and time scales in the field and the laboratory. The different spatial scales vary from $1 - 10$ [m] in field studies, $10^{-1} - 1$ [m] in packed columns, 10^{-2} [m] in micro-models (e.g., microfluidic devices), 10^{-3} [m] in capillary assay and $10^{-5} - 10^{-6}$ [m] in tracing microscopes.

1.2.1 Bacterial Random Motility in Porous Media

The ability of the bacterium to navigate the solid matrix in a static porous medium is impacted by the limited amount of space it must move before changing orientation. Because of this, the actual overall movement of the swimming bacterium is longer than what it would be in a bulk aqueous solution. Many experimental studies [164, 23, 24, 153, 178, 144] have qualitatively supported the predicted decrease in the random motility of bacteria in porous media. To describe the random motility, these studies used the following up-scaling defined as [24]

$$\frac{\mu_{\text{eff}}^*}{\epsilon} = \frac{\mu_0^*}{\tau_b}, \tag{1.2.1}$$

where μ_{eff}^* is the effective random motility, ϵ is the porosity and τ_b is the bacterial tortuosity. Note that, the up-scaling in Eq.(1.2.1) has the same form as the conventional method for up-scaling the diffusion parameter of a solute, D_s^*,

$$\frac{D_{\text{eff}}^*}{\epsilon} = \frac{D_s^*}{\tau_0}, \tag{1.2.2}$$

where τ_0 is the solute tortuosity, which is an empirical parameter that accounts for the effect of the morphology of the porous medium on diffusion [26]. To estimate τ_b,

the bacteria is assumed to be more likely to collide with solid surfaces, a behaviour similar to Knudsen diffusion given by

$$\mu_k^* = \frac{d_p v_s}{3}, \tag{1.2.3}$$

where d_p is the mean-pore size [89, 23, 65, 24, 77, 64, 45]. When the Knudsen diffusion dominates, the bacterial tortuosity is defined as

$$\tau_b = \tau_0\Big(1 + \frac{\mu_0^*}{\mu_k^*}\Big). \tag{1.2.4}$$

Note that if the pore size exceeds the mean bacterial run length, the tortuosities of the substrate and bacteria are assumed to be equal [124]. In many experimental studies, gas kinetic theory significantly underestimated bacterial tortuosity in static saturated soil columns [145]. Chen et al. [45] reported that the failure was due to a violation of the majority of the assumptions required to apply Knudson diffusion. Unlike gaseous particles, bacteria do not reflect when they come into contact with a solid surface; instead, they exhibit steric inhibition, where they start a series of tumbles (hops) until a sufficiently large turn angle is achieved that leads to moving away from the solid surface [197, 107, 119, 108, 120, 34, 106].

Several studies were devoted to quantifying the bacterial behaviour near solid surfaces. Nonetheless, these previous microscope observations gave divergent observations. For example, some experimental studies reported that motility decreases deposition at the solid surface [55], while others reported higher deposition of motile strains in parallel plate flow [131]. In addition, some packed-bed studies reported that motile bacteria strains have less surface attachment than non-motile bacteria [164, 43, 127]. On the other hand, recent research by Mok et al. [136] reported a higher accumulation of motile bacteria on flat surfaces than on concave surfaces. To derive the random motility of the bacteria in view of the swimming behaviour of the bacteria near the solid porous phase, Licata et al. [117] modified the random motility in Eq.(1.1.1) using analysis similar to what was used in [126] to a homogeneous porous medium. The analysis demonstrated that bacterial diffusivity differs from Knudson diffusion. Moreover, they argued that in the limit of large pore size, $d_p \gg v_s\tau$, the bacteria's random motility at the pore level is the same as in Eq.(1.1.1). At small pore size, $d_p \ll v_s\tau$, the modified random motility is set as

$$\mu_p^* = \frac{1}{6}\frac{(1 + \langle\cos\theta\rangle)}{1 - \langle\cos\theta\rangle} v_s\tau. \tag{1.2.5}$$

However, the directional persistence $\langle\cos\theta\rangle$ values depend on the effect of the confined geometries on the turning mechanism of the bacterium and the effect of steric inhibition.

A recent work by Bhattacharjee and Datta [35] focused on the swimming trajectories generated by the steric inhibition. They suggested a new method to estimate

the long-time bacterial translational diffusivity using experimental measurements of bacterial hopping and trapping near solid surfaces, thus, the long-time diffusivity is measured as $\approx \langle l_h \rangle / 3\langle \tau_t \rangle$, where l_h is the hop lengths and τ_t is the trapping durations of the bacteria on the solid surface. Here, the hop lengths are assumed to be much larger than the run length of the bacterium in bulk liquid, which reflects the profound effect of small pore size on bacterial random motility. Later Dehkharghani et al. [58] suggested the large-scale diffusivity in pore space is regulated by the cutoff of their persistent motility,

$$\mu_p^* = \frac{\mu_0^*}{\left(1 + \frac{l_{\text{run}}}{d_p}(1 - \langle \cos\theta \rangle)\right)}, \tag{1.2.6}$$

where, $l_{\text{run}} = v_s \tau$ is the bacterium's run length in bulk. However, they also reported that this local measurement of random motility fails to predict effective diffusivity for relatively larger pore sizes.

Flow in porous media complicates the interactions between bacteria and the solid matrix. The transport of bacteria in advective flows has often been treated in the same manner as the solute dispersion experiments in porous media. Thus, the effects of the flow on the bacteria's motility can be quantified with the bacterial longitudinal α_L and transverse dispersion α_T; the dispersion coefficients defined as

$$\mu_L^* = \alpha_L v_{\text{f}} + \frac{\mu_{\text{eff}}^*}{\epsilon}, \qquad \mu_T^* = \alpha_T v_{\text{f}} + \frac{\mu_{\text{eff}}^*}{\epsilon}, \tag{1.2.7}$$

where v_{f} is the averaged linear velocity of the flow, and the conventional upscaling of a solute's diffusivity is defined as

$$D_L^* = \alpha_L^s v_{\text{f}} + \frac{D_{\text{eff}}^*}{\epsilon}, \qquad D_T^* = \alpha_T^s v_{\text{f}} + \frac{D_{\text{eff}}^*}{\epsilon}. \tag{1.2.8}$$

According to the Taylor–Aris dispersivity for solute [68, 53], the longitudinal dispersivity increases as a function of the pore-scale Péclet number $\text{Pe} = v_{\text{f}} d_p / \mu_0^*$. Recently, experimental observation and theoretical analysis showed that the hydrodynamic dispersion exhibited by the self-propelled bacteria could be different from passive solute particles. Dehkharghani et al. [57], in their experimental study using a microfluidic device equipped with a periodic lattice of cylindrical pillars, reported that the longitudinal dispersivity of the bacteria exhibits a non-monotonic behaviour as a function of pore-scale Péclet number. Later, Peng and Brady [154] showed, using theoretical analysis of active Brownian particles, that the shear rate can hinder the bacterial dispersion in parallel flows under certain flow and confinement circumstances. They showed that the classical Taylor dispersion theory is valid whenever the mean-pore length exceeds the bacterial run length.

1.2.2 Chemotaxis Migration in Porous Media

In static porous media, different experimental studies have identified and documented chemotactic migration. Sharma et al. [176] observed that the non–chemotactic bac-

teria migration is diffusive while the metabolic–mediated chemotactic migration is observed by the distinctive chemotactic bands formed. A chemotactic band refers to a pattern formation phenomenon in which the bacteria self-organise into a dense band when placed in one end of a capillary tube (or rings of bacteria in the case of agar plates) [99, 2]. Under specific growth conditions, the band profile is maintained, and the band propagates at constant speed as a gradient of an energy source is created, causing the population to preferentially move in the direction of the higher concentration of the chemical [113, 38]. Pedit et al. [153], detected the chemotactic response by observing the migration of the bacteria located in the glass-backed reservoir in response to a localised attractant gradient near the glass bead packed capillary essay. Pedit et al. [153] reported that the chemotactic response in capillaries filled with glass beads was found to be smaller than that observed in bulk aqueous solution. Sometimes, the chemotactic migration could not be detected in conventional sand-packed columns [164, 23] often due to limited detection methods. However, even when using magnetic resonance imaging (MRI), Olson et al. [144] only detected and quantified a small but statistically significant chemotactic response. In swarm plate assays filled with sand, Roush et al. [167] detected an enhanced chemotactic response, probably due to the relatively large gradient generated by consumption. Wang et al. [201] observed an enhanced chemotactic migration toward higher nutrient concentrations in static porous media over long periods of time. Because the attractant gradient generated by consumption is proportional to the bacterial abundance, the interplay between chemotactic bacteria and population increase is what causes the enhanced chemotactic migration.

Chemotaxis also helps bacteria move through a porous matrix with the advective flow. Wang and Ford [199, 200], observed and quantified bacterial chemotaxis migration in a heterogeneous porous media under typical groundwater flow conditions using sand columns. Interestingly, they reported that chemotactic bacteria were less likely to deposit on the solid surface compared to non-chemotactic bacteria [196, 199]. Using a microfluidic device with a periodic pattern of staggered cylinders, Long and Ford [122] observed the chemotactic bacteria's migration in a direction perpendicular to the flow. In addition, as the flow rate increased, they observed a decrease in transverse chemotactic migration. In general, bacterial chemotaxis was quantified by the effective chemotaxis sensitivity coefficient in all the above studies as [144, 122]

$$\frac{\chi^*_{\text{eff}}}{\epsilon} = \frac{\chi^*_0}{\tau_b}. \tag{1.2.9}$$

Recently, de Anna et al. [54] used a microfluidic model system. The system consists of microfluidic device fabricated to mimic heterogeneous porous microstructure using a disordered arrangement of discs and crescent-shaped obstacles. Unlike the previous studies, which focused on macro-scale observations of bacterial displacements, de Anna et al. [54] focused on observing the effect of chemical gradient distribution at the pore scale on the chemotactic bacteria.

1.2.3 Mathematical Modelling and Computations

Many of the laboratory studies mentioned above utilised mathematical simulations to broaden their findings in order to incorporate the effects of the various parameters that can influence bacterial migration in porous media, such as porosity and flow rates. Because of the small computational domain, it was possible to undertake direct simulations in certain experimental research. For instance, Dehkharghani et al. [57] examined the effect of fluid flow on the transport of swimming bacteria and conducted direct Langevin simulations. de Anna et al. [54] also was able to perform direct simulations of the Keller-Segel model [98, 100] benefiting from the small computational domain. The Keller-Segel model direct simulations consists of two equations describing the transport of chemoattractant concentration and bacterial density. The chemoattractant concentration field s^* satisfies the following advection-diffusion equation,

$$\frac{\partial s^*}{\partial t^*} = \nabla^* \cdot \big(D_s^* \nabla^* s^* - \mathbf{v}^* s^*\big), \tag{1.2.10}$$

where $\mathbf{v}^* = (u^*, v^*)$ is the velocity field that satisfies the Stokes equations with no-slip conditions on the perimeter of the solid obstacles. The bacterial concentration field b^* satisfies the following equation,

$$\frac{\partial b^*}{\partial t^*} = \nabla^* \cdot \big(\mu_0^* \nabla^* b^* - [\mathbf{v}_c^* + \mathbf{v}^*] s^*\big). \tag{1.2.11}$$

de Anna et al. [54] assumed that the chemotactic velocity of the bacteria is linearly dependent on the chemoattractant concentration gradient,

$$\mathbf{v}_c^* = \lambda \nabla^* s^*, \tag{1.2.12}$$

where λ is the strength of the chemotactic response. Both species are equipped with no-flux boundary conditions on the perimeter of pillars. In most laboratory experiments, however, it is not possible to conduct direct simulations due to the complexity of the porous structure; instead, simulations are performed on effective medium models. Olson et al. [146] proposed the following effective medium model

$$\frac{\partial s^*}{\partial t^*} = \nabla^* \cdot \big(\mathbf{D}_{\text{eff}}^* \nabla^* s^* - \bar{\mathbf{v}}^* s^*\big), \tag{1.2.13a}$$

$$\frac{\partial b^*}{\partial t^*} = \nabla^* \cdot \big(\boldsymbol{\mu}_{\text{eff}}^* \nabla^* b^* - [\bar{\mathbf{v}}_c^* + \bar{\mathbf{v}}^*] s^*\big), \tag{1.2.13b}$$

where, $\bar{\mathbf{v}}^* = (u^*, 0)$ is the averaged linear velocity of the flow (Darcy flow), and the effect chemotaxis velocity, $\bar{\mathbf{v}}_c^*$, is defined in terms of Eq.(1.1.3) and Eq.(1.2.9) as:

$$\bar{\mathbf{v}}_c^* = \frac{\chi_{\text{eff}}^*}{\epsilon} \mathbf{v}_c^*. \tag{1.2.14}$$

The effective tensors are defined in terms of Eq.(1.2.7) and Eq.(1.2.8) as

$$\mathbf{D}^*_{\text{eff}} = \begin{pmatrix} D^*_L & 0 \\ 0 & D^*_T \end{pmatrix}, \qquad \boldsymbol{\mu}^*_{\text{eff}} = \begin{pmatrix} \mu^*_L & 0 \\ 0 & \mu^*_T \end{pmatrix}. \tag{1.2.15}$$

Note that an effective medium model often refers to a macro-scale model with effective parameters that captures the effects of pores on chemotactic transport. The tortuosity τ_0 needed in the effective parameters is challenging to measure and is often obtained by the averaged best-fit solution to experimental data [144]. Olson et al. [144, 146] postulated that less chemotactic migration occurs when reducing bead size than is observed in the larger beads, and thus, the migration is reduced when the run length is similar to the mean pore size. However, Long and Ford [122] numerical simulations of the effective model above did not show any chemotactic response even though the run length was smaller than the mean pore length. In fact, under a slow flow rate, the experimentally observed chemotactic response was several orders of magnitude higher than any observed in conventionally packed columns.

Valdés-Parada et al. [194] applied the volume averaging method (VAM) to upscale the Keller-Segel model and obtained an effective medium model. Two effective coefficients concerning the bacterial chemotactic transport were introduced: a total motility tensor, representing the combined effect of the flow and chemotaxis dispersion, and a total velocity vector, representing the additive chemotaxis and flow advection. Afterward, Porter (2011) applied the effective Keller-Segel model to the experimental study of Long and Ford [122]. The simulations using the successfully predicted the chemotactic drift compared to the model in Eqs.(1.2.13). However, the model simulations underestimated the transverse chemotactic migration at slow flow rates. Although the effective medium model upscaled using VAM reduced the computational complexity due to microstructure, it continues to be numerically challenging to determine the effective parameters of the bacterial equation due to the dependence on the spatial distribution of the chemical gradient.

From this discussion, it is clear that a comprehensive understanding of chemotactic transport in porous media is lacking. Moreover, the majority of the findings of the previous studies remain at the empirical level; and the mathematical models did not successfully predict or explain many of the experimental observations. The contribution of this thesis is in the context of upscaling a Keller-Segel model which also include cellular growth/death and consumption of the attractant using asymptotic homogenisation method. Unlike volume averaging, asymptotic homogenisation requires detailed understanding of the time scales governing the mass transport models. Thus, in this thesis the effective medium model is different than the one derived in Valdés-Parada et al. [194].

1.3 Outline of Thesis

In Chapter 2, we outline a two-dimensional Keller-Segel model in arbitrary periodic porous media, considering metabolic rates and flow. First, we describe the porous domain, which is comprised of periodic subdomains, each of which is a duplicate of a typical representative volume element (RVE). After that, we give an argument concerning the validity of the continuum model at the pore scale. Namely, we follow the common assumption that the behaviour of the bacteria when the run length is much smaller than a given pore measure is diffusive. In the aqueous phase of the porous domain, the flow is unidirectional and is governed by the Stokes equations with no-slip boundary conditions at the interface between the aqueous phase and the pore solid surface. Then, we give a detailed description of a Keller-Segel model, including the attractant's consumption rates and cellular growth and death rates. The bacteria are assumed not to attach to the solid phase of the porous structure assuming that the duration the bacteria spend on the solid surface is negligible. Lastly, we perform a non-dimensional analysis of the model. This step is vital to understanding the microscopic behaviour governing the transport model. The model in this chapter is not novel. However, the argument we give to estimate the carrying capacity of the logistic growth is first proposed in our work.

In Chapter 3, we derive an effective form of the model described in Chapter 2. The chapter starts by illustrating the concepts of the formal asymptotic homogenisation method. Before applying the asymptotic homogenisation, it is vital to describe accurately the model at the micro-scale by proposing all the possible scales of the different processes governing the mass transfer of the two species. At the pore scale, we argue that the two species' mass flow is governed only by the advection strength. The main objective of Chapter 4 is to give a numerical validation of the effective models developed in Chapter 2. The work in this chapter is particularly relevant to the paper by Yan and Hilpert [211], where we compare simulations of the effective model with the direct simulations of the original model. Chapter 5 is relevant to the paper by Long and Ford [122]; where we use the relevant effective model in Chapter 3, however, since the microfluidic device is three-dimensional, it is important account for the affects of the shallow depth on the model defined in Chapter 2 and 3. For this, we introduce a depth-averaged flow and implement Taylor diffusivity theory. Then, we compare the simulation results of the effective model with the experimental data and the model's results developed by volume averaging in Porter et al. [157]. Finally, in Chapter 6, we summarise the main results and suggest some directions for future work.

1.4 Statement of Originality

In Chapter 2, the model described is not original; however, the estimation of the carrying capacity in the logistic growth term is. In Chapter 3, we claim the originality of the asymptotic homogenisation approach starting from Section 3.3. In Chapter 4, the application of the homogenised model and the analysis are original. Although the ideas behind the numerical simulations were borrowed from to the paper by Yan and Hilpert [211]. Finally, in Chapter 5 the originality is claimed starting from Section 5.2 with the except to the data used for comparison without simulation results.

Chapter 2

Keller-Segel Model Incorporating Confinement, Flow and Metabolic Rates

Microbial activity and chemotaxis play an important role in the bioremediation field in aiding the removal of subsurface contaminants [181]. However, the mathematical models used to describe the biodegradation process in a porous medium often incorporate the microbial metabolic rates but neglect the role of chemotaxis in the biodegradation process. On the other hand, mathematical models used to explore chemotaxis transport in porous media often ignored the population's metabolic processes. In this chapter, we describe a general form of the classical Keller-Segel model [99, 97, 115, 82, 50] that incorporates spatial confinement, medium flow, and microbial proliferation as in [125, 211, 212]. We will consider a simplified model as an important step toward gaining a deeper understanding of microbial chemotactic migration in subsurface environments.

We begin with a brief discussion of the assumptions that justify applying a continuum model to describe microbial transport in a porous medium. Then we describe a two-dimensional general Keller-Segel model consisting of two mass transport equations for the substrate and bacterial concentrations under flow conditions. We assume a completely dissolved substrate and bacterial suspension in the aqueous phase. Advection of the two species in an aqueous medium is described by a unidirectional laminar flow where we neglect any possible shear rate effects over the bacteria swimming behaviour. The model timescales and governing fluxes are defined using realistic parameter values found in the literature, measured in non-porous aqueous phase under quiescent conditions. We carry out a non-dimensional analysis to determine the model's characteristic time and spatial scales. This step is vital for starting the asymptotic homogenisation process in the following chapter.

2.1 Domain of the Model

Through out this chapter we assume an arbitrary periodic porous medium. The domain of interest is $\Omega^* \subset \mathbb{R}^2$ characterised by the global/macro length-scale $L^*_{x_1}$ (see Figure 2.1) and boundaries $\partial\Omega^*$ such that

$$\Omega^* = [0, L_{x_1^*}] \times [-L_{x_2^*}/2, L_{x_2^*}/2], \tag{2.1.1}$$

The domain consists of two periodic phases, a solid phase Ω^*_s and an aqueous phase Ω^*_f, such that

$$\Omega^* = \Omega^*_s \cup \Omega^*_f. \tag{2.1.2}$$

The domain boundaries consist of the solid-aqueous interface, denoted by Γ^*_s, and those of the exterior boundary, denoted by Γ^*,

$$\partial\Omega^* = \Gamma^*_s \cup \Gamma^*. \tag{2.1.3}$$

The exterior boundaries are the union of the four sides of the domain Ω^* as seen in Figure 2.1,

$$\Gamma^* = \Gamma^*_T \cup \Gamma^*_B \cup \Gamma^*_L \cup \Gamma^*_R, \tag{2.1.4}$$

without any loss of generality, we assume the exterior boundary and solid-aqueous interface do not intersect. The mass transport of both the bacteria and the attractant concentration takes place in the aqueous phase Ω^*_f which is assumed to be connected and saturated by an aqueous fluid. The aqueous phase Ω^*_f is what we refer to as a saturated porous medium. A point in Ω^*_f is referred to as $\mathbf{x}^* = (x^*_1, x^*_2)$, hence, the differential operators are of the form,

$$\nabla^* = \left(\frac{\partial}{\partial x^*_1}, \frac{\partial}{\partial x^*_2}\right), \tag{2.1.5}$$

$$\nabla^{*2} = \frac{\partial^2}{\partial x^{*2}_1} + \frac{\partial^2}{\partial x^{*2}_2}. \tag{2.1.6}$$

The domain Ω^*_f is locally periodic and defined as the union of periodic sub-domains viewed as linear translations of a spatial unit-cell characterised by the local/micro length-scale $l^*_{y_1}$. The two spatial scales are well separated, i.e.

$$\varepsilon = \frac{l^*_{y_1}}{L^*_{x_1}} \ll 1, \tag{2.1.7}$$

where ε is the dimensionless separation of scale parameter. The periodic sub-domains (microstructure) are represented either as square arrays or a periodic structure of hexagonal arrays and with porosity ϕ (see Figure 2.1). Further details are given in Section 3.1 of Chapter 3.

Remark 2.1. *In the case of a random porous medium, Auriault [20] argues that random and periodic media have the same macroscopic descriptions when they exist. Therefore, understanding the effective model in a periodic structure is an important step to gain insight into chemotactic migration in a random porous medium.*

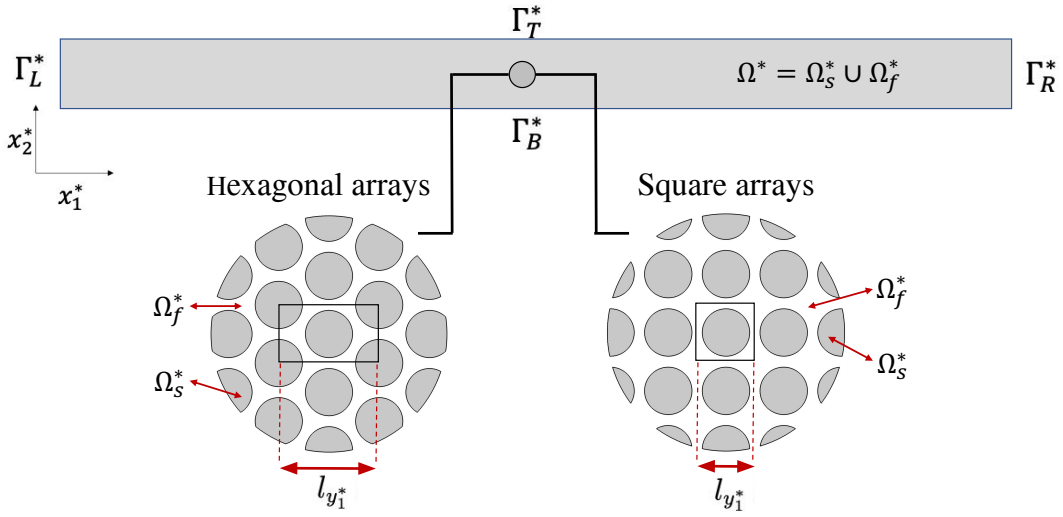


Figure 2.1: *A schematic plot of the rectangular region domain* $\Omega^* = [0, L_{x_1^*}] \times [-L_{x_2^*}/2, L_{x_2^*}/2]$. *For the solid phase,* Ω_s^*, *we consider two porous configurations: a square array of solid circular inclusions and a hexagonal array of solid circular inclusions. The aqueous phase, the saturated porous structure, of the domain is denoted by* Ω_f^*. *See text for further details. Notice that the periodic porous media are not restricted to the given two microstructures.*

2.2 Validity of the Continuum Models in Porous Media

Models of chemotactic transport in porous media have been represented either by continuum models defined at the pore scale and then upscaled to a macroscopic scale [195] or by direct pore scale simulations using Boltzmann simulations [125, 211, 212]. When developing continuum models, there are some continuum requirements that must be met at the pore scale. We inspect the validity of continuum assumptions of passive tracer transport in porous media using the Knudsen number. The Knudsen number (Kn_s) is the dimensionless ratio of the molecular mean free path length to the pore length scale, and is written:

$$\mathrm{Kn}_s = \frac{\lambda_s}{l_{y_1^*}} \ll 1. \tag{2.2.1}$$

Here λ_s is the mean free path; the mean distance travelled by a particle before colliding with another. Formally, the Knudsen number in liquids with the mean free path of

molecules of about 10^{-10}[m] [169] is small, because the typical local/micro length-scale $l^*_{y_1}$ is of order 10^{-4}[m]. Therefore, the collision of tracer molecules mainly occurs between the free molecules, this leads to Fickian diffusion, and thus the continuum assumption for the tracer equation is met [217, 84, 163].

On the other hand, the measurements of the diffusivity (random motility) of a bacterial population in aqueous bulk fluid is related to the microbial swimming behaviour. The swimming pattern of a single bacterium, such as *E. coli*, consists of a consecutive sequence of runs and tumbles that resembles a random walk [78]. A rapid tumble (0.1 [s]) interrupts a run, which usually lasts for seconds, and subsequently causes a change in direction [40, 78, 208]. Thus, the swimming dynamics of a single bacterium in confinement is different to that in bulk fluid. A Knudsen–like number, also known as the confinement parameter, is used to quantify the strength of confinement and to validate the continuum assumptions [75, 71, 154]. We set the mean path of a single bacterium – in absence of environmental cues – as the run length, $l_{\text{run}} = v_s\tau$, with single bacterium swimming speed v_s and the time between consecutive tumbles $\tau \sim 1$ [s]. For swimming speed between $20 - 40$ [μm s^{-1}] and $\tau \sim 1$ [s], we have $l_{\text{run}} \sim 20 - 40$ [μm], which gives:

$$\text{Kn}_b \approx \frac{l_{\text{run}}}{l_{y_1^*}} \sim \mathcal{O}(10^{-1}). \tag{2.2.2}$$

A bacterium travels its entire run-length of order l_{run} without colliding with the pore's solid walls in the limit $\text{Kn}_b \ll 1$. On the other hand, when $\text{Kn}_b > 1$, the swimming trajectories of the bacterium become frequently disrupted by the pore walls, affecting the swimming dynamics and the random motility of the bacterium. Thus, to ensure the validity of the continuum assumption [135, 162], we consider $l^*_{y_1}$ such that confinement parameter in (2.2.2) is less than one. In the presence of chemical cues, the bacterium travels a distance $l_{\text{ch}} = D^*_s/v_s$ to test for environmental cues before it diffuses [79], and thus, for a typical chemical diffusion, D^*_s, of order $10^{-9} - 10^{-10}$ [m^2 s^{-1}], we have:

$$\text{Kn}_{\text{ch}} \sim \frac{l_{\text{ch}}}{l_{y_1^*}} \ll 1, \tag{2.2.3}$$

which is sufficient to justify applying a continuum approach to describe chemotactic migration in porous structures. It is worth noting that the above discussion best fits the simplified case where the suspended bacterial population remains in its planktonic structure, neglecting the possibility of forming biofilm. Furthermore, the population is assumed to remain sparse to the extent that the effects of crowding-induced collisions are negligible.

Remark 2.2. *The pore confinement induces shear rates that may affect the chemotactic drift, however, as a first step toward upscaling chemotactic migration we only address the classical Keller-Segel model governed by simplified assumptions.*

2.3 Description of the Mathematical Model

In this section, we formulate the general model describing the chemotactic migration of microbial growth in a porous medium.

Mass Balance Equations. We examine a model where a substrate dissolved in an aqueous medium is degraded by the bacterial population suspension. The substrate concentration and the bacteria population are governed by the system

$$\frac{\partial s^*}{\partial t^*} + \nabla^* \cdot \mathbf{J}_s^* = G_s^*(s^*, b^*) \qquad \text{in } [0, T^*] \times \Omega_f^*, \tag{2.3.1a}$$

$$\frac{\partial b^*}{\partial t^*} + \nabla^* \cdot \mathbf{J}_b^* = G_b^*(s^*, b^*) \qquad \text{in } [0, T^*] \times \Omega_f^*. \tag{2.3.1b}$$

Eq.(2.3.1a) represents the transport of the completely dissolved substrate concentration in an aqueous fluid, $s^* = s^*(t^*, \mathbf{x}^*)$, in the aqueous phase Ω_f^* of the porous medium. Note that $\mathbf{J}_s^*$ denotes the sum of substrate fluxes. Eq.(2.3.1b) determines the evolution of the bacteria population, $b^* = b^*(t^*, \mathbf{x}^*)$, in the aqueous phase with sum of the fluxes $\mathbf{J}_b^*$. We assume that the dissolved substrate and bacteria population within a free suspension do not change the aqueous fluid viscosity. In the substrate equation, the kinetics represents the consumption of the substrate and are expressed by the function G_s^*, which depends on both species. The function G_b^* expresses the overall generation rate of the microbial population. The dissolved substrate and the bacterial suspension population are viewed as two miscible solvents having the same viscosity.

Boundary and Initial Conditions. There are two forms of boundary conditions, the solid-aqueous interface conditions defined on Γ_s^*, and exterior boundary conditions defined on Γ^*. At the solid-aqueous interface Γ_s^*, we assume a no-flux conditions for both the bacteria and substrate concentrations,

$$-\mathbf{n} \cdot \mathbf{J}_s^* = 0 \qquad \text{at } \Gamma_s^*, \tag{2.3.2a}$$

$$-\mathbf{n} \cdot \mathbf{J}_b^* = 0 \qquad \text{at } \Gamma_s^*, \tag{2.3.2b}$$

where $\mathbf{n}$ is the unit outward normal vector at the solid-aqueous interface. Thus, the interface conditions are assumed to be non-reactive with no dissolution of the substrate, or any attachment-detachment of the bacteria on the solid matrix. To close the model, we define the initial and exterior boundary conditions. The model is equipped with an initial substrate concentration and the initial microbial density in the aqueous phase given by:

$$s^*(0, \mathbf{x}^*) = s_{in}^*(\mathbf{x}^*) \qquad \text{in } \Omega_f^*, \tag{2.3.3a}$$

$$b^*(0, \mathbf{x}^*) = b_{in}^*(\mathbf{x}^*) \qquad \text{in } \Omega_f^*. \tag{2.3.3b}$$

For notational simplicity, the general form for the exterior boundary conditions is written with a slight abuse of notation as follows:

$$-\mathbf{n}\cdot\mathbf{J}_s^* = H_s^*(\mathbf{x}^*, s^*, b^*) \qquad \text{at } \Gamma^*, \tag{2.3.4a}$$
$$-\mathbf{n}\cdot\mathbf{J}_b^* = H_b^*(\mathbf{x}^*, s^*, b^*) \qquad \text{at } \Gamma^*. \tag{2.3.4b}$$

These exterior boundary conditions are represented by the two flux functions, H_s^* [M m s^{-1}] in Eq.(2.3.4a), and H_b^* [cells m s^{-1}] in Eq.(2.3.4b).

The Net Fluxes. The substrate net flux given in Eq.(2.3.1a) is the sum of molecular diffusion (modelled using Fick's law) and advection, and reads

$$\mathbf{J}_s^* = \underbrace{-D_s^*\nabla^* s^*}_{\text{diffusion flux}} + \underbrace{\mathbf{v}^* s^*}_{\text{advection flux}}, \tag{2.3.5}$$

where D_s^* is a constant diffusion coefficient and $\mathbf{v}^*$ is the medium flow within the aqueous phase. The net flux of bacteria density in Eq.(2.3.1b) accounts for both the random and biased movement under medium flow, and reads

$$\mathbf{J}_b^* = \underbrace{-D_b^*\nabla^* b^*}_{\text{diffusion flux}} + \underbrace{\mathbf{v}_c^* b^*}_{\text{chemotactic flux}} + \underbrace{\mathbf{v}^* b^*}_{\text{advection flux}}. \tag{2.3.6}$$

Here, $\mathbf{v}_c^*$ is the chemotactic velocity of the bacteria population, while D_b^* is a constant diffusivity coefficient representing the random motion of the bacteria population.

Remark 2.3. *The results throughout this thesis are also applicable if we assume constant second order tensors, that is, letting: $D_s^* := \boldsymbol{\mathcal{D}}_s^*$ and $D_b^* := \boldsymbol{\mathcal{D}}_b^*$ (see Chapter 5). In general, to apply the asymptotic homogenisation methods the tensors are assumed to be symmetric and positive definite [11].*

2.3.1 Advection Flux

The aqueous phase can be stagnant or we impose a flow with a constant velocity in the x_1-direction. The advective fluxes are modelled assuming a porous medium saturated with a Newtonian fluid (aqueous fluid). The flow at the pore scale is assumed to remain concentration-independent, and with small Reynolds number

$$\mathrm{Re} = \frac{\rho V^* l_{y_1^*}}{\mu} \ll 1, \tag{2.3.7}$$

where μ [kg m^{-1} s^{-1}], ρ [kg m^{-3}] and V^* are the viscosity, density and characteristic speed of the flow, respectively. A macroscopic gradient of pressure in the x_1^*-coordinate direction (the axial direction) forces the flow through the pores. The unidirectional velocity satisfies the following two-dimensional Stokes equations:

$$\nabla^*\cdot\mathbf{v}^* = 0 \qquad \text{in } \Omega_f^*, \tag{2.3.8a}$$

$$\mu\nabla^{*2}\mathbf{v}^* - \nabla^* p^* = 0 \qquad \text{in } \Omega_f^*, \tag{2.3.8b}$$

$$\mathbf{v}^* = \mathbf{0} \qquad \text{at } \Gamma_s^*, \tag{2.3.8c}$$

where $\mathbf{v}^* = (u^*, v^*)$ $[\mathrm{m\,s^{-1}}]$ and p^* $[\mathrm{kg\,m^{-1}\,s^{-2}}]$ are the velocity and pressure, respectively. Unless stated otherwise, the walls at $\Gamma_T^* \cup \Gamma_B^*$ are equipped with no-flow boundary conditions, i.e.

$$-\mathbf{n}\cdot\mathbf{v}^* = \mathbf{0} \qquad \text{at } \Gamma_T^* \cup \Gamma_B^*. \tag{2.3.9}$$

We set the inflow and outflow boundary conditions as

$$-\mathbf{n}\cdot\mathbf{v}^* = V^* \qquad \text{at } \Gamma_L^*, \tag{2.3.10a}$$

$$-\mathbf{n}\cdot\mathbf{v}^* = -V^* \qquad \text{at } \Gamma_R^*, \tag{2.3.10b}$$

where V^* is the characteristic velocity in a domain. We impose the conditions in Eqs.(2.3.10) for convenience. In general, these conditions should be replaced with experimentally measured pressure drop values in the domain [179, 159]. Note that the results in subsequent chapters can easily be modified to include the effect of stresses on the lateral walls Γ_T^* and Γ_B^*. Great care should be taken when considering the effect of the global shear rate on the microbial population with dominant advection, and thus, any possible affects of the induced shear rates on the microbial swimming behaviour should be investigated [154].

Remark 2.4. *Under the assumption that all the forces, including the pressure gradients, remain constant over the entire domain Ω_f^*, posing Stokes equations* (2.3.8) *and* (2.3.10) *on porous media generates purely periodic velocity fields [161]. Furthermore, the Neumann boundary condition in* (2.3.9) *gives uniform flow (plug flow) free from global shear affects.*

2.3.2 Chemotactic Flux

The chemotactic drift in Eq.(2.3.6) is expressed in the following generic form,

$$\mathbf{v}_c^* = \chi^*(s^*)\nabla^* s^*, \tag{2.3.11}$$

where $\chi^*(s^*)$ is a chemotactic sensitivity function and $\nabla^* s^*$ is the gradient of a non-metabolic attractant concentration. The functional form of $\chi^*(s^*)$ is not well established [114], and in Table 2.1 we give a few of the most commonly used chemotactic sensitivity functions.

The chemotactic velocity developed in Rivero et al. [166] was first derived for one-dimensional domains and has since been extended to two dimensions by Ford and Cummings [76] and to three dimensions by Chen et al. [44]. The model has the following form:

$$\mathbf{v}_c^* = \frac{2}{3} v_s \tanh\left(\frac{\chi_0^*}{2v_s}\frac{K_d^*\,\|\nabla^* s^*\|}{\left(K_d^* + s^*\right)^2}\right)\frac{\nabla^* s^*}{\|\nabla^* s^*\|}. \tag{2.3.12}$$

Chemotactic Velocity	Form of $\chi^*(s^*)$
Constant	$\bar{\chi}_0^*$
Logarithmic	$\dfrac{\chi_0^*}{s^*}$
Receptor Law	$\chi_0^* \dfrac{K_d^*}{3(s^*+K_d^*)^2}$
Rivero et al. [166]	$\dfrac{2}{3} v_s \tanh\left(\dfrac{\chi_0^*}{2v_s}\dfrac{K_d^*\,\|\nabla^* s^*\|}{(K_d^*+s^*)^2}\right)\dfrac{1}{\|\nabla^* s^*\|}$

Table 2.1: *Some Chemotactic velocity models that have been used in experimental studies. Here, K_d^*, v_s, and χ_0^* are the receptor constant, the bacteria swimming velocity, and the chemotactic sensitivity constant, respectively. They are related by $\bar{\chi}_0^* = \chi_0^*/K_d^*$.*

Here, the unit vector $\nabla^* s^*/\|\nabla^* s^*\|$ points in the direction of the gradient of the attractant concentration, v_s is the swimming speed of the bacteria, χ_0^* is the chemotactic sensitivity parameter, and K_d^* is the receptor saturation constant. The bacteria will increase their chemotactic velocity up to the maximum theoretical chemotactic velocity, which is given by

$$\max_{t^*,\ \mathbf{x}^*} |\mathbf{v}_c^*| = \frac{2}{3} v_s. \tag{2.3.13}$$

The maximum theoretical chemotactic velocity is in good agreement with the experimental observations in Ahmed and Stocker [5], where the experimentally evaluated chemotactic velocity can reach $\sim 36\%$ of the *E.coli* swimming speed. In the same context, Chen et al. [44] reported that in most experimental settings, the argument in Eq.(2.3.12) is bounded like

$$\xi^* = \frac{\chi_0^*}{2v_s}\frac{K_d^*}{(K_d^*+s^*)^2}\|\nabla^* s^*\| \ll 1, \tag{2.3.14}$$

which gives:

$$\|\nabla^* s^*\| \ll \frac{2v_s(s^*+K_d^*)^2}{\chi_0^* K_d^*}. \tag{2.3.15}$$

If the condition in Eq.(2.3.14) holds, then the chemotactic velocity is often reduced to a simpler form of the receptor law,

$$\mathbf{v}_c^* \sim \frac{\chi_0^* K_d^*}{3(s^*+K_d^*)^2}\nabla^* s^*. \tag{2.3.16}$$

The advantage of the chemotactic velocity defined in Eq.(2.3.12) is that the velocity never exceeds the bacterial swimming speed. In contrast, large gradients of chemoattractant concentration can lead to an unrealistic population velocity when using the receptor law in Eq.(2.3.16).

In Figure 2.2, we plotted the magnitude of chemotactic velocity in Eq.(2.3.12) as a function of the chemoattractant gradient and concentration. The plots show that the computed chemotactic velocities reach 1.4×10^{-3} [cm s^{-1}], which is about 60% of the swimming speed of *E.coli*, and is thus within the theoretical chemotactic velocity. On the other hand, in Figure 2.3, the magnitude of chemotactic velocity is plotted using the receptor law in Eq.(2.3.16), for the same values used in Figure 2.2, and we see that it exceeded the bacteria swimming speed. The region where the receptor law gives unrealistic chemotactic velocity values in Figure 2.3(a) is when $\xi^* > 1$. On the other hand, the velocities shown in Figure 2.3(b), computed using the receptor law when for $\xi^* < 1$, are close to the ones seen in Figure 2.2(b). Thus, the receptor law is valid for shallow chemoattractant gradient values, mathematically:

$$\|\nabla^* s^*\| \ll 2 \ [\mathrm{mM\,cm^{-1}}]. \tag{2.3.17}$$

This demonstrates that the receptor law is a good general approximation of the chemotactic velocity, provided that condition (2.3.15) is satisfied. In most microfluidic experiments the generated chemical gradients are shallow, so the condition in (2.3.15) is satisfied. There are some exceptions found in the Dahlquist et al. [51] and Ahmed and Stocker [5] studies, where the non-dimensional argument ξ^* was reported to exceed unity. As the steepness of the gradient is temporary and covers a short spatial region, the receptor law has been reported to fit the data most closely [114].

2.3.3 Model Kinetics

Motivated by biodegradation, the general Keller-Segel model represents a reactive transport model where the population migrates toward a fully dissolved chemoattractant which is consumed as a source–energy taxis [189, 7, 123]. The energy gained by the bacteria is transformed to another component by a co-metabolic process to be utilised for maintenance and growth [6]. We describe a simple reactive process where the substrate decays due to bacteria consumption. In the following, we will consider specific forms for G_s^* and G_b^* in Eq.(2.3.1b) to capture the population consumption, growth, and decay.

2.3.3.1 Saturated Monod Kinetics

The bacteria growth starts when there is an energy source available to support both cell maintenance and growth. Using Michaelis-Menten kinetics, the uptake rate of a planktonic microbial population is written as

$$q_s^* = -\frac{\mathrm{ds}^*}{\mathrm{dt}^*} = q_{\max}^* \frac{s^*}{s^* + K_s^*}, \tag{2.3.18}$$

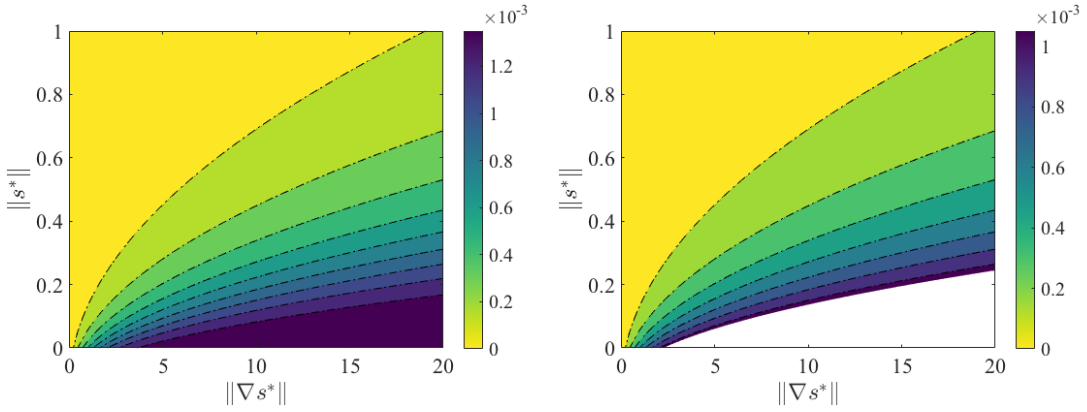


Figure 2.2: *Plots of the magnitude of chemotactic velocity,* $\|\mathbf{v}_c^*\|$ $[\mathrm{cm\,s^{-1}}]$ *of E.coli bacteria under a chemoattractant gradient in 1D using Eq.*(2.3.12)*. The values of the gradient,* $\|\nabla^* s^*\|$ $[\mathrm{mM\,cm^{-1}}]$*, vary from* 0 *to* 20 $[\mathrm{mM\,cm^{-1}}]$*, and the chemoattractant concentration* $\|s^*\|$ [mM] *varies from* 0 *to* 1 [mM]*. The magnitude of chemotactic velocity defined in Eq.(2.3.12) is plotted in (a), and in (b) we plotted* $\|\mathbf{v}_c^*\|$ *when* $\xi^* < 1$*. For these simulations we assumed the following values of the parameters,* $v_s = 22$ $[\mu\mathrm{m\,s^{-1}}]$*,* $\chi_0^* = 4 \times 10^{-5}$ $[\mathrm{cm^2\,s^{-1}}]$*,* $K_d^* = 0.125$ [mM] *[5].*

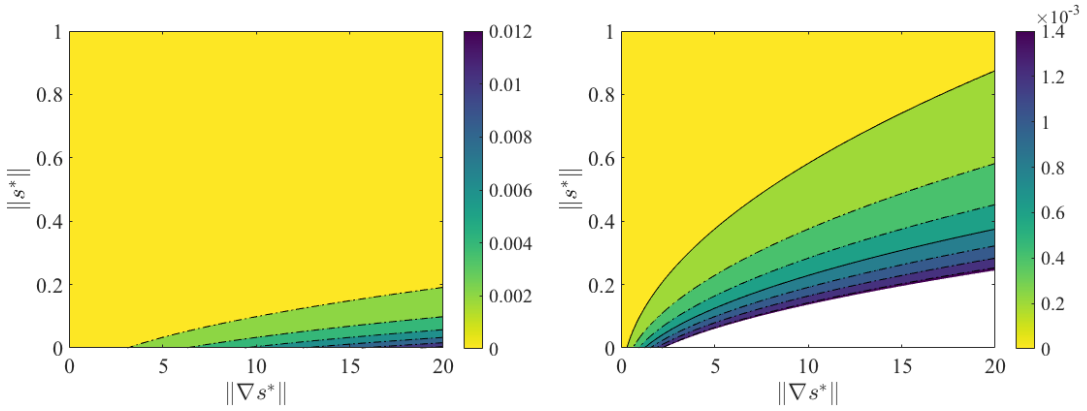


Figure 2.3: *Plots of the magnitude of chemotactic velocity,* $\|\mathbf{v}_c^*\|$ $[\mathrm{cm\,s^{-1}}]$ *with the same parameter values used in Figure 2.2. Here we used the chemotactic velocity defined using the receptor law in Eq.(2.3.16). The chemotactic velocity plotted exceeds the bacteria swimming speed in (a), but in (b) when satisfying the conditions* $\xi^* < 1$*, the magnitude of chemotactic velocity remains in an acceptable range as in Figure 2.2.*

where $q^*_{\max}$ [(mg substrate/mg cells)s^{-1}] is the maximum specific uptake rate and K^*_s is the same as the constant of the Michaelis-Menten kinetics [42]. The enzyme reactions at the microbial membrane limit the substrate flux into the cell, which is reflected in the saturation in the uptake kinetics [42]. When the bacteria consumption reaches saturation, an analogy between the microbial uptake and the Michaelis-Menten enzymic kinetics is possible. At saturation the specific growth rate, μ^*_b [s^{-1}], is related to Eq.(2.3.18) in the following way [42, 182]:

$$\mu^*_b = Y q^*_s, \qquad 0 < \mu^*_b < \mu^*_{\max}, \tag{2.3.19}$$

where $\mu^*_{\max}$ [s^{-1}] is the maximum specific growth rate and Y [mg cells/mg substrate], is the yield coefficient,

$$\frac{\mathrm{d}b^*}{\mathrm{d}t^*} = -Y^* \frac{\mathrm{d}s^*}{\mathrm{d}t^*}. \tag{2.3.20}$$

Setting the maximum specific growth to be

$$\mu^*_{\max} = Y^* q^*_{\max}, \tag{2.3.21}$$

and the specific growth rate to be

$$\mu^*_b = \mu^*_{\max} \frac{s^*}{s^* + K^*_s}, \tag{2.3.22}$$

the uptake rate can be rewritten as:

$$\mu^*_s = -\frac{\mu^*_{\max}}{Y^*} \frac{s^*}{s^* + K^*_s}. \tag{2.3.23}$$

The relation given in Eq.(2.3.22) is referred to as Monod kinetics, an empirical relation valid in the case of saturated kinetics [42]. The bacteria decay rate is set using the natural decay of the bacteria, expressed by a first-order reaction, r^*_{decay}, as

$$r^*_{\text{decay}} = K^*_b b^*, \tag{2.3.24}$$

where K^*_b [s^{-1}] is the constant bacteria death rate.

2.3.3.2 Kinetics of Inhibition

The microbial growth kinetics are affected by competitive inhibition, non-competitive inhibition, self-inhibition, and product and toxicity inhibition. The kinetics of inhibition are used to describe the observed growth limitation that is not captured by the Monod kinetics. There are many models used to describe different inhibitions, wherein the inhibition kinetics reduce the growth rate of the population. Here, we are interested in competitive inhibition, which we also refer to as growth inhibition,

where the population growth is described using the product of Monod kinetics with a logistic growth term,

$$\mu_i^* = \mu_{\max}^* \frac{s^*}{s^* + K_s^*} \left(1 - \frac{b^*}{K_c^*}\right), \tag{2.3.25}$$

such that μ_i^* is the Monod-inhibition growth kinetics, with carrying capacity constant K_c^*. Taking cues from Sakanoue [170], we can express the carrying capacity constant of the population as a function of the microbial biochemistry properties, hence

$$K_c^* = (1 - \omega)\, b_{\max}^*, \tag{2.3.26}$$

where the dimensionless parameter $\omega = K_b^*/\mu_{\max}^*$ is the ratio between the constant decay rate and the maximum specific growth rate. Note that the death rate, K_b^* , commonly used in the literature is always smaller than $\mu_{\max}^*$, and thus, $\omega < 1$. One possible estimation of $b_{\max}^*$ is taken to be the maximum population size sustained by a bacteria population at the end of batch growth as reported in Kargi [95]. In a batch culture the nutrients are available to sustain population growth without any spatial restrictions. The rate of change of the bacteria concentration in batch growth is defined in Eq.(2.3.20), where at the end of a batch growth the bacteria concentration estimation is as follows:

$$b_{\max}^* = b_{in}^* + Y^*(s_{in}^* - s_{\min}^*), \tag{2.3.27}$$

where s_{in}^* and $s_{\min}^*$ are the concentrations at the beginning and the end of the batch growth. Here, the values of b_{in}^* and $s_{\min}^*$ are negligible when compared with $b_{\max}^*$ and s_{in}^* [95]. Thus, we can approximate Eq.(2.3.27) as:

$$b_{\max}^* \sim Y^* s_{\text{in}}^*. \tag{2.3.28}$$

From Eq.(2.3.28) and ω, we have a new measurable estimation of K_c^* connecting the carrying capacity of the logistic growth with the bioavailability of the substrate to the population.

2.3.3.3 The Net Generation and Consumption Rate

While the substrate consumption rate is expressed using saturated Michaelis-Menten kinetics, the bacteria net generation rate is expressed as the sum of the saturated Monod-inhibition kinetics and the natural decay rate. Therefore, the final form of the generation and consumption rates read,

$$G_b^*(s^*, b^*) = \mu_{\max}^* \frac{s^*}{s^* + K_s^*} \left(1 - \frac{b^*}{K_c^*}\right) b^* - K_b^* b^*, \tag{2.3.29a}$$

$$G_s^*(s^*, b^*) = -\frac{\mu_{\max}^*}{Y^*} \frac{s^*}{s^* + K_s^*} b^*. \tag{2.3.29b}$$

The biomass accumulation due to growth can affect the model in different ways. First, the biomass can change the viscosity of the aqueous fluid [121]. Second, the collective swimming behaviour can affect the spatial distribution of the chemoattractant gradient [47]. Third, the accumulation of biomass leads to clogging of the pores, increased crowding-induced collisions [34, 36, 17] and the formation of biofilm [138, 158]. In our simplified model, we assume that the population remains below a threshold, that is, $b^*_{\max} < b^*_{\text{crowd}}$, and thus, we avoid dealing with such effects.

2.3.4 Solid-Aqueous Interface

To restrict the chemotactic drift to the fluid phase, we set a non-reactive solid-aqueous interface. Such simplification can be justified when considering several experimental studies involving microfluidic devices [122, 87, 106]. Thus, we set Neumann boundary conditions for both species,

$$-\mathbf{n}^* \cdot (D_s^* \nabla^* s^*) = 0 \qquad \text{on } \Gamma_s^*, \tag{2.3.30a}$$
$$-\mathbf{n}^* \cdot (D_b^* \nabla^* b^*) = 0 \qquad \text{on } \Gamma_s^*, \tag{2.3.30b}$$

where we used the flow condition, $\mathbf{v}^* = \mathbf{0}$ (see Eq.(2.3.8c)).

2.4 The Mathematical Model

From the preceding section, we write the model describing chemotactic migration of bacterial population in a saturated porous medium as

$$\frac{\partial s^*}{\partial t^*} = \nabla^* \cdot (D_s^* \nabla^* s^* - \mathbf{v}^* s^*) - \frac{\mu^*_{\max}}{Y^*} \frac{s^*}{s^* + K_s^*} b^* \qquad \text{in } [0, T^*] \times \Omega_f^*, \tag{2.4.1a}$$

$$\frac{\partial b^*}{\partial t^*} = \nabla^* \cdot (D_b^* \nabla^* b^* - [\mathbf{v}^* + \chi^*(s^*) \nabla^* s^*] b^*), \\ + \mu^*_{\max} \frac{s^*}{s^* + K_s^*} \left(1 - \frac{b^*}{K_c^*}\right) b^* - K_b^* b^* \qquad \text{in } [0, T^*] \times \Omega_f^*, \tag{2.4.1b}$$

where $\mathbf{v}^*$ is an incompressible steady flow. The chemotactic transport model is supplemented by appropriate boundary conditions on the solid-aqueous interface and the external boundaries, and by an initial data condition. The initial datum is:

$$s^*(t, \mathbf{x}) = s^*_{in}(\mathbf{x}), \qquad \text{and} \qquad b^*(t, \mathbf{x}) = b^*_{in}(\mathbf{x}), \tag{2.4.2}$$

defined on Ω_f^*. Thus, the initial data regularity is postulated, and consequently, the model is well-posed. On the solid-aqueous interface, we have

$$-\mathbf{n}^* \cdot (D_s^* \nabla^* s^*) = -\mathbf{n}^* \cdot (D_b^* \nabla^* b^*) = 0 \qquad \text{on } \Gamma_s^*. \tag{2.4.3}$$

The Neumann boundary condition at the interface in (2.4.3) correspond to a non-reactive transport regime at the pore boundaries. With a slight abuse of notation, the other external boundary conditions are expressed as:

$$-\mathbf{n}\cdot(D_s^*\nabla^* s^* - \mathbf{v}^* s^*) = H_s^*(\mathbf{x}^*, s^*, b^*), \tag{2.4.4a}$$

$$-\mathbf{n}\cdot(D_b^*\nabla^* b^* - [\mathbf{v}^* + \chi^*(s^*)\nabla^* s^*]b^*) = H_b^*(\mathbf{x}^*, s^*, b^*). \tag{2.4.4b}$$

The exact definitions of H_b^* and H_b^* are detailed in the two case studies in Chapter 4 and Chapter 5. Lastly, as stated earlier, we assume a no-flow and no-flux external boundary condition at Γ_T^* and Γ_B^*, such that in (2.4.4b) we have:

$$H_s^*(\mathbf{x}^*, s^*, b^*) = H_b^*(\mathbf{x}^*, s^*, b^*) = 0. \tag{2.4.5}$$

2.5 The Mathematical Model Time Scales

For a system of this nature, there are several timescales that affect the transport dynamic at the pore scale. To characterise the system, it is crucial to understand the relative magnitudes of the various timescales involved in the system dynamics. Here, we choose to define the system time using the longitudinal length of the domain, $L_{x_1^*}$. The characteristic diffusivity times of the two species read

$$T_s^* = \frac{L_{x_1^*}^2}{D_s^*}, \qquad T_b^* = \frac{L_{x_1^*}^2}{D_b^*}, \tag{2.5.1}$$

where T_s^* is the time scale of substrate diffusion and T_b^* is the time scale of the bacteria's random motility. The characteristic time for the medium advection is expressed as

$$T_V^* = \frac{L_{x_1^*}}{V^*}, \tag{2.5.2}$$

where V^* is the averaged velocity of the flow. The advection times are typically shorter than the diffusivity times. Advection becomes negligible if the ratio of advective times to the diffusion times satisfies

$$T_V^*/T_s^* \leq \mathcal{O}(\varepsilon), \tag{2.5.3}$$

where ε is the separation of scale parameter given in Eq.(2.1.7). Hence, the two species passively diffuse at the pore scale, and mass transport is dominated by diffusion and random motility. The swimming motion of bacteria is characterised by a sequence of runs and reorientation (tumble) phases. For convenience, we assume that the bacteria swim in a unidirectional fashion and define the bacterial swimming time as:

$$T_{\text{swim}}^* \sim \frac{L_{x_1^*}}{v_s^*}, \tag{2.5.4}$$

where v_s^* is the average swimming speed [202]. Note that when defining T^*_{swim} we are imposing that the bacterium does not change direction while swimming, which is not true. In contrast, the run time between two successive tumbles τ, briefly discussed in Section 2.2, gives a better biological meaning to the swimming time of the bacteria. When exposed to chemoattractant signals, the bacteria travel up the gradient via a sensing and adaptation process [184, 48, 214]. The adaptation response is determined when the bacteria recognise a change in attractant concentration. As a result, the chemotactic drift time scale depends on the spatiotemporal distribution of the attractant stimuli. An estimate for the chemotactic drift time scale is

$$T^*_\chi \sim \frac{L^*}{V_c^*}, \tag{2.5.5}$$

where V_c^* ($V_c^* \neq 0$) is an estimation of the chemotactic velocity magnitude at $(t^*, \mathbf{x}^*)$. The characteristic length, L^*, is the sensing length in the direction of the attractant. Determining the characteristic length, L^* is not easy, and is affected by the complexity of the spatiotemporal environment surrounding the swimming bacteria. In general, $L^* \ll L_{x_1^*}$, and thus,

$$T^*_\chi \ll \mathcal{O}(T^*_{\text{swim}}). \tag{2.5.6}$$

The characteristic different kinetics rates are defined as

$$T^*_{\max} = \frac{1}{\mu^*_{max}}, \qquad T^*_{\text{decay}} = \frac{1}{K^*_b}, \tag{2.5.7}$$

where $T^*_{\max}$ and T^*_{decay} are the time scales of maximum metabolic rate and microbial death rate, respectively. Finally, we assume that the mass fluxes defined at Γ^*_L and Γ^*_R do not affect the mass transfer inside the domain.

2.6 Non-dimensionalisation

We set the characteristic length to be the longitude length, $L_{x_1^*}$ [59, 156]. Thus, the two-dimensional Cartesian coordinate system becomes:

$$(x_1^*, x_2^*) = L_{x_1^*}(x_1, x_2). \tag{2.6.1}$$

Consequently, in Section 2.1 the domain Ω with boundaries $\partial\Omega$ is

$$\Omega = [0, 1] \times [-L_{x_2}/2, L_{x_2}/2], \tag{2.6.2}$$

where $L_{x_2} = L_{x_2^*}/L_{x_1^*}$. Thus, the domain consists of two phases, a solid phase Ω_s, and an aqueous phase Ω_f, can be rewritten as

$$\Omega = \Omega_s \cup \Omega_f. \tag{2.6.3}$$

The domain boundaries are denoted as

$$\partial\Omega = \Gamma_s \cup \Gamma. \tag{2.6.4}$$

where Γ_s represents the solid-aqueous interfaces, and Γ represents the exterior boundary,

$$\Gamma = \Gamma_T \cup \Gamma_B \cup \Gamma_L \cup \Gamma_R. \tag{2.6.5}$$

We fix the characteristic time scale to be the diffusion time scale of the substrate (chemical)

$$t^* = T_s^* t = \frac{L_{x_1^*}^2}{D_s^*} t. \tag{2.6.6}$$

It follows from (2.6.1) and (2.6.6) that the dimensionless differential operators are

$$\frac{\partial}{\partial t^*} = \frac{1}{T_s^*} \frac{\partial}{\partial t}, \tag{2.6.7a}$$

$$\nabla^* = \frac{1}{L_{x_1^*}} \nabla, \tag{2.6.7b}$$

$$\nabla^{*2} = \frac{1}{L_{x_1^*}^2} \nabla^2. \tag{2.6.7c}$$

Note that the aforementioned characteristic scales are fixed throughout this work.

2.6.1 Dimensionless Stokes Equations

In addition to introducing the spatial change of variables given in (2.6.1) into (2.3.8), we scale the following variables as follows

$$\mathbf{v}^* = V^* \mathbf{v}, \qquad p^* = P^* p, \tag{2.6.8}$$

where V^* is the characteristic scalar velocity, and the viscous pressure scale is given as

$$P^* \sim \frac{\mu V^*}{L_{x_1^*}}, \tag{2.6.9}$$

where μ is the aqueous fluid viscosity. It follows that the dimensionless form of the Stokes equations are

$$\nabla \cdot \mathbf{v} = 0 \qquad \text{in } \Omega_f, \tag{2.6.10a}$$

$$\nabla^2 \mathbf{v} - \nabla p = 0 \qquad \text{in } \Omega_f, \tag{2.6.10b}$$

$$\mathbf{v} = \mathbf{0} \qquad \text{at } \Gamma_s. \tag{2.6.10c}$$

The Neumann boundary conditions, Eq.(2.3.10), are

$$-\mathbf{n} \cdot \mathbf{v} = \quad 1 \qquad \text{at } \Gamma_L, \tag{2.6.11a}$$

$$-\mathbf{n} \cdot \mathbf{v} = -1 \qquad \text{at } \Gamma_R, \tag{2.6.11b}$$

and at $\Gamma_T \cup \Gamma_B$ we have the no-flow conditions $-\mathbf{n} \cdot \mathbf{v} = \mathbf{0}$.

2.6.2 Dimensionless Keller-Segel Model

We derive the dimensionless form of the balance equations in Eqs.(2.4.1) using the spatial and temporal scaling given by Eq.(2.6.1) and Eq.(2.6.6) while scaling the substrate and bacteria concentrations by

$$s^* = s^*_{\mathrm{m}} s, \qquad b^* = b^*_{\mathrm{m}} b, \tag{2.6.12}$$

where s^*_{m} and b^*_{m} are a pair of constant reference concentrations. The dimensionless chemotactic migration model is

$$\frac{\partial s}{\partial t} = \nabla \cdot (\nabla s - \mathrm{Pe}\,\mathbf{v} s) - \frac{\mathrm{Da}}{Y} \frac{s}{s+\kappa_s} b \qquad \text{in } [0,T] \times \Omega_f, \tag{2.6.13a}$$

$$\frac{\partial b}{\partial t} = \nabla \cdot (\delta \nabla b - [\mathrm{Pe}\,\mathbf{v} + \mathrm{Pe}_b\, \chi(s) \nabla s] b), + \mathrm{Da}\, \frac{s}{s+\kappa_s} \left(1 - \frac{b}{\kappa_c}\right) b - \kappa_b b \qquad \text{in } [0,T] \times \Omega_f. \tag{2.6.13b}$$

The dimensionless form of the solid-aqueous interface conditions in (2.4.3) is

$$-\mathbf{n} \cdot (\nabla s) = 0 \qquad \text{at } \Gamma_s, \tag{2.6.14a}$$

$$-\mathbf{n} \cdot (\delta \nabla b) = 0 \qquad \text{at } \Gamma_s. \tag{2.6.14b}$$

With the initial substrate concentration and bacteria density initial concentrations given in Eq.(2.3.3b). They are non-dimensionalised as

$$s(0, \mathbf{x}) = s_{in}(\mathbf{x}), \qquad b(0, \mathbf{x}) = b_{in}(\mathbf{x}), \tag{2.6.15}$$

defined on Ω_f, where $s_{in}(\mathbf{x}) = s^*_{in}(\mathbf{x}^*)/s^*_{\mathrm{m}}$ and $b_{in}(\mathbf{x}) = b^*_{in}(\mathbf{x}^*)/b^*_{\mathrm{m}}$. The dimensionless numbers in (2.6.13)–(2.6.22) are defined as

$$\mathrm{Pe} = \frac{T^*_s}{T^*_V}, \qquad \mathrm{Pe}_b = \frac{T^*_s}{T^*_{\mathrm{swim}}}, \qquad \mathrm{Da} = \frac{L^2_{x^*_1} \mu^*_{\max}}{D^*_s}, \qquad \kappa_b = \frac{L^2_{x^*_1} K}{D^*_s}, \tag{2.6.16}$$

where Pe is the advective Péclet number, Pe_b is the bacterial swimming Péclet number, and Da and κ_b are the metabolic and decay Damkóhler numbers, respectively. In addition, because of the non-dimensionalisation we have the following new dimensionless parameters,

$$\delta = \frac{D^*_b}{D^*_s}, \qquad \kappa_s = \frac{K^*_s}{s^*_{\mathrm{m}}}, \qquad \kappa_c = \frac{K^*_c}{b^*_{\mathrm{m}}}, \qquad Y = Y^*\Big(\frac{s^*_{\mathrm{m}}}{b^*_{\mathrm{m}}}\Big). \tag{2.6.17}$$

Here, $\delta \ll 1$ is the dimensionless bacterial motility coefficient, and κ_s is the dimensionless half-saturation constant of the Monod kinetics. Using Eq.(2.3.26), the dimensionless carrying capacity constant, κ_c, is written as:

$$\kappa_c = (1-\omega) \frac{b^*_{\max}}{b^*_{\mathrm{m}}}. \tag{2.6.18}$$

The chemotaxis velocity is scaled by the bacteria swimming speed, hence

$$\chi(s)\nabla s = \frac{\chi^*(s^*)\nabla^* s^*}{v_s}. \tag{2.6.19}$$

As such, in (2.6.19) the chemotaxis sensitivity functions defined in Eq.(2.3.12) and Eq.(2.6.20a) have the following dimensionless forms

$$\chi(s) = \frac{2}{3}\tanh\left(\Upsilon_0 \frac{\kappa_d}{(s+\kappa_d)^2}\|\nabla s\|\right)\frac{1}{\|\nabla s\|}, \tag{2.6.20a}$$

$$\chi(s) = \chi_0 \frac{\kappa_d}{(s+\kappa_d)^2}. \tag{2.6.20b}$$

The dimensionless parameters in Eq.(2.6.20a) are

$$\Upsilon_0 = \frac{\chi_0^*}{2v_s L_{x_1^*}} \qquad \kappa_d = \frac{K_d^*}{s_{\mathrm{m}}^*}, \qquad \chi_0 = \frac{\chi_0^*}{3v_s L_{x_1^*}}, \tag{2.6.21}$$

where κ_d is the dimensionless receptor constant and χ_0 is the receptor sensitivity constant.

Dimensionless External Boundaries. Finally, the external boundary conditions can be written with a slight abuse of notation as:

$$-\mathbf{n}\cdot(\nabla s - \mathrm{Pe}\,\mathbf{v}s) = H_s(\mathbf{x}, s, b), \tag{2.6.22a}$$

$$-\mathbf{n}\cdot(\delta\nabla b - [\mathrm{Pe}\,\mathbf{v} + \mathrm{Pe}_b\,\chi(s)\nabla s]b) = H_b(\mathbf{x}, s, b), \tag{2.6.22b}$$

where H_s and H_b are the dimensionless mass influx for the substrate and bacteria, respectively. In addition to no-flux and no-flow boundaries at Γ_T and Γ_B:

$$H_s(\mathbf{x}, s, b) = H_s(\mathbf{x}, s, b) = 0. \tag{2.6.23}$$

The dimensionless forms of the external boundaries at Γ_T and Γ_B are given in later chapters.

2.7 Concluding Remarks

This chapter describes a general Keller-Segel model in a saturated periodic porous medium. Although the model itself is not novel, the novelty in our work comes from the upscaling of the model in the next chapters. Therefore, the aim of defining the model under simplified assumptions is to focus on upscaling the chemotactic transport mechanism in the aqueous phase only. We started by defining a simplified two-dimensional periodic porous structure saturated with an aqueous fluid of constant viscosity in the x_1-direction. Lastly, we introduced the two coupled reactive

transport equations of a dissolved substrate concentration consumed by the bacteria for growth; and the bacterial population that exhibits chemotactic migration toward a higher gradient concentration of the substrate. We included a logistic term to control the growth density accumulation and gave an estimation to the carrying capacity parameter. Logistic growth is also used to justify the simplified assumption of no pore-clogging, constant fluid viscosity and ignoring biofilm formation. In the upcoming chapters, to investigate the effect of a steep gradient, we shall apply both chemotactic velocities defined in Eq.(2.3.12)-(2.3.16). Below we state the main limitations of the current model.

We can extend the model's domain to three-dimensions, providing we apply the Neumann boundary conditions to the medium flow to the lateral walls. This will avoid the cases where the population exhibits trapping by the shear rate at lateral walls. Furthermore, due to the assumption of weak porosity and the sparse suspended population, we can neglect the clogging of the pore and the influence of density-dependent cell-cell collisions. Thus, we considered constant motility and chemotactic sensitivity parameters [34, 17, 37]. The metabolic reactions only appear in the fluid phase, and no reactions occur in the solid phase. The chemotactic drift occurs in the aqueous phase; therefore, we assumed a non-reactive solid-aqueous interface to ensure that neither bacterium nor the substrate is being absorbed.

Chapter 3

Asymptotic Homogenisation Method

In this chapter we aim to apply the asymptotic homogenisation method – the two-scale expansion method – to develop a macroscopic model for the chemotactic migration model based on the Keller-Segel model described in Chapter 2. The macroscopic model, also known as the effective model (upscaled model), is obtained by deriving effective parameters (upscaled parameters) which capture the influence of the porous medium on the transported species [8, 21]. The asymptotic expansion method is an upscaling technique referred to as "Homogenisation" in the mathematics literature. As with the volume averaging method (VAM) [203], the asymptotic homogenisation method is a formal upscaling method, as there is no guarantee that the asymptotic expansion holds. The results from the two-scale method can be made mathematically rigorous using two-scale homogenisation theory [30]. However, using such rigorous methods is beyond the scope of our work. The effective models in this chapter are novel in the field of homogenisation. These models are a much-needed tool to investigate the role of chemotaxis in the biodegradation of a contaminate in porous media.

In Section 3.1, we state some of the basic concepts used in the asymptotic homogenisation procedure. Next, in Section 3.2, we write the classical derivation of Darcy's law using the asymptotic homogenisation of the Stokes equations. Our contribution to the field of asymptotic homogenisation starts from Section 3.3 where we present the microscopic description for the three limiting cases of the general Keller-Segel model stated in Chapter 2. The asymptotic homogenisation of the three limiting cases is detailed in Section 3.4, 3.5 and 3.6.

3.1 Preliminaries

Formal homogenisation approaches are based on the concept of representing a heterogeneous medium by an equivalent macroscopically homogeneous one (see Figure 3.1). The first step is to identify two spatial scales. First is the global (large) scale $L_{x_1^*}$, at which the flow, transport, and other processes are observed; and second is the local scale $l_{y_1^*}$ on which we observe small fluctuations at the pore scale. Assuming separation of the two spatial scales, the ratio between the two scales is defined by

$$\varepsilon = \frac{l_{y_1^*}}{L_{x_1^*}} \ll 1, \tag{3.1.1}$$

where the dimensionless geometric factor in (3.1.1) is referred to as the dimensionless separation of scale parameter. We denote the saturated porous medium as Ω_ε to indicate that the domain is ε-periodic. Furthermore, $\psi_\varepsilon(t, \mathbf{x})$ is said to be an ε-periodic function if

$$\psi_\varepsilon(t, \mathbf{x} + \varepsilon \mathbf{e}_i) = \psi_\varepsilon(t, \mathbf{x}), \tag{3.1.2}$$

where $\mathbf{e}_i$ $(i = 1, 2)$ is the Cartesian unit vector. The unit periodicity cell Y (also known as the representative volume element (RVE)) consists of a smooth partition

$$Y = Y^0 \cup \Sigma^0, \tag{3.1.3}$$

where Y^0 is the local fluid phase and Σ^0 is the local solid phase. For each multi-index $j \in \mathbb{Z}^2$, we write Ω_ε as

$$\Omega_\varepsilon = \bigcup_{j \in \mathbb{Z}^2} Y_\varepsilon^j, \tag{3.1.4}$$

where $\Omega_\varepsilon \subset \Omega = [0, L_{x_1}] \times [-L_{x_2}/2, L_{x_2}/2]$ represents the aqueous phase of the porous medium. For each j, Y_ε^j is homothetic to Y^0 such that

$$Y_\varepsilon^j = \varepsilon \left(Y^0 + j \right). \tag{3.1.5}$$

Furthermore, the solid-aqueous interface phase of the domain is

$$\Gamma_s = \bigcup_{j \in \mathbb{Z}^2} \partial\Sigma_\varepsilon^j, \tag{3.1.6}$$

such that $\partial\Sigma_\varepsilon^j = \varepsilon \left(\partial\Sigma^0 + j \right)$. Thus, we introduce the microscopic (local/fast) spatial variable $\mathbf{y}$

$$\mathbf{y} = \frac{\mathbf{x}}{\varepsilon}, \tag{3.1.7}$$

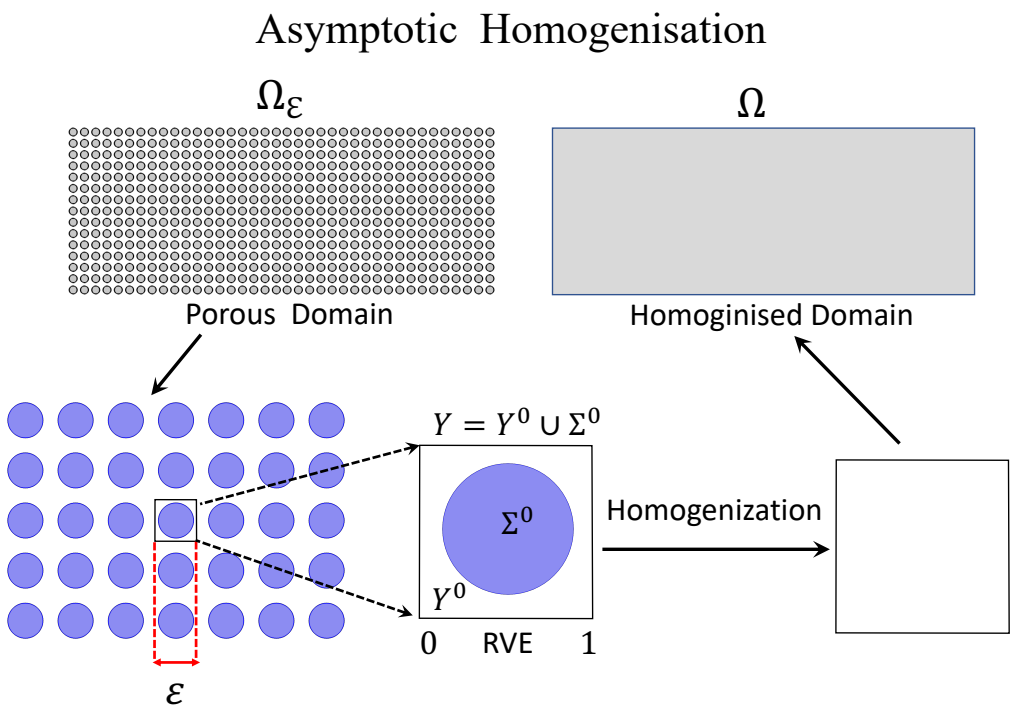


Figure 3.1: *Conceptual illustration of the asymptotic homogenisation approach (dimensionless). For more details, please refer to text.*

here $\mathbf{x}$ is what we refer to as the macroscopic (global/slow) spatial variable. Thereby, we write the ε-periodic function given in Eq.(3.1.2) in terms of the two spatial variables:

$$\psi_\varepsilon = \psi_\varepsilon(t, \mathbf{x}, \mathbf{x}/\varepsilon) = \psi_\varepsilon(t, \mathbf{x}, \mathbf{y}), \tag{3.1.8}$$

where $(t, \mathbf{x}, \mathbf{y}) \in [0, T] \times \Omega_\varepsilon \times Y^0$. Here the function ψ_ε is Y-periodic but not periodic in time. The method of asymptotic expansions begins with an assumption that the pore scale function in (3.1.8) is expanded in terms of the period ε,

$$\psi_\varepsilon = \underbrace{\psi_0}_{\text{zero order approximation}} + \underbrace{\varepsilon\psi_1}_{\text{first order correction}} + \underbrace{\varepsilon^2\psi_2}_{\text{second order correction}} + \mathcal{O}(\varepsilon^3), \tag{3.1.9}$$

wherein $\psi_k = \psi_k(t, \mathbf{x}, \mathbf{y})$ for $k = 1, 2, \ldots$ are Y-periodic. We define our first order approximation as the sum of the zero and the first order correction functions given in Eq.(3.1.9),

$$\psi_{1,\varepsilon} \sim \psi_0 + \varepsilon\psi_1. \tag{3.1.10}$$

Using the chain rule, we obtain

$$\nabla\psi_\varepsilon = \nabla_{\mathbf{x}}\psi_\varepsilon + \varepsilon^{-1}\nabla_{\mathbf{y}}\psi_\varepsilon, \tag{3.1.11a}$$

$$\nabla^2\psi_\varepsilon = \nabla^2_{\mathbf{x}}\psi_\varepsilon + 2\varepsilon^{-1}\nabla_{\mathbf{x}}\cdot\nabla_{\mathbf{y}}\psi_\varepsilon + \varepsilon^{-2}\nabla^2_{\mathbf{y}}\psi_\varepsilon, \tag{3.1.11b}$$

where $\nabla_{\mathbf{x}} = \big(\partial/\partial x_1, \partial/\partial x_2\big)$ and $\nabla_{\mathbf{y}} = \big(\partial/\partial y_1, \partial/\partial y_2\big)$. We also introduce the following averaging operators

$$\langle\psi_\varepsilon\rangle_{Y^0} = \frac{1}{|Y^0|}\int_{Y^0}\psi_\varepsilon d\mathbf{y}, \tag{3.1.12a}$$

$$\langle\psi_\varepsilon\rangle = \frac{1}{|Y|}\int_{Y^0}\psi_\varepsilon d\mathbf{y}, \tag{3.1.12b}$$

where ψ_ε depends on the local spatial scale, $|Y^0|$ is the area (or volume in three dimensions) of the fluid phase (RVE) and $|Y|$ is area (or volume) of the union of the fluid and solid phase (RVE or the unit periodic cell). We refer to (3.1.12a) as the average operator over Y^0 and (3.1.12a) as the average over Y. These two operators are related in the following way:

$$\langle\psi_\varepsilon\rangle = \phi\langle\psi_\varepsilon\rangle_{Y^0}, \tag{3.1.13}$$

where $\phi = |Y^0|/|Y|$ is the porosity in the periodic porous structure.

Next, we use the formal asymptotic homogenisation to derive Darcy's law and the homogenised form of the model stated in Chapter 2.

3.2 Darcy Velocity

The method of two-scale asymptotic expansions has been used to deduce Darcy's law starting with the steady Stokes equations at the pore scale [102, 101, 118, 172, 21]. In this section we give a detailed description of this derivation. At the pore scale a steady flow is possible if the ratio between the pressure gradient at the global scale and the viscosity term at the local scale is fixed [21]. The order of the corresponding pressure gradient in the dimensional Stokes equation in Eqs.(2.6.10) is

$$\nabla^* p^* \sim \mathcal{O}\left(\frac{P^*}{L_{x_1^*}}\right), \tag{3.2.1}$$

where P^* is the global pressure drop, then we have the order of the dimensionless pressure gradient with respect to the parameter ε is

$$\nabla p \sim \mathcal{O}\left(\varepsilon^0\right). \tag{3.2.2}$$

The order of the dimensional viscous term at the local scale is

$$\mu\nabla^{*2}\mathbf{v}^* \sim \mathcal{O}\left(\frac{\mu V^*}{l^2_{y_1^*}}\right). \tag{3.2.3}$$

Returning to the dimensional Stokes equation in Eqs.(2.6.10), we assume that the fluid pressure balances the local viscous force, the pressure gradient should assume the same order of magnitude as the viscous term,

$$\frac{\mu V^*}{l_{y_1^*}^2} \sim \mathcal{O}\left(\frac{P^*}{L_{x_1^*}}\right). \tag{3.2.4}$$

Therefore, in the scaling from Section 2.6, the order of the dimensionless viscous term with respect to the parameter ε is

$$\nabla^2 \mathbf{v} \sim \mathcal{O}(\varepsilon^2). \tag{3.2.5}$$

Thus the Stokes equations at the microscopic scale are

$$\nabla \cdot \mathbf{v}_\varepsilon = 0 \qquad \text{in } \Omega_\varepsilon \times Y^0, \tag{3.2.6a}$$
$$\varepsilon^2 \nabla^2 \mathbf{v}_\varepsilon - \nabla p_\varepsilon = \mathbf{0} \qquad \text{in } \Omega_\varepsilon \times Y^0, \tag{3.2.6b}$$
$$\mathbf{v}_\varepsilon = \mathbf{0} \qquad \text{on } \partial\Sigma^0, \tag{3.2.6c}$$

where $\mathbf{v}_\varepsilon$ and p_ε are periodic in $\mathbf{y}$. We start with the asymptotic expansion for the pressure and the velocity field:

$$p_\varepsilon(\mathbf{x}, \mathbf{y}) = p_0 + \varepsilon p_1 + \varepsilon^2 p_2 + \mathcal{O}(\varepsilon^3), \tag{3.2.7}$$
$$\mathbf{v}_\varepsilon(\mathbf{x}, \mathbf{y}) = \mathbf{v}_0 + \varepsilon \mathbf{v}_1 + \varepsilon^2 \mathbf{v}_2 + \mathcal{O}(\varepsilon^3), \tag{3.2.8}$$

where $\mathbf{v}_i$ and p_i are periodic in $\mathbf{y}$ for $i = 1, 2, \cdots$. The formal asymptotic expansion starts with substituting (3.2.7), (3.2.8) and the differential operators in (3.1.11) into (3.2.6) to obtain a cascade of equations corresponding to different orders in ε

$$\mathcal{O}(\varepsilon^{-1}): \qquad \nabla_{\mathbf{y}} p_0(\mathbf{x}, \mathbf{y}) = 0 \qquad \text{in } Y^0, \tag{3.2.9}$$
$$\nabla_{\mathbf{y}} \cdot \mathbf{v}_0(\mathbf{x}, \mathbf{y}) = 0 \qquad \text{in } Y^0, \tag{3.2.10}$$
$$\mathcal{O}(\varepsilon^0): \qquad \nabla_{\mathbf{y}}^2 \mathbf{v}_0 - \nabla_{\mathbf{y}} p_1(\mathbf{x}, \mathbf{y}) - \nabla_{\mathbf{x}} p_0(\mathbf{x}, \mathbf{y}) = 0 \qquad \text{in } Y^0, \tag{3.2.11}$$
$$\nabla_{\mathbf{x}} \cdot \mathbf{v}_0(\mathbf{x}, \mathbf{y}) + \nabla_{\mathbf{y}} \cdot \mathbf{v}_1(\mathbf{x}, \mathbf{y}) = 0 \qquad \text{in } Y^0. \tag{3.2.12}$$

The expansion of the solid interface boundary condition given in Eq.(3.2.6c) implies

$$\mathbf{v}_k = \mathbf{0} \qquad \text{on} \quad \partial\Sigma^0 \qquad \text{for } k = 0, 1, \ldots. \tag{3.2.13}$$

At the lowest order, we obtain the following local problem,

$$\nabla_{\mathbf{y}} p_0 = \mathbf{0} \qquad \text{in } Y^0, \tag{3.2.14a}$$
$$\nabla_{\mathbf{y}} \cdot \mathbf{v}_0 = 0 \qquad \text{in } Y^0, \tag{3.2.14b}$$
$$\mathbf{v}_0 = \mathbf{0} \qquad \text{on } \partial\Sigma^0, \tag{3.2.14c}$$

and we note that $p_0 = p_0(\mathbf{x})$ depends only on the global variable, $\mathbf{x}$. Next, we solve for $\mathbf{v}_0$ and p_1 using the following equations:

$$\nabla^2_{\mathbf{y}}\mathbf{v}_0 - \nabla_{\mathbf{x}}p_0 - \nabla_{\mathbf{y}}p_1 = \mathbf{0}, \qquad \text{in } Y^0, \tag{3.2.15a}$$

$$\nabla_{\mathbf{y}} \cdot \mathbf{v}_0 = 0 \qquad \text{in } Y^0, \tag{3.2.15b}$$

$$\mathbf{v}_0 = \mathbf{0} \qquad \text{on } \partial\Sigma^0. \tag{3.2.15c}$$

The linear problem defined in Eqs.(3.2.15) is a well-posed boundary value problem for $\mathbf{v}_0$, and the solution $\mathbf{v}_0$ exists and is unique [21]. Since the forcing term $\nabla_{\mathbf{x}}p_0$ only depends on the global variable, this motivates a solution of the form

$$\mathbf{v}_0 = -\mathbf{K}^j(\mathbf{y})\frac{\partial p_0}{\partial x_j}, \qquad p_1 = -\pi_j(\mathbf{y})\frac{\partial p_0}{\partial x_j} + \bar{p}_1(\mathbf{x}). \tag{3.2.16}$$

Here we are using the Einstein summation convention for the index $j = 1, 2$. The functions $\mathbf{K}^j(\mathbf{y}) = (K^j_1, K^j_2)$ and $\pi_j(\mathbf{y})$ (for $j = 1, 2$) are unknown functions of the local scale and represent the local variations in $\mathbf{v}_0$ and p_1, respectively. The term $\bar{p}_1(\mathbf{x})$ is constant on the local scale and is introduced as an additive constant function with respect to $\mathbf{y}$. In general, the term $\bar{p}_1(\mathbf{x})$ is neglected unless we are interested in computing the first correction $\mathbf{v}_1$. The functions $\mathbf{K}_j(\mathbf{y})$ and $\pi_j(\mathbf{y})$ are obtained by substituting Eqs.(3.2.16) into the local problem given in Eqs.(3.2.15) to give the *cell-problem*

$$\nabla_{\mathbf{y}} \cdot \mathbf{K}^j = 0 \qquad \text{in } Y^0, \tag{3.2.17a}$$

$$\nabla_{\mathbf{y}}\pi_j = \nabla^2_{\mathbf{y}}\mathbf{K}^j + \mathbf{e}_j \qquad \text{in } Y^0, \tag{3.2.17b}$$

$$\mathbf{K}^j = \mathbf{0} \qquad \text{on } \partial\Sigma^0, \tag{3.2.17c}$$

such that $\langle \pi_j \rangle = 0$, and π_j, $\mathbf{K}^j$ are Y-periodic in $\mathbf{y}$, and $\mathbf{e}_j$ is the Cartesian unit vector in the j-th direction. The system in Eqs.(3.2.17) describes a classical formulation of a cell problem that can be solved numerically for a prescribed RVE, Y^0. Once solved, we can take the average of the velocity in Eq.(3.2.16) over the periodic cell, Y. The permeability tensor $\mathbf{K}^0$ relates to the effective velocity, Darcy's law, as

$$\langle \mathbf{v}_0 \rangle = -\mathbf{K}^0 \nabla_{\mathbf{x}} \langle p_0 \rangle, \tag{3.2.18}$$

where the intrinsic permeability tensor, $\mathbf{K}^0$, with components given by the expression

$$K^0_{ij} = \frac{1}{|Y^0|}\int_{Y^0} K^j_i(\mathbf{y}) d\mathbf{y}, \quad i, j = 1, 2. \tag{3.2.19}$$

The permeability tensor is a symmetric positive-definite tensor that depends upon the RVE geometry. The effective velocity given by Eq.(3.2.18) defines Darcy's law via homogenisation using a two-scale expansion method. The pressure field is derived from the expansion of the divergence equation at $\mathcal{O}(\varepsilon^0)$:

$$\nabla_{\mathbf{x}} \cdot \mathbf{v}_0 + \nabla_{\mathbf{y}} \cdot \mathbf{v}_1 = 0, \tag{3.2.20}$$

which, when integrated over the RVE, yields

$$\int_{Y^0} \nabla_{\mathbf{y}} \cdot \mathbf{v}_1 d\mathbf{y} = -\nabla_{\mathbf{x}} \cdot \int_{Y^0} \mathbf{v}_0 d\mathbf{y}. \tag{3.2.21}$$

Using the divergence theorem we have,

$$\int_{Y^0} \nabla_{\mathbf{y}} \cdot \mathbf{v}_1 d\mathbf{y} = \int_{\partial\Sigma^0} \mathbf{v}_1 \cdot \mathbf{n} ds = 0, \tag{3.2.22}$$

where we have used the periodicity of $\mathbf{v}_1$ and the boundary condition in (3.2.13). Then we deduce that

$$\nabla_{\mathbf{x}} \cdot \langle \mathbf{v}_0 \rangle = -\nabla_{\mathbf{y}} \cdot \langle \mathbf{v}_1 \rangle = 0. \tag{3.2.23}$$

Eq.(3.2.18) and the incompressibility condition in Eq.(3.2.23) defines Darcy's law with the permeability tensor as in Eq.(3.2.19). Corresponding to Eq.(3.2.18) and Eq.(3.2.23), Darcy's law leads to

$$\nabla_{\mathbf{x}} \cdot \Big(- \mathbf{K}^0 \nabla_{\mathbf{x}} \langle p_0 \rangle \Big) = 0 \qquad \text{on } \Omega. \tag{3.2.24}$$

Local Darcy Velocity The spatial distribution of the flow fluxes at the micro-scale is visualised using the zero-order approximation given in Eq.(3.2.16), hence

$$\mathbf{v}_0 = -\mathbf{K}(\mathbf{y}) \cdot \nabla_{\mathbf{x}} p_0 \qquad \text{in } Y^0, \tag{3.2.25a}$$

$$\nabla_{\mathbf{y}} \cdot \mathbf{v}_0 = 0 \qquad \text{in } Y^0, \tag{3.2.25b}$$

$$\mathbf{v}_0 = 0 \qquad \text{on } \partial\Sigma^0. \tag{3.2.25c}$$

Taking the average of the local flow in (3.2.25) over Y^0 gives the averaged-pore flow (seepage flow), that is, $\langle \mathbf{v}_0 \rangle_{Y^0}$; and from (3.1.13) we have

$$\langle \mathbf{v}_0 \rangle = \phi \langle \mathbf{v}_0 \rangle_{Y^0}. \tag{3.2.26}$$

Furthermore, the $\mathbf{v}_i$ are divergence-free in $\mathbf{y}$ for $i = 1, 2 \ldots$, meaning

$$\mathbf{v}_i = 0 \qquad \text{on } \partial\Sigma^0, \tag{3.2.27a}$$

$$\mathbf{n} \cdot \mathbf{v}_i = 0 \qquad \text{on } \partial\Sigma^0. \tag{3.2.27b}$$

Revisiting the expansion of the incompressibility condition, we have

$$\sum_{i=0}^{\infty} \varepsilon^i \big[\nabla_{\mathbf{x}} \cdot \mathbf{v}_i + \nabla_{\mathbf{y}} \cdot \mathbf{v}_{i+1} \big] = 0, \tag{3.2.28}$$

where, for $i = 0$ we proved in Eq.(3.2.21) that the mean zero order approximation is divergence free. Using the same steps, we show that for $i = 0, 1, \cdots$, we have

$$\nabla_{\mathbf{x}} \cdot \langle \mathbf{v}_i \rangle = 0. \tag{3.2.29}$$

The identities in Eqs.(3.2.25) and (3.2.25) are used in the upcoming derivation of the effective form of the mass transport model.

The Effective External Conditions. The Stokes equations in (3.2.6), when posed in a porous material, produce purely periodic velocity fields only if all forces, including pressure gradients, are constant across the domain [73]. The effective form of the Neumann conditions are

$$-\mathbf{n} \cdot \langle \mathbf{v}_0 \rangle = 1 \qquad \text{at } \Gamma_L, \tag{3.2.30a}$$
$$-\mathbf{n} \cdot \langle \mathbf{v}_0 \rangle = -1 \quad \text{at } \Gamma_R, \tag{3.2.30b}$$
$$-\mathbf{n} \cdot \langle \mathbf{v}_0 \rangle = 0 \qquad \text{at } \Gamma_T \cup \Gamma_B. \tag{3.2.30c}$$

Note that the Darcy velocity in Eq.(3.2.18) and Eq.(3.2.24) generates uniform flow (plug flow) and, as expected, the local velocities depend on the local spatial variable (for all $i = 1$), hence

$$\mathbf{v}_i = \mathbf{v}_i(\mathbf{y}). \tag{3.2.31}$$

By using the Neumann boundary conditions and eliminating any normal stresses generated at the walls, we avoid dealing with entry effects and boundary layers at the walls. Thus, the averaged flow is constant on the whole domain and purely periodic on the local scale.

3.3 Microscopic Description of the Model

The heuristic derivation of an effective model using asymptotic homogenisation starts with a microscopic description of the model. The model should be constructed using estimates of the relative "weights" of the system's various processes using the non-dimensional microscopic parameter ε. For any time scale T, a parameter, $\mathbb{P} = T_s^*/T^*$ is said to be of order ε^p if [168],

$$\mathcal{O}(\varepsilon^{p+1}) \ll \mathbb{P} \ll \mathcal{O}(\varepsilon^{p-1}). \tag{3.3.1}$$

The expression in (3.3.1) is referred to as the domain of validity of the parameter $\mathbb{P}$. To set the different microscopic descriptions we utilise the different time scales defined in Section 2.5 of Chapter 2.

Remark 3.1. *The arguments follow the dimensional analysis in Chapter 3 and are based on the known parameter values used in Chapter 4 and Chapter 5.*

Advection Mass Flow. The flowing groundwater bulk motion carries both microbes and contaminants. The advective transport of the microorganisms in the porous medium has an average value equal to the average velocity of the flow, provided the microorganisms do not interact with the solid interface [191, 155]. Since groundwater velocities vary significantly between locations, we consider three scenarios of advective flow regimes classified by the Péclet number, $\mathrm{Pe} = T_s^*/T_V^*$, where T_s^*

is the substrate diffusion time and T_V^* is the advection time as discussed in Section 2.5 of Chapter 2. According to the literature (e.g., Auriault and Adler [21], Royer [168]) we have:

$$\begin{aligned}
&\text{Diffusion regime} &:\ &\text{Pe} \leq \mathcal{O}(\varepsilon) &(3.3.2)\\
&\text{Advection–diffusion regime} &:\ &\text{Pe} = \mathcal{O}(\varepsilon^0) &(3.3.3)\\
&\text{Advection–dispersion regime:} &\ &\text{Pe} = \mathcal{O}(\varepsilon^{-1}) &(3.3.4)\\
&\text{No continuum macromodel} &:\ &\text{Pe} \geq \mathcal{O}(\varepsilon^{-2}). &(3.3.5)
\end{aligned}$$

The diffusion regime describes solute transport in stagnant flow, where diffusion dominates advection. When the weights of advection and diffusion are equivalent on the micro-scale, we have an advection-diffusion regime. Note that both the diffusion regime and the advection-diffusion regime are categorised as "diffusion dominated mixing" regimes when the transport diffusion is more pronounced at the microscopic scale. The advection-dispersion regime is categorised as "Taylor dispersion mediated mixing" when the transport process from advection dominates over those of diffusion at the macroscopic scale causing particles to be distributed at the microscale. At high Péclet number, $\text{Pe} \geq \mathcal{O}(\varepsilon^{-2})$, homogenisation cannot be used, and transport is completely dependent upon the macroscopic boundary conditions [21, 168].

Metabolic Reactions. The reaction rate is described using a Damköhler–like number in (2.6.16), which measures the speed of changes in the substrate concentration due to consumption in well-stirred mixtures. From known values of the metabolic rates, we deduce that

$$\begin{aligned}
\text{Da} &= T_s^*/T_{\max}^* \sim \mathcal{O}(\varepsilon^{-1}), &(3.3.6)\\
\kappa_b &= T_s^*/T_{\text{decay}}^* \sim \mathcal{O}(\varepsilon^{-1}), &(3.3.7)
\end{aligned}$$

with $\kappa_b < \text{Da}$. Here $T_{\max}^*$ and T_{decay}^* are the time scales of maximum metabolic rate and microbial death rate, respectively (see Eq.(2.5.7) in Section 2.5). Despite this, we will formally assume these parameters are of $\mathcal{O}(\varepsilon^0)$ in the following section. Note that the Damköhler–like number is associated with microbial consumption. However, since the metabolic reaction rates are diffusion limited, bacteria consumption generates the rate of depletion for the substrate, which is also related to the rate of the population's growth expansion. We approximate the depletion/growth expansion velocity as:

$$\begin{aligned}
\eta_\mu^* &\sim \sqrt{D_s^*/T_{\max}^*}\ [\text{m s}^{-1}], &(3.3.8)\\
\eta_K^* &\sim \sqrt{D_s^*/T_{K^*}^*}\ [\text{m s}^{-1}], &(3.3.9)
\end{aligned}$$

and subsequently the time scale for the depletion time is:

$$T_\mu^* = \frac{L_{x_1}^*}{\eta_\mu^*}. \tag{3.3.10}$$

Its is worth noting that the time scale in Eq.(3.3.10) is significantly smaller than it counterpart in well-stirred mixtures, hence

$$T_\mu^* \ll T_{\max}^*. \tag{3.3.11}$$

Using (3.3.10) we define a Péclet–like number as the ratio between the diffusion time and the metabolic velocity speed time, hence

$$\mathrm{Pe}_\mu \sim T_s^*/T_\mu^* = \sqrt{\mathrm{Da}} \sim \mathcal{O}\Big(\frac{1}{\sqrt{\varepsilon}}\Big). \tag{3.3.12}$$

We postulate due to the mesoscale order of the depletion flow it is sufficient to neglect the effect of the generating mass fluxes at the macroscopic scale. As a result, the metabolic times do not define a limiting case in our work. Note that, the reaction rates dominate when the Damköhler number is of order ε^{-2}. Therefore, we consider $\mathrm{Da} \sim \mathcal{O}(\varepsilon^0)$ in the following sections.

Chemotactic Drift The last process to discuss is the chemotactic transport of the microbial population. We define a chemotactic Péclet–like number as:

$$\mathrm{Pe}_\chi = T_s^*/T_\chi^*. \tag{3.3.13}$$

As explained in Section 2.5, determining T_χ^*, the chemotactic drift time scale, is not straightforward since it varies in time and space. Thus, in the upcoming homogenisation we only consider chemotactic fluxes with time scales equivalent to the substrate diffusion times, hence

$$\mathrm{Pe}_\chi \sim \mathcal{O}(\varepsilon^0). \tag{3.3.14}$$

Note that since $\mathrm{Pe}_b \sim \mathcal{O}(\varepsilon^{-1})$ it safe to assume that the chemotactic drift is always slowly varying in time, that is $\mathrm{Pe}_b\chi(s_\varepsilon) \sim \mathcal{O}(\mathrm{Pe}_\chi)$.

Initial Conditions. We only assume initial concentrations which are defined globally, that is

$$s_\varepsilon(0, \mathbf{x}, \mathbf{y}) = s_{in}(\mathbf{x}), \qquad b_\varepsilon(0, \mathbf{x}, \mathbf{y}) = b_{in}(\mathbf{x}). \tag{3.3.15}$$

This lets us avoid dealing with sophisticated extensions resulting from local fluctuations generated by the locally defined initial conditions.

External Boundary Conditions. The time scales governing the mathematical model inside the domain are assumed to remain unaffected by any mass fluxes at the external boundaries. Therefore, it suffices to apply the homogenisation procedure, assuming $\Omega = \mathbb{R}^2$. Later, in Chapters 4 and 5, the relevant homogenised external boundary conditions are imposed while asserting the system's well-posedness.

Finally, throughout this thesis, it should be clear that the only limiting cases relevant to the model we intend to upscale are the ones related to the three advective Péclet regimes shown in Figure 3.2.

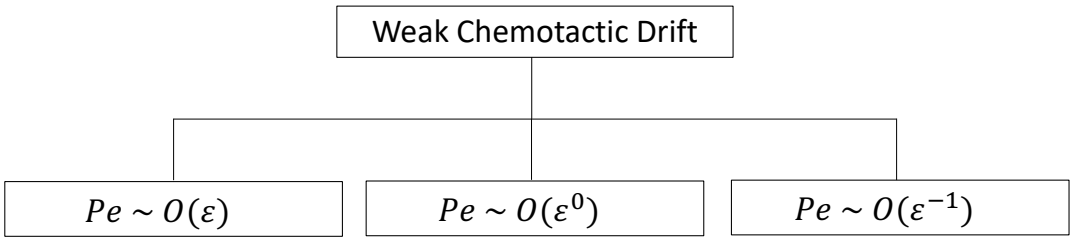


Figure 3.2: *The three limiting cases we upscale in this chapter.*

Remark 3.2. *As stated before, the formal method of asymptotic expansions can be made rigorous using two-scale homogenisation theory. In loose terms, the mathematical theory aims at establishing the existence and uniqueness of a solution ψ_ε in some energy space (see Allaire et al. [11]), and that the solution ψ_ε converges as $\varepsilon \to 0$. However, this is beyond the scope of this study.*

3.4 Chemotactic Transport in a Diffusion Regime

In a diffusion-dominated regime, the diffusion time scale dominates the mixing environment whereas advection becomes negligible at the macro-scale. Such a regime is characterised by the advective Péclet number in the following range,

$$\mathcal{O}(\varepsilon^2) \ll \mathrm{Pe} \ll \mathcal{O}(\varepsilon^0). \tag{3.4.1}$$

Chemotactic transport at the microscope scale in a diffusion-dominated mixing environment is described as:

$$\frac{\partial s_\varepsilon}{\partial t} = \nabla \cdot \left(\nabla s_\varepsilon - \varepsilon\widetilde{\mathrm{Pe}}\mathbf{v}_\varepsilon s_\varepsilon\right) - \frac{\mathrm{Da}}{Y}\frac{s_\varepsilon}{s_\varepsilon + \kappa_s} b_\varepsilon \qquad \text{in } [0,T]\times\Omega_\varepsilon\times Y^0, \tag{3.4.2a}$$

$$\begin{aligned}\frac{\partial b_\varepsilon}{\partial t} = \nabla \cdot \Big(\delta\nabla b_\varepsilon - \Big\{\varepsilon\widetilde{\mathrm{Pe}}\mathbf{v}_\varepsilon + \mathrm{Pe}_b\chi(s_\varepsilon)\nabla s_\varepsilon\Big\} b_\varepsilon\Big) \\ + \mathrm{Da}\frac{s_\varepsilon}{s_\varepsilon+\kappa_s}\left(1 - \frac{b_\varepsilon}{\kappa_c}\right) b_\varepsilon - \kappa_b b_\varepsilon \qquad \text{in } [0,T]\times\Omega_\varepsilon\times Y^0,\end{aligned} \tag{3.4.2b}$$

such that $\mathrm{Pe} = \varepsilon\widetilde{\mathrm{Pe}}$ where $\widetilde{\mathrm{Pe}} = \mathcal{O}(\varepsilon^0)$. At the solid-aqueous interface we assume no-flux and no-slip conditions, hence

$$-\mathbf{n}\cdot\nabla s_\varepsilon = -\mathbf{n}\cdot(\delta\nabla b_\epsilon) = 0. \tag{3.4.2c}$$

We close the model with the initial concentrations defined in (3.3.15).

3.4.1 The Homogenised Model

Assuming separation of spatial scales, $\varepsilon \ll 1$, the formal asymptotic homogenisation method begins by expanding the two species in terms of ε,

$$s_\varepsilon(t,\mathbf{x},\mathbf{y}) = s_0 + \varepsilon s_1 + \varepsilon^2 s_2 + \mathcal{O}(\varepsilon^3), \tag{3.4.3a}$$
$$b_\varepsilon(t,\mathbf{x},\mathbf{y}) = b_0 + \varepsilon b_1 + \varepsilon^2 b_2 + \mathcal{O}(\varepsilon^3), \tag{3.4.3b}$$

where the functions $s_i = s_i\,(t,\mathbf{x},\mathbf{y})$ and $b_i = b_i\,(t,\mathbf{x},\mathbf{y})$ are periodic in $\mathbf{y}$. For simplicity, we assume a uniform flow that depends solely on the local variable, $\mathbf{y}$, and thus the velocity can be expanded as:

$$\mathbf{v}_\varepsilon(\mathbf{y}) = \mathbf{v}_0 + \varepsilon\mathbf{v}_1 + \varepsilon^2\mathbf{v}_2 + \mathcal{O}(\varepsilon^3). \tag{3.4.4}$$

A preliminary step before starting the asymptotic expansion is to expand the nonlinear terms in the model. First, we expand the chemotaxis sensitivity function $\chi(s_\varepsilon)$ using the Taylor expansion about s_0, hence

$$\begin{cases} \chi(s_\varepsilon) = & \chi(s_0) + \varepsilon\{s_1 + \varepsilon s_2 + \cdots\}\chi'(s_0) \\ & +\dfrac{1}{2}\varepsilon^2\{s_1 + \varepsilon s_2 + \cdots\}^2\chi''(s_0) + \mathcal{O}(\varepsilon^3) \\ & = \hat{\chi}_0 + \varepsilon\hat{\chi}_1 + \varepsilon^2\hat{\chi}_2 + \mathcal{O}(\varepsilon^3), \end{cases} \tag{3.4.5}$$

where $\chi_0,\ \chi_1$, and χ_2 in the last line of (3.4.5) are given by

$$\begin{cases} \hat{\chi}_0 = & \chi(s_0) \\ \hat{\chi}_1 = & s_1\chi'(s_0) \\ \hat{\chi}_2 = & \{s_2\chi'(s_0) + \frac{1}{2}s_1^2\chi''(s_0)\}. \end{cases} \tag{3.4.6}$$

Then we expand the substrate gradient,

$$\begin{cases} \nabla s_\varepsilon = & \varepsilon^{-1}\nabla_{\mathbf{y}} s_0 + [\nabla_{\mathbf{x}} s_0 + \nabla_{\mathbf{y}} s_1] \\ & +\varepsilon[\nabla_{\mathbf{x}} s_1 + \nabla_{\mathbf{y}} s_2] + \varepsilon^2[\nabla_{\mathbf{x}} s_2 + \nabla_{\mathbf{y}} s_3] + \mathcal{O}(\varepsilon^3). \end{cases} \tag{3.4.7}$$

Combining the two expansions in (3.4.5) and (3.4.7), we obtain the expansion of the chemotaxis velocity

$$\begin{cases} \mathbf{v}_\varepsilon^c & = \mathrm{Pe}_b\chi(s_\varepsilon)\nabla s_\varepsilon \\ & = \varepsilon^{-1}\mathrm{Pe}_b\hat{\chi}_0\nabla_{\mathbf{y}} s_0 + \mathrm{Pe}_b\big\{\hat{\chi}_0[\nabla_{\mathbf{x}} s_0 + \nabla_{\mathbf{y}} s_1] + \hat{\chi}_1\nabla_{\mathbf{y}} s_0\big\} \\ & +\varepsilon\mathrm{Pe}_b\left\{\hat{\chi}_0[\nabla_{\mathbf{x}} s_1 + \nabla_{\mathbf{y}} s_2] + \hat{\chi}_1[\nabla_{\mathbf{x}} s_0 + \nabla_{\mathbf{y}} s_1] + \hat{\chi}_2\nabla_{\mathbf{y}} s_0\right\} + \mathcal{O}(\varepsilon^2) \\ & = \varepsilon^{-1}\mathbf{v}_c^{-1} + \mathbf{v}_c^0 + \varepsilon\mathbf{v}_c^1 + \mathcal{O}(\varepsilon^2). \end{cases} \tag{3.4.8}$$

We expand the nonlinear kinetics using Taylor expansion about (s_0, b_0). Due to the slow mass flow generated by the kinetics, it suffices to consider the zero-order

approximation, for which the approximated kinetics read

$$\begin{cases} G_s(s_\varepsilon, b_\varepsilon) & \approx \dfrac{\mathrm{Da}}{Y}\dfrac{s_0}{s_0+\kappa_s}, \\ G_b(s_\varepsilon, b_\varepsilon) & \approx \mathrm{Da}\dfrac{s_0}{s_0+\kappa_s}\left(1-\dfrac{b_0}{\kappa_c}\right)b_0 - \kappa b_0. \end{cases} \tag{3.4.9}$$

To perform a formal asymptotic expansion of the model in Eqs.(3.4.2) we postulate the ansatz s_ε and b_ε in Eqs.(3.4.3)–(3.4.4) and all the associated expansions therein. The asymptotic homogenisation result concerning the model in Eqs.(3.4.2) is given below.

Proposition 3.3. *Under the assumptions in Eqs.*(3.4.3)–(3.4.4) *and assuming the parameters other than* ε *are formally of* $\mathcal{O}(\varepsilon^0)$*, the averaged zero order approximations*

$$\mathcal{S}(t,\mathbf{x}) = s_0(t,\mathbf{x}), \qquad \textit{and} \qquad \mathcal{B}(t,\mathbf{x}) = b_0(t,\mathbf{x}), \tag{3.4.10}$$

are the solutions of the homogenised model

$$\begin{cases} \dfrac{\partial \mathcal{S}}{\partial t} = \nabla\cdot\left(\mathbf{D}^h\nabla\mathcal{S}\right) - \dfrac{\mathrm{Da}}{Y}\dfrac{\mathcal{S}}{\mathcal{S}+\kappa_s}\mathcal{B} & \textit{in } [0,T]\times\Omega, \\ \dfrac{\partial \mathcal{B}}{\partial t} = \nabla\cdot\Big(\delta\mathbf{D}^h\nabla\mathcal{B} - \big[\mathrm{Pe}_b\big\{\mathbf{D}^{\mathrm{h}}\chi(\mathcal{S})\nabla\mathcal{S}\big\}\big]\mathcal{B}\Big) & \\ \qquad\qquad + \mathrm{Da}\dfrac{\mathcal{S}}{\mathcal{S}+\kappa_s}\left(1-\dfrac{\mathcal{B}}{\kappa_c}\right)\mathcal{B} - \kappa_b\mathcal{B} & \textit{in } [0,T]\times\Omega, \end{cases} \tag{3.4.11}$$

with the effective diffusion tensor given by

$$\mathbf{D}^h = \Big\langle (\nabla_{\mathbf{y}}\boldsymbol{\omega})^T + \mathbf{I}\Big\rangle_{Y^0}, \tag{3.4.12}$$

where $\boldsymbol{\omega}(\mathbf{y}) = (\omega_1(\mathbf{y}), \omega_2(\mathbf{y}))^T$ *is the solution of the cell-problem, such that the two components satisfy the following cell-problem* ($j = 1,\ 2$)*:*

$$\begin{cases} \nabla_{\mathbf{y}}\cdot[\nabla_{\mathbf{y}}\omega_i + \mathbf{e}_i] = 0 & \textit{in } Y^0, \\ -\mathbf{n}\cdot[\nabla_{\mathbf{y}}\omega_i + \mathbf{e}_i] = 0 & \textit{on } \partial\Sigma^0, \\ \omega_i \textit{ is } Y-\textit{periodic, and } \langle\omega_i\rangle_{Y^0} = 0, & \end{cases} \tag{3.4.13}$$

with the initial conditions

$$\begin{cases} \mathcal{S}(0,\mathbf{x}) = \mathcal{S}_{in}(\mathbf{x}) = s_{in}(\mathbf{x}), \\ \mathcal{B}(0,\mathbf{x}) = \mathcal{B}_{in}(\mathbf{x}) = b_{in}(\mathbf{x}). \end{cases} \tag{3.4.14}$$

The homogenised chemotactic sensitivity function defined is written as:

$$\chi(\mathcal{S}) = \frac{2}{3}\tanh\left(\Upsilon_0\frac{\kappa_d}{(\mathcal{S}+\kappa_d)^2}\|\nabla\mathcal{S}\|\right)\frac{1}{\|\nabla\mathcal{S}\|}, \tag{3.4.15a}$$

$$\chi(\mathcal{S}) = \chi_0 \frac{\kappa_d}{(\mathcal{S}+\kappa_d)^2}. \tag{3.4.15b}$$

We remark that the velocity field no longer appears in the cell problem Eqs.(3.4.13), suggesting that it does not play a role in the transport process at the pore scale. Additionally, it is worth noting that the velocity has no effect on the homogenised model in Eqs.(3.4.11). Thus, for Péclet number of order $\mathcal{O}(\varepsilon)$ the model is equivalent to stagnated flow, that is, when $\mathbf{v}_\varepsilon = \mathbf{0}$.

The derivation of the effective model is detailed in the next section using formal asymptotic techniques. However, as stated in Remark 3.2, undertaking the rigorous justification to prove the existence and uniqueness of the two homogenised solutions $(\mathcal{S}, \mathcal{B})$ as $\varepsilon \to 0$ is beyond the scope of this thesis.

3.4.2 The Formal Asymptotic Expansion

As in any method of asymptotic analysis, we need to substitute the postulated ansatz into Eq.(3.4.3)–(3.4.9) together with substituting the differential operators in (3.1.11) into the partial differential equation under consideration. We then obtain a cascade of local substrate and bacteria problems at different orders of ε. At $\mathcal{O}(\varepsilon^{-2})$, we have the following local substrate problem:

$$\nabla_{\mathbf{y}}^2 s_0 = 0 \qquad \text{in } Y^0, \tag{3.4.16a}$$

$$-\mathbf{n}\cdot\nabla_{\mathbf{y}} s_0 = 0 \qquad \text{on } \partial\Sigma^0. \tag{3.4.16b}$$

At the same order, the local equations for the bacteria are:

$$\nabla_{\mathbf{y}}(\delta\nabla_{\mathbf{y}} b_0 - \mathrm{Pe}_b\{b_0\hat{\chi}_0\nabla_{\mathbf{y}} s_0\}) = 0 \qquad \text{in } Y^0, \tag{3.4.17a}$$

$$-\mathbf{n}\cdot(\delta\nabla_{\mathbf{y}} b_0 - \mathrm{Pe}_b\{b_0\hat{\chi}_0\nabla_{\mathbf{y}} s_0\}) = 0 \qquad \text{on } \partial\Sigma^0. \tag{3.4.17b}$$

The solution of the substrate problem at order ε^{-2} is unique and depends only on the global variable $\mathbf{x}$. To prove this, we multiply the boundary value problem in (3.4.16) by s_0 and integrate the results over Y^0. Utilising Green's formula and the periodicity assumption over Y, we find:

$$\begin{aligned} 0 &= \int_{Y^0} s_0 \nabla_{\mathbf{y}}\cdot(\nabla_{\mathbf{y}} s_0)\, d\mathbf{y} \\ &= -\int_{Y^0} \nabla_{\mathbf{y}} s_0 \cdot \nabla_{\mathbf{y}} s_0 d\mathbf{y} + \underbrace{\int_{\partial\Sigma^0} \mathbf{n}\cdot\nabla_{\mathbf{y}} s_0 d\mathbf{s}}_{=0} \\ &= -\int_{Y^0} |\nabla_{\mathbf{y}} s_0|^2 d\mathbf{y}, \end{aligned} \tag{3.4.18}$$

which implies that the zero-order approximation of the substrate concentration is a constant function in $\mathbf{y}$,

$$s_0 = s_0(t, \mathbf{x}). \tag{3.4.19}$$

From the result in (3.4.19), we have $\nabla_{\mathbf{y}} s_0 = \mathbf{0}$. Thus, the bacteria equation in (3.4.17) is reduced to

$$\nabla_{\mathbf{y}}(\delta \nabla_{\mathbf{y}} b_0) = 0 \qquad \text{in } Y^0, \tag{3.4.20a}$$
$$-\mathbf{n} \cdot (\delta \nabla_{\mathbf{y}} b_0) = 0 \qquad \text{on } \partial\Sigma^0. \tag{3.4.20b}$$

Repeating the same argument used to show the result in (3.4.18), the local bacteria problem given in (3.4.20) has solution

$$b_0 = b_0\left(t, \mathbf{x}\right). \tag{3.4.21}$$

At $\mathcal{O}(\varepsilon^{-1})$, we have the following local substrate problem,

$$\nabla_{\mathbf{y}} \cdot [\nabla_{\mathbf{x}} s_0 + \nabla_{\mathbf{y}} s_1] = -\nabla_{\mathbf{x}} \cdot \nabla_{\mathbf{y}} s_0 \qquad \text{in } Y^0, \tag{3.4.22a}$$
$$-\mathbf{n} \cdot [\nabla_{\mathbf{x}} s_0 + \nabla_{\mathbf{y}} s_1] = 0 \qquad \text{on } \partial\Sigma^0, \tag{3.4.22b}$$

with the local bacteria problem at $\mathcal{O}(\varepsilon^{-1})$ given by

$$\begin{aligned} \nabla_{\mathbf{y}} \cdot (\delta\big[\nabla_{\mathbf{x}} b_0 + \nabla_{\mathbf{y}} b_1\big]) &= \nabla_{\mathbf{y}} \cdot \big(\mathrm{Pe}_b b_0 \hat{\chi}_0 \nabla_{\mathbf{y}} s_0\big) \\ &\quad + \nabla_{\mathbf{y}} \cdot \big(\mathrm{Pe}_b \hat{\chi}_0 [\nabla_{\mathbf{x}} s_0 + \nabla_{\mathbf{y}} s_1] b_0\big) \\ &\quad + \nabla_{\mathbf{y}} \cdot \big(\mathrm{Pe}_b [b_1 \hat{\chi}_0 + b_0 \hat{\chi}_1] \nabla_{\mathbf{y}} s_0\big) \\ &\quad - \nabla_{\mathbf{x}} \cdot \big(\delta \nabla_{\mathbf{y}} b_0\big) \qquad \text{in } Y^0, \end{aligned} \tag{3.4.23a}$$
$$-\mathbf{n} \cdot \big(\delta[\nabla_{\mathbf{x}} b_0 + \nabla_{\mathbf{y}} b_1]\big) = 0 \qquad \text{on } \partial\Sigma^0. \tag{3.4.23b}$$

Since s_0 and b_0 are functions of $\mathbf{x}$ only, we have

$$\nabla_{\mathbf{y}} s_0 = \nabla_{\mathbf{y}} b_0 = \mathbf{0}. \tag{3.4.24}$$

Thereby, the terms involving the local gradients in Eq.(3.4.22) and Eq.(3.4.23) vanish. Therefore, the local substrate equation in Eq.(3.4.22) is simplified to

$$\nabla_{\mathbf{y}} \cdot [\nabla_{\mathbf{x}} s_0 + \nabla_{\mathbf{y}} s_1] = 0 \qquad \text{in } Y^0, \tag{3.4.25a}$$
$$-\mathbf{n} \cdot [\nabla_{\mathbf{x}} s_0 + \nabla_{\mathbf{y}} s_1] = 0 \qquad \text{on } \partial\Sigma^0. \tag{3.4.25b}$$

Furthermore, since b_0 and $\hat{\chi}_0$ are functions of $\mathbf{x}$ only, utilising the local problem (3.4.25), we see that the following term in Eq.(3.4.23) vanishes,

$$\nabla_{\mathbf{y}} \cdot \big(\mathrm{Pe}_b \hat{\chi}_0 [\nabla_{\mathbf{x}} s_0 + \nabla_{\mathbf{y}} s_1] b_0\big) = \mathrm{Pe}_b b_0 \hat{\chi}_0 \nabla_{\mathbf{y}} \cdot \big([\nabla_{\mathbf{x}} s_0 + \nabla_{\mathbf{y}} s_1]\big) = 0. \tag{3.4.26}$$

Therefore, (3.4.23) become

$$\nabla_{\mathbf{y}} \cdot (\delta\left[\nabla_{\mathbf{x}} b_0 + \nabla_{\mathbf{y}} b_1\right]) = 0 \qquad \text{in } Y^0, \tag{3.4.27a}$$
$$-\mathbf{n} \cdot (\delta\left[\nabla_{\mathbf{x}} b_0 + \nabla_{\mathbf{y}} b_1\right]) = 0 \qquad \text{on } \partial\Sigma^0. \tag{3.4.27b}$$

We notice that at $\mathcal{O}(\varepsilon^{-1})$ both local problems in (3.4.25) and (3.4.27) have the same structure. As a direct consequence of the *Fredholm Alternative* stated in Lemma 3.4 [70, 13], the local boundary value problems in (3.4.25) and (3.4.27) admit two unique solutions up to an additive constant function in $\mathbf{x}$.

Lemma 3.4. *There is a unique solution, up to an additive constant, to the boundary value problem*

$$\nabla_{\mathbf{y}}^2 \zeta(\mathbf{y}) = g(\mathbf{y}) \qquad \text{in } Y^0, \tag{3.4.28}$$

$$-\mathbf{n} \cdot \nabla_{\mathbf{y}} \zeta(\mathbf{y}) = h(\mathbf{y}) \qquad \text{on } \partial\Sigma^0, \tag{3.4.29}$$

where ζ is periodic in $\mathbf{y}$, if and only if the compatibility condition

$$\int_{Y^0} g(\mathbf{y}) d\mathbf{y} = \int_{\partial\Sigma^0} h(\mathbf{y}) d\mathbf{s}, \tag{3.4.30}$$

is satisfied.

The two solutions s_1 and b_1 take the following form:

$$s_1(t, \mathbf{x}, \mathbf{y}) = \boldsymbol{\omega}(\mathbf{y}) \cdot \nabla_{\mathbf{x}} s_0 + \bar{s}_1(t, \mathbf{x}), \tag{3.4.31a}$$

$$b_1(t, \mathbf{x}, \mathbf{y}) = \boldsymbol{\omega}(\mathbf{y}) \cdot \nabla_{\mathbf{x}} b_0 + \bar{b}_1(t, \mathbf{x}), \tag{3.4.31b}$$

where $\bar{s}_1$ and $\bar{b}_1$ are additive functions independent of $\mathbf{y}$. The first correction functions of the bacteria and substrate concentrations in Eqs.(3.4.31) are defined using the correction vector function $\boldsymbol{\omega}(\mathbf{y}) = (\omega_1(\mathbf{y}), \omega_2(\mathbf{y}))^T$, where the two components satisfy the following *cell-problem*:

$$\begin{cases} \nabla_{\mathbf{y}} \cdot [\nabla_{\mathbf{y}} \omega_i + \mathbf{e}_i] = 0 & \text{in } Y^0, \\ -\mathbf{n} \cdot [\nabla_{\mathbf{y}} \omega_i + \mathbf{e}_i] = 0 & \text{on } \partial\Sigma^0, \\ \omega_i \text{ is } Y - \text{periodic, and } \langle \omega_i \rangle_{Y^0} = 0. \end{cases} \tag{3.4.32}$$

The final step in the asymptotic homogenisation starts with collecting terms of $\mathcal{O}(\varepsilon^0)$. The local substrate problem at this order is

$$\begin{aligned} \nabla_{\mathbf{y}} \cdot [\nabla_{\mathbf{x}} s_1 + \nabla_{\mathbf{y}} s_2] = \frac{\partial s_0}{\partial t} - \nabla_{\mathbf{x}} \cdot ([\nabla_{\mathbf{x}} s_0 + \nabla_{\mathbf{y}} s_1]) \\ + \frac{\mathrm{Da}}{Y} \frac{s_0}{s_0 + \kappa_s} b_0 \qquad \text{in } Y^0, \end{aligned} \tag{3.4.33a}$$

$$-\mathbf{n} \cdot [\nabla_{\mathbf{x}} s_1 + \nabla_{\mathbf{y}} s_2] = 0 \qquad \text{on } \partial\Sigma^0, \tag{3.4.33b}$$

and the local bacteria problem is

$$\begin{aligned} \nabla_{\mathbf{y}} \cdot \big(\delta \big[\nabla_{\mathbf{x}} b_1 + \nabla_{\mathbf{y}} b_2\big]\big) = \frac{\partial b_0}{\partial t} - \nabla_{\mathbf{x}} \cdot \big(\delta \left[\nabla_{\mathbf{x}} b_0 + \nabla_{\mathbf{y}} b_1\right]\big) \\ + \nabla_{\mathbf{x}} \cdot \big(\mathrm{Pe}_b \hat{\chi}_0 [\nabla_{\mathbf{x}} s_0 + \nabla_{\mathbf{y}} s_1] b_0\big) \\ + \nabla_{\mathbf{x}} \cdot \big\{\mathrm{Pe}_b (b_1 \hat{\chi}_0 + b_0 \hat{\chi}_1) \nabla_{\mathbf{y}} s_0\big\} \\ + \nabla_{\mathbf{y}} \cdot (\mathrm{Pe}_b \{b_0 \hat{\chi}_2 + b_1 \hat{\chi}_1 + b_2 \hat{\chi}_0\} \nabla_{\mathbf{y}} s_0) \\ + \nabla_{\mathbf{y}} \cdot \big(\mathrm{Pe}_b \{b_1 \hat{\chi}_0 + b_0 \hat{\chi}_1\} [\nabla_{\mathbf{x}} s_0 + \nabla_{\mathbf{y}} s_1]\big) \end{aligned}$$

$$
\begin{aligned}
&+ \nabla_{\mathbf{y}} \cdot (\mathrm{Pe}_b \hat{\chi}_0 [\nabla_{\mathbf{x}} s_1 + \nabla_{\mathbf{y}} s_2] b_0) \\
&- \mathrm{Da}\, \frac{s_0}{s_0 + \kappa_s} \left(1 - \frac{b_0}{\kappa_c}\right) b_0 + \kappa_b b_0 \qquad \text{in } Y^0, \qquad (3.4.34a)\\
-\mathbf{n} \cdot \big(\delta\, [\nabla_{\mathbf{x}} b_1 + \nabla_{\mathbf{y}} b_2]\,\big) &= 0 \qquad \text{on } \partial\Sigma^0. \qquad (3.4.34b)
\end{aligned}
$$

As a result of (3.4.24), the terms containing the local gradient of the substrate vanish; hence, the local equation in (3.4.34) reduces to

$$
\begin{aligned}
\nabla_{\mathbf{y}} \cdot (\delta\, [\nabla_{\mathbf{x}} b_1 + \nabla_{\mathbf{y}} b_2]) = \frac{\partial b_0}{\partial t} &- \nabla_{\mathbf{x}} \cdot \big(\delta \big[\nabla_{\mathbf{x}} b_0 + \nabla_{\mathbf{y}} b_1\big]\big) \\
&+ \nabla_{\mathbf{x}} \cdot \big(\mathrm{Pe}_b \hat{\chi}_0 [\nabla_{\mathbf{x}} s_0 + \nabla_{\mathbf{y}} s_1] b_0\big) \\
&+ \nabla_{\mathbf{y}} \cdot \big(\mathrm{Pe}_b \{b_1 \hat{\chi}_0 + b_0 \hat{\chi}_1\} [\nabla_{\mathbf{x}} s_0 + \nabla_{\mathbf{y}} s_1] b_0\big) \\
&+ \nabla_{\mathbf{y}} \cdot (\mathrm{Pe}_b \hat{\chi}_0 [\nabla_{\mathbf{x}} s_1 + \nabla_{\mathbf{y}} s_2] b_0) \\
&- \mathrm{Da}\, \frac{s_0}{s_0 + \kappa_s} \left(1 - \frac{b_0}{\kappa_c}\right) b_0 + \kappa_b b_0 \qquad \text{in } Y^0, \qquad (3.4.35a)\\
-\mathbf{n} \cdot (\delta\, [\nabla_{\mathbf{x}} b_1 + \nabla_{\mathbf{y}} b_2]) &= 0 \qquad \text{on } \partial\Sigma^0. \qquad (3.4.35b)
\end{aligned}
$$

The local problem in (3.4.33) admits a unique solution if and only if the following solvability condition is satisfied,

$$
\int_{Y^0} \Big\{ \frac{\partial s_0}{\partial t} - \nabla_{\mathbf{x}} \cdot \big(\big[\nabla_{\mathbf{x}} s_0 + \nabla_{\mathbf{y}} s_1\big]\big) + \frac{\mathrm{Da}}{Y} \frac{s_0}{s_0 + \kappa_s} b_0 \Big\} d\mathbf{y} = 0. \qquad (3.4.36)
$$

Next, substituting s_1 given by (3.4.31a) into (3.4.36), we write the solvability condition in terms of the averaged operator (see Eq.(3.1.12b)) as:

$$
\begin{aligned}
\frac{\partial \langle s_0 \rangle}{\partial t} &= \nabla_{\mathbf{x}} \cdot \Big\{ \frac{1}{|Y|} \int_Y \Big[\nabla_{\mathbf{x}} s_0 + \nabla_{\mathbf{y}} \big(\boldsymbol{\omega}(\mathbf{y}) \nabla_{\mathbf{x}} s_0 + \bar{s}_1\big) + \frac{\mathrm{Da}}{Y} \frac{s_0}{s_0 + \kappa_s} b_0 \Big] d\mathbf{y} \Big\} \\
&= \nabla_{\mathbf{x}} \cdot \big(\langle \mathbf{I} + \nabla_{\mathbf{y}} \boldsymbol{\omega}^T \rangle_{Y^0} \nabla_{\mathbf{x}} \langle s_0 \rangle\big) - \frac{\mathrm{Da}}{Y} \Big\langle \frac{s_0}{s_0 + \kappa_s} b_0 \Big\rangle \\
&= \nabla_{\mathbf{x}} \cdot \big(\mathbf{D}^h \nabla_{\mathbf{x}} \langle s_0 \rangle\big) - \frac{\mathrm{Da}}{Y} \Big\langle \frac{s_0}{s_0 + \kappa_s} b_0 \Big\rangle, \qquad (3.4.37)
\end{aligned}
$$

where the effective diffusion tensor $\mathbf{D}^h$ is defined by:

$$
\mathbf{D}^h = \langle \mathbf{I} + \nabla_{\mathbf{y}} \boldsymbol{\omega}^T \rangle_{Y^0}. \qquad (3.4.38)
$$

Note that in Eqs.(3.4.37) we utilised the following relationship

$$
\nabla_{\mathbf{x}} s_0 = \langle \nabla_{\mathbf{x}} s_0 \rangle_{Y^0} = \frac{1}{\phi} \langle \nabla_{\mathbf{x}} s_0 \rangle = \frac{1}{\phi} \nabla_{\mathbf{x}} \langle s_0 \rangle. \qquad (3.4.39)
$$

Similarly, the local bacteria problem in (3.4.35) admits a unique solution provided the following solvability condition is satisfied:

$$
\int_{Y^0} \Big\{ \frac{\partial b_0}{\partial t} - \nabla_{\mathbf{x}} \cdot \Big(\delta [\nabla_{\mathbf{x}} b_0 + \nabla_{\mathbf{y}} b_1] - \big\{ \mathrm{Pe}_b \hat{\chi}_0 [\nabla_{\mathbf{x}} s_0 + \nabla_{\mathbf{y}} s_1] \big\} b_0 \Big)
$$

$$
\begin{aligned}
&+ \nabla_{\mathbf{y}} \cdot \Big(\mathrm{Pe}_b \hat{\chi}_0 [\nabla_{\mathbf{x}} s_0 + \nabla_{\mathbf{y}} s_1] b_1 \Big) \\
&+ \nabla_{\mathbf{y}} \cdot \Big(\mathrm{Pe}_b \hat{\chi}_1 [\nabla_{\mathbf{x}} s_0 + \nabla_{\mathbf{y}} s_1] b_0 \Big) \\
&+ \nabla_{\mathbf{y}} \cdot \Big(\mathrm{Pe}_b \hat{\chi}_0 [\nabla_{\mathbf{x}} s_1 + \nabla_{\mathbf{y}} s_2] b_0 \Big) \\
&- \mathrm{Da} \frac{s_0}{s_0 + \kappa_s} \Big(1 - \frac{b_0}{\kappa_c} \Big) b_0 + \kappa_b b_0 \Big\} d\mathbf{y} = 0. \qquad (3.4.40)
\end{aligned}
$$

As a result of the solid-aqueous interface conditions in (3.4.25) and (3.4.33) and since $\hat{\chi}_0$ is independent of $\mathbf{y}$, the following terms in (3.4.40) vanish, hence

$$
\begin{cases}
\displaystyle\int_{Y^0} \nabla_{\mathbf{y}} \cdot (\mathrm{Pe}_b \hat{\chi}_0 [\nabla_{\mathbf{x}} s_0 + \nabla_{\mathbf{y}} s_1] b_0) d\mathbf{y} &= \displaystyle\int_{\partial \Sigma^0} \mathrm{Pe}_b \hat{\chi}_0 b_0 \{ \mathbf{n} \cdot [\nabla_{\mathbf{x}} s_0 + \nabla_{\mathbf{y}} s_1] \} d\mathbf{s} = 0, \\
\displaystyle\int_{Y^0} \nabla_{\mathbf{y}} \cdot (\mathrm{Pe}_b \hat{\chi}_0 [\nabla_{\mathbf{x}} s_0 + \nabla_{\mathbf{y}} s_1] b_1) d\mathbf{y} &= \displaystyle\int_{\partial \Sigma^0} \mathrm{Pe}_b \hat{\chi}_0 b_1 \{ \mathbf{n} \cdot [\nabla_{\mathbf{x}} s_0 + \nabla_{\mathbf{y}} s_1] \} d\mathbf{s} = 0, \\
\displaystyle\int_{Y^0} \nabla_{\mathbf{y}} \cdot (\mathrm{Pe}_b \hat{\chi}_0 [\nabla_{\mathbf{x}} s_1 + \nabla_{\mathbf{y}} s_2] b_0) d\mathbf{y} &= \displaystyle\int_{\partial \Sigma^0} \mathrm{Pe}_b \hat{\chi}_0 b_0 \{ \mathbf{n} \cdot [\nabla_{\mathbf{x}} s_1 + \nabla_{\mathbf{y}} s_2] \} d\mathbf{s} = 0.
\end{cases} \qquad (3.4.41)
$$

As before, rewriting the solvability condition in (3.4.40) using the average operator, we have

$$
\begin{aligned}
\frac{\partial \langle b_0 \rangle}{\partial t} = \frac{1}{|Y|} \int_{Y^0} \Big(& \underbrace{\nabla_{\mathbf{x}} \cdot (\delta [\nabla_{\mathbf{x}} b_0 + \nabla_{\mathbf{y}} b_1])}_{\mathrm{I}_1} - \underbrace{\nabla_{\mathbf{x}} \cdot \{ \mathrm{Pe}_b \hat{\chi}_0 [\nabla_{\mathbf{x}} s_0 + \nabla_{\mathbf{y}} s_1] b_0 \}}_{\mathrm{I}_2} d\mathbf{y} \Big) \\
& + \left\langle \mathrm{Da} \frac{s_0}{s_0 + \kappa_s} \left(1 - \frac{b_0}{\kappa_c} \right) b_0 - \kappa_b b_0 \right\rangle. \qquad (3.4.42)
\end{aligned}
$$

Substituting b_1, given in (3.4.31b), into I_1 gives

$$
\begin{aligned}
\mathrm{I}_1 &= \nabla_{\mathbf{x}} \cdot \Big\{ \frac{\delta}{|Y|} \int_{Y^0} [\nabla_{\mathbf{x}} b_0 + \nabla_{\mathbf{y}} b_1] d\mathbf{y} \Big\} \\
&= \nabla_{\mathbf{x}} \cdot \Big\{ \frac{\delta}{|Y|} \int_{Y^0} [\nabla_{\mathbf{x}} b_0 + \nabla_{\mathbf{y}} \{ \boldsymbol{\omega} \nabla_{\mathbf{x}} b_0 + \bar{b}_1 \}] d\mathbf{y} \Big\} \\
&= \nabla_{\mathbf{x}} \cdot \big(\delta \langle \mathbf{I} + \nabla_{\mathbf{y}} \boldsymbol{\omega}^T \rangle_{Y^0} \nabla_{\mathbf{x}} \langle b_0 \rangle \big) \\
&= \nabla_{\mathbf{x}} \cdot \big(\delta \mathbf{D}^h \nabla_{\mathbf{x}} \langle b_0 \rangle \big) . \qquad (3.4.43)
\end{aligned}
$$

Next, substituting s_1 into I_2 we obtain

$$
\begin{aligned}
\mathrm{I}_2 &= \nabla_{\mathbf{x}} \cdot \Big(\frac{\mathrm{Pe}_b b_0 \hat{\chi}_0}{|Y|} \Big\{ \int_{Y^0} [\nabla_{\mathbf{x}} s_0 + \nabla_{\mathbf{y}} s_1] d\mathbf{y} \Big\} \Big) \\
&= \nabla_{\mathbf{x}} \cdot \Big(\frac{\mathrm{Pe}_b b_0 \hat{\chi}_0}{|Y|} \Big\{ \int_{Y^0} [\nabla_{\mathbf{x}} s_0 + \nabla_{\mathbf{y}} \{ \boldsymbol{\omega} \nabla_{\mathbf{x}} s_0 + \bar{s} \}] d\mathbf{y} \Big\} \Big) \\
&= \nabla_{\mathbf{x}} \cdot \Big(\big\langle \mathbf{I} + (\nabla_{\mathbf{y}} \boldsymbol{\omega})^T \big\rangle_{Y^0} \big\langle \mathrm{Pe}_b b_0 \hat{\chi}_0 \nabla_{\mathbf{x}} s_0 \big\rangle \Big)
\end{aligned}
$$

$$= \nabla_{\mathbf{x}} \cdot \Big(\mathbf{D}^h \big\langle \mathrm{Pe}_b b_0 \hat{\chi}_0 \nabla_{\mathbf{x}} s_0 \big\rangle \Big). \tag{3.4.44}$$

Therefore, from Eq.(3.4.43) and Eq.(3.4.44), the solvability condition in (3.4.42) becomes

$$\begin{aligned} \frac{\partial \langle b_0 \rangle}{\partial t} = \nabla_{\mathbf{x}} \cdot \Big(\delta \mathbf{D}^h \nabla_{\mathbf{x}} \langle b_0 \rangle - \mathbf{D}^h \big\langle \mathrm{Pe}_b b_0 \hat{\chi}_0 \nabla_{\mathbf{x}} s_0 \big\rangle \Big) \\ + \left\langle \mathrm{Da} \frac{s_0}{s_0 + \kappa_s} \left(1 - \frac{b_0}{\kappa_c} \right) b_0 - \kappa_b b_0 \right\rangle. \end{aligned} \tag{3.4.45}$$

Since the equations in (3.4.37) and (3.4.45) are independent of the local variable, using (3.1.13) yields:

$$\phi \frac{\partial s_0}{\partial t} = \nabla_{\mathbf{x}} \cdot \big(\phi \mathbf{D}^h \nabla_{\mathbf{x}} s_0 \big) - \phi \Big(\frac{\mathrm{Da}}{Y} \frac{s_0}{s_0 + \kappa_s} b_0 \Big), \tag{3.4.46}$$

$$\begin{aligned} \phi \frac{\partial b_0}{\partial t} = \nabla_{\mathbf{x}} \cdot \Big(\phi \delta \mathbf{D}^h \nabla_{\mathbf{x}} b_0 - \phi \mathbf{D}^h \mathrm{Pe}_b \big[\chi(s_0) \nabla_{\mathbf{x}} s_0 \big] b_0 \Big) \\ + \phi \left(\mathrm{Da} \frac{s_0}{s_0 + \kappa_s} \left(1 - \frac{b_0}{\kappa_c} \right) b_0 - \kappa_b b_0 \right). \end{aligned} \tag{3.4.47}$$

Then, by dividing by the porosity parameter, ϕ, in (3.4.47) we obtain the homogenised transport equations in (3.4.11) after setting

$$\mathcal{S} = s_0, \qquad \text{and} \qquad \mathcal{B} = b_0. \tag{3.4.48}$$

The initial conditions in Eq.(3.3.15) are upscaled by simply taking the average of their zero order approximations over Y, hence

$$\mathcal{S}(0, \mathbf{x}) = \mathcal{S}_{in} = s_{in}(\mathbf{x}), \tag{3.4.49}$$

$$\mathcal{B}(0, \mathbf{x}) = \mathcal{B}_{in} = b_{in}(\mathbf{x}). \tag{3.4.50}$$

3.5 Chemotactic Transport in an Advection-Diffusion Regime

In this section we assume an advection-diffusion mixing environment where the time scales of both diffusion and advection are comparable, which defines the next interesting case in the category of "diffusion-dominated mixing". This regime is characterised by the following range of the global Péclet number:

$$\mathcal{O}(\varepsilon) \ll \mathrm{Pe} \ll \mathcal{O}(\varepsilon^{-1}). \tag{3.5.1}$$

The chemotactic transport in an advection-diffusion mixing regime is

$$\frac{\partial s_\varepsilon}{\partial t} = \nabla \cdot (\nabla s_\varepsilon - \mathrm{Pe} \mathbf{v}_\varepsilon s_\varepsilon) - \frac{\mathrm{Da}}{Y} \frac{s_\varepsilon}{s_\varepsilon + \kappa_s} b_\varepsilon \qquad \text{in } [0, T] \times \Omega_\varepsilon \times Y^0, \tag{3.5.2a}$$

$$\frac{\partial b_\varepsilon}{\partial t} = \nabla \cdot (\delta \nabla b_\varepsilon - \{\mathrm{Pe}\mathbf{v}_\varepsilon + \mathrm{Pe}_b \chi(s_\varepsilon)\nabla s_\varepsilon\} b_\varepsilon) + \mathrm{Da}\frac{s_\varepsilon}{s_\varepsilon + \kappa_s}\left(1 - \frac{b_\varepsilon}{\kappa_c}\right) b_\varepsilon - \kappa_b b_\varepsilon \qquad \text{in } [0,T] \times \Omega_\varepsilon \times Y^0, \tag{3.5.2b}$$

with the solid-aqueous interface conditions defined as:

$$-\mathbf{n} \cdot \nabla s_\varepsilon = -\mathbf{n} \cdot (\delta \nabla b_\epsilon) = 0, \tag{3.5.2c}$$

and the globally defined initial conditions given in Eq.(3.3.15).

3.5.1 The Homogenised Model

For the formal asymptotic expansion of the model in Eqs.(3.5.2) we apply the same ansatz used for Proposition 3.3. The results concerning the model in Eqs.(3.5.2) are given below.

Proposition 3.5. *Under the assumptions in Eqs.*(3.4.3)–(3.4.4) *and assuming the parameters other than* ε *are formally of* $\mathcal{O}(\varepsilon^0)$*, the averaged zero order approximations*

$$\mathcal{S}(t,\mathbf{x}) = s_0(t,\mathbf{x}) \quad \textit{and} \quad \mathcal{B}(t,\mathbf{x}) = b_0(t,\mathbf{x}), \tag{3.5.3}$$

are the solutions of the homogenised model

$$\begin{cases} \dfrac{\partial \mathcal{S}}{\partial t} = \nabla \cdot \left(\mathbf{D}^h \nabla \mathcal{S} - \mathrm{Pe}\langle \mathbf{v}_0 \rangle_{Y^0} \mathcal{S}\right) - \dfrac{\mathrm{Da}}{Y}\dfrac{\mathcal{S}}{\mathcal{S}+\kappa_s}\mathcal{B} & \textit{in } [0,T]\times\Omega, \\ \dfrac{\partial \mathcal{B}}{\partial t} = \nabla \cdot \Big(\delta \mathbf{D}^h \nabla \mathcal{B} - \big[\mathrm{Pe}\langle \mathbf{v}_0 \rangle_{Y^0} + \mathrm{Pe}_b\big\{\mathbf{D}^{\mathrm{h}}\chi(\mathcal{S})\nabla\mathcal{S}\big\}\big]\mathcal{B}\Big) \\ \qquad\qquad + \mathrm{Da}\dfrac{\mathcal{S}}{\mathcal{S}+\kappa_s}\left(1 - \dfrac{\mathcal{B}}{\kappa_c}\right)\mathcal{B} - \kappa_b \mathcal{B} & \textit{in } [0,T]\times\Omega, \end{cases} \tag{3.5.4}$$

where $\langle \mathbf{v}_0 \rangle_{Y^0}$ *is the averaged zero order approximation of the Darcy velocity, with the effective diffusion tensor given by*

$$\mathbf{D}^h = \left\langle (\nabla_{\mathbf{y}} \boldsymbol{\omega})^T + \mathbf{I} \right\rangle_{Y^0}, \tag{3.5.5}$$

with $\boldsymbol{\omega}(\mathbf{y}) = (\omega_1(\mathbf{y}), \omega_2(\mathbf{y}))^T$*, where the two components satisfy the cell-problem (*$j = 1,\ 2$*):*

$$\begin{cases} \nabla_{\mathbf{y}} \cdot [\nabla_{\mathbf{y}} \omega_i + \mathbf{e}_i] = 0 & \textit{in } Y^0, \\ -\mathbf{n} \cdot [\nabla_{\mathbf{y}} \omega_i + \mathbf{e}_i] = 0 & \textit{on } \partial\Sigma^0, \\ \omega_i \textit{ is } Y-\textit{periodic, and } \langle \omega_i \rangle_{Y^0} = 0, \end{cases} \tag{3.5.6}$$

with the initial conditions

$$\mathcal{S}(0,\mathbf{x}) = \mathcal{S}_{in}(\mathbf{x}), \qquad \textit{and} \qquad \mathcal{B}(0,\mathbf{x}) = \mathcal{B}_{in}(\mathbf{x}), \tag{3.5.7}$$

where $\mathcal{S}_{in}(\mathbf{x}) = s_{in}(\mathbf{x})$ *and* $\mathcal{B}_{in}(\mathbf{x}) = b_{in}(\mathbf{x})$*.*

Here we have the same upscaled chemotactic function given in Eqs.(3.4.15). We point out that the *cell-problem* in (3.5.6) remains independent of the advection indicating that the diffusion is dominant at the pore scale. This is also the case for $\mathrm{Pe} \approx \mathcal{O}(\varepsilon)$. However, in the case of $\mathrm{Pe} \approx \mathcal{O}(\varepsilon)$ we have a pure diffusion model while in the case of $\mathrm{Pe} \approx \mathcal{O}(\varepsilon^0)$ advection appears at the macroscopic scale.

3.5.2 The Formal Asymptotic Homogenisation

Following the same steps as in Section 3.4.1, at $\mathcal{O}(\varepsilon^{-2})$ we obtain two local problems identical to (3.4.17) and (3.4.16), respectively. The zero order approximations of the two concentrations depend only on the global variables, hence

$$s_0 = s_0\left(t, \mathbf{x}\right), \qquad b_0 = b_0\left(t, \mathbf{x}\right). \tag{3.5.8}$$

At $\mathcal{O}(\varepsilon^{-1})$, we have the following local substrate problem,

$$\begin{aligned}
&\nabla_{\mathbf{y}} \cdot \left[\nabla_{\mathbf{x}} s_0 + \nabla_{\mathbf{y}} s_1\right] = \nabla_{\mathbf{y}} \cdot \left(\mathrm{Pe}\mathbf{v}_0 s_0\right) - \nabla_{\mathbf{x}} \cdot \nabla_{\mathbf{y}} s_0 && \text{in } Y^0, && \text{(3.5.9a)}\\
&-\mathbf{n} \cdot \left[\nabla_{\mathbf{x}} s_0 + \nabla_{\mathbf{y}} s_1\right] = 0 && \text{on } \partial\Sigma^0, && \text{(3.5.9b)}
\end{aligned}$$

and the following local bacteria problem,

$$\begin{aligned}
\nabla_{\mathbf{y}} \cdot \left(\delta\big[\nabla_{\mathbf{x}} b_0 + \nabla_{\mathbf{y}} b_1\big]\right) = \nabla_{\mathbf{y}} \cdot \big(\{&\mathrm{Pe}\mathbf{v}_0\\
&+ \nabla_{\mathbf{y}} \cdot \left(\mathrm{Pe}_b b_0 \hat{\chi}_0 \nabla_{\mathbf{y}} s_0\right)\\
&+ \nabla_{\mathbf{y}} \cdot \left(\mathrm{Pe}_b \hat{\chi}_0 [\nabla_{\mathbf{x}} s_0 + \nabla_{\mathbf{y}} s_1] b_0\right)\\
&+ \nabla_{\mathbf{y}} \cdot \left(\mathrm{Pe}_b [b_1 \hat{\chi}_0 + b_0 \hat{\chi}_1] \nabla_{\mathbf{y}} s_0\right)\\
&- \nabla_{\mathbf{x}} \cdot \left(\delta \nabla_{\mathbf{y}} b_0\right) && \text{in } Y^0, && \text{(3.5.10a)}\\
-\mathbf{n} \cdot \left(\delta[\nabla_{\mathbf{x}} b_0 + \nabla_{\mathbf{y}} b_1]\right) = 0 && \text{on } \partial\Sigma^0. && \text{(3.5.10b)}
\end{aligned}$$

Comparing the local problems given in Eqs.(3.5.9) and Eqs.(3.5.10) with their counterparts in Eqs.(3.4.22) and Eqs.(3.4.23), we notice they are similar, except for the new addition of an advection flux. Thus, to avoid redundancy, we omit the terms shown to vanish in the previous section, and in this section we show how the new advection fluxes in (3.5.9) and (3.5.10) vanish. We compute

$$\nabla_{\mathbf{y}} \cdot \left(\mathrm{Pe}\mathbf{v}_0 s_0\right) = \mathrm{Pe}\Big[s_0 \underbrace{\nabla_{\mathbf{y}} \cdot \mathbf{v}_0}_{=0} + \mathbf{v}_0 \cdot \underbrace{\nabla_{\mathbf{y}} s_0}_{=0}\Big] = 0, \tag{3.5.11}$$

$$\nabla_{\mathbf{y}} \cdot \left(\mathrm{Pe}\mathbf{v}_0 b_0\right) = \mathrm{Pe}\Big[b_0 \underbrace{\nabla_{\mathbf{y}} \cdot \mathbf{v}_0}_{=0} + \mathbf{v}_0 \cdot \underbrace{\nabla_{\mathbf{y}} b_0}_{=0}\Big] = 0. \tag{3.5.12}$$

Then the local substrate equations at $\mathcal{O}(\varepsilon^{-1})$ are

$$\nabla_{\mathbf{y}} \cdot \left[\nabla_{\mathbf{x}} s_0 + \nabla_{\mathbf{y}} s_1\right] = 0 \qquad \text{in } Y^0, \tag{3.5.13a}$$

$$-\mathbf{n}\cdot[\nabla_{\mathbf{x}}s_0+\nabla_{\mathbf{y}}s_1]=0 \qquad \text{on } \partial\Sigma^0. \tag{3.5.13b}$$

As we have seen in Section 3.4, the local problem in (3.5.13) leads to the following simplified local problem,

$$\nabla_{\mathbf{y}}\cdot(\delta\,[\nabla_{\mathbf{x}}b_0+\nabla_{\mathbf{y}}b_1])=0 \qquad \text{in } Y^0, \tag{3.5.14a}$$
$$-\mathbf{n}\cdot(\delta\,[\nabla_{\mathbf{x}}b_0+\nabla_{\mathbf{y}}b_1])=0 \qquad \text{on } \partial\Sigma^0. \tag{3.5.14b}$$

At this order, the flow has no role in distributing the two species at the local level. Furthermore, the two local problems have a similar structure to their counterparts in Section 3.4, which means they have the same unique solutions s_1 and b_1 in (3.4.31). The correction vector function $\boldsymbol{\omega}(\mathbf{y})=(\omega_1(\mathbf{y}),\omega_2(\mathbf{y}))^T$ is a solution of the *cell-problem*

$$\begin{cases} \nabla_{\mathbf{y}}\cdot[\nabla_{\mathbf{y}}\omega_i+\mathbf{e}_i]=0 & \text{in } Y^0,\\ -\mathbf{n}\cdot[\nabla_{\mathbf{y}}\omega_i+\mathbf{e}_i]=0 & \text{on } \partial\Sigma^0,\\ \omega_i \text{ is } Y-\text{periodic, and } \langle\omega_i\rangle_{Y^0}=0. \end{cases} \tag{3.5.15}$$

As always, the last step in the asymptotic homogenisation begins by collecting the terms at $\mathcal{O}(\varepsilon^0)$, hence

$$\begin{aligned}\nabla_{\mathbf{y}}\cdot[\nabla_{\mathbf{x}}s_1+\nabla_{\mathbf{y}}s_2]=&\frac{\partial s_0}{\partial t}-\nabla_{\mathbf{x}}\cdot([\nabla_{\mathbf{x}}s_0+\nabla_{\mathbf{y}}s_1]-\mathrm{Pe}\mathbf{v}_0s_0)\\ &+\nabla_{\mathbf{y}}\cdot(\mathrm{Pe}\{\mathbf{v}_0s_1+\mathbf{v}_1s_0\})\\ &+\frac{\mathrm{Da}}{Y}\frac{s_0}{s_0+\kappa_s}b_0 \qquad \text{in } Y^0,\end{aligned} \tag{3.5.16a}$$
$$-\mathbf{n}\cdot[\nabla_{\mathbf{x}}s_1+\nabla_{\mathbf{y}}s_2]=0 \qquad \text{on } \partial\Sigma^0, \tag{3.5.16b}$$

and for the bacteria we have

$$\begin{aligned}\nabla_{\mathbf{y}}\cdot\big(\delta\big[\nabla_{\mathbf{x}}b_1+\nabla_{\mathbf{y}}b_2\big]\big)=&\frac{\partial b_0}{\partial t}-\nabla_{\mathbf{x}}\cdot(\delta\,[\nabla_{\mathbf{x}}b_0+\nabla_{\mathbf{y}}b_1]-\mathrm{Pe}\mathbf{v}_0b_0)\\ &+\nabla_{\mathbf{y}}\cdot(\mathrm{Pe}\{\mathbf{v}_0b_1+\mathbf{v}_1b_0\})\\ &+\nabla_{\mathbf{x}}\cdot\big(\mathrm{Pe}_b\hat{\chi}_0[\nabla_{\mathbf{x}}s_0+\nabla_{\mathbf{y}}s_1]b_0\big)\\ &+\nabla_{\mathbf{x}}\cdot\big\{\mathrm{Pe}_b(b_1\hat{\chi}_0+b_0\hat{\chi}_1)\nabla_{\mathbf{y}}s_0\big\}\\ &+\nabla_{\mathbf{y}}\cdot(\mathrm{Pe}_b\{b_0\hat{\chi}_2+b_1\hat{\chi}_1+b_2\hat{\chi}_0\}\nabla_{\mathbf{y}}s_0)\\ &+\nabla_{\mathbf{y}}\cdot\big(\mathrm{Pe}_b\{b_1\hat{\chi}_0+b_0\hat{\chi}_1\}[\nabla_{\mathbf{x}}s_0+\nabla_{\mathbf{y}}s_1]\big)\\ &+\nabla_{\mathbf{y}}\cdot(\mathrm{Pe}_b\hat{\chi}_0[\nabla_{\mathbf{x}}s_1+\nabla_{\mathbf{y}}s_2]b_0)\\ &-\mathrm{Da}\frac{s_0}{s_0+\kappa_s}\left(1-\frac{b_0}{\kappa_c}\right)b_0+\kappa_bb_0 \qquad \text{in } Y^0,\end{aligned} \tag{3.5.17a}$$
$$-\mathbf{n}\cdot\big(\delta\,[\nabla_{\mathbf{x}}b_1+\nabla_{\mathbf{y}}b_2]\big)=0 \qquad \text{on } \partial\Sigma^0. \tag{3.5.17b}$$

Once more, we notice the apparent similarities between the local problems in (3.5.16) and (3.5.17) and their counterparts in (3.4.33) and (3.4.34), apart from the advective

fluxes. As before, Lemma 3.4 guarantees unique solutions, s_2 and b_2, to the two local problems if and only if certain solvability conditions are met. The solvability condition for the boundary value problem (3.5.16) is

$$\int_{Y^0} \Big\{ \frac{\partial s_0}{\partial t} - \nabla_{\mathbf{x}} \cdot \big(\big[\nabla_{\mathbf{x}} s_0 + \nabla_{\mathbf{y}} s_1 \big] - \mathrm{Pe} \mathbf{v}_0 s_0 \big) + \nabla_{\mathbf{y}} \cdot \big(\mathrm{Pe} \{ \mathbf{v}_0 s_1 + \mathbf{v}_1 s_0 \} \big) + \frac{\mathrm{Da}}{Y} \frac{s_0}{s_0 + \kappa_s} b_0 \Big\} d\mathbf{y} = 0. \tag{3.5.18}$$

As result of the divergence theorem, the no-slip condition of the local velocities in (3.2.27) and the perspicuity of the expansions, we show that the terms in (3.5.18) vanish in the following fashion,

$$\int_{Y^0} \nabla_{\mathbf{y}} \cdot \big(\mathrm{Pe} \{ \mathbf{v}_0 s_1 \} \big) \, d\mathbf{y} = \mathrm{Pe} \int_{\partial \Sigma^0} s_1 \{ \mathbf{n} \cdot \mathbf{v}_0 \} d\mathbf{s} = 0, \tag{3.5.19a}$$

$$\int_{Y^0} \nabla_{\mathbf{y}} \cdot \big(\mathrm{Pe} \{ \mathbf{v}_0 s_1 \} \big) \, d\mathbf{y} = \mathrm{Pe} \int_{\partial \Sigma^0} s_0 \{ \mathbf{n} \cdot \mathbf{v}_1 \} d\mathbf{s} = 0. \tag{3.5.19b}$$

Then, we rewrite the solvability condition using the average operator over Y as

$$\begin{aligned} \frac{\partial \langle s_0 \rangle}{\partial t} = & \underbrace{\nabla_{\mathbf{x}} \cdot \left\{ \frac{1}{|Y|} \int_{Y^0} (\nabla_{\mathbf{x}} s_0 + \nabla_{\mathbf{y}} s_1) d\mathbf{y} \right\}}_{\mathrm{I}_a} \\ & - \underbrace{\nabla_{\mathbf{x}} \cdot \left\{ \frac{1}{|Y|} \int_{Y^0} \big(\mathrm{Pe} \mathbf{v}_0 s_0 \big) d\mathbf{y} \right\}}_{\mathrm{I}_b} \\ & + \frac{\mathrm{Da}}{Y} \underbrace{\left\{ \frac{1}{|Y|} \int_{Y^0} \Big(\frac{s_0}{s_0 + \kappa_s} b_0 \Big) d\mathbf{y} \right\}}_{\mathrm{I}_c}. \end{aligned} \tag{3.5.20}$$

Substituting for s_1, given (3.4.31), we obtain

$$\begin{aligned} \mathrm{I}_a &= \nabla_{\mathbf{x}} \cdot \left\{ \frac{1}{|Y|} \int_{Y^0} (\nabla_{\mathbf{x}} s_0 + \nabla_{\mathbf{y}} s_1) d\mathbf{y} \right\} \\ &= \nabla_{\mathbf{x}} \cdot \left\{ \frac{1}{|Y|} \int_{Y^0} \Big(\nabla_{\mathbf{x}} s_0 + \nabla_{\mathbf{y}} \big\{ \boldsymbol{\omega}(\mathbf{y}) \nabla_{\mathbf{x}} s_0 + \bar{s}_1 \Big) d\mathbf{y} \big\} \right\} \\ &= \nabla_{\mathbf{x}} \cdot \left\{ \frac{1}{|Y|} \int_{Y^0} \Big(\big[\mathbf{I} + \nabla_{\mathbf{y}} \boldsymbol{\omega}^T \big] \nabla_{\mathbf{x}} s_0 \Big) d\mathbf{y} \right\} \\ &= \nabla_{\mathbf{x}} \cdot \Big(\phi \langle \mathbf{I} + \nabla_{\mathbf{y}} \boldsymbol{\omega}^T \rangle_{Y^0} \nabla_{\mathbf{x}} s_0 \Big) \\ &= \nabla_{\mathbf{x}} \cdot \Big(\langle \mathbf{I} + \nabla_{\mathbf{y}} \boldsymbol{\omega}^T \rangle_{Y^0} \nabla_{\mathbf{x}} \langle s_0 \rangle \Big), \end{aligned} \tag{3.5.21}$$

where the last line of Eq.(3.5.21) is derived using the fact that s_0 is a function of $\mathbf{x}$ only, along with the identities given in Eq.(3.1.13) and Eq.(3.4.39). Finally, we write Eq.(3.5.21) using the effective diffusion tensor $\mathbf{D}^h$ in Eq.(3.4.38) as

$$\mathrm{I}_a = \nabla_{\mathbf{x}} \cdot \big(\mathbf{D}^h \nabla_{\mathbf{x}} \langle s_0 \rangle\big). \tag{3.5.22}$$

Along the same lines, we show that I_b has the following form

$$\begin{aligned}
\mathrm{I}_b &= \nabla_{\mathbf{x}} \cdot \bigg\{ \frac{1}{|Y|} \int_{Y^0} \big(\mathrm{Pe}\mathbf{v}_0 s_0\big) d\mathbf{y} \bigg\} \\
&= \nabla_{\mathbf{x}} \cdot \Big\{ \mathrm{Pe} \langle \mathbf{v}_0 s_0 \rangle \Big\} \\
&= \nabla_{\mathbf{x}} \cdot \Big\{ \mathrm{Pe} \langle \mathbf{v}_0 \rangle_{Y^0} \langle s_0 \rangle \Big\}.
\end{aligned} \tag{3.5.23}$$

The consumption rate in I_c is approximated in a similar fashion as in Section 3.4, so that we have

$$\mathrm{I}_c = \frac{1}{|Y|} \int_{Y^0} \Big(\frac{s_0}{s_0 + \kappa_s} b_0 \Big) d\mathbf{y} = \Big\langle \frac{s_0}{s_0 + \kappa_s} b_0 \Big\rangle. \tag{3.5.24}$$

Finally, from Eq.(3.5.22), Eq.(3.5.23) and Eq.(3.5.24) we arrive at the final form of the homogenised substrate equation in (3.5.2a),

$$\frac{\partial \langle s_0 \rangle}{\partial t} = \nabla_{\mathbf{x}} \cdot \big(\mathbf{D}^h \nabla_{\mathbf{x}} \langle s_0 \rangle - \mathrm{Pe} \langle \mathbf{v}_0 \rangle_{Y^0} \langle s_0 \rangle \big) - \frac{\mathrm{Da}}{Y} \Big\langle \frac{s_0}{s_0 + \kappa_s} b_0 \Big\rangle. \tag{3.5.25}$$

Following the same argument as for the local substrate equation, the local bacteria problem in (3.5.17) admits a unique solution b_2 if and only if the following condition is satisfied:

$$\begin{aligned}
\int_{Y^0} \Big\{ \frac{\partial b_0}{\partial t} &- \nabla_{\mathbf{x}} \cdot \Big(\delta [\nabla_{\mathbf{x}} b_0 + \nabla_{\mathbf{y}} b_1] - \big\{ \mathrm{Pe}\mathbf{v}_0 + \mathrm{Pe}_b \hat{\chi}_0 [\nabla_{\mathbf{x}} s_0 + \nabla_{\mathbf{y}} s_1] \big\} b_0 \Big) \\
&+ \nabla_{\mathbf{y}} \cdot \big(\mathrm{Pe} \big\{ \mathbf{v}_0 b_1 + \mathbf{v}_1 b_0 \big\} \big) + \nabla_{\mathbf{y}} \cdot \big(\mathrm{Pe}_b \{ b_0 \hat{\chi}_2 + b_1 \hat{\chi}_1 + b_2 \hat{\chi}_0 \} \nabla_{\mathbf{y}} s_0 \big) \\
&+ \nabla_{\mathbf{y}} \cdot \big(\mathrm{Pe}_b \{ b_1 \hat{\chi}_0 + b_0 \hat{\chi}_1 \} [\nabla_{\mathbf{x}} s_0 + \nabla_{\mathbf{y}} s_1] \big) \\
&+ \nabla_{\mathbf{y}} \cdot \big(\mathrm{Pe}_b \hat{\chi}_0 [\nabla_{\mathbf{x}} s_1 + \nabla_{\mathbf{y}} s_2] b_0 \big) \\
&- \mathrm{Da} \frac{s_0}{s_0 + \kappa_s} \Big(1 - \frac{b_0}{\kappa_c} \Big) b_0 + \kappa_b b_0 \Big\} d\mathbf{y} = 0.
\end{aligned} \tag{3.5.26}$$

Once more, we remove the terms containing the local gradient of substrate as a result of Eq.(3.4.24). Moreover, we exclude the chemotactic and advective fluxes following the same arguments in (3.4.41) and (3.5.19), respectively. Thereby, the solvability condition in (3.5.26) written in terms of the averaged operator becomes

$$\frac{\partial \langle b_0 \rangle}{\partial t} = \underbrace{\nabla_{\mathbf{x}} \cdot \bigg\{ \frac{\delta}{|Y|} \int_{Y^0} (\nabla_{\mathbf{x}} b_0 + \nabla_{\mathbf{y}} b_1) d\mathbf{y} \bigg\}}_{\mathrm{I}_{1a}}$$

$$
\begin{aligned}
&\underbrace{-\nabla_{\mathbf{x}}\cdot\left\{\frac{1}{|Y|}\int_{Y^0}\big(\mathrm{Pe}\mathbf{v}_0 b_0\big)d\mathbf{y}\right\}}_{\mathrm{I}_{1b}}\\
&\underbrace{-\nabla_{\mathbf{x}}\cdot\left\{\frac{1}{|Y|}\int_{Y^0}\big(\mathrm{Pe}_b\hat{\chi}_0[\nabla_{\mathbf{x}}s_0+\nabla_{\mathbf{y}}s_1]\big\}b_0\big)d\mathbf{y}\right\}}_{\mathrm{I}_{1c}}\\
&\underbrace{+\left\{\frac{\mathrm{Da}}{|Y|}\int_{Y^0}\left(\frac{s_0}{s_0+\kappa_s}\Big(1-\frac{b_0}{\kappa_c}\Big)b_0-\kappa_b b_0\right)d\mathbf{y}\right\}}_{\mathrm{I}_{1d}}.
\end{aligned}
\tag{3.5.27}
$$

Substituting b_1, given in (3.4.31b), into I_{1a}, we obtain:

$$
\begin{aligned}
\mathrm{I}_{1\mathrm{a}} &= \nabla_{\mathbf{x}}\cdot\left\{\frac{\delta}{|Y|}\int_{Y^0}\nabla_{\mathbf{x}}\cdot(\nabla_{\mathbf{x}}b_0+\nabla_{\mathbf{y}}b_1)d\mathbf{y}\right\}\\
&= \nabla_{\mathbf{x}}\cdot\left\{\frac{\delta}{|Y|}\int_{Y^0}\big(\nabla_{\mathbf{x}}b_0+\nabla_{\mathbf{y}}\{\boldsymbol{\omega}\nabla_{\mathbf{x}}b_0+\bar{b}_1\}\big)d\mathbf{y}\right.\\
&= \nabla_{\mathbf{x}}\cdot\big(\delta\langle\mathbf{I}+\nabla_{\mathbf{y}}\boldsymbol{\omega}^T\rangle_{Y^0}\nabla_{\mathbf{x}}\langle b_0\rangle\big)\\
&= \nabla_{\mathbf{x}}\cdot\big(\delta\mathbf{D}^h\nabla_{\mathbf{x}}\langle b_0\rangle\big).
\end{aligned}
\tag{3.5.28}
$$

In the same way as in (3.5.23), we write I_{1b} as

$$
\mathrm{I}_{1b}=\nabla_{\mathbf{x}}\cdot\left\{\frac{1}{|Y|}\int_{Y^0}\big(\mathrm{Pe}\mathbf{v}_0 b_0\big)d\mathbf{y}\right\}=\nabla_{\mathbf{x}}\cdot\Big\{\mathrm{Pe}\langle\mathbf{v}_0\rangle_{Y^0}\langle b_0\rangle\Big\}.
\tag{3.5.29}
$$

For the chemotactic flux in I_{1c} we use s_1 given in (3.4.31a), to obtain the following:

$$
\begin{aligned}
\mathrm{I}_{1\mathrm{c}} &= \nabla_{\mathbf{x}}\cdot\left\{\frac{1}{|Y|}\int_{Y^0}\Big(\mathrm{Pe}_b\hat{\chi}_0[\nabla_{\mathbf{x}}s_0+\nabla_{\mathbf{y}}s_1]b_0\Big)d\mathbf{y}\right\}\\
&= \nabla_{\mathbf{x}}\cdot\left\{\frac{\mathrm{Pe}_b b_0\hat{\chi}_0}{|Y|}\Big(\int_{Y^0}[\nabla_{\mathbf{x}}s_0+\nabla_{\mathbf{y}}\{\boldsymbol{\omega}\nabla_{\mathbf{x}}s_0+\bar{s}\}]d\mathbf{y}\Big)b_0\right\}\\
&= \nabla_{\mathbf{x}}\cdot\left\{\frac{\mathrm{Pe}_b b_0\hat{\chi}_0}{|Y|}\int_{Y^0}\Big(\big[\mathbf{I}+\nabla_{\mathbf{y}}\boldsymbol{\omega}^T\big]\nabla_{\mathbf{x}}s_0\Big)d\mathbf{y}\right\}\\
&= \nabla_{\mathbf{x}}\cdot\Big\{\big\langle\mathbf{I}+\nabla_{\mathbf{y}}\boldsymbol{\omega}\big\rangle_{Y^0}\big\langle\mathrm{Pe}_b\{\hat{\chi}_0\nabla_{\mathbf{x}}s_0\}b_0\big\rangle\Big\}\\
&= \nabla_{\mathbf{x}}\cdot\Big(\mathbf{D}^h\big\langle\{\mathrm{Pe}_b\hat{\chi}_0\nabla_{\mathbf{x}}s_0\}b_0\big\rangle\Big).
\end{aligned}
\tag{3.5.30}
$$

The kinetics in I_{1d} are

$$
\mathbf{I}_{1d}=\Big\langle\mathrm{Da}\frac{s_0}{s_0+\kappa_s}\left(1-\frac{b_0}{\kappa_c}\right)b_0-\kappa_b b_0\Big\rangle.
\tag{3.5.31}
$$

From (3.5.28), (3.5.29), (3.5.30) and (3.5.31), we obtain the final form of the effective bacteria equation, hence

$$\begin{aligned}\frac{\partial\langle b_0\rangle}{\partial t} =&\nabla_{\mathbf{x}}\cdot\left(\delta\mathbf{D}^h\nabla_{\mathbf{x}}\langle b_0\rangle - \Big[\mathrm{Pe}\langle\mathbf{v}_0\rangle_{Y^0}\langle b_0\rangle + \mathrm{Pe}_b\big\{\mathbf{D}^h\langle\hat{\chi}_0 b_0\nabla_{\mathbf{x}}s_0\rangle\big\}\Big]\right)\\ &+\left\langle \mathrm{Da}\frac{s_0}{s_0+\kappa_s}\left(1-\frac{b_0}{\kappa_c}\right)b_0 - \kappa_b b_0\right\rangle. \end{aligned} \tag{3.5.32}$$

The two effective equations in (3.5.25) and (3.5.32) are independent of the local variable, and thus we can omit the average operator as we did in Section 3.4.1. Finally, writing the effective equations in terms of $\mathcal{S}$ and $\mathcal{B}$ leads to the desired results in (3.5.4). The initial conditions are the same as in Eqs.(3.4.50).

3.6 Chemotactic Migration in an Advection-Dispersion Regime

In this section we deal with a transport model where the advection time scale is much shorter than that of diffusion for the two species, while the chemotactic drift time scale is comparable to that of substrate diffusion. Such regimes are classified by the following range of Péclet number values

$$\mathcal{O}(\varepsilon^{-1}) \leq \mathrm{Pe} \ll \mathcal{O}(\varepsilon^{-2}). \tag{3.6.1}$$

In such cases, a local Péclet number is introduced and is defined as: $\mathrm{Pe}_{loc} = (Vl_{y_1^*})/D_s^*$, such that

$$\mathrm{Pe} = \varepsilon^{-1}\mathrm{Pe}_{loc}. \tag{3.6.2}$$

Thereby, the microscopic description of the model is as follows

$$\frac{\partial s_\varepsilon}{\partial t} = \nabla\cdot\left(\nabla s_\varepsilon - \varepsilon^{-1}\mathrm{Pe}_{loc}\mathbf{v}_\varepsilon s_\varepsilon\right) - \frac{\mathrm{Da}}{Y}\frac{s_\varepsilon}{s_\varepsilon+\kappa_s}b_\varepsilon \qquad \text{in } [0,T]\times\Omega_\varepsilon\times Y^0, \tag{3.6.3a}$$

$$\begin{aligned}\frac{\partial b_\varepsilon}{\partial t} =& \nabla\cdot\left(\delta\nabla b_\varepsilon - \left\{\varepsilon^{-1}\mathrm{Pe}_{loc}\mathbf{v}_\varepsilon + \mathrm{Pe}_b\hat{\chi}(s_\varepsilon)\nabla s_\varepsilon\right\}b_\varepsilon\right)\\ &+\mathrm{Da}\frac{s_\varepsilon}{s_\varepsilon+\kappa_s}\left(1-\frac{b_\varepsilon}{\kappa_c}\right)b_\varepsilon - \kappa_b b_\varepsilon \qquad \text{in } [0,T]\times\Omega_\varepsilon\times Y^0. \end{aligned} \tag{3.6.3b}$$

We note that the presence of ε^{-1} means that the advection, diffusion, and reaction terms are all of the same order of magnitude. The model is equipped with the same interface conditions and initial conditions as in the previous section.

3.6.1 The Homogenised Model

The local Péclet number in Eq.(3.6.2) asserts that at the local scale the advection time is shorter than the diffusion time. Thus, at the microscopic scale we introduce a fast time, $\tau = t/\varepsilon$, associated with advection acting on a short time scale. We write down the asymptotic expansion for the species at the micro-scale as [39]:

$$s_\varepsilon(t,\tau,\mathbf{x},\mathbf{y}) = s_0 + \varepsilon s_1 + \varepsilon^2 s_2 + \mathcal{O}(\varepsilon^3), \tag{3.6.4a}$$
$$b_\varepsilon(t,\tau,\mathbf{x},\mathbf{y}) = b_0 + \varepsilon b_1 + \varepsilon^2 b_2 + \mathcal{O}(\varepsilon^3), \tag{3.6.4b}$$

where s_i and b_i are periodic in $\mathbf{y}$, but not periodic in τ, hence

$$s_i = s_i(t,\tau,\mathbf{x},\mathbf{y}), \tag{3.6.5}$$
$$b_i = b_i(t,\tau,\mathbf{x},\mathbf{y}). \tag{3.6.6}$$

The time differential operator at the local scale is written [39]:

$$\frac{\partial \psi_\varepsilon}{\partial t} \mapsto \frac{\partial \psi_\varepsilon}{\partial t} + \varepsilon^{-1}\frac{\partial \psi_\varepsilon}{\partial \tau}. \tag{3.6.7}$$

Now, we state our formal asymptotic result. As before, we postulate the expansions s_ε and b_ε in Eqs.(3.6.4), and the flow velocity expansion given in (3.4.4).

Proposition 3.6. *Let us assume the expansions as in Eq.*(3.4.4) *and Eqs.*(3.6.4)*, and assuming the parameters other than ε are formally of $\mathcal{O}(\varepsilon^0)$, the averaged first order approximations,*

$$\begin{cases} \mathcal{S}(t,\mathbf{x}) &= s_0(t,\mathbf{x}) + \varepsilon \bar{s}_1(t,\mathbf{x}), \\ \mathcal{B}(t,\mathbf{x}) &= b_0(t,\mathbf{x}) + \varepsilon \bar{b}_1(t,\mathbf{x}), \end{cases} \tag{3.6.8}$$

and $\mathcal{V}(\mathbf{x}) = \langle \mathbf{v}_0 \rangle_{Y^0} + \langle \mathbf{v}_1 \rangle_{Y^0}$, are the solutions of the homogenised model

$$\begin{cases} \dfrac{\partial \mathcal{S}}{\partial t} = \nabla \cdot \Big(\mathbf{D}^{\mathrm{dis}} \nabla \mathcal{S} - \mathrm{Pe}\mathcal{V}\mathcal{S} \Big) - \dfrac{\mathrm{Da}}{Y} \dfrac{\mathcal{S}}{\mathcal{S}+\kappa_s}\mathcal{B} & \text{in } [0,T]\times\Omega, \\ \dfrac{\partial \mathcal{S}}{\partial t} = \nabla \cdot \Big(\bar{\mathbf{D}}^{\mathrm{dis}} \nabla \mathcal{B} - \big[\mathrm{Pe}\mathcal{V} + \mathrm{Pe}_b \big\{ \mathbf{D}^{\mathrm{ch}} \chi(\mathcal{S}) \nabla \mathcal{S} \big\} \big] \mathcal{B} \Big) \\ \qquad\qquad + \mathrm{Da} \dfrac{\mathcal{S}}{\mathcal{S}+\kappa_s} \left(1 - \dfrac{\mathcal{B}}{\kappa_c} \right) \mathcal{B} - \kappa_b \mathcal{B} & \text{in } [0,T]\times\Omega, \end{cases} \tag{3.6.9}$$

with the dispersion tensors

$$\begin{cases} \mathbf{D}^{\mathrm{dis}} &= \Big\langle \big[(\nabla_{\mathbf{y}} \boldsymbol{\xi})^T + \mathbf{I} \big] - \mathrm{Pe}_{loc} \big[\mathbf{v}_0 \otimes \boldsymbol{\xi} \big] \Big\rangle_{Y^0}, \\ \bar{\mathbf{D}}^{\mathrm{dis}} &= \Big\langle \delta \big[(\nabla_{\mathbf{y}} \boldsymbol{\xi}^\delta)^T + \mathbf{I} \big] - \mathrm{Pe}_{loc} \big[\mathbf{v}_0 \otimes \boldsymbol{\xi}^\delta \big] \Big\rangle_{Y^0}, \\ \mathbf{D}^{\mathrm{ch}} &= \Big\langle (\nabla_{\mathbf{y}} \boldsymbol{\xi})^T + \mathbf{I} \Big\rangle_{Y^0}, \end{cases} \tag{3.6.10}$$

where $\boldsymbol{\xi}(\mathbf{y}) = (\xi_1, \xi_2)^T$ *is the solution of the cell-problem*

$$\begin{cases} \mathrm{Pe}_{loc}\mathbf{v}_0 \cdot \nabla_{\mathbf{y}}\xi_i - \nabla_{\mathbf{y}} \cdot [\nabla_{\mathbf{y}}\xi_i + \mathbf{e}_i] = \mathrm{Pe}_{loc}\{\langle \mathbf{v}_0 \rangle_{Y^0} - \mathbf{v}_0\} \cdot \mathbf{e}_i & \text{in } Y^0, \\ -\mathbf{n} \cdot [\nabla_{\mathbf{y}}\xi_i + \mathbf{e}_i] = 0 & \text{on } \partial\Sigma^0, \\ \xi_i \text{ is } Y - \text{periodic, and } \langle \xi_i \rangle_{Y^0} = 0, \end{cases} \tag{3.6.11}$$

and $\boldsymbol{\xi}^\delta(\mathbf{y}) = (\xi_1^\delta, \xi_2^\delta)^T$ *is the solution of the cell-problem*

$$\begin{cases} \mathrm{Pe}_{loc}\mathbf{v}_0 \cdot \nabla_{\mathbf{y}}\xi_i^\delta - \nabla_{\mathbf{y}} \cdot \left(\delta \left[\nabla_{\mathbf{y}}\xi_i^\delta + \mathbf{e}_i\right]\right) = \mathrm{Pe}_{loc}\{\langle \mathbf{v}_0 \rangle_{Y^0} - \mathbf{v}_0\} \cdot \mathbf{e}_i & \text{in } Y^0, \\ -\mathbf{n} \cdot \left(\delta \left[\nabla_{\mathbf{y}}\xi_i^\delta + \mathbf{e}_i\right]\right) = 0 & \text{on } \partial\Sigma^0, \\ \xi_i^\delta \text{ is } Y - \text{periodic, and } \langle \xi_i^\delta \rangle_{Y^0} = 0, \end{cases} \tag{3.6.12}$$

with the initial conditions

$$\mathcal{S}(0, \mathbf{x}) = \mathcal{S}_{in}(\mathbf{x}), \qquad \text{and} \qquad \mathcal{B}(0, \mathbf{x}) = \mathcal{B}_{in}(\mathbf{x}), \tag{3.6.13}$$

where $\mathcal{S}_{in}(\mathbf{x}) = s_{in}(\mathbf{x})$ *and* $\mathcal{B}_{in}(\mathbf{x}) = b_{in}(\mathbf{x})$.

Remark 3.7. *The outer-product in* (3.6.10) *defines a tensor, and therefore for any two vectors* $\mathbf{a}$ *and* $\mathbf{b}$ *we have* $\left[\mathbf{a} \otimes \mathbf{b}\right]_{ij} = a_i b_j$.

The upscaled chemotactic function given in Eqs.(3.4.15). The model in Proposition 3.6 is referred to as the "Taylor mediated mixing regime" analogous to Taylor's examination of dispersion in a tube [190]. In these advective regimes we consider the interplay between advection and diffusion at the pore-scale level. Proposition 3.6 shows two effective models. In contrast to the previous sections, the pore flow appears in the two *cell-problems* in (3.6.11) and (3.6.12), with a forcing term that measures the fluctuations between the local pore flow and the averaged pore flow. The second effective model, given by Eqs.(3.6.8), is defined at the macroscopic scale, with effective species concentrations assuming the sum of the first two non-oscillating expansions. On the other hand, the effective velocity is comprised of the sum of the mean zero and first pore flow approximation. In theory, the flow may depend on both local (fast) and global (slow) spatial variables. However, under the assumptions we imposed on the Stokes equations, the Darcy flow is purely periodic; it depends only on the fast variable. Furthermore, if the averaged pore flow (seepage flow) is derived as in Section 3.2, then $\langle \mathbf{v}_1 \rangle_{Y^0} = 0$ [132, 133]. Thus, in (3.6.8) we have

$$\mathcal{V} = \langle \mathbf{v}_0 \rangle_{Y^0}. \tag{3.6.14}$$

Unlike the previous two regimes the cell problems Eqs.(3.6.11)–(3.6.12) have contributions from both advection and diffusion. The tensors $\mathbf{D}^{\mathrm{dis}}$ and $\bar{\mathbf{D}}^{\mathrm{dis}}$ in (3.6.10) are referred to as the hydrodynamic dispersion tensors, which resemble the classical models dealing with hydrodynamic dispersion in porous media (e.g., [26, 27]). The

two tensors can be broken into diffusive and mechanical dispersion components. For the substrate dispersion tensor, we have

$$\mathbf{D}^{\mathrm{dis}} = \underbrace{\left\langle (\nabla_{\mathbf{y}}\boldsymbol{\xi})^T + \mathbf{I} \right\rangle_{Y^0}}_{\text{diffusion}} - \underbrace{\left\langle \mathrm{Pe}_{loc}\left[\mathbf{v}_0 \otimes \boldsymbol{\xi}\right] \right\rangle_{Y^0}}_{\text{mechanical-dispersion}} , \tag{3.6.15}$$

and the same realisation applies to $\bar{\mathbf{D}}^{\mathrm{dis}}$. The chemotactic tensor $\mathbf{D}^{\mathrm{ch}}$ appearing in the chemotactic flux term consists only of the diffusion component of the substrate tensor (3.6.15), which indicates the slow nature of the chemotactic drift. In addition, it reflects the fact that the chemotactic sensitivity mechanism is restricted to the diffusive flux close to the cell.

Remark 3.8. *The factor ε^{-1} is the natural scaling factor for the advection term [150] for infinite thin cylindrical domains, in particular. Note that we can use the natural scale for all the three limiting cases, however, the trade-off is to solve three cell-problems. However, if the local Péclet number is $\mathrm{Pe}_{loc} \ll 1$, we can safely assume that we are dealing with advection-diffusion regimes, and thus we can use a more convenient scale. Otherwise, the natural scaling is used.*

3.6.2 Formal Asymptotic

As in the previous sections, we start the upscaling process by substituting the asymptotic expansions shown in (3.4.4), (3.6.4), (3.4.5), (3.1.11) and (3.6.7) into the model (3.6.3). Then we collect the terms of $\mathcal{O}(\varepsilon^{-2})$, which gives the local problem of the substrate

$$\nabla_{\mathbf{y}} \cdot (\nabla_{\mathbf{y}} s_0 - \mathrm{Pe}_{loc}\mathbf{v}_0 s_0) = 0 \qquad \text{in } Y^0, \tag{3.6.16a}$$

$$-\mathbf{n} \cdot \nabla_{\mathbf{y}} s_0 = 0 \qquad \text{on } \partial\Sigma^0, \tag{3.6.16b}$$

and the local problem of the bacteria

$$\nabla_{\mathbf{y}} \cdot \left(\delta \nabla_{\mathbf{y}} b_0 - \left[\mathrm{Pe}_{loc}\mathbf{v}_0 + \mathrm{Pe}_b \hat{\chi}_0 \nabla_{\mathbf{y}} s_0\right] b_0\right) = 0 \qquad \text{in } Y^0, \tag{3.6.17a}$$

$$-\mathbf{n} \cdot \left(\delta \nabla_{\mathbf{y}} b_0\right) = 0 \qquad \text{on } \partial\Sigma^0. \tag{3.6.17b}$$

As in the previous sections, the two local problems' solutions are independent of the local variable $\mathbf{y}$. To prove this, we multiply (3.6.16) by s_0 and integrate over Y^0, to find:

$$\begin{aligned} 0 &= \int_{Y^0} \left\{ s_0 \nabla_{\mathbf{y}}^2 s_0 - s_0 \nabla_{\mathbf{y}} \cdot (\mathrm{Pe}_{loc}\mathbf{v}_0 s_0) \right\} d\mathbf{y} \\ &= \underbrace{\int_{Y^0} s_0 \nabla_{\mathbf{y}}^2 s_0 d\mathbf{y}}_{\mathrm{I}_{3a}} - \underbrace{\int_{Y^0} s_0 \nabla_{\mathbf{y}} \cdot (\mathrm{Pe}_{loc}\mathbf{v}_0 s_0)\, d\mathbf{y}}_{\mathrm{I}_{3b}} . \end{aligned} \tag{3.6.18}$$

We start with $\mathrm{I}_{3\mathrm{a}}$ in (3.6.18), which can be rewritten as:

$$\mathrm{I}_{3\mathrm{a}} = \int_{Y^0} s_0 \nabla_{\mathbf{y}}^2 s_0 = \int_{Y^0} \left\{ \nabla_{\mathbf{y}} \cdot (s_0 \nabla_{\mathbf{y}} s_0) - |\nabla_{\mathbf{y}} s_0|^2 \right\} d\mathbf{y}. \tag{3.6.19}$$

By applying the divergence theorem, the periodicity of s_0 on Y, and the solid-aqueous interface condition given in (3.6.16), we have

$$\begin{aligned} \mathrm{I}_{3\mathrm{a}} &= \int_{Y^0} \left\{ \nabla_{\mathbf{y}} \cdot (s_0 \nabla_{\mathbf{y}} s_0) - |\nabla_{\mathbf{y}} s_0|^2 \right\} d\mathbf{y} \\ &= \int_{\partial\Sigma^0} s_0 \left[\mathbf{n} \cdot (\nabla_{\mathbf{y}} s_0) \right] d\mathbf{s} - \int_{Y^0} |\nabla_{\mathbf{y}} s_0|^2 d\mathbf{y} \\ &= - \int_{Y^0} |\nabla_{\mathbf{y}} s_0|^2 d\mathbf{y}. \end{aligned} \tag{3.6.20}$$

Note that we can rewrite $\mathrm{I}_{3\mathrm{b}}$ as:

$$\mathrm{I}_{3\mathrm{b}} = \int_{Y^0} s_0 \nabla_{\mathbf{y}} \cdot (\mathrm{Pe}_{loc}[s_0 \mathbf{v}_0]) \, d\mathbf{y} = \int_{Y^0} s_0 \left(\mathrm{Pe}_{loc} \left[\mathbf{v}_0 \cdot \nabla_{\mathbf{y}} s_0 \right] \right) d\mathbf{y}, \tag{3.6.21}$$

we can also rewrite $\mathrm{I}_{3\mathrm{b}}$ as:

$$\begin{aligned} \mathrm{I}_{3\mathrm{b}} &= \int_{Y^0} s_0 \nabla_{\mathbf{y}} \cdot (\mathrm{Pe}_{loc}[s_0 \mathbf{v}_0]) \, d\mathbf{y} \\ &= \int_{Y^0} s_0^2 \left(\mathrm{Pe}_{loc} \left[\nabla_{\mathbf{y}} \cdot \mathbf{v}_0 \right] \right) d\mathbf{y} + \int_{Y^0} s_0 \left(\mathrm{Pe}_{loc} \left[\mathbf{v}_0 \cdot \nabla_{\mathbf{y}} s_0 \right] \right) d\mathbf{y}. \end{aligned} \tag{3.6.22}$$

We introduce the following integral

$$\begin{aligned} \mathrm{I}_{3\mathrm{c}} &= \int_{Y^0} \nabla_{\mathbf{y}} \cdot \left(\mathrm{Pe}_{loc} \left[s_0^2 \mathbf{v}_0 \right] \right) d\mathbf{y} \\ &= \int_{Y^0} s_0^2 \left(\mathrm{Pe}_{loc} \left[\nabla_{\mathbf{y}} \cdot \mathbf{v}_0 \right] \right) d\mathbf{y} + 2 \int_{Y^0} s_0 \left(\mathrm{Pe}_{loc} \left[\mathbf{v}_0 \cdot \nabla_{\mathbf{y}} s_0 \right] \right) d\mathbf{y}. \end{aligned} \tag{3.6.23}$$

Then from Eq.(3.6.21), Eq.(3.6.22) and Eq.(3.6.23), we can rewrite $\mathrm{I}_{3\mathrm{b}}$ in the following way:

$$\begin{aligned} \mathrm{I}_{3\mathrm{b}} &= \int_{Y^0} s_0 \nabla_{\mathbf{y}} \cdot (\mathrm{Pe}_{loc}[s_0 \mathbf{v}_0]) \, d\mathbf{y} \\ &= \underbrace{\int_{Y^0} \nabla_{\mathbf{y}} \cdot \left(\mathrm{Pe}_{loc} \left[s_0^2 \mathbf{v}_0 \right] \right) d\mathbf{y}}_{\mathrm{I}_{3\mathrm{c}}} - \underbrace{\int_{Y^0} s_0 \nabla_{\mathbf{y}} \cdot \left(\mathrm{Pe}_{loc} \left[s_0 \mathbf{v}_0 \right] \right) d\mathbf{y}}_{\mathrm{I}_{3\mathrm{b}}}. \end{aligned} \tag{3.6.24}$$

We can show that $\mathrm{I}_{3\mathrm{c}}$ vanishes by means of the divergence theorem, periodicity, and the solid-aqueous interface condition:

$$\mathrm{I}_{3\mathrm{c}} = \int_{Y^0} \nabla_{\mathbf{y}} \cdot \left(\mathrm{Pe}_{loc} \left[s_0^2 \mathbf{v}_0 \right] \right) d\mathbf{y} = \mathrm{Pe}_{loc} \int_{\partial\Sigma^0} s_0^2 \big(\mathbf{n} \cdot \mathbf{v}_0 \big) d\mathbf{s} = 0. \tag{3.6.25}$$

Thus, from the result in (3.6.25) in (3.6.24) we find that

$$\mathrm{I}_{3\mathrm{d}} = \int_{Y^0} s_0 \nabla_{\mathbf{y}} \cdot (\mathrm{Pe}_{loc}[s_0 \mathbf{v}_0])\, d\mathbf{y} = 0. \tag{3.6.26}$$

Collecting the results above yields:

$$-\int_{Y^0} |\nabla_{\mathbf{y}} s_0|^2 d\mathbf{y} = 0. \tag{3.6.27}$$

Thus, the zero-order approximation, s_0, depends only on the global spatial variable $\mathbf{x}$, that is

$$s_0 = s_0(t, \tau, \mathbf{x}). \tag{3.6.28}$$

With this, and because of Eq.(3.6.28), the local gradient of the substrate seen in Eq.(3.6.17) vanishes, hence $\nabla_{\mathbf{y}} s_0 = \mathbf{0}$. Thus, the chemotactic flux term in (3.6.17) disappears and the local problem becomes

$$\nabla_{\mathbf{y}} \cdot (\delta \nabla_{\mathbf{y}} b_0 - \mathrm{Pe}_{loc} \mathbf{v}_0 b_0) = 0 \qquad \text{in } Y^0, \tag{3.6.29a}$$

$$-\mathbf{n} \cdot \big(\delta \nabla_{\mathbf{y}} b_0\big) = 0 \qquad \text{on } \partial\Sigma^0. \tag{3.6.29b}$$

The local problem in Eqs.(3.6.29) has the same structure as the local problem in Eqs.(3.6.16), and when applying the same argument, we conclude that

$$b_0 = b_0(t, \tau, \mathbf{x}). \tag{3.6.30}$$

At $\mathcal{O}(\varepsilon^{-1})$, we obtain the following local problem for the substrate

$$\begin{aligned} \nabla_{\mathbf{y}} \cdot ([\nabla_{\mathbf{x}} s_0 + \nabla_{\mathbf{y}} s_1] - \mathrm{Pe}_{loc} \mathbf{v}_0 s_1) = {} & \frac{\partial s_0}{\partial \tau} - \nabla_{\mathbf{x}} \cdot \nabla_{\mathbf{y}} s_0 \\ & + \nabla_{\mathbf{x}} \cdot \{\mathrm{Pe}_{loc} \mathbf{v}_0 s_0\} \\ & + \nabla_{\mathbf{y}} \cdot \{\mathrm{Pe}_{loc} \mathbf{v}_1 s_0\} \qquad \text{in } Y^0, \end{aligned} \tag{3.6.31a}$$

$$-\mathbf{n} \cdot [\nabla_{\mathbf{x}} s_0 + \nabla_{\mathbf{y}} s_1] = 0 \qquad \text{on } \partial\Sigma^0. \tag{3.6.31b}$$

For the bacteria equation we have

$$\begin{aligned} \nabla_{\mathbf{y}} \cdot (\delta[\nabla_{\mathbf{x}} b_0 + \nabla_{\mathbf{y}} b_1] - \mathrm{Pe}_{loc} \mathbf{v}_0 b_1) = {} & \frac{\partial b_0}{\partial \tau} - \nabla_{\mathbf{x}} \cdot \nabla_{\mathbf{y}} b_0 \\ & + \nabla_{\mathbf{x}} \cdot \{\mathrm{Pe}_{loc} \mathbf{v}_0 b_0\} \\ & + \nabla_{\mathbf{y}} \cdot (\mathrm{Pe}_{loc} \mathbf{v}_1 b_0) \\ & + \nabla_{\mathbf{x}} \cdot \big(\mathrm{Pe}_b b_0 \hat{\chi}_0 \nabla_{\mathbf{y}} s_0\big) \\ & + \nabla_{\mathbf{y}} \cdot \big(\mathrm{Pe}_b [b_1 \hat{\chi}_1 + b_1 \hat{\chi}_0] \nabla_{\mathbf{y}} s_0\big) \\ & + \nabla_{\mathbf{y}} \cdot \{\mathrm{Pe}_b \hat{\chi}_0 [\nabla_{\mathbf{x}} s_0 + \nabla_{\mathbf{y}} s_1] b_0\} \quad \text{in } Y^0, \end{aligned} \tag{3.6.32a}$$

$$-\mathbf{n}\cdot\left(\delta\left[\nabla_{\mathbf{x}}b_0+\nabla_{\mathbf{y}}b_1\right]\right)=0 \qquad \text{on } \partial\Sigma^0. \tag{3.6.32b}$$

As previously stated, the zero order approximations for both species are independent of the local variable $\mathbf{y}$, which implies

$$\nabla_{\mathbf{y}}s_0=\nabla_{\mathbf{y}}b_0=\mathbf{0}. \tag{3.6.33}$$

So the relevant terms in (3.6.31) and (3.6.32) vanish. As a result of (3.6.33) and (3.2.27), the following terms in (3.6.31) and (3.6.32) vanish,

$$\nabla_{\mathbf{y}}\cdot(\mathrm{Pe}_{loc}\mathbf{v}_1s_0)=\mathrm{Pe}_{loc}\{s_0\underbrace{\nabla_{\mathbf{y}}\cdot\mathrm{v}_1}_{=0}+\mathrm{v}_1\cdot\underbrace{\nabla_{\mathbf{y}}s_0}_{=0}\}=0, \tag{3.6.34}$$

$$\nabla_{\mathbf{y}}\cdot(\mathrm{Pe}_{loc}\mathbf{v}_1b_0)=\mathrm{Pe}_{loc}\{b_0\underbrace{\nabla_{\mathbf{y}}\cdot\mathrm{v}_1}_{=0}+\mathrm{v}_1\cdot\underbrace{\nabla_{\mathbf{y}}b_0}_{=0}\}=0. \tag{3.6.35}$$

This reduces the local problem in (3.6.31) to the following form

$$\begin{aligned}\mathrm{Pe}_{loc}\mathbf{v}_0\cdot\nabla_{\mathbf{y}}s_1-\nabla_{\mathbf{y}}\cdot[\nabla_{\mathbf{x}}s_0+\nabla_{\mathbf{y}}s_1]&=-\frac{\partial s_0}{\partial\tau}\\ &\quad-\nabla_{\mathbf{x}}\cdot\{\mathrm{Pe}_{loc}\mathbf{v}_0s_0\} && \text{in } Y^0, && (3.6.36a)\\ -\mathbf{n}\cdot[\nabla_{\mathbf{x}}s_0+\nabla_{\mathbf{y}}s_1]&=0 && \text{on } \partial\Sigma^0, && (3.6.36b)\end{aligned}$$

and the local problem in (3.6.32) to:

$$\begin{aligned}\mathrm{Pe}_{loc}\mathbf{v}_0\cdot\nabla_{\mathbf{y}}b_1-\nabla_{\mathbf{y}}\cdot(\delta\,[\nabla_{\mathbf{x}}b_0+\nabla_{\mathbf{y}}b_1])&=-\frac{\partial b_0}{\partial\tau}\\ &\quad-\nabla_{\mathbf{x}}\cdot\{\mathrm{Pe}_{loc}\mathbf{v}_0b_0\}\\ &\quad-\nabla_{\mathbf{y}}\cdot\{b_0\mathbf{v}_c^0\} && \text{in } Y^0, && (3.6.37a)\\ -\mathbf{n}\cdot(\delta\,[\nabla_{\mathbf{x}}b_0+\nabla_{\mathbf{y}}b_1]&=0 && \text{on } \partial\Sigma^0, && (3.6.37b)\end{aligned}$$

where in (3.6.37), the zero-order approximation of the chemotaxis velocity is

$$\mathbf{v}_c^0=\mathrm{Pe}_b\hat{\chi}_0[\nabla_{\mathbf{x}}s_0+\nabla_{\mathbf{y}}s_1]. \tag{3.6.38}$$

To show that the two local problems in (3.6.36) and (3.6.37) admit a unique solution up to an additive constant function (independent of $\mathbf{y}$) we use the results in Lemma 3.9 [12].

Lemma 3.9. *The boundary value problem*

$$\begin{aligned}\mathrm{Pe}_{loc}\mathbf{v}_0\,(\mathbf{y})\cdot\nabla_{\mathbf{y}}\zeta-\nabla_{\mathbf{y}}^2\zeta(\mathbf{y})&=g(\mathbf{y}) && \textit{in } Y^0, && (3.6.39a)\\ -\mathbf{n}\cdot\nabla_{\mathbf{y}}\zeta(\mathbf{y})&=h(\mathbf{y}) && \textit{on } \partial\Sigma^0, && (3.6.39b)\end{aligned}$$

has a unique solution in $H^1(Y^0)$, up to an additive constant, if and only if the compatibility condition

$$\int_{Y^0}g(\mathbf{y})d\mathbf{y}=\int_{\partial\Sigma^0}h(\mathbf{y})d\mathbf{s} \tag{3.6.40}$$

is satisfied.

As a result of Lemma 3.9, the local problem for the substrate in (3.6.36) admits a unique solution s_1 if and only if the following solvability condition is satisfied:

$$\int_{Y^0} \Big(\frac{\partial s_0}{\partial \tau} + \nabla_{\mathbf{x}} \cdot \{ \mathrm{Pe}_{loc} \mathbf{v}_0 s_0 \} \Big) d\mathbf{y} = 0. \tag{3.6.41}$$

The integral in (3.6.41) gives the first effective problem at $\mathcal{O}(\varepsilon^{-1})$, and can be described in terms of the averaged operator in Eq.(3.1.12b) as:

$$\frac{\partial \langle s_0 \rangle}{\partial \tau} + \langle \nabla_{\mathbf{x}} \cdot \{ \mathrm{Pe}_{loc} \mathbf{v}_0 s_0 \} \rangle = 0. \tag{3.6.42}$$

Since s_0 is independent of $\mathbf{y}$, we may write Eq.(3.6.42) as:

$$\frac{\partial s_0}{\partial \tau} + \mathrm{Pe}_{loc} \langle \mathbf{v}_0 \rangle_{Y^0} \cdot \nabla_{\mathbf{x}} s_0 = 0. \tag{3.6.43}$$

Then, when substituting (3.6.43) into (3.6.36), we can eliminate the local time variable, and thus we have

$$\mathrm{Pe}_{loc} \mathbf{v}_0 \cdot \nabla_{\mathbf{y}} s_1 - \nabla_{\mathbf{y}} \cdot [\nabla_{\mathbf{x}} s_0 + \nabla_{\mathbf{y}} s_1] = \mathrm{Pe}_{loc} \Big(\langle \mathbf{v}_0 \rangle_{Y^0} - \mathbf{v}_0 \Big) \cdot \nabla_{\mathbf{x}} s_0 \quad \text{in } Y^0, \tag{3.6.44a}$$

$$-\mathbf{n} \cdot [\nabla_{\mathbf{x}} s_0 + \nabla_{\mathbf{y}} s_1] = 0 \quad \text{on } \partial\Sigma^0. \tag{3.6.44b}$$

As before, we seek a solution to the local problem in (3.6.44) having the form:

$$s_1(t, \mathbf{x}, \mathbf{y}) = \boldsymbol{\xi}(\mathbf{y}) \cdot \nabla_{\mathbf{x}} s_0(t, \mathbf{x}) + \bar{s}_1(t, \mathbf{x}), \tag{3.6.45}$$

where the two components of the vector function, $\boldsymbol{\xi}(\mathbf{y}) = (\xi_1(\mathbf{y}), \xi_2(\mathbf{y}))^T$, satisfy the following *cell-problem*:

$$\begin{cases} \mathrm{Pe}_{loc} \mathbf{v}_0 \cdot \nabla_{\mathbf{y}} \xi_i - \nabla_{\mathbf{y}} \cdot [\nabla_{\mathbf{y}} \xi_i + \mathbf{e}_i] = \mathrm{Pe}_{loc} \{ \langle \mathbf{v}_0 \rangle_{Y^0} - \mathbf{v}_0 \} \cdot \mathbf{e}_i & \text{in } Y^0, \\ -\mathbf{n} \cdot [\nabla_{\mathbf{y}} \xi_i + \mathbf{e}_i] = 0 & \text{on } \partial\Sigma^0, \\ \xi_i \text{ is } Y - \text{periodic, and } \langle \xi_i \rangle_{Y^0} = 0. \end{cases} \tag{3.6.46}$$

Here, the vector function $\boldsymbol{\xi}$ captures the corrections corresponding to the axial and transverse dispersions acting on the solute concentration at the microscopic scale. On the other hand, from Lemma 3.9, the local problem of the bacteria in (3.6.37) has a unique solution up to a constant function with respect to $\mathbf{y}$, if and only if the following solvability condition is satisfied:

$$\int_{Y^0} \Big(\frac{\partial b_0}{\partial \tau} + \nabla_{\mathbf{x}} \cdot \{ \mathrm{Pe}_{loc} \mathbf{v}_0 b_0 \} + b_0 \{ \nabla_{\mathbf{y}} \cdot \mathbf{v}_c^0 \} \Big) d\mathbf{y} = 0. \tag{3.6.47}$$

At this order, and with the aid of the local substrate problem in (3.6.44), we have:

$$\int_{Y^0} b_0 \{ \nabla_{\mathbf{y}} \cdot \mathbf{v}_c^0 \} d\mathbf{y} = \int_{Y^0} \nabla_{\mathbf{y}} \cdot \{ \mathrm{Pe}_b \hat{\chi}_0 [\nabla_{\mathbf{x}} s_0 + \nabla_{\mathbf{y}} s_1] b_0 \} d\mathbf{y}$$

$$= \mathrm{Pe}_b \hat{\chi}_0 b_0 \Big(\int_{\partial\Sigma^0} \mathbf{n} \cdot [\nabla_{\mathbf{x}} s_0 + \nabla_{\mathbf{s}} s_1] d\mathbf{s} \Big)$$
$$= 0. \tag{3.6.48}$$

Then, we write the integral in (3.6.48) in terms of the averaged operator, giving:

$$\frac{\partial \langle b_0 \rangle}{\partial \tau} = -\nabla_{\mathbf{x}} \cdot \langle \mathrm{Pe}_{loc} \mathbf{v}_0 b_0 \rangle = -\mathrm{Pe}_{loc} \langle \mathbf{v}_0 \cdot \nabla_{\mathbf{x}} b_0 \rangle. \tag{3.6.49}$$

Following the same steps as before, we rewrite (3.6.49) to obtain the first effective equation for the bacteria at $\mathcal{O}(\varepsilon^{-1})$, hence

$$\frac{\partial b_0}{\partial \tau} + \mathrm{Pe}_{loc} \langle \mathbf{v}_0 \rangle_{Y^0} \cdot \nabla_{\mathbf{x}} b_0 = 0. \tag{3.6.50}$$

We use Eq.(3.6.50) to remove the local time variable from the local problem in (3.6.37). Thus, we have

$$\begin{aligned} \mathrm{Pe}_{loc} \mathbf{v}_0 \cdot \nabla_{\mathbf{y}} b_1 - \nabla_{\mathbf{y}} \cdot \big(\delta [\nabla_{\mathbf{x}} b_0 + \nabla_{\mathbf{y}} b_1] \big) &= \mathrm{Pe}_{loc} \big(\langle \mathbf{v}_0 \rangle_{Y^0} - \mathbf{v}_0 \big) \cdot \nabla_{\mathbf{x}} b_0 \\ &\quad - b_0 \nabla_{\mathbf{y}} \cdot \mathbf{v}_c^0 \qquad \text{in } Y^0, \qquad (3.6.51a) \\ -\mathbf{n} \cdot [\nabla_{\mathbf{x}} b_0 + \nabla_{\mathbf{y}} b_1] &= 0 \qquad \text{on } \partial\Sigma^0. \qquad (3.6.51b) \end{aligned}$$

Comparing the local problem of the substrate in Eqs.(3.6.44) with the local problem of the bacteria in Eqs.(3.6.51), we notice that the latter has an extra term consisting of the local divergence for the chemotactic velocity, $\nabla_{\mathbf{y}} \cdot \mathbf{v}_c^0$. This new term did not appear in the two regimes discussed in Section 3.4 and Section 3.5. Note that, although the chemotaxis velocity is not divergence free with respect to the local variable $\mathbf{y}$,

$$\nabla_{\mathbf{y}} \cdot \mathbf{v}_c^0 \neq 0, \tag{3.6.52}$$

the local problem in (3.6.51) is still a linear problem with respect to b_1. As a result, we seek a solution for the local problem in (3.6.51) with a different structure to that for the substrates, such that

$$b_1(t, \mathbf{x}, \mathbf{y}) = \boldsymbol{\xi}^{\delta}(\mathbf{y}) \cdot \nabla_{\mathbf{x}} b_0 + \hat{\xi} b_0 + \bar{b}_1(t, \mathbf{x}). \tag{3.6.53}$$

Here, the components of the vector function $\boldsymbol{\xi}^{\delta}(\mathbf{y}) = (\xi_1^{\delta}(\mathbf{y}), \xi_2^{\delta}(\mathbf{y}))^T$ are the solutions of following *cell problem*:

$$\begin{cases} \mathrm{Pe}_{loc} \mathbf{v}_0 \cdot \nabla_{\mathbf{y}} \xi_i^{\delta} - \nabla_{\mathbf{y}} \cdot \big(\delta \left[\nabla_{\mathbf{y}} \xi_i^{\delta} + \mathbf{e}_i \right] \big) = \mathrm{Pe}_{loc} \{ \langle \mathbf{v}_0 \rangle_{Y^0} - \mathbf{v}_0 \} \cdot \mathbf{e}_i & \text{in } Y^0, \\ -\mathbf{n} \cdot \big(\delta \left[\nabla_{\mathbf{y}} \xi_i^{\delta} + \mathbf{e}_i \right] \big) = 0 & \text{on } \partial\Sigma^0, \\ \xi_i^{\delta} \text{ is } Y - \text{periodic, and } \langle \xi_i^{\delta} \rangle_{Y^0} = 0. \end{cases} \tag{3.6.54}$$

The scalar function $\hat{\xi}$ is the solution of the following *cell problem*:

$$\begin{cases} \mathrm{Pe}_{loc}\mathbf{v}_0 \cdot \nabla_{\mathbf{y}}\hat{\xi} - \nabla_{\mathbf{y}} \cdot \big(\delta \nabla_{\mathbf{y}}\hat{\xi}\big) = -\nabla_{\mathbf{y}} \cdot \mathbf{v}_c^0 & \text{in } Y^0, \\ -\mathbf{n} \cdot \big(\delta \nabla_{\mathbf{y}}\hat{\xi}\big) = 0 & \text{on } \partial\Sigma^0, \\ \hat{\xi} \text{ is } Y-\text{periodic, and } \langle \hat{\xi} \rangle_{Y^0} = 0. \end{cases} \tag{3.6.55}$$

We rewrite the chemotactic drift in (3.6.38) by inserting s_1 given in (3.6.45), hence

$$\mathbf{v}_c^0 = \mathrm{Pe}_b \hat{\chi}_0 [\mathbf{I} + \nabla_{\mathbf{y}}\xi] \nabla_{\mathbf{x}} s_0. \tag{3.6.56}$$

Thus we have a scalar function $\hat{\xi}$ that depends on both the macroscopic and microscopic spatial variables.

Next, the terms of $\mathcal{O}(\varepsilon^0)$ give the local substrate equation:

$$\begin{aligned} \mathrm{Pe}_{loc}\mathbf{v}_0 \cdot \nabla_{\mathbf{y}} s_2 - \nabla_{\mathbf{y}} \cdot \big[\nabla_{\mathbf{x}} s_1 + \nabla_{\mathbf{y}} s_2\big] &= -\Big[\frac{\partial s_0}{\partial t} + \frac{\partial s_1}{\partial \tau}\Big] \\ &\quad + \nabla_{\mathbf{x}} \cdot [\nabla_{\mathbf{y}} s_1 + \nabla_{\mathbf{x}} s_0] \\ &\quad - \nabla_{\mathbf{x}} \cdot \{\mathrm{Pe}_{loc}[\mathbf{v}_1 s_0 + \mathbf{v}_0 s_1]\} \\ &\quad - \nabla_{\mathbf{y}} \cdot \{\mathrm{Pe}_{loc}[\mathbf{v}_2 s_0 + \mathbf{v}_1 s_1]\} \\ &\quad + \frac{\mathrm{Da}}{Y} \frac{s_0}{s_0 + \kappa_s} b_0 \qquad \text{in } Y^0, \end{aligned} \tag{3.6.57a}$$

$$-\mathbf{n} \cdot [\nabla_{\mathbf{x}} s_1 + \nabla_{\mathbf{y}} s_2] = 0 \qquad \text{on } \partial\Sigma^0, \tag{3.6.57b}$$

and the local bacteria equation:

$$\begin{aligned} \mathrm{Pe}_{loc}\mathbf{v}_0 \cdot \nabla_{\mathbf{y}} b_2 - \nabla_{\mathbf{y}} \cdot \big(\delta\big[\nabla_{\mathbf{x}} b_1 + \nabla_{\mathbf{y}} b_2\big]\big) &= -\Big[\frac{\partial b_0}{\partial t} + \frac{\partial b_1}{\partial \tau}\Big] \\ &\quad + \nabla_{\mathbf{x}} \cdot \big(\delta[\nabla_{\mathbf{y}} b_1 + \nabla_{\mathbf{x}} b_0]\big) \\ &\quad - \nabla_{\mathbf{x}} \cdot \{\mathrm{Pe}_{loc}[\mathbf{v}_1 b_0 + \mathbf{v}_0 b_1]\} \\ &\quad - \nabla_{\mathbf{y}} \cdot \{\mathrm{Pe}_{loc}[\mathbf{v}_2 b_0 + \mathbf{v}_1 b_1]\} \\ &\quad - \nabla_{\mathbf{x}} \cdot \{\mathrm{Pe}_b b_0 \hat{\chi}_0 [\nabla_{\mathbf{x}} s_0 + \nabla_{\mathbf{y}} s_1]\} \\ &\quad - \nabla_{\mathbf{x}} \cdot \big\{\mathrm{Pe}_b (b_1 \hat{\chi}_0 + b_0 \hat{\chi}_1) \nabla_{\mathbf{y}} s_0\big\} \\ &\quad - \nabla_{\mathbf{y}} \cdot \{\mathrm{Pe}_b b_0 \hat{\chi}_0 [\nabla_{\mathbf{x}} s_1 + \nabla_{\mathbf{y}} s_2]\} \\ &\quad - \nabla_{\mathbf{y}} \cdot \{\mathrm{Pe}_b (b_1 \hat{\chi}_0 + b_0 \hat{\chi}_1) [\nabla_{\mathbf{x}} s_0 + \nabla_{\mathbf{y}} s_1]\} \\ &\quad - \nabla_{\mathbf{y}} \cdot \big(\mathrm{Pe}_b (b_2 \hat{\chi}_0 + b_1 \hat{\chi}_1 + b_0 \hat{\chi}_2) \nabla_{\mathbf{y}} s_0\big) \\ &\quad - \mathrm{Da} \frac{s_0}{s_0 + \kappa_s} \Big(1 - \frac{b_0}{\kappa_c}\Big) b_0 + \kappa_b b_0 \qquad \text{in } Y^0, \end{aligned} \tag{3.6.58a}$$

$$-\mathbf{n} \cdot [\nabla_{\mathbf{x}} b_1 + \nabla_{\mathbf{y}} b_2] = 0 \qquad \text{on } \partial\Sigma^0. \tag{3.6.58b}$$

Invoking Lemma 3.9 for the solvability of the above local problem leads to the following condition:

$$\int_{Y^0} \Big(\Big[\frac{\partial s_0}{\partial t} + \frac{\partial s_1}{\partial \tau}\Big] - \underbrace{\{\nabla_{\mathbf{x}} \cdot [\nabla_{\mathbf{y}} s_1 + \nabla_{\mathbf{x}} s_0] - \mathrm{Pe}_{loc}\mathbf{v}_0 s_1\}}_{\mathrm{I}_{2\mathrm{a}}} + \underbrace{\nabla_{\mathbf{x}} \cdot \{\mathrm{Pe}_{loc}\mathbf{v}_1 s_0\}}_{\mathrm{I}_{2\mathrm{b}}}$$

$$+\underbrace{\nabla_{\mathbf{y}}\cdot\{\mathrm{Pe}_{loc}[\mathbf{v}_2 s_0+\mathbf{v}_1 s_1]\}}_{\mathrm{I}_{2c}}-\frac{\mathrm{Da}}{Y}\frac{s_0}{s_0+\kappa_s}b_0\Big)d\mathbf{y}=0. \tag{3.6.59}$$

Using the local velocity's properties, it is straightforward to show that in (3.6.59) the following integral vanishes,

$$\begin{aligned}
\mathrm{I}_{2c} &= \int_{Y^0}\nabla_{\mathbf{y}}\cdot\{\mathrm{Pe}_{loc}[\mathbf{v}_2 s_0+\mathbf{v}_1 s_1]\}\,d\mathbf{y}\\
&= \int_{Y_0}\nabla_{\mathbf{y}}\cdot\{\mathrm{Pe}_{loc}[\mathbf{v}_2 s_0+\mathbf{v}_1 s_1]\}\,d\mathbf{y}\\
&= \mathrm{Pe}_{loc}\int_{\partial\Sigma^0}\mathbf{n}\cdot\big[\mathbf{v}_2 s_0+\mathbf{v}_1 s_1\big]d\mathbf{y}\\
&= \mathrm{Pe}_{loc}\int_{\partial\Sigma^0}\big\{\underbrace{\big[\mathbf{n}\cdot\mathbf{v}_2\big]}_{=0}s_0+\underbrace{\big[\mathbf{n}\cdot\mathbf{v}_1\big]}_{=0}s_1\big\}d\mathbf{y}=0.
\end{aligned} \tag{3.6.60}$$

Next, substituting s_1 given in (3.6.45) into I_{2a}, and integrating over Y^0, we find

$$\begin{aligned}
\mathrm{I}_{2a} &= \int_{Y^0}\{\nabla_{\mathbf{x}}\cdot[\nabla_{\mathbf{y}}s_1+\nabla_{\mathbf{x}}s_0]-\mathrm{Pe}_{loc}\mathbf{v}_0 s_1\}d\mathbf{y}\\
&= \nabla_{\mathbf{x}}\cdot\Bigg(\int_{Y^0}\Big(\big[\nabla_{\mathbf{y}}\big\{\boldsymbol{\xi}(\mathbf{y})\cdot\nabla_{\mathbf{x}}s_0+\bar{s}_1(t,\mathbf{x})\big\}+\nabla_{\mathbf{x}}s_0\big]\\
&\qquad\qquad -\mathrm{Pe}_{loc}\mathbf{v}_0\big\{\boldsymbol{\xi}(\mathbf{y})\cdot\nabla_{\mathbf{x}}s_0+\bar{s}_1(t,\mathbf{x})\big\}\Big)d\mathbf{y}\Bigg)\\
&= \nabla_{\mathbf{x}}\cdot\Big(\int_{Y^0}\Big(\big\{[\nabla_{\mathbf{y}}\boldsymbol{\xi}^T+\mathbf{I}]\nabla_{\mathbf{x}}s_0-\mathrm{Pe}_{loc}[\mathbf{v}_0\otimes\boldsymbol{\xi}]\nabla_{\mathbf{x}}s_0\big\}-\mathrm{Pe}_{loc}\mathbf{v}_0\bar{s}_1\Big)d\mathbf{y}\Big).
\end{aligned} \tag{3.6.61}$$

Rewriting (3.6.61) in terms of the averaged operator gives

$$\begin{aligned}
\mathrm{I}_{2a} &= \nabla_{\mathbf{x}}\cdot\Big(\Big\langle\big[(\nabla_{\mathbf{y}}\boldsymbol{\xi})^T+\mathbf{I}\big]-\mathrm{Pe}_{loc}\big[\mathbf{v}_0\otimes\boldsymbol{\xi}\big]\Big\rangle_{Y^0}\nabla_{\mathbf{x}}\langle s_0\rangle-\mathrm{Pe}_{loc}\langle\mathbf{v}_0\rangle_{Y^0}\langle\bar{s}_1\rangle\Big)\\
&= \nabla_{\mathbf{x}}\cdot\Big(\mathbf{D}^{\mathrm{dis}}\nabla_{\mathbf{x}}\langle s_0\rangle-\mathrm{Pe}_{loc}\langle\mathbf{v}_0\rangle_{Y^0}\langle\bar{s}_1\rangle\Big),
\end{aligned} \tag{3.6.62}$$

where $\mathbf{D}^{\mathrm{dis}}$ is a dispersion tensor defined as:

$$\mathbf{D}^{\mathrm{dis}}=\Big\langle\big[(\nabla_{\mathbf{y}}\boldsymbol{\xi})^T+\mathbf{I}\big]-\mathrm{Pe}_{loc}\big[\mathbf{v}_0\otimes\boldsymbol{\xi}\big]\Big\rangle_{Y^0}. \tag{3.6.63}$$

Lastly, rewriting I_{2b} in terms of the averaged operators yields:

$$\big\langle\nabla_{\mathbf{x}}\cdot[\mathbf{v}_1 s_0]\big\rangle=\nabla_{\mathbf{x}}\cdot\big(\langle\mathbf{v}_1\rangle_{Y^0}\{\phi s_0\}\big)=\nabla_{\mathbf{x}}\cdot\big(\langle\mathbf{v}_1\rangle_{Y^0}\ \langle s_0\rangle\big). \tag{3.6.64}$$

From (3.6.60), (3.6.62) and (3.6.64), the solvability condition in (3.6.59) gives us the following effective equation:

$$\begin{aligned}\frac{\partial\langle s_0\rangle}{\partial t}+\frac{\partial\langle s_1\rangle}{\partial\tau}=&\nabla_{\mathbf{x}}\cdot\Big(\mathbf{D}^{\mathrm{dis}}\nabla_{\mathbf{x}}\langle s_0\rangle-\mathrm{Pe}_{loc}\big[\langle\mathbf{v}_0\rangle_{Y^0}\langle\bar{s}_1\rangle+\langle\mathbf{v}_1\rangle_{Y^0}\langle\bar{s}_0\rangle\big]\Big)\\&-\frac{\mathrm{Da}}{Y}\Big\langle\frac{s_0}{s_0+\kappa_s}b_0\Big\rangle.\end{aligned}\tag{3.6.65}$$

Combining (3.6.43) and (3.6.65) by multiplying (3.6.65) with ε and then adding the result to (3.6.43), we obtain:

$$\begin{aligned}\frac{\partial\langle s_0\rangle}{\partial\tau}+\varepsilon\frac{\partial\langle s_1\rangle}{\partial\tau}=&\nabla_{\mathbf{x}}\cdot\Big(\varepsilon\mathbf{D}^{\mathrm{dis}}\nabla_{\mathbf{x}}\langle s_0\rangle-\mathrm{Pe}_{loc}\big[\langle\mathbf{v}_0\rangle_{Y^0}\langle s_0+\varepsilon\bar{s}_1\rangle+\varepsilon\langle\mathbf{v}_1\rangle_{Y^0}\langle s_0\rangle\big]\Big)\\&-\varepsilon\frac{\mathrm{Da}}{Y}\Big\langle\frac{s_0}{s_0+\kappa_s}b_0\Big\rangle.\end{aligned}\tag{3.6.66}$$

Note that we neglected the term $\partial\langle s_0\rangle/\partial t$ from Eq.(3.6.65), representing the small time behaviour, since it is of order ε. Taking the average of the first order approximation for the substrate concentration and using (3.6.45) yields the sum of the first two non-oscillating terms of the expansion

$$\begin{aligned}\langle s_{1,\varepsilon}\rangle&=\langle s_0+\varepsilon s_1\rangle\\&=\langle s_0\rangle+\varepsilon\langle s_1\rangle\\&=\langle s_0\rangle+\varepsilon\big\langle\boldsymbol{\xi}(\mathbf{y})\cdot\nabla_{\mathbf{x}}s_0+\bar{s}_1\big\rangle\\&=\langle s_0\rangle+\varepsilon\langle\boldsymbol{\xi}(\mathbf{y})\rangle\cdot\nabla_{\mathbf{x}}\langle s_0\rangle+\langle\bar{s}_1\rangle\\&=\langle s_0\rangle+\varepsilon\langle\bar{s}_1\rangle.\end{aligned}\tag{3.6.67}$$

Furthermore, at the slow scale, we can extrapolate the following approximation:

$$\varepsilon\langle s_{1,\varepsilon}\rangle=\varepsilon\langle s_0\rangle+\mathcal{O}(\varepsilon^2)\sim\varepsilon\langle s_0\rangle.\tag{3.6.68}$$

Then we rewrite the effective equation in (3.6.66) in terms of (3.6.67) and (3.6.68) as:

$$\begin{aligned}\frac{\partial\langle s_{1,\varepsilon}\rangle}{\partial\tau}=&\nabla_{\mathbf{x}}\cdot\Big(\varepsilon\mathbf{D}^{\mathrm{dis}}\nabla_{\mathbf{x}}\langle s_{1,\varepsilon}\rangle-\mathrm{Pe}_{loc}\big[\langle\mathbf{v}_0\rangle_{Y^0}+\langle\mathbf{v}_1\rangle_{Y^0}\big]\langle s_{1,\varepsilon}\rangle\Big)\\&-\varepsilon\frac{\mathrm{Da}}{Y}\Big\langle\frac{s_0}{s_0+\kappa_s}b_0\Big\rangle.\end{aligned}\tag{3.6.69}$$

Then, writing the effective model in (3.6.69) in terms of the slow time variable yields

$$\begin{aligned}\frac{\partial\langle s_{1,\varepsilon}\rangle}{\partial t}=&\nabla_{\mathbf{x}}\cdot\Big(\mathbf{D}^{\mathrm{dis}}\nabla_{\mathbf{x}}\langle s_{1,\varepsilon}\rangle-\varepsilon^{-1}\mathrm{Pe}_{loc}\big[\langle\mathbf{v}_0\rangle_{Y^0}+\langle\mathbf{v}_1\rangle_{Y^0}\big]\langle s_{1,\varepsilon}\rangle\Big)\\&-\frac{\mathrm{Da}}{Y}\Big\langle\frac{s_0}{s_0+\kappa_s}b_0\Big\rangle.\end{aligned}\tag{3.6.70}$$

Omitting the terms involving the local gradient of the substrate from (3.6.71) leads to the local bacteria equation that reads

$$\begin{aligned}
\mathrm{Pe}_{loc}\mathbf{v}_0\cdot\nabla_{\mathbf{y}}b_2-\nabla_{\mathbf{y}}\cdot\big(\delta\big[\nabla_{\mathbf{x}}b_1+\nabla_{\mathbf{y}}b_2\big]\big) &= -\Big[\frac{\partial b_0}{\partial t}+\frac{\partial b_1}{\partial \tau}\Big] \\
&+\nabla_{\mathbf{x}}\cdot\big(\delta[\nabla_{\mathbf{y}}b_1+\nabla_{\mathbf{x}}b_0]\big) \\
&-\nabla_{\mathbf{x}}\cdot\{\mathrm{Pe}_{loc}[\mathbf{v}_1b_0+\mathbf{v}_0b_1]\} \\
&-\nabla_{\mathbf{y}}\cdot\{\mathrm{Pe}_{loc}[\mathbf{v}_2b_0+\mathbf{v}_1b_1]\} \\
&-\nabla_{\mathbf{x}}\cdot\{\mathrm{Pe}_b b_0\hat{\chi}_0[\nabla_{\mathbf{x}}s_0+\nabla_{\mathbf{y}}s_1]\} \\
&-\nabla_{\mathbf{y}}\cdot\{\mathrm{Pe}_b b_0\hat{\chi}_0[\nabla_{\mathbf{x}}s_1+\nabla_{\mathbf{y}}s_2]\} \\
&-\nabla_{\mathbf{y}}\cdot\{\mathrm{Pe}_b(b_1\hat{\chi}_0+b_0\hat{\chi}_1)[\nabla_{\mathbf{x}}s_0+\nabla_{\mathbf{y}}s_1]\} \\
&-\mathrm{Da}\frac{s_0}{s_0+\kappa_s}\Big(1-\frac{b_0}{\kappa_c}\Big)b_0+\kappa_b b_0 \qquad \text{in } Y^0, \qquad (3.6.71a)\\
-\mathbf{n}\cdot[\nabla_{\mathbf{x}}b_1+\nabla_{\mathbf{y}}b_2] &= 0 \qquad \text{on } \partial\Sigma^0. \qquad (3.6.71b)
\end{aligned}$$

Then, the solvability of the local bacterial equation states that the local problem in (3.6.71) admits a unique solution if and only if the following compatibility condition is satisfied:

$$\begin{aligned}
\int_{Y^0}\Big(\Big[\frac{\partial b_0}{\partial t}+\frac{\partial b_1}{\partial \tau}\Big] &- \underbrace{\{\nabla_{\mathbf{x}}\cdot\big(\delta[\nabla_{\mathbf{y}}b_1+\nabla_{\mathbf{x}}b_0]\big)-\mathrm{Pe}_{loc}\mathbf{v}_0b_1\big)\}}_{\mathrm{I_{3a}}} \\
&+\Big\{\underbrace{\nabla_{\mathbf{x}}\cdot\mathrm{Pe}_{loc}\mathbf{v}_1b_0\Big\}}_{\mathrm{I_{3b}}}+\underbrace{\nabla_{\mathbf{y}}\cdot\{\mathrm{Pe}_{loc}[\mathbf{v}_2b_0+\mathbf{v}_1b_1]\}}_{\mathrm{I_{3c}}} \\
&+\underbrace{\nabla_{\mathbf{x}}\cdot\Big\{\mathrm{Pe}_b b_0\hat{\chi}_0[\nabla_{\mathbf{x}}s_0+\nabla_{\mathbf{y}}s_1]\Big\}}_{\mathrm{I_{3d}}} \\
&+\underbrace{\nabla_{\mathbf{y}}\cdot\Big\{\mathrm{Pe}_b b_0\hat{\chi}_0[\nabla_{\mathbf{x}}s_1+\nabla_{\mathbf{y}}s_2]\Big\}}_{\mathrm{I_{3e}}} \\
&+\underbrace{\nabla_{\mathbf{y}}\cdot\Big\{\mathrm{Pe}_b(b_1\hat{\chi}_0+b_0\hat{\chi}_1)[\nabla_{\mathbf{x}}s_0+\nabla_{\mathbf{y}}s_1]\Big\}}_{\mathrm{I_{3f}}} \\
&-\mathrm{Da}\frac{s_0}{s_0+\kappa_s}\Big(1-\frac{b_0}{\kappa_c}\Big)b_0+\kappa_b b_0\Big)d\mathbf{y}=0. \qquad (3.6.72)
\end{aligned}$$

The two terms in $\mathrm{I_{3b}}$ and $\mathrm{I_{3c}}$ have a similar structure to $\mathrm{I_{2b}}$ and $\mathrm{I_{bc}}$ treated earlier, and thus $\mathrm{I_{3c}}$ vanishes, while $\mathrm{I_{3b}}$ yields:

$$\big\langle\nabla_{\mathbf{x}}\cdot[\mathbf{v}_1b_0]\big\rangle=\nabla_{\mathbf{x}}\cdot\big(\langle\mathbf{v}_1\rangle_{Y^0}\,\langle b_0\rangle\big). \qquad (3.6.73)$$

Next, because of the solid-aqueous interface conditions in (3.6.57) and the divergence theorem, the integral $\mathrm{I_{3e}}$ vanishes in the following manner:

$$\mathrm{I_{3e}}=\int_{Y^0}\nabla_{\mathbf{y}}\cdot\big\{\mathrm{Pe}_b b_0\hat{\chi}_0[\nabla_{\mathbf{x}}s_1+\nabla_{\mathbf{y}}s_2]\big\}d\mathbf{y}$$

$$= \mathrm{Pe}_b b_0 \hat{\chi}_0 \int_{\partial\Sigma^0} \underbrace{\mathbf{n} \cdot [\nabla_{\mathbf{x}} s_1 + \nabla_{\mathbf{y}} s_2]}_{=0} d\mathbf{s}$$
$$= 0. \tag{3.6.74}$$

In a similar way, we use the divergence theorem and the interface conditions in (3.6.44) to show that the integral $\mathrm{I}_{3\mathrm{f}}$ also vanishes,

$$\begin{aligned}
\mathrm{I}_{3\mathrm{f}} &= \int_{Y^0} \nabla_{\mathbf{y}} \cdot \big\{ \mathrm{Pe}_b (b_1 \hat{\chi}_0 + b_0 \hat{\chi}_1) [\nabla_{\mathbf{x}} s_0 + \nabla_{\mathbf{y}} s_1] b_0 \big\} d\mathbf{y} \\
&= \mathrm{Pe}_b \int_{\partial\Sigma^0} (b_1 \hat{\chi}_0 + b_0 \hat{\chi}_1) \big(\underbrace{\mathbf{n} \cdot [\nabla_{\mathbf{x}} s_0 + \nabla_{\mathbf{y}} s_1]}_{=0} \big) d\mathbf{s} \\
&= 0.
\end{aligned} \tag{3.6.75}$$

Next, when we substitute s_1 in (3.6.45) into $\mathrm{I}_{3\mathrm{b}}$ and rewrite $\mathrm{I}_{3\mathrm{b}}$ in terms of the average operator to obtain:

$$\begin{aligned}
\mathrm{I}_{3\mathrm{b}} &= \frac{1}{|Y|} \int_{Y^0} \nabla_{\mathbf{x}} \cdot \big\{ \mathrm{Pe}_b \hat{\chi}_0 [\nabla_{\mathbf{x}} s_0 + \nabla_{\mathbf{y}} s_1] b_0 \big\} d\mathbf{y} \\
&= \nabla_{\mathbf{x}} \cdot \left(\frac{\mathrm{Pe}_b \hat{\chi}_0}{|Y|} \int_{Y^0} \big[\nabla_{\mathbf{x}} s_0 + \nabla_{\mathbf{y}} \big\{ \boldsymbol{\xi} \nabla_{\mathbf{x}} s_0 + \bar{s}_1 \big\} \big] b_0 d\mathbf{y} \right) \\
&= \nabla_{\mathbf{x}} \cdot \left(\mathrm{Pe}_b b_0 \hat{\chi}_0 \left[\frac{1}{|Y|} \int_{Y^0} [\mathbf{I} + \nabla_{\mathbf{y}} \boldsymbol{\xi}^T] d\mathbf{y} \right] \nabla_{\mathbf{x}} s_0 \right), \\
&= \nabla_{\mathbf{x}} \cdot \left(\mathrm{Pe}_b b_0 \hat{\chi}_0 \phi \left[\frac{1}{|Y^0|} \int_{Y^0} [\mathbf{I} + \nabla_{\mathbf{y}} \boldsymbol{\xi}^T] d\mathbf{y} \right] \nabla_{\mathbf{x}} s_0 \right), \\
&= \nabla_{\mathbf{x}} \cdot \Big(\mathbf{D}^{\mathrm{ch}} \mathrm{Pe}_b \big\langle b_0 \hat{\chi}_0 \nabla_{\mathbf{x}} s_0 \big\rangle \Big),
\end{aligned} \tag{3.6.76}$$

where, $\mathbf{D}^{\mathrm{ch}}$ is referred to as the chemotactic dispersion tensor, and is defined as

$$\mathbf{D}^{\mathrm{ch}} = \langle \mathbf{I} + (\nabla_{\mathbf{y}} \boldsymbol{\xi})^T \rangle_{Y^0}, \tag{3.6.77}$$

Note that $\mathbf{D}^{\mathrm{ch}}$ consists of the diffusion part of the substrate dispersion tensor $\mathbf{D}^{\mathrm{dis}}$. Moving forward, we resolve $\mathrm{I}_{3\mathrm{a}}$ by substituting b_1 in (3.6.53) into $\mathrm{I}_{3\mathrm{a}}$, which we express in terms of the averaged operator as:

$$\begin{aligned}
\mathrm{I}_{3\mathrm{a}} &= \frac{1}{|Y|} \int_{Y^0} \Big\{ \nabla_{\mathbf{x}} \cdot \big(\delta [\nabla_{\mathbf{y}} b_1 + \nabla_{\mathbf{x}} b_0] \big) - \mathrm{Pe}_{loc} \mathbf{v}_0 b_1 \Big\} d\mathbf{y} \\
&= \nabla_{\mathbf{x}} \cdot \left(\frac{1}{|Y|} \int_{Y^0} \Big\{ \delta \big[\nabla_{\mathbf{y}} \big\{ \boldsymbol{\xi}^{\delta}(\mathbf{y}) \cdot \nabla_{\mathbf{x}} b_0 + \hat{\xi} b_0 + \bar{s}_1 \big\} + \nabla_{\mathbf{x}} b_0 \big] \right. \\
&\qquad \left. - \mathrm{Pe}_{loc} \mathbf{v}_0 \big\{ \boldsymbol{\xi}^{\delta}(\mathbf{y}) \cdot \nabla_{\mathbf{x}} b_0 + \hat{\xi} b_0 + \bar{b}_1 \big\} \Big\} d\mathbf{y} \right)
\end{aligned}$$

$$= \nabla_{\mathbf{x}} \cdot \left(\frac{1}{|Y|} \int_{Y^0} \Big(\delta[\nabla_{\mathbf{y}} \boldsymbol{\xi}^{\delta} + \mathbf{I}] - \mathrm{Pe}_{loc}[\mathbf{v}_0 \otimes \boldsymbol{\xi}^{\delta}] \Big) \nabla_{\mathbf{x}} b_0 - \mathrm{Pe}_{loc} \big[\mathbf{v}_0 \bar{b}_1 \right.$$

$$\left. + \big(\delta \nabla_{\mathbf{y}} \hat{\xi} - \mathrm{Pe}_{loc} \mathbf{v}_0 \hat{\xi} \big) b_0 \big] d\mathbf{y} \right). \tag{3.6.78}$$

We set $\bar{\mathbf{D}}^{\mathrm{dis}}$ as the dispersion tensor for the bacteria density:

$$\bar{\mathbf{D}}^{\mathrm{dis}} = \Big\langle \delta \big[(\nabla_{\mathbf{y}} \boldsymbol{\xi}^{\delta})^T + \mathbf{I} \big] - \mathrm{Pe}_{loc} \big[\mathbf{v}_0 \otimes \boldsymbol{\xi}^{\delta} \big] \Big\rangle_{Y^0}. \tag{3.6.79}$$

Also, we set $\langle \mathbf{u} \rangle_{Y^0}$ as the pore average drift velocity:

$$\langle \hat{\mathbf{u}} \rangle_{Y^0} = \langle \delta \nabla_{\mathbf{y}} \hat{\xi} - \mathrm{Pe}_{loc} \{ \mathbf{v}_0 \hat{\xi} \} \rangle_{Y^0}, \tag{3.6.80}$$

where $\hat{\xi}$ depends on the local and global scales. We rewrite the compatibility condition (3.6.71) as:

$$\begin{aligned} \frac{\partial \langle b_0 \rangle}{\partial t} + \frac{\partial \langle b_1 \rangle}{\partial \tau} = \nabla_{\mathbf{x}} \cdot \Big(& \bar{\mathbf{D}}^{\mathrm{dis}} \nabla_{\mathbf{x}} \langle b_0 \rangle - \big\{ \mathrm{Pe}_{loc} \big[\langle \mathbf{v}_0 \rangle_{Y^0} \langle \bar{b}_1 \rangle + \langle \mathbf{v}_1 \rangle_{Y^0} \langle b_0 \rangle \big] \big\} \\ & - \big[\langle \mathbf{u} \rangle_{Y^0} \langle b_0 \rangle + \mathbf{D}^{\mathrm{ch}} \big\langle \mathrm{Pe}_b b_0 \hat{\chi}_0 \nabla_{\mathbf{x}} s_0 \big\rangle \big] \Big) \\ & + \Big\langle \mathrm{Da} \frac{s_0}{s_0 + \kappa_s} \left(1 - \frac{b_0}{\kappa_c} \right) b_0 - \kappa_b b_0 \Big\rangle. \end{aligned} \tag{3.6.81}$$

Note that as in the substrate equation, we neglect the term $\partial \langle b_0 \rangle / \partial t$ representing the short time behaviour since it is of order ε. We derive the final form for the effective bacteria equation by applying the same argument used for (3.6.65)-(3.6.70). First, we deduce the following identities involving the first order approximation for the bacteria:

$$\langle b_{1,\varepsilon} \rangle = \langle b_0 \rangle + \varepsilon \langle \bar{b}_1 \rangle, \tag{3.6.82a}$$

$$\varepsilon \langle b_{1,\varepsilon} \rangle \sim \varepsilon \langle b_0 \rangle. \tag{3.6.82b}$$

Then, we multiply (3.6.81) by ε. Adding the first effective equation (3.6.50) and (3.6.81) and rescaling for the global time yields:

$$\begin{aligned} \frac{\partial \langle b_{1,\varepsilon} \rangle}{\partial t} = \nabla_{\mathbf{x}} \cdot \Big(& \bar{\mathbf{D}}^{\mathrm{dis}} \nabla_{\mathbf{x}} \langle b_{1,\varepsilon} \rangle - \big\{ \mathrm{Pe} \big[\langle \mathbf{v}_0 \rangle_{Y^0} + \langle \mathbf{v}_1 \rangle_{Y^0} \big] \langle b_{1,\varepsilon} \rangle \\ & + \big[\varepsilon^{-1} \langle \hat{\mathbf{u}} \rangle_{Y^0} \langle b_{1,\varepsilon} \rangle + \mathbf{D}^{\mathrm{ch}} \mathrm{Pe}_b \big\langle b_0 \hat{\chi}_0 \nabla_{\mathbf{x}} s_0 \big\rangle \big] \big\} \Big) \\ & + \Big\langle \mathrm{Da} \frac{s_0}{s_0 + \kappa_s} \left(1 - \frac{b_0}{\kappa_c} \right) b_0 - \kappa_b b_0 \Big\rangle. \end{aligned} \tag{3.6.83}$$

Note that, the drift velocity $\mathbf{u}$ depends on two different spatial scales. To amend this, we rescale the drift velocity into the global scale in the following way:

$$\hat{\mathbf{u}}(t, \mathbf{x}, \mathbf{y}) = \varepsilon \big(\nabla_{\mathbf{x}} \xi - \mathrm{Pe} \xi \mathbf{v}_0 \big) = \varepsilon \mathbf{u}(t, \mathbf{x}). \tag{3.6.84}$$

Moreover, the average operator is $\langle\star\rangle_{Y^0} = \varepsilon^2\langle\star\rangle_{\varepsilon Y^0}$. Finally, we have the effective problem expressed as:

$$\begin{aligned}\frac{\partial\langle b_{1,\varepsilon}\rangle}{\partial t} = \nabla_{\mathbf{x}}\cdot\Big(\bar{\mathbf{D}}^{\mathrm{dis}}\nabla_{\mathbf{x}}\langle b_{1,\varepsilon}\rangle - \Big\{&\varepsilon^{-1}\mathrm{Pe}_{loc}\big[\langle\mathbf{v}_0\rangle_{Y^0} + \langle\mathbf{v}_1\rangle_{Y^0}\big]\langle b_{1,\varepsilon}\rangle \\ &+ \varepsilon^2\langle\mathbf{u}\rangle_{\varepsilon Y^0}\langle b_0\rangle + \mathbf{D}^{\mathrm{ch}}\big\langle\mathrm{Pe}_b\hat{\chi}_0\nabla_{\mathbf{x}}s_0 b_0\big\rangle\Big\}\Big) \\ &- \Big\langle\mathrm{Da}\frac{s_0}{s_0+\kappa_s}\left(1-\frac{b_0}{\kappa_c}\right)b_0 - \kappa_b b_0\Big\rangle. \end{aligned} \tag{3.6.85}$$

As a result of the scaling, we note that the scaled drift velocity is of order ε^s, and thus, it is negligible. Lastly, letting

$$\begin{cases}\phi\mathcal{S} &= \langle s_{1,\varepsilon}\rangle = \phi[s_0 + \varepsilon\bar{s}], \\ \phi\mathcal{B} &= \langle b_{1,\varepsilon}\rangle = \phi[b_0 + \varepsilon\bar{b}], \\ \mathcal{V} &= \langle\mathbf{v}_0\rangle_{Y0} + \langle\mathbf{v}_1\rangle_{Y0}, \end{cases} \tag{3.6.86}$$

we write the two effective equations accordingly as:

$$\begin{cases}\dfrac{\partial\mathcal{S}}{\partial t} = \nabla\cdot\Big(\mathbf{D}^{\mathrm{dis}}\nabla\mathcal{S} - \mathrm{Pe}\mathcal{V}\mathcal{S}\Big) - \dfrac{\mathrm{Da}}{Y}\dfrac{\mathcal{S}}{\mathcal{S}+\kappa_s}\mathcal{B} & \text{in } [0,T]\times\Omega, \\ \dfrac{\partial\mathcal{B}}{\partial t} = \nabla\cdot\Big(\bar{\mathbf{D}}^{\mathrm{dis}}\nabla\mathcal{B} - \big[\mathrm{Pe}\mathcal{V} + \mathrm{Pe}_b\big\{\mathbf{D}^{\mathrm{ch}}\chi(\mathcal{S})\nabla\mathcal{S}\big\}\big]\mathcal{B}\Big) & \\ \qquad + \mathrm{Da}\dfrac{\mathcal{S}}{\mathcal{S}+\kappa_s}\left(1-\dfrac{\mathcal{B}}{\kappa_c}\right)\mathcal{B} - \kappa_b\mathcal{B} & \text{in } [0,T]\times\Omega. \end{cases} \tag{3.6.87}$$

The effective model has the same effective initial conditions as (3.4.50). Since the first order approximation of the flow velocity, we have

$$\mathcal{V} = \langle\mathbf{v}_0\rangle_{Y^0}. \tag{3.6.88}$$

3.7 Concluding Remarks

Using the formal asymptotic expansion technique, we developed an effective (upscaled) form of the general Keller-Segel model described in Chapter 2. To initiate the asymptotic homogenisation, we provided a microscopic description of the model, in which we asserted that the chemotactic velocity and reaction rates generating fluxes vary slowly. As a result, there are only three limiting cases regarding advective flow to consider. The advective Péclet number identifies three transport regimes. $\mathrm{Pe} \leq \mathcal{O}(\varepsilon)$ corresponds to the diffusion regime, $\mathrm{Pe} = \mathcal{O}(\varepsilon^0)$ to the advection-diffusion regime, and $\mathrm{Pe} = \mathcal{O}(\varepsilon^{-1})$ to the advection-dispersion regime. The fluxes of the substrate equation when scaled up are

$$\mathrm{Pe} \leq \mathcal{O}(\varepsilon) \quad : \quad \mathbf{J}_s^h = \mathbf{D}^h\nabla\mathcal{S}, \tag{3.7.1a}$$

$$\mathrm{Pe} = \mathcal{O}(\varepsilon^0) \ : \quad \mathbf{J}_s^h = \mathbf{D}^h \nabla \mathcal{S} - \mathrm{Pe} \langle \mathbf{v}_0 \rangle_{Y^0} \mathcal{S}, \tag{3.7.1b}$$

$$\mathrm{Pe} = \mathcal{O}(\varepsilon^{-1}): \quad \mathbf{J}_s^{\mathrm{dis}} = \mathbf{D}^{\mathrm{dis}} \nabla \mathcal{S} - \mathrm{Pe} \langle \mathbf{v}_0 \rangle_{Y^0} \mathcal{S}, \tag{3.7.1c}$$

where $\mathcal{S}$, $\mathbf{D}^h$, $\mathbf{D}^{\mathrm{dis}}$ and $\langle \mathbf{v}_0 \rangle_{Y^0}$ are the effective substrate concentration, the effective diffusion tensor, the dispersion tensor, and the mean-pore flow (seepage flow), respectively. The upscaled bacterial population fluxes read as:

$$\mathrm{Pe} \leq \mathcal{O}(\varepsilon) \quad : \quad \mathbf{J}_s^h = \delta \mathbf{D}^h \nabla \mathcal{B} - \mathrm{Pe}_b \big\{ \mathbf{D}^h \chi(\mathcal{S}) \nabla \mathcal{S} \big\} \mathcal{B}, \tag{3.7.2a}$$

$$\mathrm{Pe} = \mathcal{O}(\varepsilon^0) \ : \quad \mathbf{J}_s^h = \delta \mathbf{D}^h \nabla \mathcal{B} - \big[\mathrm{Pe} \langle \mathbf{v}_0 \rangle_{Y^0} + \mathrm{Pe}_b \big\{ \mathbf{D}^h \chi(\mathcal{S}) \nabla \mathcal{S} \big\} \big] \mathcal{B}, \tag{3.7.2b}$$

$$\mathrm{Pe} = \mathcal{O}(\varepsilon^{-1}): \quad \mathbf{J}_s^{\mathrm{dis}} = \bar{\mathbf{D}}^{\mathrm{dis}} \nabla \mathcal{B} - \big[\mathrm{Pe} \langle \mathbf{v}_0 \rangle_{Y^0} + \mathrm{Pe}_b \big\{ \mathbf{D}^{\mathrm{ch}} \chi(\mathcal{S}) \nabla \mathcal{S} \big\} \big] \mathcal{B}, \tag{3.7.2c}$$

where $\mathcal{B}$ and $\mathbf{D}$ are the effective bacterial density and chemotactic tensor, respectively. The effective diffusion tensor associated with the random motility of bacteria, substrate diffusion, and chemotactic drift is identical and is obtained by solving the *cell-problem* provided in Eqs.(3.4.13).

On the other hand, when transport is dominated by advection, this gave rise to the dispersion tensors $\bar{\mathbf{D}}^{\mathrm{dis}}$ and $\mathbf{D}^{\mathrm{dis}}$ computed using *cell-problems* in Eqs.(3.6.11) and Eqs.(3.6.12), while the chemotactic tensor $\mathbf{D}^{\mathrm{ch}}$ consists of the diffusion part of the substrate dispersion tensor. Although the divergence of the chemotactic velocity appears at the local scale, as shown in (3.6.51), at the global scale these effects are of order ε^2, and thus are neglected. Notably, the chemotactic velocity has no dispersion effects on the population.

Note that the effective model's primary objective is to approximate the effect of the microstructure on substrate transport and chemotactic bacteria populations. Consequently, the effective model has the same modelling restrictions as the original model. Furthermore, the upscaling can be applied to different versions of the generalised Keller-Segel model provided the proposed changes have no effect on the scaling argument underlying the three limiting cases. For instance, we can include a globally defined retardation factor, or assume flow velocity profiles with dependency on the spatial global variable.

Chapter 4

Travelling Chemotactic Waves in a Periodic Porous Medium

In the previous chapter, the derivation of effective models for the Keller-Segel model using formal asymptotic homogenisation was presented based on the assumption that advective flow is the only important process affecting the homogenisation procedure. This chapter uses the effective models developed in Chapter 3 in a numerical study relating to the travelling chemotactic bacteria bands (travelling wave solutions) within the subsurface contamination bioremediation field. We aim to demonstrate that the asymptotic homogenisation method is reliable for deriving simple, effective models that can easily be used in numerical studies of the Keller-Segel model in porous media. Also, we aim to validate the effective model numerically by comparing the simulation results of the effective model with direct simulations of the original model.

This chapter is structured as follows: In Section 4.1, we provide a brief overview on travelling chemotactic bands, thereby highlighting the novelty in applying the effective models developed using asymptotic homogenisation in this thesis. In Section 4.2, the mathematical models used in this chapter are described in reference to the models in Chapter 2. In Section 4.3, we introduce a new reference frame suitable for simulating travelling wave solutions. Next, the different microscopic models considered in this chapter are connected to the related homogenisation results in Chapter 3 using the new reference frame. In Section 4.4, we conduct several numerical investigations to study the effects of chemotaxis on the travelling bands and also to evaluate the validity and accuracy of the effective model in comparison to direct simulations of the original model.

4.1 Background Studies

It is widely known that the formation of chemotactically moving bands in capillary tubes was first observed by Adler [2], and the study reported that the moving bands

are caused by the chemical gradients formed when microorganisms consume their energy source. Kennedy and Aris [103] were the first to explore the effects of growth and decay on travelling bands using mathematical analysis. They discovered that while travelling bands can be generated without chemotaxis, the chemotaxis effect is characterised by an increase in the speed of travelling bands. Lauffenburger et al. [114] extended the mathematical study of Kennedy and Aris [103] by examining the effect of varying chemosensory sensitivity functions on the chemotactic bands. Subsequently, to have a non-dissipating chemotactic travelling wave solution for the Keller-Segel model described in Chapter 2, cell growth and death must be considered. However, a travelling wave solution can be generated without chemotaxis if the logistic growth is added to model [210, 141]. On the other hand, the formation of a chemotactic travelling wave solution in a Keller-Segel system without microbial metabolic activity is possible. It has been ascribed to singularities in the logarithmic sensitivity function (see Table 2.1, Chapter 2). Conversely, when the model is equipped with a receptor sensitivity, while excluding the bacteria growth, the system only produces dissipating travelling bands that eventually vanish [210].

Travelling chemotactic bacteria bands in porous media have been observed and investigated in several studies related to the bioremediation of subsurface contamination. For instance, Pedit et al. [153] investigated the role of chemotaxis and microbial metabolic activities in promoting the biodegradation of subsurface contaminants and observed that chemotaxis could occur in porous media using modified capillary experiments. The experimental results revealed that the fitted data for the effective chemotactic sensitivity parameters are less directly quantifiable than the other model parameters. To simulate travelling chemotactic bands in porous media, Long and Hilpert [125] and Yan and Hilpert [211] implemented the Lattice-Boltzman method to the upscaled Keller-Segel model suggested in Olson et al. [144] in a mobile aqueous phase using hydrodynamic dispersion and tortuosity parameters based on empirical observations reported in the literature (see Eqs.(1.2.13) in Section 1.2.3 of the Introduction). Therefore, to the best of our knowledge, the use of formal mathematical upscaling to derive a simplified, effective form of the chemotaxis–diffusion–advection–reaction model to study chemotactic bands in porous media has not been reported.

4.2 Mathematical Model

In our set-up we consider the rectangular domain described in Chapter 2 with a length of $L^*_{x_1} = 6.25$ [cm] and width of $L^*_{x_2} = 0.65$ [cm]. The porous structure consisted of a square array of circular inclusions with a porosity of 0.45 (Figure 4.1). The medium flow satisfied the Stokes equations described in Eqs.(2.3.8), and the mass transport equations satisfy Eqs.(2.4.1). As mentioned previously in Section 2.4 of Chapter 2, there are no-flux and no-flow conditions at the solid–aqueous interface (Eq.(2.4.3)), and the typical no-flux and no-flow conditions at the lateral walls, Γ^*_T and Γ^*_B, that

is,

$$H_s^*(\mathbf{x}^*, s^*, b^*) = H_b^*(\mathbf{x}^*, s^*, b^*) = 0. \tag{4.2.1}$$

To close the model, it is essential to assign the initial concentrations of the two species and the external boundary conditions at Γ_R and Γ_L. Through the model closure, we identify different case studies, which we utilise to conduct different numerical investigations. In the first case study, we consider the case of in an immobile aqueous phase. For the second case study, advective flow is included to examine the effect of the flow on the chemotactic bands. The initial concentration of the substrate is assumed to be uniformly distributed on Ω_f^*, that is,

$$s^*(0, \mathbf{x}^*) = s_{\text{in}}^*, \tag{4.2.2}$$

whereas the initial concentration of the bacteria is injected into subdomain Ω_{in}^*; hence,

$$b^*(0, \mathbf{x}) = b_{in}^* \mathbb{1}_{\Omega_{in}^*}(\mathbf{x}). \tag{4.2.3}$$

More details on the model closure will be introduced in the subsequent chapter. The parameter values are listed in Table 4.1. More details on the model closure will be introduced in the subsequent chapter.

Remark 4.1. *It should be noted that $\mathbb{1}_{\mathbf{A}}$ is the indicator function defined using the Iverson bracket as: $\mathbb{1}_{\mathbf{A}}(\mathbf{x}) = [\mathbf{x} \in \mathbf{A}]$.*

Non-dimensionalisation. We assume that $l_{y_1^*} = l_{y_2^*} = 250$ [µm] is the microscopic length scale and $L_{x_1^*} = 6.25$ [cm] is the macroscopic length scale, and thus the separation of scales assumption holds, that is, $\varepsilon = l_{y_1^*}/L_{x_1^*} \sim 4 \times 10^{-3} \ll 1$. Following the same dimensionless analysis as in Section 2.6, we can obtain the Stokes equations in Eqs.(2.6.10) and Eqs.(2.6.11). We choose the reference concentrations of the two species as their initial concentrations:

$$s_{\text{m}}^* = s_{in}^*, \qquad b_{\text{m}}^* = b_{in}^*. \tag{4.2.4}$$

Therefore, the dimensionless initial concentrations are expressed as:

$$s(0, \mathbf{x}) = 1, \qquad b(0, \mathbf{x}) = \mathbb{1}_{\Omega_{in}}. \tag{4.2.5}$$

Thus, we have the dimensionless equations that satisfy the mass transfer of the two species in (2.6.13), the solid–aqueous interface in (2.6.14), and the no-flux conditions at the lateral walls in (2.6.23). Lastly, the boundary conditions at Γ_L and Γ_R is left to be specified later in this chapter. The dimensionless parameters used are listed in Table 4.2. Note that any change in these values will be highlighted in the text.

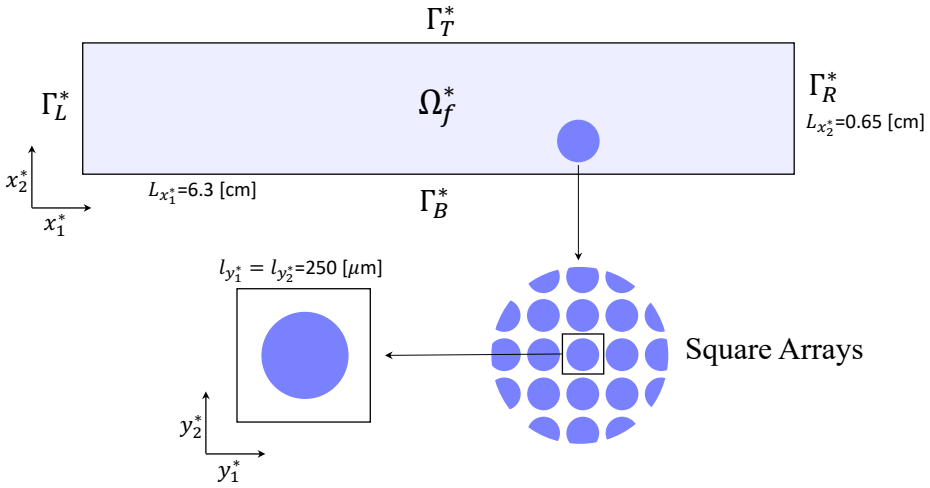


Figure 4.1: *Schematic sketch of the porous domain investigated in this chapter. Where the domain length is* $L_{x_1}^* = 6.25$ [cm] *and width is* $L_{x_2}^* = 0.65$ [cm]. *The microstructure consisting of square arrays of circular inclusions, where the dimension of the representative volume element is* $l_{y_1^*} = l_{y_2^*} = 250$ [µm].

4.3 Changing Variables for Numerical Simulations

As the bacterial bands and substrate waves are very thin compared to the size of the domain, front propagation is traditionally resolved numerically in large computational domains. Therefore, we proposed a change of variables to transform the domain Ω_ε into a larger domain. Based on the work of Allaire and El Ganaoui [9] and Allaire and Habibi [10], we fixed the size of the periodic cell as Y_ε^i, and increased the total number of cells. Consequently, the size of the global domain was changed to an order of $1/\varepsilon$ (Figure 4.2). Particularly, rather than using the macroscopic space variable, $\mathbf{x} \in \Omega_\varepsilon$, the microscopic space variable, $\mathbf{y} = \mathbf{x}/\varepsilon$, is utilised. Similarly, the microscopic diffusion time variable,

$$\tau = \varepsilon^{-2} t \tag{4.3.1}$$

with $t \in [0, T]$, is utilised. Within this new frame of reference, all periodicity cells are of a unit size, and the computational domain, $\widehat{\Omega}_\varepsilon = \varepsilon^{-1}\Omega_\varepsilon$, as well as the computational time interval, $[0, \hat{T}] = [0, \varepsilon^{-2}T]$, increased as $\varepsilon \to 0$.

According to the new frame, we reformulated the ε-periodic domain in Section 3.1 of Chapter 3 in the following way:

$$\widehat{\Omega}_\varepsilon = \bigcup_{j \in \mathbb{Z}^2} \widehat{Y}_\varepsilon^j \subset \widehat{\Omega}. \tag{4.3.2}$$

Parameter	Dimensional value and units	References
$L^*_{x_1}$	6.25 cm	Assumed
$L^*_{x_2}$	0.75 cm	Assumed
$l^*_{y_1} = l^*_{y_2}$	250 µm	Assumed
D^*_s	7.5×10^{-10} m^{2}s^{-1}	Pedit et al. [153]
D^*_b	3.2×10^{-11} m^{2}s^{-1}	Pedit et al. [153]
χ^*_0	1.8×10^{-9} m^{2}s^{-1}	Pedit et al. [153]
K^*_d	2.1 mg L^{-1}	Yan et al. [212]
v^*_s	4.8×10^{-5} m s^{-1}	Pedit et al. [153]
K^*_b	1.66×10^{-5} s^{-1}	Yan et al. [212]
$q^*_{\max}$	1.42×10^{-4} (mg substrate/mg cell) s^{-1}	Yan et al. [212]
Y^*	1.79 mg cell/mg substrate	Yan et al. [212]
K^*_s	0.5 mg L^{-1}	Yan et al. [212]
$\mu^*_{\max}$	2.54×10^{-4} s^{-1}	Computed
b^*_{in}	22.3 mg L^{-1}	Yan et al. [212]
s^*_{in}	28.3 mg L^{-1}	Yan et al. [212]
$b^*_{\max}$	50.65 mg L^{-1}	Computed

Table 4.1: *Dimensional parameters of the P. putida G7 bacterial strain, which is known to be attracted to naphthalene (the substrate). Any addition or change in the parameter values will be highlighted in the text.*

For simplicity, we assumed a domain consisting of $N \times M$ periodic units, such that both N and M are integer numbers defined by:

$$\begin{cases} N = \varepsilon^{-1} L_{x_1}, \\ M = \varepsilon^{-1} L_{x_2}. \end{cases} \tag{4.3.3}$$

The periodicity of the domain in the new frame is defined by linear translations using:

$$\widehat{Y}^j_\varepsilon = \left(Y^0 + j\right), \tag{4.3.4}$$

where $j \in \mathbb{Z}^2$ and $Y^0 \subset Y = [0,1]^2$ (Figure 4.3). It should be noted that the periodic units Y and Y^0 are the same as those listed in Section 3.1. Hereafter, all quantities are denoted using a hat, and for any periodic function, $u_\varepsilon(t, \mathbf{x})$, defined on $[0,T] \times \Omega_\varepsilon$, we introduce a rescaled function, $\hat{u}_\varepsilon(\tau, \mathbf{y})$, defined on $[0, \hat{T}] \times \widehat{\Omega}_\varepsilon$, as:

$$\hat{u}_\varepsilon(\tau, \mathbf{y}) = u_\varepsilon(\varepsilon^2 \tau, \varepsilon \mathbf{y}) = u_\varepsilon(t, \mathbf{x}), \tag{4.3.5}$$

which satisfies the following relations

$$\begin{cases} \nabla_{\mathbf{y}} \hat{u}_\varepsilon(\tau, \mathbf{y}) = \varepsilon \nabla_{\mathbf{x}} u_\varepsilon(\varepsilon^2 \tau, \varepsilon \mathbf{y}) = \varepsilon \nabla_{\mathbf{x}} u_\varepsilon(t, \mathbf{x}), \\ \dfrac{\partial \hat{u}_\varepsilon(\tau, \mathbf{y})}{\partial \tau} = \varepsilon^2 \dfrac{\partial u_\varepsilon(\varepsilon^2 \tau, \varepsilon \mathbf{y})}{\partial t} = \varepsilon^2 \dfrac{\partial u_\varepsilon(t, \mathbf{x})}{\partial t}. \end{cases} \tag{4.3.6}$$

Parameter	Definition	Value
ε	$l_{y_1^*}/L_{x_1^*}$	4×10^{-3}
δ	D_b^*/D_s^*	0.04267
Da	$\mu_{\max}^* L_{x_1^*}^2/D_s^*$	112.18
ω	$K_b^*/\mu_{\max}^*$	0.065
κ_c	$(1-\omega)\big(b_{\max}^*/b_{in}^*\big)$	2.12
κ_b	$K_b L_{x_1}^2/D_s^*$	7.33
κ_d	K_d/s_{in}^*	-
κ_s	K_s/s_{in}^*	-
Pe_b	$v_s L_{x_1^*}/D_s^*$	4×10^3
χ_0	$\chi_0^*/(3v_s L_{x_1^*})$	2×10^{-4}
Υ_0	$\chi_0^*/(2v_s L_{x_1^*})$	1×10^{-3}
λ	$\mathrm{Pe}_b\chi_0$	0.8
Y	$Y^*\big(s_{in}^*/b_{in}^*\big)$	2.27
b_{in}		1
s_{in}		1

Table 4.2: *Computed dimensionless parameter values according to Table 4.1. Any addition or changes to the listed parameter values will be highlighted in the text.*

Lastly, the periodic flow velocity is rescaled as:

$$\hat{\mathbf{v}}(\mathbf{y}) = \mathbf{v}(\varepsilon\mathbf{y}) = \mathbf{v}(\mathbf{x}). \tag{4.3.7}$$

Therefore, our model of interest can be redefined on $[0, \widehat{T}] \times \widehat{\Omega}_\varepsilon$, and is rewritten (after dropping the subscript $\mathbf{y}$) as:

$$\frac{\partial \hat{s}_\varepsilon}{\partial \tau} = \nabla \cdot (\nabla \hat{s}_\varepsilon - \widehat{\mathrm{Pe}}\, \hat{\mathbf{v}}_\varepsilon) - \frac{\widehat{\mathrm{Da}}}{Y} \frac{\hat{s}_\varepsilon}{\hat{s}_\varepsilon + \kappa_s} \hat{b}_\varepsilon \qquad \text{in } [0, \hat{T}] \times \widehat{\Omega}_\varepsilon, \tag{4.3.8a}$$

$$\begin{aligned} \frac{\partial \hat{b}_\varepsilon}{\partial \tau} = {} & \nabla \cdot (\delta \nabla \hat{b}_\varepsilon - [\widehat{\mathrm{Pe}}\, \hat{\mathbf{v}}_\varepsilon + \widehat{\mathrm{Pe}}_b \chi(\hat{s}_\varepsilon) \nabla \hat{s}_\varepsilon] \hat{b}_\varepsilon) \\ & + \widehat{\mathrm{Da}}\, \frac{\hat{s}_\varepsilon}{\hat{s}_\varepsilon + \kappa_s} \left(1 - \frac{\hat{b}_\varepsilon}{\kappa_c}\right) \hat{b}_\varepsilon - \widehat{\kappa}_b \hat{b}_\varepsilon \qquad \text{in } [0, \hat{T}] \times \widehat{\Omega}_\varepsilon. \end{aligned} \tag{4.3.8b}$$

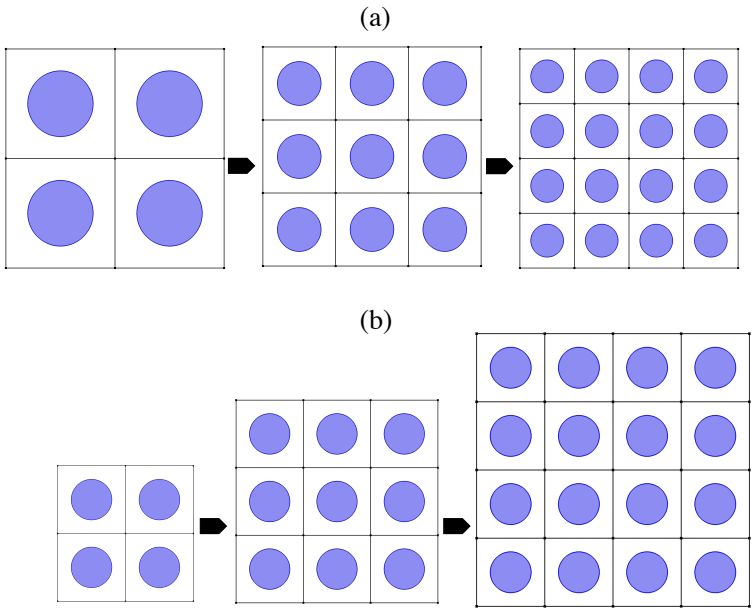


Figure 4.2: *Schematic illustration adapted from [10] showing in (a) the standard homogenisation in a fixed domain Ω_ε and in (b) the rescaled homogenisation process with a constant periodicity cell and increasing domain $\widehat{\Omega}_\varepsilon = \varepsilon^{-1}\Omega_\varepsilon$.*

In addition, the non-dimensional parameters are rescaled as:

$$\widehat{\mathrm{Pe}} = \varepsilon\,\mathrm{Pe}, \qquad \widehat{\mathrm{Pe}_\mathrm{b}} = \varepsilon\,\mathrm{Pe}_\mathrm{b} \qquad \widehat{\mathrm{Da}} = \varepsilon^2\,\mathrm{Da}, \qquad \widehat{\kappa_b} = \varepsilon^2\kappa_b. \tag{4.3.9}$$

The no-flux boundary conditions at the solid–aqueous interface, $\partial\Sigma^0$, are expressed as:

$$-\mathbf{n}\cdot(\nabla\hat{s}_\varepsilon) = -\mathbf{n}\cdot\left(\delta\nabla\hat{b}_\varepsilon\right) = 0. \tag{4.3.10}$$

The three limiting cases are classifies in the new reference frame as:

$$\begin{cases} \widehat{\mathrm{Pe}} \sim \mathcal{O}(\varepsilon^2) & \Longleftrightarrow \quad \mathrm{Pe} \sim \mathcal{O}(\varepsilon) \\ \widehat{\mathrm{Pe}} \sim \mathcal{O}(\varepsilon) & \Longleftrightarrow \quad \mathrm{Pe} \sim \mathcal{O}(\varepsilon^0), \\ \widehat{\mathrm{Pe}} \sim \mathcal{O}(\varepsilon^0) & \Longleftrightarrow \quad \mathrm{Pe} \sim \mathcal{O}(\varepsilon^{-1}). \end{cases} \tag{4.3.11}$$

It should be noted that the homogenisation developed in Chapter 3 is invariant under the proposed change of variable. In the subsequent sections, we reformulate the homogenised models presented in Chapter 3 according to the different limiting cases.

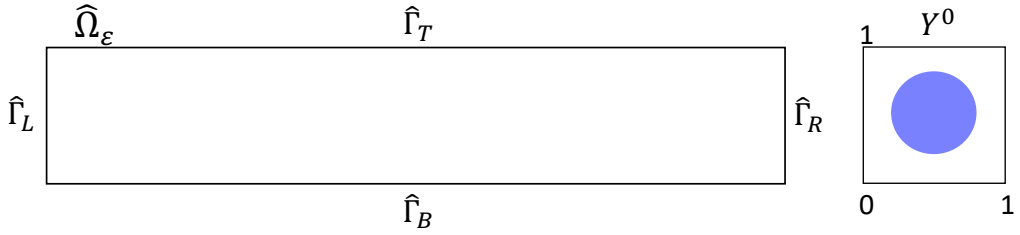


Figure 4.3: *Schematic sketch of the domain using the new reference frame* $\widehat{\Omega}_\varepsilon$ *where* $\widehat{\Gamma}_s = \varepsilon^{-1}\Gamma_s$ *and* $\widehat{\Gamma} = \varepsilon^{-1}\Gamma$. *The domain consists of* $M \times N = 30 \times 25$ *periodic unit cells* $\widehat{Y}_\varepsilon$, *where each cell is a translation of the unit cell* Y^0;

The rest of this chapter focuses on the numerical simulation of the related effective (upscaled) models in Chapter 2. Primarily, we seek to investigate the various aspects that influence the formation of chemotactic travelling wave solutions, and validating the model whenever possible.

4.4 Numerical Investigations

In this section, we perform a series of numerical simulations. Furthermore, when feasible, direct simulations of the periodic porous structure were performed. All the numerical simulation results are generated using the finite element simulation software COMSOL Multiphysics™(version 5.3a). A mesh refinement procedure is used in all of the simulations to verify that the simulation results are numerically stable.

4.4.1 Immobile Aqueous Phase

Microbial transport in an immobile aqueous phase is relevant in the bioremediation field. Typically, the underground flow is very slow (e.g. 1 ft/year) [14], and even when the rate of movement of the underground water is higher, the bacteria may be drawn to stagnant flow regions. In this case study, we assume that the effects of the medium flow at the pore scale are negligible. It should be noted that the case study considered in this section describes bacterial population chemotactic flow triggered by chemical gradients which are generated by the metabolic consumption of the population.

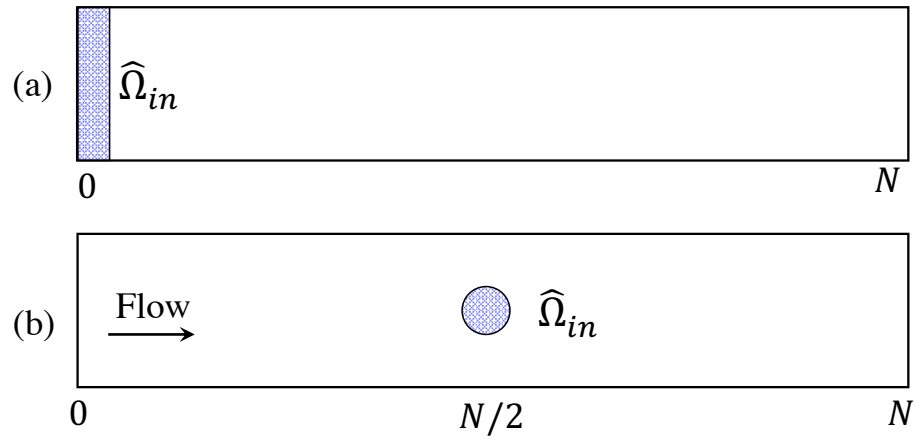


Figure 4.4: *Schematic sketch showing the initial bacteria concentrations injected into $\widehat{\Omega}_{in}$. (a) represents the case study when we assume an immobile aqueous phase, and (b) the case study when we assume a mobile aqueous phase. The dimensionless length and diameter of the initial injections is set as* 20.

4.4.1.1 The Homogenised Model

Here, $\widehat{\mathrm{Pe}} \sim \mathcal{O}(\varepsilon^2)$, which corresponds to the work in Section 3.4, Chapter 3. As previously discussed, we can obtain the following effective model when rescaling:

$$\frac{\partial \hat{\mathcal{S}}}{\partial \tau} = \nabla \cdot \left(\mathbf{D}^h \nabla \hat{\mathcal{S}}\right) - \frac{\widehat{\mathrm{Da}}}{Y} \frac{\hat{\mathcal{S}}}{\hat{\mathcal{S}} + \kappa_s} \hat{\mathcal{B}}, \tag{4.4.1a}$$

$$\frac{\partial \hat{\mathcal{B}}}{\partial \tau} = \nabla \cdot \left(\delta \mathbf{D}^h \nabla \hat{\mathcal{B}} - \left\{\widehat{\mathrm{Pe}}_b \left\{\mathbf{D}^h \chi(\hat{\mathcal{S}}) \nabla \hat{\mathcal{S}}\right\}\right\} \hat{\mathcal{B}}\right) + \widehat{\mathrm{Da}} \frac{\hat{\mathcal{S}}}{\hat{\mathcal{S}} + \kappa_s} \left(1 - \frac{\hat{\mathcal{B}}}{\kappa_c}\right) \hat{\mathcal{B}} - \widehat{\kappa}_b \hat{\mathcal{B}}, \tag{4.4.1b}$$

for all $(\tau, \mathbf{y}) \in [0, \hat{T}] \times \widehat{\Omega}_\varepsilon$. We close the model using no-flux external boundary conditions at $\widehat{\Gamma}_L$ and $\widehat{\Gamma}_R$:

$$\widehat{H}_s(\mathbf{y}, \hat{\mathcal{S}}, \hat{\mathcal{B}}) = \widehat{H}_b(\mathbf{y}, \hat{\mathcal{S}}, \hat{\mathcal{B}}) = 0. \tag{4.4.2}$$

For the initial bacterial concentration, we assume that it to be injected into the locations shown in Figure 4.4. In the subsequent simulations, we assume that $\phi = 0.45$. Note that the homogenised chemotactic velocity is written as:

$$\hat{\mathbf{v}}_0^c = \widehat{\mathrm{Pe}}_b \left\{\chi(\hat{\mathcal{S}}) \nabla \hat{\mathcal{S}}\right\}, \tag{4.4.3}$$

Porosity (ϕ)	0.35	0.45	0.55	0.65	0.75	0.85
D^h	0.524	0.615	0.679	0.738	0.799	0.869

Table 4.3: *Some values of the effective diffusion parameters, D^h, computed by assuming Y^0 as in Figure 4.3 for different porosities.*

For the sensitivity function, we have the homogenised receptor sensitivity function,

$$\chi(\hat{\mathcal{S}}) = \chi_0 \frac{\kappa_d}{(\hat{\mathcal{S}} + \kappa_d)^2}, \tag{4.4.4}$$

with the parameter values given in Table 4.2.

4.4.1.2 Effective Diffusion Tensors

We computed the effective diffusion tensors using the *cell-problem* in Eqs.(3.4.13), stated in Section 3.4 of Chapter 3, on Y^0 at a fixed porosity, ϕ. The computed effective diffusion tensors are diagonal, that is,

$$\mathbf{D}^h = D^h \mathbf{I}, \tag{4.4.5}$$

where $\mathbf{I}$ is an identity tensor. The only parameter affecting $\mathbf{D}^h$ is the porosity, ϕ. As illustrated in Table 4.3, the effective diffusion increases with increasing porosity.

4.4.1.3 Effects of Growth Kinetics

For the first numerical investigation, we excluded the bacterial growth and decay rates, and thus in effective model we set,

$$\widehat{\mathrm{Da}} \frac{\hat{\mathcal{S}}}{\hat{\mathcal{S}} + \kappa_s} \left(1 - \frac{\hat{\mathcal{B}}}{\kappa_c}\right) \hat{\mathcal{B}} - \widehat{\kappa}_b \hat{\mathcal{B}} \sim 0. \tag{4.4.6}$$

To demonstrate the evolution of the bacterial waves, we plotted 1D advancing bacterial wave solutions at the domain centreline. The advancing bands in Figure 4.5 can be observed to dissipate rapidly while leaving a microbial density tailing behind close to the initial injection location. When $\delta \sim 0.04$, which corresponds to the substrate diffusion coefficient: $D_s^* = 7.5 \times 10^{-10}$ [m^2/s], the results revealed that the population is less likely to drift away in search of energy sources in the absence of population growth.

Similar to the simulations in Yan and Hilpert [211], when $\delta \sim 0.4$, that is, $D_s^* = 7.5 \times 10^{-11}$ [m^2/s], we observe in Figure 4.6 that the population travelled a longer distance in shorter times, indicating an increase in the wave speed. Consequently, an enhancement in the substrate removal is observed compared to when

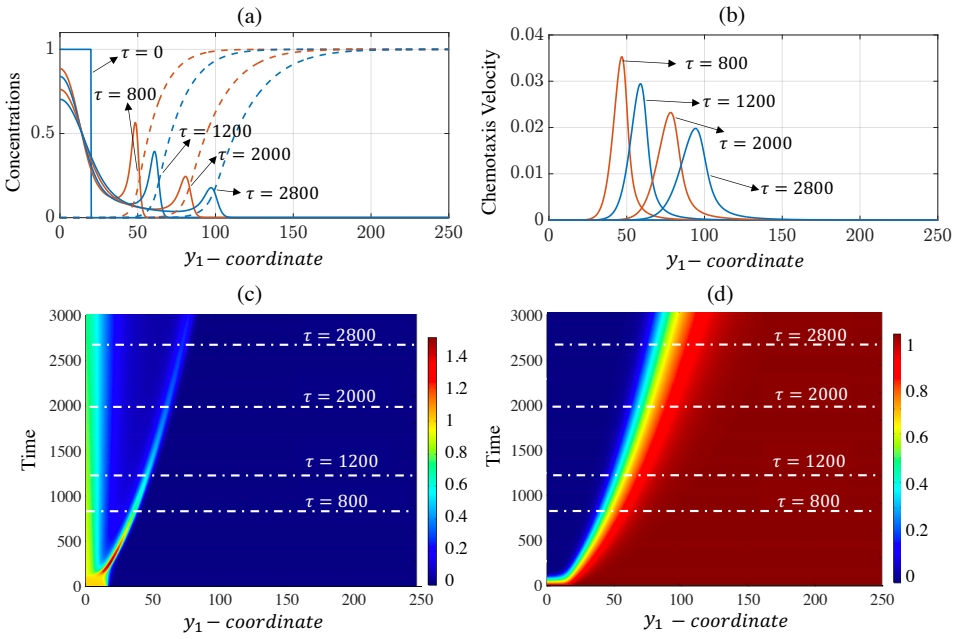


Figure 4.5: *Plots showing the simulation results for the model in Eqs.*(4.4.1) *assuming the absence of growth/decay kinetics with the relevant parameters in Table 4.2. In (a) we give a one-dimensional (1D) bacteria traveling wave solution (solid lines) and the substrate fronts (dashed lines) plotted at* $\tau = 0,\ 800,\ 1200,\ 2000,\ 2800$. *In (b) we plotted the profiles of the chemotactic velocity given in Eq.*(4.4.3) *at* $\tau = 800,\ 1200,\ 2000,\ 2800$. *The plot in (c) shows the time evolution of 1D bacterial traveling bands and in (d) the plot shows the time evolution of 1D substrate fronts. The dashed lines in (c) and (d) corresponds to the travelling waves plotted in (a) at* $\tau = 0,\ 800,\ 1200,\ 2000,\ 2800$.

$\delta \sim 0.04$ is used. These results indicate that uptake alone can sufficiently generate sustainable gradient concentrations to achieve travelling waves covering the entire domain when the substrate diffusion is on the same order as the bacterial motility. However, substrate diffusion generally is one order of magnitude less than bacterial motility.

To understand how the consumption rate and substrate diffusivity influence the formation of chemotactic travelling wave solutions, we estimate their effects on the chemotactic drift. Without loss of generality, we assumed that the bacterial waves follows the trail of the front of the substrate concentration $s^*_{\min}$, and that the concentration is sufficient for bacterial to consume to survive, such that

$$s^*_{\min} \ll K^*_s \qquad \text{and} \qquad s^*_{\min} \ll K^*_d, \tag{4.4.7}$$

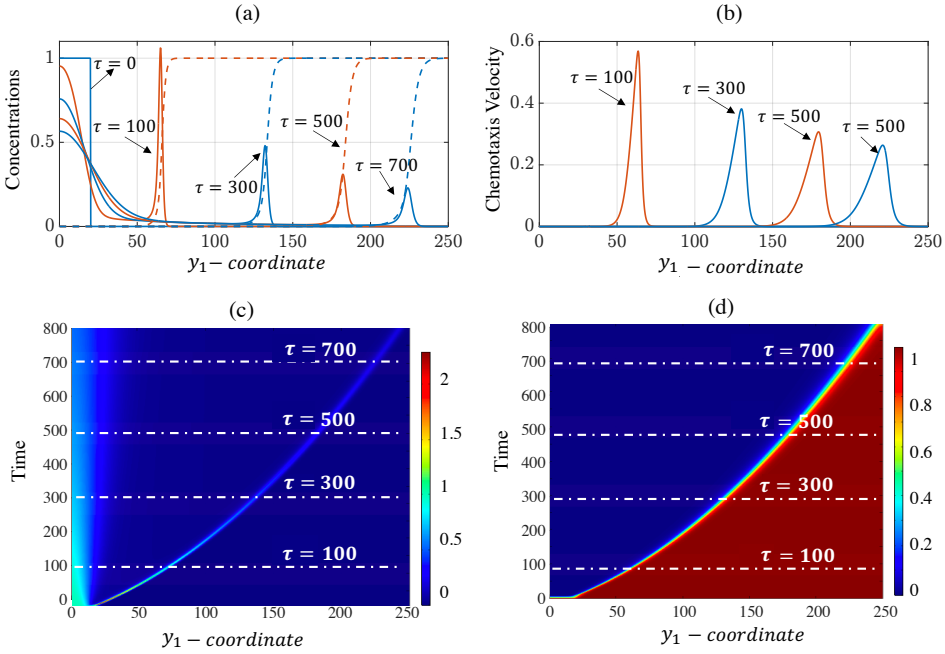


Figure 4.6: *Results of the simulations of the same model in Figure 4.5 for* $\delta = 0.4$. *In (a) we show the one-dimensional (1D) bacteria bands (solid lines) and the substrate fronts (dashed lines) plotted at* $\tau = 0,\ 100,\ 300,\ 500,\ 700$. *In (b) we plotted the profiles of the chemotactic velocity at* $\tau = 100,\ 300,\ 500,\ 700$ *for the same chemotactic velocity used in Figure 4.5. In (c) we plotted the time evolution of 1D bacterial traveling wave solutions (bands) and in (d) we plotted the time evolution of 1D substrate fronts. The dashed lines in (c) and (d) corresponds to the travelling waves plotted in (a) at* $\tau = 100,\ 300,\ 500,\ 700$.

where K_s^* and K_b^* are the Michaelis constant and the receptor saturation constant, respectively. Then, from (4.4.7) we have constant chemotactic sensitivity function and the linear uptake rate:

$$\chi^*(s^*_{\min}) = \bar{\chi}^*_0, \quad \text{and} \quad k_s^*(s^*) \sim k^*_{\min} s^*_{\min}, \tag{4.4.8}$$

where $\bar{\chi}^*_0 \sim \chi^*_0/K^*_d$ (Table 2.1) and $k^*_{\min}$ $[\mathrm{s}^{-1}]$ is set as:

$$k^*_{\min} \sim \frac{\mu^*_{\max}}{K^*_s Y^*} b^*_{in}. \tag{4.4.9}$$

Assuming a non-porous medium, the uptake rate in Eq.(4.4.9) generates mass flow, which can be defined as

$$V^*_{\min} \sim s^*_{\min} \sqrt{k^*_{\min} D^*_s}, \tag{4.4.10}$$

where $V^*_{\min}$ [m s^{-1}mg L^{-1}(substrate)]. Thus, the substrate concentration fluxes can be approximated using

$$\nabla^* s^* \sim \frac{V^*_{\min}}{D^*_s}. \tag{4.4.11}$$

Lastly, the strength of the chemotactic velocity is estimated using the following chemotactic Péclet–like number approximated as:

$$\widehat{\mathrm{Pe}}_\chi \sim \frac{\bar{\chi}^*_0 V^*_{\min} L^*_{x_1^*}}{D^*_s D^*_b}. \tag{4.4.12}$$

Therefore, at a low substrate concentration $s^*_{\min} = 0.01 \ll K^*_s$, we have

$$\delta = 0.04 \Longrightarrow \widehat{\mathrm{Pe}}_\chi \sim 0.06, \tag{4.4.13}$$

$$\delta = 0.4 \quad \Longrightarrow \widehat{\mathrm{Pe}}_\chi \sim 0.6. \tag{4.4.14}$$

This indicates that a slower substrate diffusion enhances the strength of the chemotactic drifts, or equivalently, the chemotactic drift mechanism enhanced the bioavailability of the substrate.

However, the random motility rate is generally one order of magnitude less than the diffusivity of most dissolved chemicals, and thus this argument is nonrealistic. Eqs.(4.4.7)–(4.4.12) suggest that the chemotactic strength can be increased by increasing the initial density of the population, which can be achieved by including the growth kinetics, which we can see in Figure 4.7. The plots of the simulations of the full model in Figure 4.7 generated travelling wave solutions at a constant speed with a higher peak values, despite the fact that the chemotactic velocities plotted in Figure 4.7(b) are slower than those in Figure 4.6(b). This suggests that the enhancement in the qualitative and quantitative properties of the travelling wave can be attributed to the combined contributions from both the chemotactic and growth mechanisms.

4.4.1.4 Effects of Chemotaxis Drift

By neglecting the chemotactic drift (i.e., $\chi_0 = 0$), we obtained a model closely related to Fisher–Kolmogorov–Petrovsky–Piskunov equation (F-KPP) [141]. We simulated the F-KPP-like model and compared the obtained travelling wave solution plotted in Figure 4.8(b) to the chemotactic wave solution in Figure 4.7(a). The chemotactic wave solutions appear to be faster, and exhibited higher peak values and sharp fronts compared to the F-KPP wave solutions. It should be noted that the exclusion of both chemotactic drift and logistic growth terms inhibited the formation of travelling waves, as it is demonstrated in Figure 4.8(a) where the density diffuses near the initial injection site. In contrast, chemotactic models can generate travelling waves solution in the absence of the logistic term, as reported in Yan and Hilpert [211] and Yan et al. [212]. Furthermore, in their study they estimated the effective diffusion coefficients by Taylor dispersion theory in the tube.

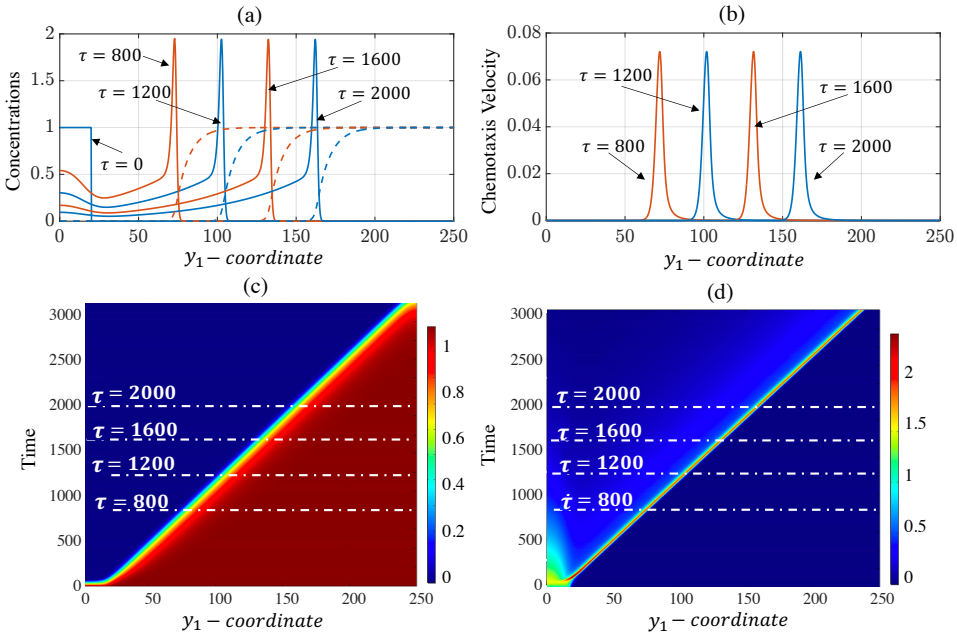


Figure 4.7: *Simulation plots of the full model given in Eqs.*(4.4.1) *with the growth/decay kinetics for the parameters given in Table 4.2, where* $\delta = 0.04$. *The plots in (a) show the bacterial chemotactic bands (solid lines) and substrate fronts (dashed lines) plotted at* $\tau = 0,\ 800,\ 1200,\ 2000,\ 2800$, *(b) chemotactic velocity plotted at* $\tau = 800,\ 1200,\ 2000,\ 2800$. *In (c) and (d) plots show the time evolution of the 1D bacterial waves and 1D substrate fronts, respectively. The dashed lines in (c) and (d) corresponds with the bacterial bands and substrate waves in (a).*

4.4.1.5 Initial Substrate Concentration Effects

From a strictly mathematical perspective, the carrying capacity parameter value, κ_c, bounds the microbial density; thus, the logistic term serves as a competitive inhibition bounding the microbial density growth. But, it can also highlight how the initial substrate concentration influences the buildup of biomass in the domain. Recall that

$$\begin{cases} K_c^* \ \sim (1-\omega) b_{\max}^*, \\ b_{\max}^* \sim Y^* s_{in}^*, \end{cases} \tag{4.4.15}$$

where $\omega = K_b^*/\mu_{\max}^*$ (refer to Eq.(2.3.26) and Eq.(2.3.28) in Section 2.3, Chapter 2). Therefore, any decrease in the initial concentration of the substrate results in a decrease in $b_{\max}^*$. Thus, by substituting $b_{\max}^*$ for b_{in}^* in Eqs.(4.4.7)–(4.4.12), we deduce that decreasing the initial substrate concentration decreases the chemotaxis effects,

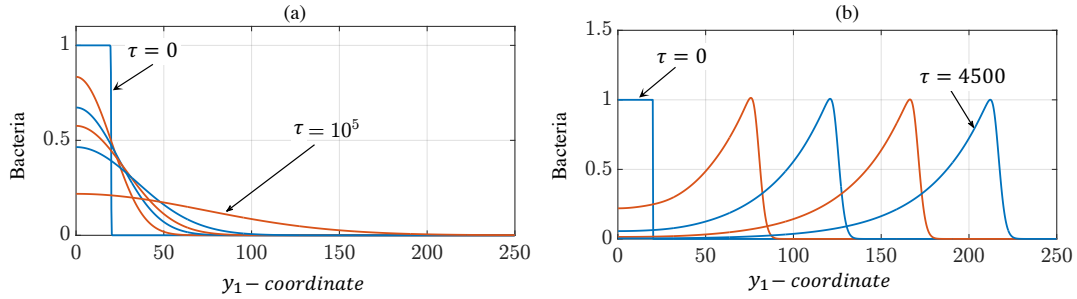


Figure 4.8: *Using the parameter values in Table 4.2, in (a) we show the simulation results of the effective chemotactic model in Eqs.*(4.4.1) *in the absence of any metabolic rates, and in (b) we show the propagating Fisher–Kolmogorov–Petrovsky–Piskunov equation (F-KPP) waves obtained when* $\chi_0 = 0$ *in Eqs.*(4.4.1).

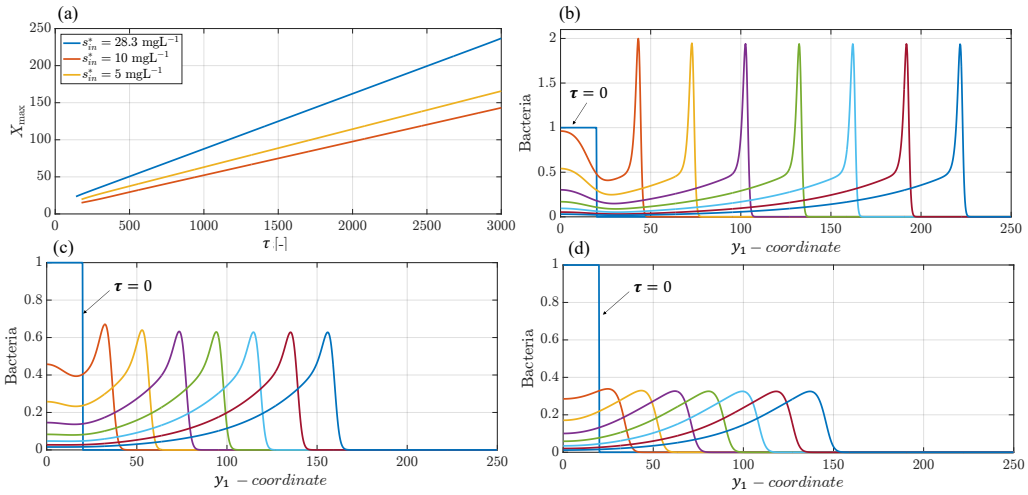


Figure 4.9: *Plots showing the chemotactic bacterial bands for the full chemotactic model Eqs.*(4.4.1)*, including the growth/decay kinetics assuming the parameter values in Table 4.2. (a) Wave speeds for the three initial concentrations plotted for the same time interval. The wave speeds in (a) were plotted by tracking the position of position of the band peak against time* τ*. In (b) we plotted the travelling bacterial bands when* $s^*_{in} = 28.3$ [mgL^{-1}]*, (c) when* $s^*_{in} = 10$ [mgL^{-1}]*, and (d) when* $s^*_{in} = 5$ [mgL^{-1}].

thus affecting the qualitative properties of the travelling wave solutions. The travelling wave solution plots in Figure 4.9 illustrate the correlation between the decreased initial concentration values and the decreased speed and peak values.

4.4.2 Mobile Aqueous Phase

The Darcy flow presented in Section 3.2, Chapter 3 is used to calculate the local flow $\hat{\mathbf{v}}_0(\mathbf{y})$ and the pore-averaged flow $\langle\hat{\mathbf{v}}_0\rangle_{Y^0}$. Under the new reference frame, the effective model is expressed as:

$$\frac{\partial\hat{\mathcal{S}}}{\partial\tau} = \nabla\cdot\left(\mathbb{D}_s\nabla\hat{\mathcal{S}} - \widehat{\mathrm{Pe}}\langle\hat{\mathbf{v}}_0\rangle_{Y^0}\hat{\mathcal{S}}\right) - \frac{\widehat{\mathrm{Da}}}{Y}\frac{\hat{\mathcal{S}}}{\hat{\mathcal{S}}+\kappa_s}\hat{\mathcal{B}} \tag{4.4.16a}$$

$$\begin{aligned}\frac{\partial\hat{\mathcal{B}}}{\partial\tau} = \nabla\cdot\Big(\mathbb{D}_b\nabla\hat{\mathcal{B}} - \big[\widehat{\mathrm{Pe}}\langle\hat{\mathbf{v}}_0\rangle_{Y^0} + \widehat{\mathrm{Pe}}_b\Big\{\mathbb{D}^{\mathrm{ch}}\chi(\hat{\mathcal{S}})\nabla\hat{\mathcal{S}}\Big\}\big]\hat{\mathcal{B}}\Big)\\ + \widehat{\mathrm{Da}}\frac{\hat{\mathcal{S}}}{\hat{\mathcal{S}}+\kappa_s}\left(1-\frac{\hat{\mathcal{B}}}{\kappa_c}\right)\hat{\mathcal{B}} - \widehat{\kappa_b}\hat{\mathcal{B}}.\end{aligned} \tag{4.4.16b}$$

The effective tensors in Eqs.(4.4.16) are as defined in Chapter 3 according to the remaining two limiting cases. We close the effective model by defining the initial concentrations and the external boundary conditions. As before, the initial substrate concentration is uniformly distributed throughout the domain. The initial bacteria concentration occupies a circular subdomain $\widehat{\Omega}_{in}$ of radius $\hat{r}\sim 10$ (Figure 4.4(b)). At $\widehat{\Gamma}_L$ and $\widehat{\Gamma}_R$, we assign periodic boundary conditions such that the observed domain is expanded by translations in the axial direction (flow direction). The periodic conditions described are written in terms of the new coordinates as:

$$-\mathbf{n}\cdot(\mathbb{D}_s\nabla\hat{\mathcal{S}} - \widehat{\mathrm{Pe}}\langle\hat{\mathbf{v}}_0\rangle_{Y^0}\hat{\mathcal{S}})|_{\widehat{\Gamma}_L} = \hat{H}_s(\mathbf{y},\hat{\mathcal{S}},\hat{\mathcal{B}})|_{\widehat{\Gamma}_R}, \tag{4.4.17a}$$

$$-\mathbf{n}\cdot(\mathbb{D}_b\nabla\hat{\mathcal{B}} - [\widehat{\mathrm{Pe}}\langle\hat{\mathbf{v}}_0\rangle_{Y^0} + \widehat{\mathrm{Pe}}_b\big\{\mathbb{D}^{\mathrm{ch}}\chi(\hat{\mathcal{S}})\nabla\hat{\hat{\mathcal{S}}}\big\}]\hat{\mathcal{B}})|_{\widehat{\Gamma}_L} = \hat{H}_b(\mathbf{y},\hat{\mathcal{S}},\hat{\mathcal{B}})|_{\widehat{\Gamma}_R}. \tag{4.4.17b}$$

The right-hand side of (4.4.17) is expressed as:

$$\hat{H}_s(\mathbf{y},\hat{\mathcal{S}},\hat{\mathcal{B}}) = \mathbf{n}\cdot(\mathbb{D}_s\nabla\hat{\mathcal{S}} - \widehat{\mathrm{Pe}}\langle\hat{\mathbf{v}}_0\rangle_{Y^0}\hat{\mathcal{S}}), \tag{4.4.18}$$

$$\hat{H}_b(\mathbf{y},\hat{\mathcal{S}},\hat{\mathcal{B}}) = \mathbf{n}\cdot(\mathbb{D}_b\nabla\hat{\mathcal{B}} - [\widehat{\mathrm{Pe}}\langle\hat{\mathbf{v}}_0\rangle_{Y^0} + \widehat{\mathrm{Pe}}_b\big\{\mathbb{D}^{\mathrm{ch}}\chi(\hat{\mathcal{S}})\nabla\hat{\mathcal{S}}\big\}]\hat{\mathcal{B}}). \tag{4.4.19}$$

For continuity, the concentrations are set as:

$$\hat{\mathcal{S}}(\tau,\mathbf{y})|_{\widehat{\Gamma}_L} = \hat{\mathcal{S}}(\tau,\mathbf{y})|_{\widehat{\Gamma}_R}, \qquad \text{and} \qquad \hat{\mathcal{B}}(\tau,\mathbf{y})|_{\widehat{\Gamma}_L} = \hat{\mathcal{B}}(\tau,\mathbf{y})|_{\widehat{\Gamma}_R}. \tag{4.4.20}$$

The effective flow conditions at the inlet and outlet is expressed as:

$$-\mathbf{n}\cdot\langle\hat{\mathbf{v}}_0\rangle_{Y^0}|_{\widehat{\Gamma}_L} = \mathbf{n}\cdot\langle\hat{\mathbf{v}}_0\rangle_{Y^0}|_{\widehat{\Gamma}_R}, \qquad \text{and} \qquad -\langle\hat{\mathbf{v}}_0\rangle_{Y^0}|_{\widehat{\Gamma}_L} = \langle\hat{\mathbf{v}}_0\rangle_{Y^0}|_{\widehat{\Gamma}_R}. \tag{4.4.21}$$

As mentioned previously (see Remark 3.8 in Section 3.6 of Chapter 3), the natural scaling of the Péclet number in infinite cylinders is $\mathrm{Pe}\sim\mathcal{O}(\varepsilon^{-1})$. Hence, in the new reference frame, it is equivalent to $\widehat{\mathrm{Pe}}\geq\mathcal{O}(\varepsilon^0)$; otherwise, we assume that we are dealing with an advection–diffusion regime.

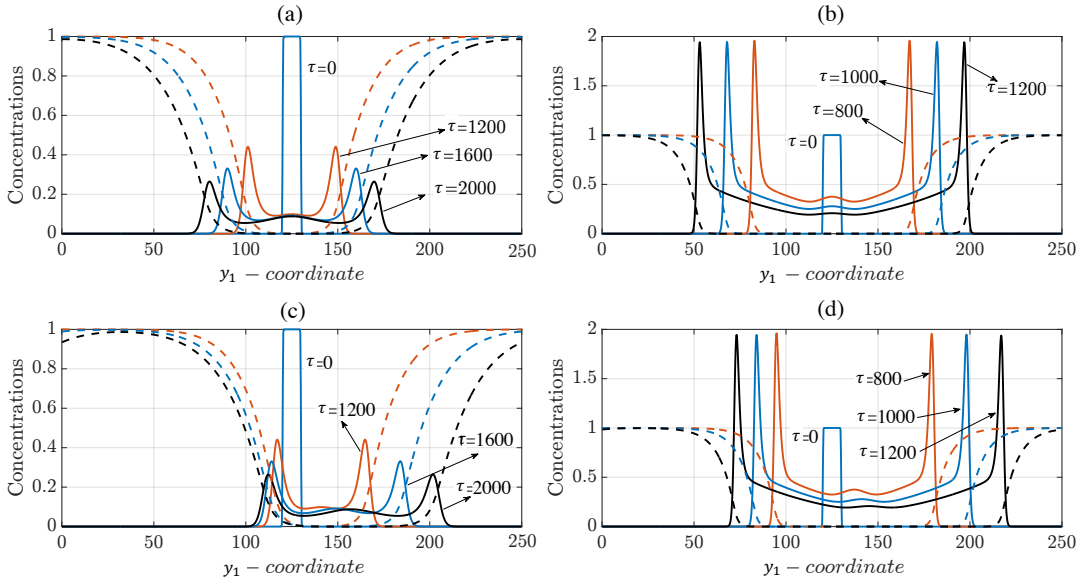


Figure 4.10: *Plots showing the simulation results of the model described in Section 4.4.2 of the chemotactic bacterial waves (solid lines) and the substrate (dashed lines) in stagnant flow (a) when no growth/decay kinetics were considered and (b) when growth/decay kinetics were considered at* $\tau = 0,\ 800,\ 1000,\ 1200$. *The plots in (c) and (d) are repeated simulation results when* $\widehat{\mathrm{Pe}} = 0.02$ *at* $\tau = 0,\ 800,\ 1000,\ 1200$. *Note that the parameters given in Table 4.2 were used.*

4.4.2.1 Advection–Diffusion Regime

When there is an advection–diffusion regime, the effective model shown in Section 3.5, Chapter 3, is applied by letting

$$\mathbb{D}_s := \mathbf{D}^h, \qquad \mathbb{D}_b := \delta \mathbf{D}^h, \qquad \mathbb{D}^{\mathrm{ch}} := \mathbf{D}^h, \tag{4.4.22}$$

where $\mathbf{D}^h$ is the same effective diffusion tensor computed in Eq.(4.4.5). Next, we simulate the effective model for $\widehat{\mathrm{Pe}} = 0.02,\ 0.1$. For better visualisation of the effect of flow on the travelling band, we compare between the two numerical simulations when assuming an immobile aqueous phase and in an advective flow. The plots in Figure 4.10(a) and (b), in the absence of flow, show the microbial density splitting into two travelling peaks moving downstream and upstream. As expected, the exclusion of the growth term resulted in the generation of slower travelling bands that dissipated rapidly (Figure 4.10(a)) when compared to the behaviour observed during the simulation of the full model (Figure 4.10(b)). Moreover, the full model simulation generates travelling bands that move faster with higher density peaks. On the

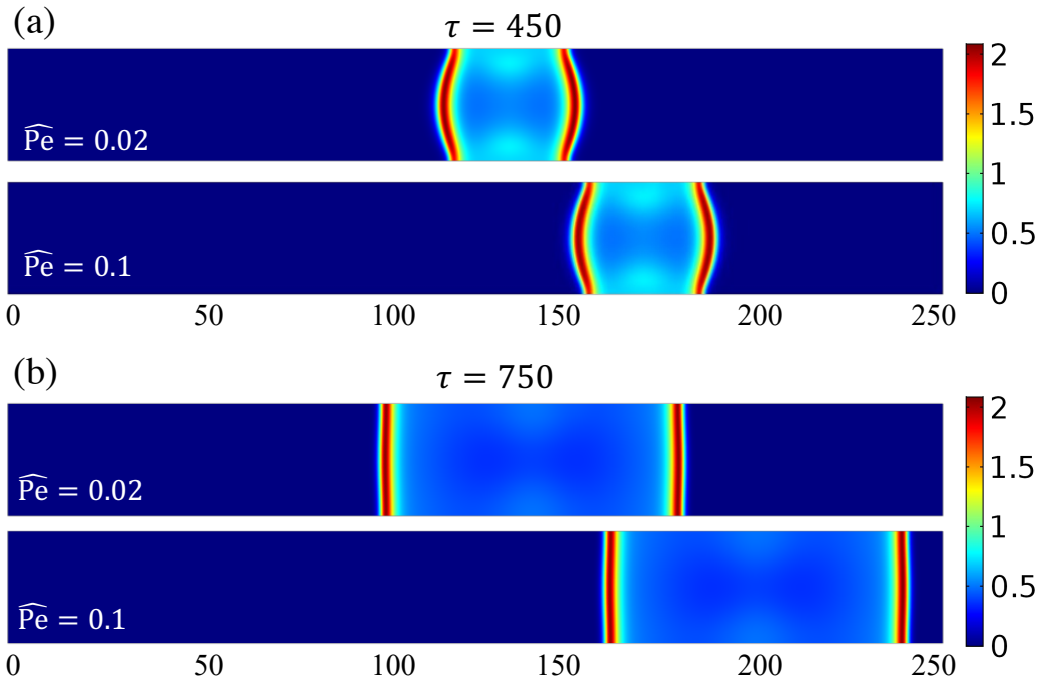


Figure 4.11: *Numerical simulations for the full effective model in Eqs.*(4.3.8) *and Eqs.*(4.3.10) *when (a)* $\widehat{\mathrm{Pe}} = 0.02$ *and (b)* $\widehat{\mathrm{Pe}} = 0.1$ *at* $\tau = 450,\ 750$. *Note that the plots here are 2D visualisation of the bacteria bands given in Figure 4.10(c) and (d).*

other hand, the plots in Figure 4.10(c) and (d) show that the flow simply carries the travelling bands, where the bands appear to be translated by the same distance in the direction of the flow.

The plots in Figure 4.11 show a two-dimensional illustration of the behaviour of the travelling bands under the effects of the two flow regimes: $\widehat{\mathrm{Pe}} = 0.02$ and $\widehat{\mathrm{Pe}} = 0.1$. We observe that the density profiles plotted at the same time, $t = 450, 750$, were identical in shape regardless of the flow velocity values. Thus, we conclude that in such advective-diffusion regimes, chemotactic bands are invariant under uniform flow. This observed Galilean invariance behaviour of the chemotactic waves has been reported in Yan and Hilpert [211].

4.4.2.2 Advection–Dispersion Regimes

When $\widehat{\mathrm{Pe}} \geq 1$, we have the effective model developed in Section 3.6, Chapter 3. Therefore, we assign

$$\mathbb{D}_s := \mathbf{D}^{\mathrm{dis}}, \qquad \mathbb{D}_b := \bar{\mathbf{D}}^{\mathrm{dis}}, \qquad \mathbb{D}^{\mathrm{ch}} := \mathbf{D}^{\mathrm{ch}}. \tag{4.4.23}$$

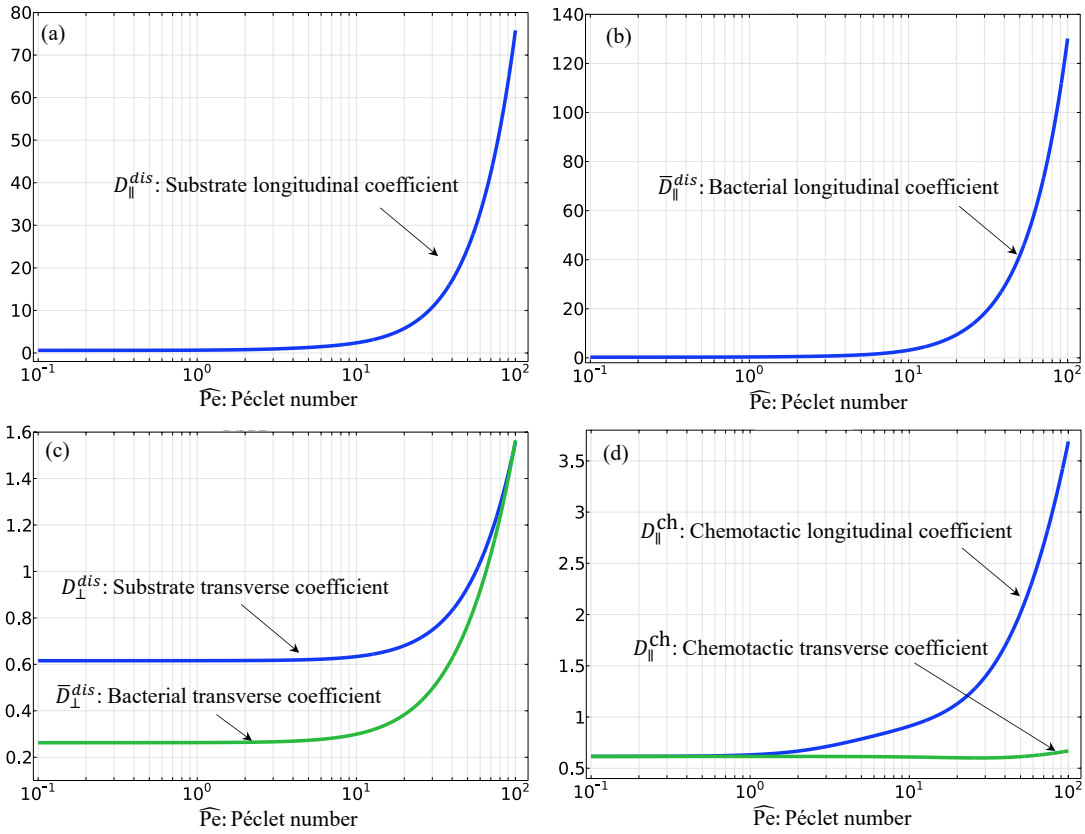


Figure 4.12: *Semi-log plots for the eigenvalues of the dispersion tensors of the substrate, the bacteria, and the chemotactic drift. The x-axis is the logarithmic scale of the Péclet number and y-axis is the linear scale of the bacterial dispersion tensors components.*

Next, we compute the effective dispersion tensors by simulating the *cell-problems* shown in Eqs.(3.6.11)–(3.6.12). The simulation results of the tensor components are $\widehat{\text{Pe}} = 0-100$ are shown in the semi-log plots in Figure 4.12. When $\widehat{\text{Pe}} < 1$, we retrieve the diffusion tensor defined in (4.4.5), as expected. However, for $\widehat{\text{Pe}} \gg 1$, we have dispersion tensors written as

$$D_s^{\text{dis},ij} = D_{\perp}^{\text{dis}}\delta_{ij} + (D_{\parallel}^{\text{dis}} - D_{\perp}^{\text{dis}})\frac{u_i u_j}{|\mathbf{u}|^2}, \tag{4.4.24a}$$

$$D_b^{\text{dis},ij} = D_{\perp}^{\text{dis}}\delta_{ij} + (D_{\parallel}^{\text{dis}} - D_{\perp}^{\text{dis}})\frac{u_i u_j}{|\mathbf{u}|^2}, \tag{4.4.24b}$$

where δ_{ij} is the Kronecker delta and $\mathbf{u} = \text{Pe}\langle \mathbf{v_0} \rangle_{Y^0}$ [81]. The two eigenvalues, $D_{\parallel}^{\text{dis}}$ and $D_{\perp}^{\text{dis}}$, represent the longitudinal and transverse components of the dispersion tensor. The following observations arise from the semi-log plots. First, Figure 4.12(a),

(b), and (c) reveal that $D_{\parallel}^{\text{dis}} > D_{\perp}^{\text{dis}}$ for both species with an increase in the Péclet number values. Second, the bacteria have larger dispersions than the substrate. The chemotactic longitudinal dispersion values grow as the Péclet number increases, while the transverse dispersion values increase at a considerably slower rate. The computed dispersion tensors in Figure 4.12 suggest that the injected bacterial density should exhibit axial elongation in the direction of the flow.

It is noteworthy to mention that employing the same numerical methods as those used in the scenario where $\widehat{\text{Pe}} > 1$ resulted in a negative bacterial density and ultimately led to divergence. There has been a lot of work going into developing stable numerical methods to simulate unsteady dynamical transport for a single species [177, 207]. For instance, the Lattice-Boltzmann method has been used to provide numerically stable solutions in the case of a single transport equation [198]. Later, the Lattice-Boltzmann method was developed for chemotactic bacteria [125, 211]. However, we were not able to apply any alternative numerical methods in this chapter.

To illustrate the effect of the dispersion on the bacterial bands profiles, we assume the traveling bacteria bands remain being Galilean invariant under the unidirectional flow for larger Péclete numbers. As such the expanding bacterial bands are moved by the translational velocity. There are two frames of reference here: $(\tau, \mathbf{y})$ the frame where the fluid particles are moving at a constant speed in the y_1 direction, and $(\tau', \mathbf{y}')$ the frame which is moving with the fluid particles. Thus, for the Galilean translation of position and time we have,

$$\mathbf{y} = \mathbf{y}' + \widehat{\text{Pe}}\langle \hat{\mathbf{v}}_0 \rangle_{Y^0} \tau', \tag{4.4.25}$$

$$\tau = \tau', \tag{4.4.26}$$

where $\langle \hat{\mathbf{v}}_0 \rangle_{Y^0}$ is the unidirectional flow in the y_1 direction. Then by transforming the model in Section 4.4.2 via

$$\hat{\mathcal{S}}(\tau, \mathbf{y}) := \hat{s}(\tau', \mathbf{y}'), \qquad \hat{\mathcal{B}}(\tau, \mathbf{y}) := \hat{b}(\tau', \mathbf{y}'), \tag{4.4.27}$$

and by the expanded partial derivatives using chain rule,

$$\frac{\partial}{\partial \tau'} = \frac{\partial}{\partial \tau} + \widehat{\text{Pe}}\langle \hat{\mathbf{v}}_0 \rangle_{Y^0} \cdot \nabla, \tag{4.4.28}$$

$$\nabla' = \nabla, \tag{4.4.29}$$

we obtain the following dispersive set of equations,

$$\frac{\partial \hat{s}}{\partial \tau'} = \nabla' \cdot \left(\mathbb{D}_s \nabla' \hat{s} \right) - \frac{\widehat{\text{Da}}}{Y} \frac{\hat{s}}{\hat{s} + \kappa_s} \hat{b} \tag{4.4.30a}$$

$$\frac{\partial \hat{b}}{\partial \tau'} = \nabla' \cdot \left(\mathbb{D}_b \nabla' \hat{b} - \widehat{\text{Pe}}_b \left\{ \mathbb{D}^{\text{ch}} \chi(\hat{s}) \nabla' \hat{s} \right\} \hat{b} \right)$$

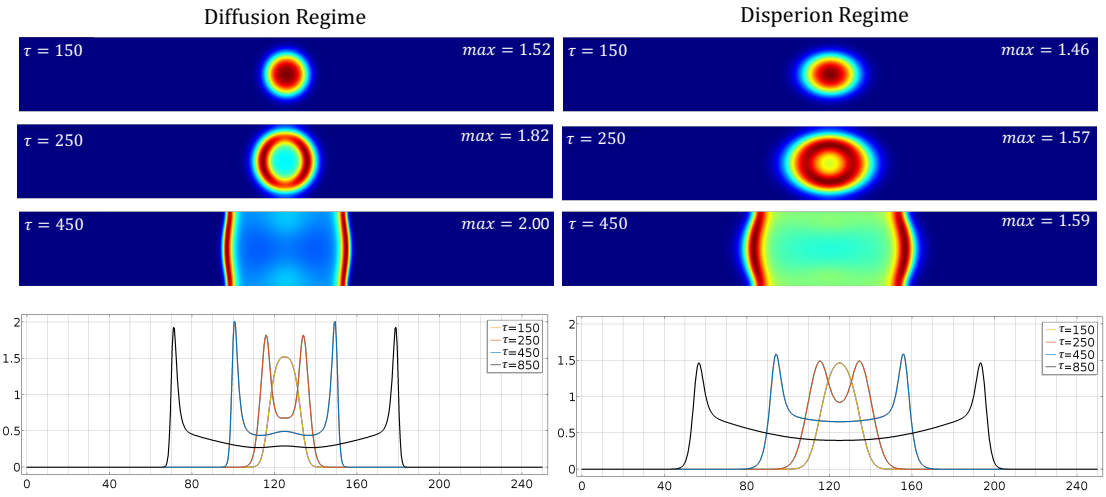


Figure 4.13: *Plots showing the numerical simulations of the model described in Eqs.*(4.4.30). *The Plots show the effect of the effective diffusion tensor (left) and dispersion tensor (right) on the growth expansion of the population. The dispersion tensor is computed for* $\widehat{\mathrm{Pe}} = 5$.

$$+ \widehat{\mathrm{Da}} \frac{\hat{s}}{\hat{s} + \kappa_s} \left(1 - \frac{\hat{b}}{\kappa_c}\right) \hat{b} - \widehat{\kappa_b} \hat{b}, \tag{4.4.30b}$$

and with the corresponding transformed periodic boundary conditions. The two tensors $\mathbb{D}_s$, $\mathbb{D}_b$ and $\mathbb{D}^{\mathrm{ch}}$ in the case of an advection-diffusion regime are defined in Eq.(4.4.22), and in the case of a advection-dispersion regime the tensors are defined Eq.(4.4.23).

In Figure 4.13 we plotted the simulation results of the model in Eqs.(4.4.30) showing the effect of the diffusion and dispersion tensors on the expanding bacterial bands when $\widehat{\mathrm{Pe}} = 5$. In comparison to the travelling bands governed by diffusion alone, the dispersion tensor appears to smooth out the chemotactic fronts without compromising their symmetry. Furthermore, the dispersion effects appears to produce shallower chemotactic peaks.

It is worth noting that Yan and Hilpert [211] numerical study using multiple-relaxation-time (MRT) lattice-Boltzmann method showed that the uniform velocity does not affect the formation and the shape of bacterial bands when $\widehat{\mathrm{Pe}} = 0.01,\ 1$. Their numerical observations agree with what is well known: that advection transports the microbial population with an equal average velocity to that of the underground flow as long as there is no interaction between the porous solid matrix [191]. However, when $\widehat{\mathrm{Pe}} = 10$, Yan and Hilpert [211] reported that the downstream bands become much more populated than the upstream ones. Thus, it remains to be verified if utilising the MRT lattice-Boltzmann method with the current effective dispersion

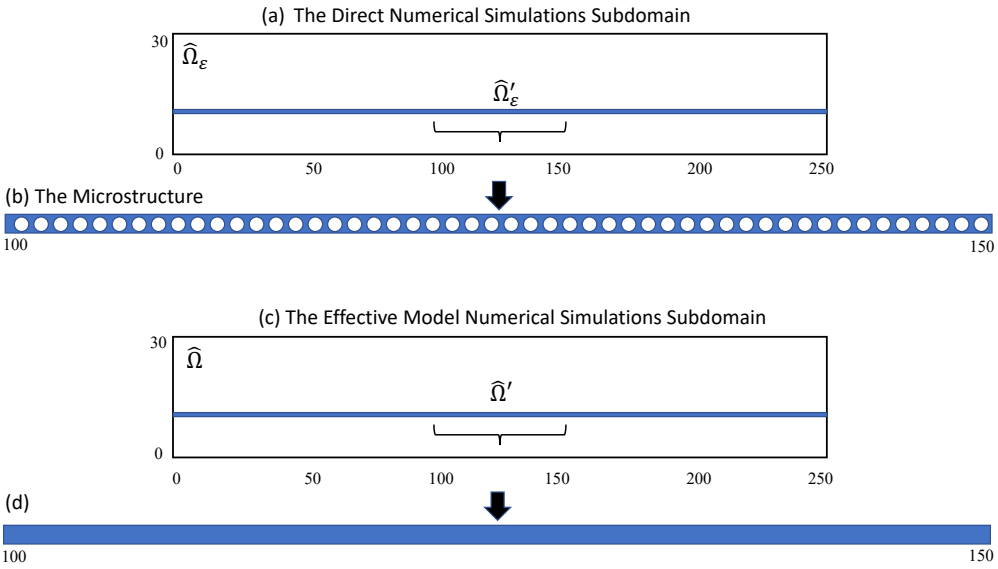


Figure 4.14: *Schematic sketch showing (a) the subdomain $\widehat{\Omega}'_\varepsilon$ with microstructure consisting of $N = 250$ circular inclusion, where in (b) we give a closer look at the microstructure of the subdomain. The homogenised subdomain is shown in (c) and (d).*

components calculated in this thesis would provide the same outcomes.

Next, we investigate the validity and accuracy of the model based on the results of the previous numerical simulations.

4.4.3 Model Validation

In previous sections, we were able to provide numerical simulations of effective models in both the mobile and immobile aqueous phases, which are primarily influenced by diffusion. However, due to the inherent numerical instability of the unsteady advection-dispersion system, it is not possible to do similar numerical simulations when advection dominates the transport. In this section, we validate the effective models by comparing the numerical results of the direct simulation of the model in a porous domain with the results of the simulation of the effective models.

The direct numerical simulation at the microscale is carried out on a subdomain $\widehat{\Omega}'_\varepsilon$, as shown in Figure 4.14. The subdomain, which consists of a single array of circular inclusions with a porosity of 0.45, we are able to conduct direct simulations as a result of the symmetry of the transport problem. Thus, by direct simulations we refer to the numerical simulations of model stated in Eqs.(4.3.8) defined on $\widehat{\Omega}'_\varepsilon$ with no-flux boundary conditions at the solid–aqueous interface and external boundaries.

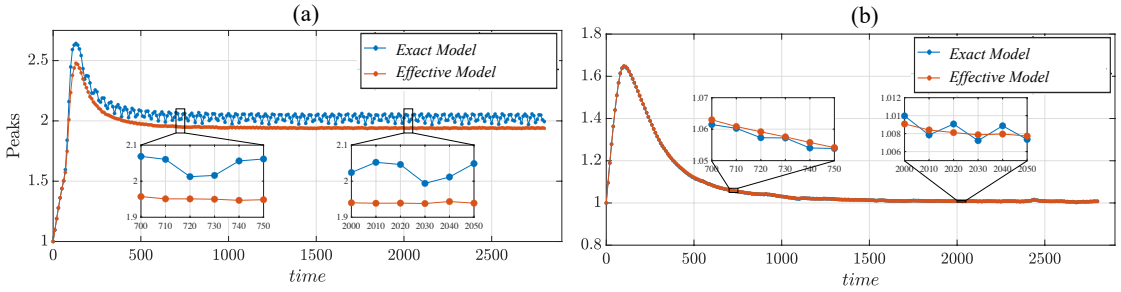


Figure 4.15: *Plots of the simulation results showing the location of the peaks for both the exact and effective travelling waves using the parameter values listed in Table 4.2. The density peaks obtained from the chemotactic model simulation and the density peaks obtained from the F-KPP model simulation are plotted for the same time steps in (a) and (b), respectively.*

On the other hand, the simulations of the corresponding homogenised model are carried out on the homogenised subdomain $\widehat{\Omega}'$

The validation process involves computing the relative errors between the exact and effective wave solutions using the density peak values and the travelling wave speed. We defined the relative variation as:

$$\mathcal{E}(\hat{u}_\varepsilon) = \frac{|\hat{u}_\varepsilon(\tau, \mathbf{y}) - \hat{\mathcal{U}}(\tau, \mathbf{y})|}{|\hat{u}_\varepsilon(\tau, \mathbf{y})|}, \tag{4.4.31}$$

where $\hat{u}_\varepsilon$ and $\hat{\mathcal{U}}$ represent the exact (direct) and effective numerical solutions in terms of the new reference frame explained in Section 4.3, respectively. The relative errors in Eq.(4.4.31) are computed at equidistant time steps ($\Delta t = 10$) and same location on both domains. Furthermore, we consider the relative maximum and minimum bounds defined as:

$$\text{Min} = \min_{t \in \hat{I}} |\mathcal{E}(u)|, \qquad \text{and} \qquad \text{Max} = \max_{t \in \hat{I}} |\mathcal{E}(u)|, \tag{4.4.32}$$

where $\hat{I} \subset [0, \hat{T}]$ is the time interval where the formation of the travelling wave solutions at a constant speed occurs.

We start our investigation by plotting the direct and effective chemotactic and F-KPP travelling wave solutions. Figure 4.15(a) shows that at each time step, the exact chemotactic travelling wave solution bounds the effective travelling wave solution from above. In contrast, the exact and effective F-KPP travelling wave solution is almost identical. Consequently, it suggests that the accuracy of the homogenised travelling wave solutions depends on the homogenised effective chemotactic velocity term.

In the classical homogenisation theory, the estimated errors in a pure diffusion process are of $\mathcal{O}(\varepsilon)$ and the error of gradients is estimated to be $\mathcal{O}(\sqrt{\varepsilon})$ [10]. When

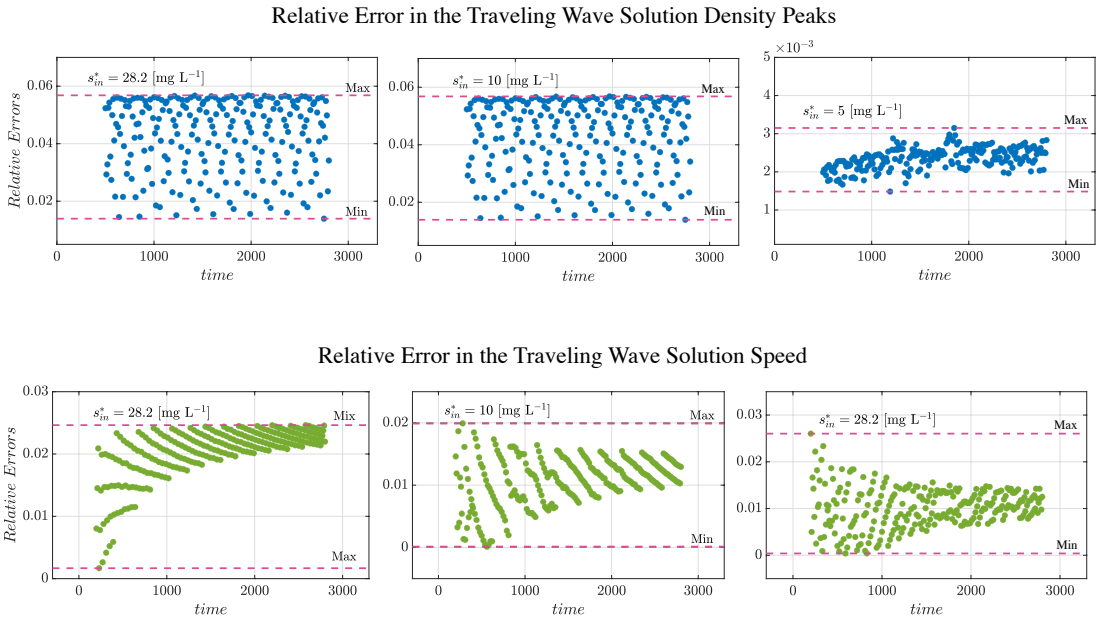


Figure 4.16: *Relative errors in the density peaks and speed, plotted for the same time steps for different initial substrate concentrations.*

computing and plotting the relative errors of the travelling wave solutions shown in Figure 4.9 in Figure 4.16, we notice that the relative errors in all the plots are of order $\sqrt{\varepsilon}$ or less ($\varepsilon = l_{y_1^*}/L_{x_1^*} = 4 \times 10^{-3}$). In particular, we observe that the maximum relative error is of order $\sqrt{\varepsilon}$ when the initial concentration is $s_{in}^* = 28.2$ [mg/L], and is of order ε when the initial concentration is $s_{in}^* = 5$ [mg/L]. Hence, the effective substrate gradient that results from bacterial consumption explains the observed large relative errors. On the other hand, the chemotactic density peaks get smoother when the bioavailability of the substrate goes down (see Figure 4.9). Consequently, the gradients generated by bacterial consumption are shallow, leading to better accuracy. Thus, the travelling bacterial bands at low initial substrate concentrations depend more on bacterial growth. Note that the error analysis supports what was stated in Chapter 3, namely that the effects of metabolic terms on the overall mass flow at the microscale level are negligible.

In the case of advection-diffusion-chemotaxis regimes, simulations produced bacterial bands that display Galilean invariance. Based on this, the error analysis is similar to the one conducted assuming stagnant flow. However, we cannot provide a definitive numerical error analysis for a dispersion-advection-chemotaxis regime. If the expected behaviour of the travelling bands remains Galilean invariance, then the previous error analysis is valid. However, using the MRT Lattice-Boltzman method, Yan and Hilpert [211] reported different behaviour for large Péclet numbers where the two chemotactic travelling peaks fail to maintain symmetry. Therefore, more numerical

research needs to be developed to fully understand how chemotactic bacteria move when large-scale advection is the dominant force.

4.5 Concluding Remarks

In this chapter, we used a case study concerning travelling chemotactic bands to test the accuracy of the effective models developed in Chapter 3. The effective models followed the simple assumptions presented in Chapter 2, in which the transport of the bacterial population is assumed to be similar to that of passive solutes, so it was easier to focus on the mathematical homogenisation performance and accuracy. First, we examined the effects of solute diffusion, metabolic rate, chemotactic drift, and bioavailability of the initial substrate on the travelling chemotactic bands. Then, we used these simulations to conduct numerical error analysis, comparing the effective models' simulations with the original model's direct simulations. The analysis showed that the effective substrate gradient generated errors in the chemotactic advective term. The results support the conclusion that the homogenised model produces a good approximation of the exact model. Unfortunately, our conclusions were restricted to chemotactic bands at static and weak flow rates, as we could not conduct complete numerical simulations in the case of dominant advective flow.

Chapter 5

The Transverse Chemotactic Migration in a Porous Microfluidic Device

In this chapter, we continue the argument started in Chapter 4 in order to assess and validate the effective models presented in Chapter 3. Previously, in Chapter 4, we were able to provide numerical validation analysis for two of the three limiting cases and the related two effective models developed in Section 3.4 and Section 3.5 of Chapter 3. The numerical validation consisted of comparing the numerical data obtained from the simulations of the homogenised models with the original model's direct simulation. This chapter deals with a case study that addresses the last limiting case concerning the dominant advective flow.

In the experimental study of Long and Ford [122], a flow-based microfluidic gradient generator had been fabricated, so it consists of a periodic microstructure in a thin microchannel. They used the microfluidic device to observe and illustrate the role of chemotaxis in the transverse migration of a suspended microbial population in a direction perpendicular to the flow. Their study used an effective Keller-Segel model using conventional approaches to predict the recorded observations. However, the effective model could not produce any chemotactic drift. Even when they increased the effective chemotactic sensitivity constant by 100-fold, the simulation results failed to predict the data. Following that, Porter et al. [157] applied the effective chemotactic model developed in Valdés-Parada et al. [195] using the volume averaging method. Although their simulations generated chemotactic migration, the simulations underestimated the chemotactic migration in slow flows.

In this chapter, we start in Section 5.1 by giving an overview of Long and Ford [122]. Next, section 5.2 describes the laminar flow and the Keller-Segel model in the three-dimensional microchannel. Then, in Section 5.3, we propose a depth-average approach to redefine the mathematical model in the two-dimensional domain. Next, we develop a new depth-averaged Darcy flow model using asymptotic homogenisation,

and we upscale the effective depth-averaged mathematical model using the work in Chapter 3. Then, in Section 5.5, we conduct several analytical and numerical investigations using the effective parameters to quantify the role of the porous microstructure in mixing enhancement in a flow-based microfluidic gradient generator. Lastly, in Section 5.6, we apply the effective model developed using asymptotic homogenisation to fit the experimental data.

5.1 Overview of the Experimental Study

The microfluidic main functionality is that it provides direct visualisation and quantification through tracking of colloids [22, 25] and bacteria [67, 112, 83, 91]. In addition, experimental protocols in microfluidic technology provide means to controlling and manipulating fluid flows with length scales of less than a millimetre [186, 185], enabling the creation of highly controlled chemoattractant gradients, which are fundamentally important in studying chemotactic migration.

Long and Ford [122] fabricated a simple two-inlet microfluidic gradient generator (T-sensor) with cylindrical pillars. The device operates by injecting two injectates through two arms of the device at the same flow rates (see Figure 5.1). The two streams merge at the head of the main channel to produce an interface boundary layer, where the mixing occurs. The dimensions of the main porous T-sensor channel are:

$$\begin{cases} \text{Length} & : & L_{x_1^*} & = 8.3 & \text{[cm]}, \\ \text{Width} & : & L_{x_2^*} & = 0.6 & \text{[cm]}, \\ \text{Depth} & : & H^* & = 13 & \text{[µm]}. \end{cases} \tag{5.1.1}$$

The main channel is composed of a micro-porous structure consisting of hexagonal arrays of thin impermeable cylinders with a radius of 100 [µm] and a height of $H^* = 13$ [µm]. Thus, we choose the representative volume element (the periodic unit cell) as a three-dimensional (3D) element with the following dimensions:

$$\begin{cases} \text{Local length} & : & l_{y_1^*} & = 425.7 & \text{[µm]}, \\ \text{Local width} & : & l_{y_2^*} & = 246 & \text{[µm]}, \\ \text{Depth} & : & H^* & = 13 & \text{[µm]}. \end{cases} \tag{5.1.2}$$

Therefore, we have $\varepsilon = l_{y_1^*}/L_{x_1^*} \sim 5 \times 10^{-3} \ll 1$. Long and Ford [122] conducted several tests, including tracer, bacterial control, and chemotactic tests: The tracer test is performed by injecting a fluorescein solution and phosphate buffer; the bacterial control test involves the injection of a motile bacterial suspension (*E.coli*) and phosphate buffer, and the chemotactic test involves the use of a bacterial suspension and a chemoattractant (α-methylaspartate). Three linear velocities were used,

$$\begin{cases} V_{avg}^* = 5 \quad \text{[m/day]}, \\ V_{avg}^* = 10 \ \text{[m/day]}, \\ V_{avg}^* = 20 \ \text{[m/day]}. \end{cases} \tag{5.1.3}$$

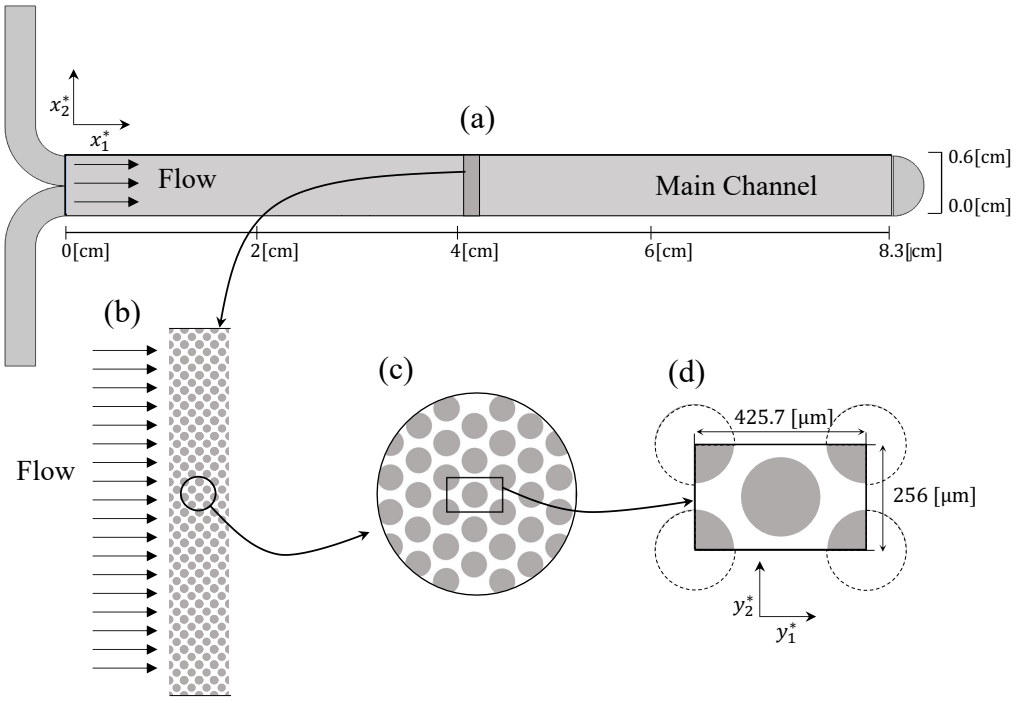


Figure 5.1: *Schematic illustration of the T-sensor, where (a) shows the top view of the device in the $x_1^* x_2^*$-plane with the main channel dimensions with length of $L_{x_1^*} = 8.3$ [cm] and width of $L_{x_2^*} = 0.6$ [cm], note that the height of the channel $H^* = 13$ [μm] is much smaller that its width. In (b) we show a cross section illustrating the microstructure of the main channel and zoomed-in view in (c). The two-dimensional periodic cell is shown in (d) with dimensions of $l_{y_1^*} = 425.7$ [μm] and $l_{y_2^*} = 246$ [μm].*

Note that, in packed column studies, the linear velocities in Eq.(5.1.3) refer to the superficial velocity, which is related to the interstitial velocity by $V_i^* = \phi^{-1} V_{avg}^*$ [160]. The data obtained were collected for all the tests at three transverse profiles in the main channel:

$$\begin{cases} l^*_{2[\text{cm}]}: & x_1^* = 2 \text{ [cm]} = 0.02 \text{ [m]}, \\ l^*_{4[\text{cm}]}: & x_1^* = 4 \text{ [cm]} = 0.04 \text{ [m]}, \\ l^*_{6[\text{cm}]}: & x_1^* = 6 \text{ [cm]} = 0.06 \text{ [m]}. \end{cases} \tag{5.1.4}$$

The normalised bacteria were counted in 23 out of the 25 pores in a square region of 50×50 μm at the centre of each pore. No measurements were taken at the pores adjacent to the lateral walls, where they observed an accumulation of bacteria.

5.2 The Mathematical Model

In this section, we focus on the main channel of a T-sensor, where we extend the mathematical model description given in Chapter 2 from a 2D to a 3D domain. Before that, we need to address a fundamental issue concerning the validity of the Keller-Segel model in the 3D microchannel. Particularly, the issue of the shallow depth of the rectangular channel. We notice that the Knudsen-like number for the channel depth H^* [75, 71, 154] exceeds unity, that is

$$\mathrm{Kn}_H = \frac{l_{\mathrm{run}}}{H^*} > 1, \tag{5.2.1}$$

where l_{run} is run length of a single bacterium (for more details see Section 2.2). However, we adopted the same assumption as Long and Ford [122] and Porter et al. [157], where they assume that the Keller-Segel model outlined in Chapter 2 remains valid. This approach implies that the bacteria at the pore level move according to the Keller-Segel model and do not experience any significant changes in their motility due to the shallow channel depth. It is important to note that this assumption may not hold, and further research is needed to understand the effect of the depth on the bacteria motility. However, it is beyond the scope of this thesis especially since these effects are not trivial [75, 96, 137, 63, 29, 33, 46].

5.2.1 Very Thin Porous Medium (VTPM)

In the porous microchannel, there are two parameters of interest: the geometrical parameter of the porous structure, $\varepsilon = l_{y_1^*}/L_{x_1^*} \sim 5\times10^{-3}$, and dimensionless thickness parameter of the channel, $H = H^*/L_{x_1^*} \sim 1.5 \times 10^{-4}$, and $H \ll \varepsilon$ constitutes a very thin porous medium (VTPM) [72]. The domain representing the main channel is expressed as:

$$\boldsymbol{\Omega}^* = \Omega^* \times [-H^*/2, H^*/2]. \tag{5.2.2}$$

Note that hereafter, the objects related to the 3D channel geometry are denoted using a bold font. We assign $\boldsymbol{\Omega}_f^* = \Omega_f^* \times [-H^*/2, H^*/2]$ to describe the fluid phase in the main channel, such that $\boldsymbol{\Omega}_f^* \subset \boldsymbol{\Omega}^*$. Therefore, the differential operators is written as:

$$\nabla^* = \left(\frac{\partial}{\partial x_1^*}, \frac{\partial}{\partial x_2^*}, \frac{\partial}{\partial z^*}\right), \tag{5.2.3}$$

$$\nabla^{*2} = \frac{\partial^2}{\partial x_1^{*2}} + \frac{\partial^2}{\partial x_2^{*2}} + \frac{\partial^2}{\partial z^{*2}}. \tag{5.2.4}$$

There are six faces of the main channel: the inlet, $\boldsymbol{\Gamma}_L^*$, and outlet, $\boldsymbol{\Gamma}_R^*$; the lateral sides $\boldsymbol{\Gamma}_T^*$ and $\boldsymbol{\Gamma}_B^*$; and the two parallel plates that form the ceiling, $\boldsymbol{\Gamma}_{\mathrm{ceiling}}^*$, and floor, $\boldsymbol{\Gamma}_{\mathrm{floor}}^*$, of the channel, and are separated by the depth, H^*. The microstructure consists of a 3D solid–aqueous interface, $\boldsymbol{\Gamma}_s^*$, which refers to the outer faces of the cylinders and the two parallel plates.

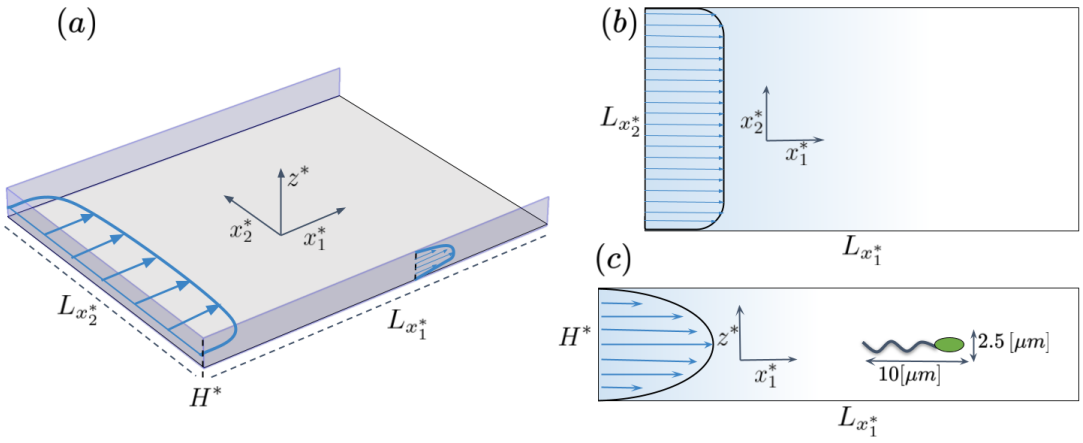


Figure 5.2: *An illustration showing the effect of the shallow channel on the flow. In (a) we plot a rectangular duct channel (not proportional to the real domain measurements); (b) shows the uniform axial flow (the axial flow in the main channel), and (c) the parabolic flow between the two parallel plates in the z^*-direction. Note that the cylindrical pillars are omitted for clarity and the horizontal velocity profile in (b) represents the homogenised/averaged velocity profile.*

5.2.2 Laminar Flow in VTPM

The fully developed flow in the main channel is laminar because the Reynolds number is very low, hence

$$\mathrm{Re} = \frac{\rho V^* d^\star}{\mu} \ll 1, \tag{5.2.5}$$

where ρ, μ, V^*, and $d^\star$ are the fluid density, dynamical viscosity, and characteristic hydraulic diameter, respectively. Here, we define the hydraulic diameter globally and locally as:

$$d^\star = \frac{2\mathrm{HW}^\star}{\mathrm{H} + \mathrm{W}^\star}, \quad W^\star \in \{L_{x_2^*}, l_{y_2^*}\}. \tag{5.2.6}$$

Thus, the values of the hydrodynamic Reynolds number are below 1 for the flow velocities reported in Long and Ford [122],

$$\mathrm{Re} \sim 10^{-2} - 10^{-4}. \tag{5.2.7}$$

Furthermore, when confined between two plates, the viscous flow in absence of a porous medium becomes almost uniform in the $x_1^* x_2^*$-plane, except for a thin boundary layer of a small thickness of $\mathcal{O}(H^*)$ near the sidewalls (Figure 5.2) [41]. The vertical

velocity component can be neglected, or equivalently, we assume a constant pressure in the z^*-direction [139, 129]. Such a flow is known as a Hele–Shaw flow, and solved using lubrication theory. However, the direct application of lubrication theory is not feasible owing to the porous structure of the model. Therefore, we model the flow using the Stokes equations in the following manner:

$$\nabla^* \cdot \mathbf{v}^* = 0 \qquad \text{in } \mathbf{\Omega}_f^*, \tag{5.2.8a}$$

$$\nabla^* p^* = \mu \nabla^{*2} \mathbf{v}^* \qquad \text{in } \mathbf{\Omega}_f^*, \tag{5.2.8b}$$

$$\mathbf{v}^* = \mathbf{0} \qquad \text{at } \mathbf{\Gamma}_s^*, \tag{5.2.8c}$$

where $\mathbf{v}^* = (u^*, v^*, w^*)$. We assign a normal inflow and outflow constant velocity at the inlet and outlet, respectively; hence,

$$-\mathbf{n} \cdot \mathbf{v}^* = V^* \qquad \text{at } \mathbf{\Gamma}_L^*, \tag{5.2.9a}$$

$$-\mathbf{n} \cdot \mathbf{v}^* = -V^* \qquad \text{at } \mathbf{\Gamma}_R^*. \tag{5.2.9b}$$

The aforementioned inlet and outlet conditions ensure that the average flow values in the main channel are consistent with the experimentally reported values. Lastly, the channel walls, $\mathbf{\Gamma}_T^*$, $\mathbf{\Gamma}_B^*$, $\mathbf{\Gamma}_{\text{ceiling}}^*$ and $\mathbf{\Gamma}_{\text{floor}}^*$, are assumed to be equipped with no-slip conditions.

5.2.3 The Keller-Segel Model in VTPM

Here, we extend the model described in Section 2.1 of Chapter 2 to a 3D domain. Since the chemoattractant α-methylaspartate is a non-metabolic chemoattractant for *E.coli* bacteria [134, 213, 206], we neglect the kinetic terms in Eqs.(2.4.1). Hence, the chemoattractant and the bacteria transport equations, including chemotaxis, satisfy the following equations in the main channel,

$$\frac{\partial s^*}{\partial t^*} = \nabla^* \cdot (D_s^* \nabla^* s^* - \mathbf{v}^* s^*) \qquad \text{in } [0, T^*] \times \mathbf{\Omega}_f^*, \tag{5.2.10a}$$

$$\frac{\partial b^*}{\partial t^*} = \nabla^* \cdot (D_b^* \nabla^* b^* - [\mathbf{v}^* + \chi^*(s^*) \nabla^* s^*] b^*) \qquad \text{in } [0, T^*] \times \mathbf{\Omega}_f^*. \tag{5.2.10b}$$

As the interface conditions, which include the two parallel plates, we have:

$$-\mathbf{n}^* \cdot (D_s^* \nabla^* s^*) = -\mathbf{n}^* \cdot (D_b^* \nabla^* b^*) = 0 \qquad \text{at } \mathbf{\Gamma}_s^*, \tag{5.2.11a}$$

We define the external boundary conditions by specifying H_s^* and H_b^* (see Section 2.4 of Chapter 2). The concentration fluxes at the inlet, $\mathbf{\Gamma}_L^*$, are described using Danckwerts boundary conditions

$$\begin{cases} H_s^*(\mathbf{x}^*, s^*, b^*) & = \mathbf{n} \cdot (\mathbf{v}^* s_i^*), \\ H_b^*(\mathbf{x}^*, s^*, b^*) & = \mathbf{n} \cdot ([\mathbf{v}^* + \chi^*(s^*) \nabla^* s^*] b_i^*), \end{cases} \tag{5.2.12}$$

Parameter	Dimensional value and units	References
D_s^* (α-methylaspartate)	8.6×10^{-10} m^{2}s^{-1}	Long and Ford [122]
D_f^* (Fluorescein)	4.9×10^{-10} m^{2}s^{-1}	Long and Ford [122]
D_b^*	3.0×10^{-10} m^{2}s^{-1}	Long and Ford [122]
χ_0^*	2.4×10^{-8} m^{2}s^{-1}	Long and Ford [122]
K_d^*	0.125 mM	Long and Ford [122]
v_s^*	2.33×10^{-5} m s^{-1}	Ahmed and Stocker [5]
$\hat{s}_i^*$ (α-methylaspartate)	0.3 mM	Long and Ford [122]
$\hat{c}_i^*$ (Fluorescein)	0.12 mM	Long and Ford [122]

Table 5.1: *Dimensional parameter values used in this chapter.*

where s_i^* and b_i^* are the injected species defined at the inlet,

$$s_i^* = \hat{s}_i^* \mathbb{1}_{[0, L_{x_2^*}/2] \times [-H^*/2, H^*/2]}, \quad \text{and} \quad b_i^* = \hat{s}_i^* \mathbb{1}_{[-L_{x_2^*}/2, 0] \times [-H^*/2, H^*/2]}. \tag{5.2.13}$$

The outlet boundary conditions, $\mathbf{\Gamma}_R^*$, are defined as:

$$\begin{cases} H_s^*(\mathbf{x}^*, s^*, b^*) & = \mathbf{n} \cdot (\mathbf{v}^* s^*), \\ H_b^*(\mathbf{x}^*, s^*, b^*) & = \mathbf{n} \cdot ([\mathbf{v}^* + \chi^*(s^*) \nabla^* s^*] b^*), \end{cases} \tag{5.2.14}$$

whereas at $\mathbf{\Gamma}_T^*$, $\mathbf{\Gamma}_B^*$, $\mathbf{\Gamma}_{\text{ceiling}}^*$ and $\mathbf{\Gamma}_{\text{floor}}^*$ we impose no-flux conditions, that is,

$$H_s^*(\mathbf{x}^*, s^*, b^*) = H_b^*(\mathbf{x}^*, s^*, b^*) = 0. \tag{5.2.15a}$$

Lastly, the initial concentrations on $\mathbf{\Omega}_f^*$ are expressed as:

$$b^*(0, \mathbf{x}^*) = s^*(0, \mathbf{x}^*) = 0. \tag{5.2.16}$$

The parameters assumed in the model are given in Table 5.1. These parameters were calculated in a bulk aqueous phase under quiescent conditions [122].

5.2.4 Non-dimensionalisation

We utilised the same scaling presented in Section 2.6, where the spatial scale is expressed as:

$$(x_1^*, x_2^*, z^*) = L_{x_1^*}(x_1, x_2, z), \tag{5.2.17}$$

where $z = z^*/L_{x_1^*}$. The differential operators in Eq.(5.2.4) are expressed as

$$\nabla = \left(\frac{\partial}{\partial x_1}, \frac{\partial}{\partial x_2}, \frac{\partial}{\partial z} \right), \tag{5.2.18}$$

$$\nabla^2 = \frac{\partial^2}{\partial x_1^2} + \frac{\partial^2}{\partial x_2^2} + \frac{\partial^2}{\partial z^2}. \tag{5.2.19}$$

Consequently, we write the model in the 3D domain expressed as:

$$\boldsymbol{\Omega} = \Omega \times [-H/2, H/2], \tag{5.2.20}$$

where $H = H^*/L_{x_1^*} \ll 1$. The non-dimensional Stokes equations are expressed as:

$$\nabla \cdot \mathbf{v} = 0 \qquad \text{in } \boldsymbol{\Omega}_f, \tag{5.2.21a}$$

$$\nabla^2 \mathbf{v} - \nabla p = 0 \qquad \text{in } \boldsymbol{\Omega}_f, \tag{5.2.21b}$$

$$\mathbf{v} = \mathbf{0} \qquad \text{at } \boldsymbol{\Gamma}_s. \tag{5.2.21c}$$

We impose no-slip boundary conditions at $\boldsymbol{\Gamma}_T$, $\boldsymbol{\Gamma}_B$, $\boldsymbol{\Gamma}_{\text{ceiling}}$ and $\boldsymbol{\Gamma}_{\text{floor}}$ and a unit normal velocity at the inlet and outlet.

For the transport equations, we apply the same scaling argument used in Section 2.6. Here, we selected the reference concentrations as:

$$s_{\text{m}}^* = \hat{s}_i^*, \qquad b_{\text{m}}^* = \hat{b}_i^*. \tag{5.2.22}$$

Thus, the chemotactic transport model is expressed as:

$$\frac{\partial s}{\partial t} = \nabla \cdot (\nabla s - \text{Pe}\mathbf{v}s) \qquad \text{in } [0,T] \times \boldsymbol{\Omega}_f, \tag{5.2.23a}$$

$$\frac{\partial b}{\partial t} = \nabla \cdot (\delta \nabla b - [\text{Pe}\mathbf{v} + \text{Pe}_b \chi(s) \nabla s] b) \qquad \text{in } [0,T] \times \boldsymbol{\Omega}_f, \tag{5.2.23b}$$

while the dimensionless interface conditions at $\boldsymbol{\Gamma}_s$ are expressed as:

$$-\mathbf{n} \cdot (\nabla s) = -\mathbf{n} \cdot (\delta \nabla b) = 0, \tag{5.2.24}$$

and the initial concentrations,

$$b(0, \mathbf{x}) = s(0, \mathbf{x}) = 0 \qquad \text{on } \boldsymbol{\Omega}_f. \tag{5.2.25}$$

The Danckwerts boundary conditions at $\boldsymbol{\Gamma}_L$ are written as:

$$\begin{cases} H_s(\mathbf{x}, s, b) & = \mathbf{n} \cdot (\text{Pe}\mathbf{v}s_i), \\ H_b(\mathbf{x}, s, b) & = \mathbf{n} \cdot ([\text{Pe}\mathbf{v} + \text{Pe}_b \chi(s) \nabla s] b_i), \end{cases} \tag{5.2.26}$$

where s_i and b_i are the dimensionless injected concentrations,

$$s_i = \mathbb{1}_{[0, L_{x_2}/2] \times [-H/2, H/2]}, \quad \text{and} \quad b_i = \mathbb{1}_{[-L_{x_2}/2, 0] \times [-H/2, H/2]}, \tag{5.2.27}$$

while the dimensionless outlet boundary conditions, $\boldsymbol{\Gamma}_R$, is expressed as:

$$\begin{cases} H_s(\mathbf{x}, s, b) & = \mathbf{n} \cdot (\text{Pe}\mathbf{v}s), \\ H_b(\mathbf{x}, s, b) & = \mathbf{n} \cdot ([\text{Pe}\mathbf{v} + \text{Pe}_b \chi(s) \nabla s] b). \end{cases} \tag{5.2.28}$$

At the channel walls, $\boldsymbol{\Gamma}_T$, $\boldsymbol{\Gamma}_B$, $\boldsymbol{\Gamma}_{\text{ceiling}}$ and $\boldsymbol{\Gamma}_{\text{floor}}$, the no-flux conditions are written as:

$$H_s(\mathbf{x}, s, b) = H_b(\mathbf{x}, s, b) = 0. \tag{5.2.29}$$

Lastly, the non-dimensional parameters of the model are given in Table 5.2.

Parameter	Definition	Value
δ (α-methylaspartate)	D_b^*/D_s^*	0.3488
δ_0 (Fluorescein)	D_b^*/D_0^*	0.6122
κ_d	K_d/s_i^*	0.41667
Pe_b	$v_s L_{x_1^*}/D_s^*$	2.25×10^3
χ_0	$\chi_0^*/(3v_s L_{x_1^*})$	4.14×10^{-3}
ε^{-1}	$(l_{y_1}^*/L_{x_1}^*)^{-1}$	195
ϕ	$\lvert\mathbf{Y}^0\rvert/\lvert\mathbf{Y}\rvert$	0.4

Table 5.2: *Following Table 5.1, we computed the dimensionless parameter values corresponding to the parameters found in Long and Ford [122].*

5.2.5 Revisiting the Periodic Homogenisation Method

As in any asymptotic homogenisation method, the domain periodicity unit should first be defined. As illustrated in Figure 5.3, the 3D representative volume element is expressed as:

$$\mathbf{Y} = \mathbf{Y^0} \cup \mathbf{\Sigma}^0, \tag{5.2.30}$$

where the fluid phase $\mathbf{Y^0}$ represents the local porous medium and $\mathbf{\Sigma}^0$ represents the solid phase, with the boundaries $\partial\mathbf{\Sigma}^0$ defining the aqueous–solid interface, such that:

$$\mathbf{Y} = Y \times [-H/2, H/2], \quad \mathbf{Y^0} = Y^0 \times [-H/2, H/2] \quad \mathbf{\Sigma^0} = \Sigma^0 \times [-H/2, H/2], \tag{5.2.31}$$

where Y, Y^0 and Σ^0 are shown in Figure 5.4. Accordingly, we reformulated the problem in the domain $\Omega_\varepsilon \times \mathbf{Y^0}$. By convention, any point $(\mathbf{x}, \mathbf{y}, z) \in \Omega_\varepsilon \times \mathbf{Y^0}$ refers to $\mathbf{x} = (x_1, x_2) \in \Omega_\varepsilon$ and $(\mathbf{y}, z) = (y_1, y_2, z) \in \mathbf{Y^0}$, where $\mathbf{y} = \mathbf{x}/\varepsilon$ is the only local variable [72]. Assuming a dominant advective Péclet regime, $\mathrm{Pe} \sim \mathcal{O}(\varepsilon^{-1})$, the asymptotic expansions are expressed as:

$$s_\varepsilon(t, \tau, \mathbf{x}, \mathbf{y}, z) = s_0 + \varepsilon s_1 + \varepsilon^2 s_2 + \mathcal{O}(\varepsilon^3), \tag{5.2.32a}$$

$$b_\varepsilon(t, \tau, \mathbf{x}, \mathbf{y}, z) = b_0 + \varepsilon b_1 + \varepsilon^2 b_2 + \mathcal{O}(\varepsilon^3), \tag{5.2.32b}$$

where $s_i = s_i(t, \tau, \mathbf{x}, \mathbf{y}, z)$, and $b_i = b_i(t, \tau, \mathbf{x}, \mathbf{y}, z)$ are periodic in $\mathbf{y}$ for $i = 1,\ 2 \ldots$ (see Section 3.1). Here $\tau = \varepsilon^{-1}t$ is the advection local time. The flow in the x_1x_2-plane is almost uniform (see Section 5.2.2). Therefore, the velocity field was asymptoticly expanded as:

$$\mathbf{v}_\varepsilon(\mathbf{y}, z) = \mathbf{v}_0 + \varepsilon \mathbf{v}_1 + \varepsilon^2 \mathbf{v}_2 + \mathcal{O}(\varepsilon^3). \tag{5.2.33}$$

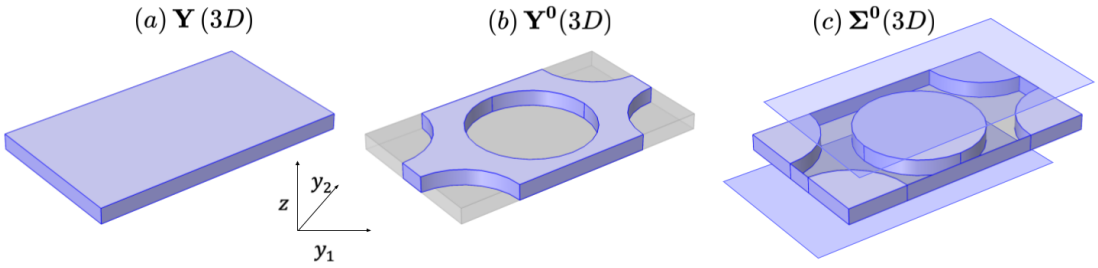


Figure 5.3: *Schematic plots showing 3D (a)* $\mathbf{Y}$ *periodic unit, (b)* $\mathbf{Y^0}$ *aqueous phase, and (c)* $\mathbf{\Sigma}^0$ *solid phase.*

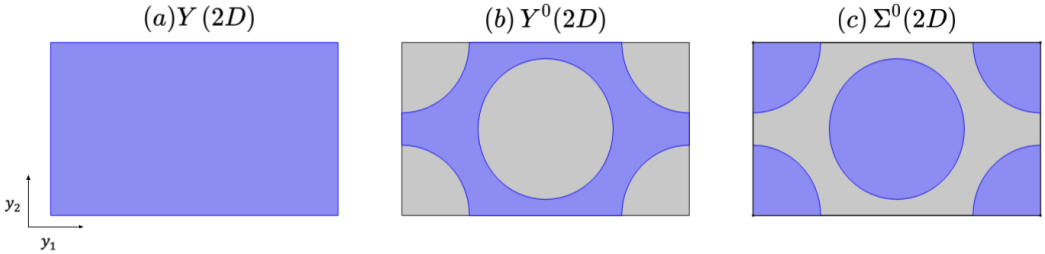


Figure 5.4: *Schematic plots showing the simplified 2D (a)* Y *periodic unit, (b)* Y^0 *aqueous phase, and (c)* Σ^0 *solid phase with boundaries defining the aqueous-solid interface* $\partial\Sigma^0$*.*

From a computational perspective, the application of the asymptotic homogenisation on $\Omega_\varepsilon \times \mathbf{Y^0}$ is accompanied by simulation difficulties owing to the high mesh resolution required to resolve the narrow gap. Whereas calculations for $\Omega_\varepsilon \times Y^0$ offer a significant reduction in the computational complexity. Therefore, we proposed a two-step procedure to derive the homogenised model. The first step aims to reduce the domain dimensionality by applying the classical Taylor–Aris dispersivity for solute [68, 53] in a rectangular duct. Hence, we employ a 2D Keller-Segel model with the concentrations and the flow written in depth-averaged form,

$$\overline{s}_\varepsilon(t,\mathbf{x},\mathbf{y}) = \frac{1}{|H|}\int_{-H/2}^{H/2} s_\varepsilon(t,\mathbf{x},\mathbf{y},z)dz, \tag{5.2.34}$$

$$\overline{b}_\varepsilon(t,\mathbf{x},\mathbf{y}) = \frac{1}{|H|}\int_{-H/2}^{H/2} b_\varepsilon(t,\mathbf{x},\mathbf{y},z)dz, \tag{5.2.35}$$

$$\overline{\mathbf{v}}_\varepsilon(\mathbf{y}) = \frac{1}{|H|}\int_{-H/2}^{H/2} \mathbf{v}_\varepsilon(\mathbf{y}, z)dz, \tag{5.2.36}$$

where $\overline{s}_\varepsilon$, $\overline{b}_\varepsilon$ and $\overline{\mathbf{v}}_\varepsilon$ are defined in $\Omega_\varepsilon \times Y^0$ (see Figure 5.4). The second step involves applying asymptotic homogenisation to the depth-averaged models.

Remark 5.1. *The dispersivities defined using the classical Taylor–Aris theory for solutes should not be confused with those arising from the porous medium when applying asymptotic homogenisation in Chapter 3.*

5.3 Depth-Averaged Flow

As illustrated in Figure 5.2, in a free microchannel (non-porous), the flow in the shallow direction is of a parabolic profile, and it is almost uniform along the width of the channel. For the aspect ratio $\bar{\epsilon} = H^*/L_{x_2^*} \ll 1$, the 3D velocity field can be approximated as follows [139]:

$$\widetilde{\mathbf{v}}(\mathbf{x}, z) = \overline{\mathbf{v}}(\mathbf{x})f(z). \tag{5.3.1}$$

The parabolic Poiseuille profile, described using $f(z)$, demands that [139],

$$\overline{f(z)} = \frac{1}{H}\int_{-H/2}^{H/2} f(z)dz = 1. \tag{5.3.2}$$

Therefore, the average value of Eq.(5.3.1) over the channel depth is the 2D depth-averaged velocity that satisfies the following Brinkman equations [140]:

$$\nabla \cdot \overline{\mathbf{v}} = 0 \qquad \text{in } \Omega_f, \tag{5.3.3a}$$

$$\nabla^2\overline{\mathbf{v}} - \nabla p = k^2\overline{\mathbf{v}} \qquad \text{in } \Omega_f, \tag{5.3.3b}$$

$$\overline{\mathbf{v}} = \mathbf{0} \qquad \text{at } \Gamma_s, \tag{5.3.3c}$$

where $k = \sqrt{12}H^{-1}$ is the square root of the dimensionless drag force. The drag force accounts for the resistance induced by the parallel plates on the flow, where the drag term is the non-dimensional form of the volume viscous drag force and is defined as [209]:

$$F_\mu^* = -12\frac{\mu V^*}{H^{*2}} \text{ [N]}. \tag{5.3.4}$$

To write the microscopic description of the Brinkman equations in Eqs.(5.3.3), we assume the fluid pressure balances the viscous force in the flow direction. Thus, the pressure gradient (dimensional) in the flow direction is expressed as:

$$\nabla^* p^* \sim \mathcal{O}\left(\frac{P^*}{L_{x_1^*}}\right). \tag{5.3.5}$$

Therefore, with respect to ε, the dimensionless pressure is

$$\nabla p \sim \mathcal{O}\left(\varepsilon^0\right). \tag{5.3.6}$$

We assume that the pressure and the local stress have the same order of magnitude (see Section 3.2), such that

$$\frac{P^*}{L_{x_1^*}} \sim \frac{\mu V^*}{l_{y_1^*}^2} \frac{12}{H^2}. \tag{5.3.7}$$

Note that, $H^2/12 \sim \mathcal{O}(\varepsilon^2)$, and thus, the dimensionless viscous term is

$$\nabla^2 \overline{\mathbf{v}}_\varepsilon \sim \mathcal{O}(\varepsilon^4). \tag{5.3.8}$$

Therefore, the microscopic Brinkman equations are written as: [1]

$$\nabla \cdot \overline{\mathbf{v}}_\varepsilon = 0 \qquad \text{in } Y^0, \tag{5.3.9a}$$
$$\varepsilon^4 \nabla^2 \overline{\mathbf{v}}_\varepsilon - \nabla p_\varepsilon = k^2 \overline{\mathbf{v}}_\varepsilon \qquad \text{in } Y^0, \tag{5.3.9b}$$
$$\overline{\mathbf{v}}_\varepsilon = \mathbf{0} \qquad \text{at } \partial\Sigma^0. \tag{5.3.9c}$$

Next, we apply the asymptotic expansion to the microscopic Brinkman equations to derive Darcy's law for VTPM.

5.3.1 Formal Asymptotic Expansion of Brinkman Equations

As in any asymptotic analysis method, the postulated ansatz should be substituted into the partial differential equation under consideration. Hence, we start by substituting the following expansion of the depth-averaged velocity,

$$\overline{\mathbf{v}}_\varepsilon(\mathbf{y}) = \overline{\mathbf{v}}_0(\mathbf{y}) + \varepsilon \overline{\mathbf{v}}_1(\mathbf{y}) + \varepsilon^2 \overline{\mathbf{v}}_2(\mathbf{y}) + \mathcal{O}(\varepsilon^3), \tag{5.3.10}$$

and the expansion of the pressure into (5.3.9). At the lowest order of $\mathcal{O}(\varepsilon^{-1})$, we have:

$$\nabla_{\mathbf{y}} p_0 = 0 \qquad \text{on } Y^0, \tag{5.3.11}$$
$$\nabla_{\mathbf{y}} \cdot \overline{\mathbf{v}}_0 = 0 \qquad \text{on } Y^0, \tag{5.3.12}$$

which implies that $p_0 = p_0(\mathbf{x})$. The next order gives:

$$k^2 \overline{\mathbf{v}}_0 - \nabla_{\mathbf{x}} p_0 - \nabla_{\mathbf{y}} p_1 = 0 \qquad \text{on } Y^0, \tag{5.3.13a}$$
$$\nabla_{\mathbf{x}} \cdot \overline{\mathbf{v}}_0 + \nabla_{\mathbf{y}} \cdot \overline{\mathbf{v}}_1 = 0 \qquad \text{on } Y^0. \tag{5.3.13b}$$

[1] In the thesis examination, the examiners expressed unease about the deduction of (5.3.9) from (5.3.3). Although the derivation has been modified in this corrected version, that unease remains.

The linear problem in Eq.(5.3.13a) has a solution (in Einstein summation convention):

$$\overline{\mathbf{v}}_0 = -\frac{\overline{\mathbf{K}}_j(\mathbf{y})}{k^2}\frac{\partial p_0}{\partial x_j}, \qquad p_1 = -q_j(\mathbf{y})\frac{\partial p_0}{\partial x_j} + \bar{q}_1(\mathbf{x}), \tag{5.3.14}$$

where q_j and $\overline{\mathbf{K}}_j$ are Y-periodic. By substituting the two solutions into Eq.(5.3.13a), we can obtain:

$$\overline{\mathbf{K}}_j^0(\mathbf{y}) = \big(\mathbf{e}_j + \nabla_{\mathbf{y}} q_j\big), \tag{5.3.15}$$

where $\mathbf{e}_j$ is the Cartesian unit vector in the j-th direction. In addition, by averaging Eq.(5.3.15) over the unit cell, we can obtain the depth-averaged permeability tensor:

$$\overline{\mathbf{K}}_j^0 = \frac{1}{|Y|}\int_{Y^0} \big(\mathbf{e}_j + \nabla_{\mathbf{y}} q_j\big) d\mathbf{y}. \tag{5.3.16}$$

From Eq.(5.3.14) and Eq.(5.3.12), we have:

$$\nabla_{\mathbf{y}} \cdot \big(\mathbf{e}_j + \nabla_{\mathbf{y}} q_j\big) = 0. \tag{5.3.17}$$

To solve Eq.(5.3.17), we will assume a boundary condition which is compatible with Eq.(5.3.17), that is

$$-\mathbf{n} \cdot \big(\mathbf{e}_j + \nabla_{\mathbf{y}} q_j\big) = 0 \qquad \text{at } \partial\Sigma^0. \tag{5.3.18}$$

Therefore, to compute the permeability tensor in Eq.(5.3.16), we solve the following *cell-problem*:

$$\nabla_{\mathbf{y}} \cdot \big(\mathbf{e}_j + \nabla_{\mathbf{y}} q_j\big) = 0 \qquad \text{on } Y^0, \tag{5.3.19}$$

$$-\mathbf{n} \cdot \big(\mathbf{e}_j + \nabla_{\mathbf{y}} q_j\big) = 0 \qquad \text{at } \partial\Sigma^0, \tag{5.3.20}$$

such that $\langle q_i \rangle = 0$. Returning to Eq.(5.3.13b) and taking the average over Y, gives

$$\nabla_{\mathbf{x}} \cdot \langle \overline{\mathbf{v}}_0 \rangle = -\nabla_{\mathbf{y}} \cdot \langle \overline{\mathbf{v}}_1 \rangle = 0, \tag{5.3.21}$$

which is the incompressibility condition. Then the 2D depth-averaged velocity in Eq.(5.3.14) is defined as:

$$\langle \overline{\mathbf{v}}_0 \rangle = -\frac{H^2}{12}\overline{\mathbf{K}}^0 \nabla_{\mathbf{x}} \langle p_0 \rangle, \tag{5.3.22}$$

and $\nabla_{\mathbf{x}} \cdot \langle \overline{\mathbf{v}}_0 \rangle = 0$. Based on the definition of the incompressibility condition in (5.3.21), the no-slip boundary conditions (Dirichlet) gives the Neumann boundary condition [88],

$$-\mathbf{n} \cdot \langle \overline{\mathbf{v}}_0 \rangle = 0 \qquad \text{at } \Gamma_T \cup \Gamma_B. \tag{5.3.23}$$

Finally, the upscaled inlet and outlet conditions written as:

$$-\mathbf{n} \cdot \langle \overline{\mathbf{v}}_0 \rangle = 1 \qquad \text{at } \Gamma_L, \tag{5.3.24a}$$

$$-\mathbf{n} \cdot \langle \overline{\mathbf{v}}_0 \rangle = -1 \quad \text{at } \Gamma_R. \tag{5.3.24b}$$

The equation in Eq.(5.3.22) is related to the averaged velocity in a Hele-Show cell and the theory of lubrication [129]. Furthermore, it is consistent with the results in Fabricius et al. [72] and Almqvist et al. [15].

5.3.2 Local Depth-Averaged Flow

The approximation for the depth-averaged velocity at the microscopic scale is purely periodic and satisfies:

$$\overline{\mathbf{v}}_0(\mathbf{y}) = -\frac{H^2}{12}\overline{\mathbf{K}^0}(\mathbf{y})\nabla_{\mathbf{x}} p_0, \tag{5.3.25a}$$

$$\nabla_{\mathbf{x}} \cdot \overline{\mathbf{v}}_0 = 0. \tag{5.3.25b}$$

Furthermore, it exhibits the following properties (for all i):

$$-\mathbf{n} \cdot \overline{\mathbf{v}}_i = 0 \qquad \text{on} \quad \partial\Sigma^0. \tag{5.3.26a}$$

Thus, we defined a 2D periodic flow that takes into account the effect of viscous drag imposed by the shallow depth of the channel.

5.4 Depth-Averaged Keller–Segel Model

It is important to note that in our analysis, we are assuming that the Keller-Segel model is valid at the pore level. This assumption means that we consider the two species are transported as passive solutes despite the shallow depth of the main channel. Thus, to construct the model in 2D, we must address the dispersal effects of shallow depth on the two species.

For times shorter than $t^* < H^{*2}/D_s^*$, the parabolic flow generates concentration gradients, whereas for $t^* > H^{*2}/D_s^*$, the gradients are uniformly spread [53, 112]. Under the assumption that the shallow depth does not affect chemotactic fluxes, Chu et al. [47] proposed that the classical Taylor–Aris dispersivity theory is valid for times greater than the cross-section (depth) diffusion time scales. Note that their proposed assumption is made without any restrictions on the values of H^*.

In the context of the experimental study in Long and Ford [122], for the main channel devoid of cylindrical pillars, we computed the cross-section diffusion time as follows: $H^{*2}/D_s^* \sim 0.2$ [s]. The short diffusion time indicates that the dispersion of the substrate begins after the concentration travels a short distance of order ε^2. Moreover, the diffusion time is much shorter than both the bacterium run time ($\tau \sim 1$ [s]) and the bias run time for chemotactic gradients $\tau_{\text{ch}} \sim v_s^2/D_s^* = 0.9$ [s]. Therefore, the gradients generated by the shallow channel depth at $t^* < H^{*2}/D_s^*$ are negligible. Thus, we have the microscopic description continuum model of the following form:

$$\frac{\partial \bar{s}_\varepsilon}{\partial t} = \nabla \cdot (\boldsymbol{\mathcal{D}}_s \nabla \bar{s}_\varepsilon - \varepsilon^{-1}\mathrm{Pe}_{loc}\overline{\mathbf{v}}_\varepsilon \bar{s}_\varepsilon), \tag{5.4.1a}$$

$$\frac{\partial \bar{b}_\varepsilon}{\partial t} = \nabla \cdot (\delta \boldsymbol{\mathcal{D}}_b \nabla \bar{b}_\varepsilon - [\varepsilon^{-1}\mathrm{Pe}_{loc}\overline{\mathbf{v}}_\varepsilon + \mathrm{Pe}_b \chi(\bar{s}_\varepsilon)\nabla \bar{s}_\varepsilon]\bar{b}_\varepsilon), \tag{5.4.1b}$$

for all $(t, \mathbf{x}) \in$ on $[0, T] \times \Omega_\varepsilon$, where $\boldsymbol{\mathcal{D}}_s$ and $\boldsymbol{\mathcal{D}}_b$ are the chemoattractant and bacterial population dispersivity with respect to the channel depth, respectively. The flow

is approximated by the depth-averaged velocity $\overline{\mathbf{v}}_\varepsilon$, satisfying the Brinkman equations (5.3.9). The boundary conditions at all external boundaries and the initial conditions for the variables in Section 5.2.4 are modified according to the discussed depth-averaged approximation. The classical Taylor–Aris dispersivity theory for solutes scales with the square of the depth Péclet number defined as:

$$\mathrm{Pe}_h = \frac{V^* D_s^*}{H^*}, \tag{5.4.2}$$

where the characteristic velocity V^* is generated by the pressure drop in a channel devoid of cylindrical pillars. The longitudinal dispersions (x_1-direction) are estimated as follows:

$$\mathcal{D}_s^{*\|} \sim D_s^*[1 + \gamma \mathrm{Pe}_h^2], \tag{5.4.3a}$$

$$\mathcal{D}_b^{*\|} \sim D_b^*[1 + \delta^{-2}\gamma \mathrm{Pe}_h^2], \tag{5.4.3b}$$

where $\gamma = 7.95/210$ [62, 61, 68, 53]. Setting

$$\mathcal{D}_s^{\|} = \mathcal{D}_s^{*\|}/D_s^*, \qquad \mathcal{D}_b^{\|} = \mathcal{D}_b^{*\|}/D_b^*, \qquad \mathcal{D}_s^{\perp} = 1, \qquad \mathcal{D}_b^{\perp} = \delta. \tag{5.4.4}$$

where the classical Taylor dispersion only appears in the flow direction [28, 61, 183]. The dispersion tensors in Eq.(5.4.1) are written as follows:

$$\mathcal{D}_s^{ij} = \mathcal{D}_s^{\perp}\delta_{ij} + (\mathcal{D}_s^{\|} - \mathcal{D}_s^{\perp})\frac{u_i u_j}{|\mathbf{u}|^2}, \tag{5.4.5}$$

$$\mathcal{D}_b^{ij} = \mathcal{D}_b^{\perp}\delta_{ij} + (\mathcal{D}_b^{\|} - \mathcal{D}_b^{\perp})\frac{u_i u_j}{|\mathbf{u}|^2}, \tag{5.4.6}$$

where δ_{ij} is the Kronecker delta and $\mathbf{u} = \mathrm{Pe}\bar{\mathbf{v}}_\varepsilon$ [81].

5.4.1 The Depth-Averaged Homogenised Keller-Segel Model

The channel-depth dispersion tensors, $\boldsymbol{\mathcal{D}}_s$ and $\boldsymbol{\mathcal{D}}_b$, are symmetric and positive definite; therefore, when we apply the asymptotic homogenisation, we obtain an upscaled model similar to the one derived in Section 3.6 of Chapter 3, hence

$$\frac{\partial \bar{\mathcal{S}}}{\partial t} = \nabla \cdot \left(\mathbb{D}_s^{\mathrm{dis}} \nabla \bar{\mathcal{S}} - \mathrm{Pe} \langle \bar{\mathbf{v}}_0 \rangle_{Y^0} \bar{\mathcal{S}} \right) \qquad \text{in } [0,T] \times \Omega, \tag{5.4.7a}$$

$$\frac{\partial \bar{\mathcal{B}}}{\partial t} = \nabla \cdot \left(\mathbb{D}_b^{\mathrm{dis}} \nabla \bar{\mathcal{B}} - \left[\mathrm{Pe} \langle \bar{\mathbf{v}}_0 \rangle_{Y^0} + \mathbb{D}^{\mathrm{ch}} \{ \mathrm{Pe}_b \chi(\bar{\mathcal{S}}) \nabla \bar{\mathcal{S}} \} \bar{\mathcal{B}} \right) \qquad \text{in } [0,T] \times \Omega. \tag{5.4.7b}$$

The dispersion tensors in Eqs.(3.6.10) are rewritten as follows:

$$\begin{cases} \mathbb{D}_s^{\mathrm{dis}} &= \left\langle \left[\boldsymbol{\mathcal{D}}_s (\nabla_{\mathbf{y}} \boldsymbol{\xi})^T + \mathbf{I} \right] - \mathrm{Pe}_{loc} \left[\bar{\mathbf{v}}_0 \otimes \boldsymbol{\xi} \right] \right\rangle_{Y^0}, \\ \mathbb{D}_b^{\mathrm{dis}} &= \left\langle \left[\delta \boldsymbol{\mathcal{D}}_b (\nabla_{\mathbf{y}} \boldsymbol{\xi})^T + \mathbf{I} \right] - \mathrm{Pe}_{loc} \left[\bar{\mathbf{v}}_0 \otimes \boldsymbol{\xi} \right] \right\rangle_{Y^0}, \\ \mathbb{D}^{\mathrm{ch}} &= \left\langle \boldsymbol{\mathcal{D}}_s (\nabla_{\mathbf{y}} \boldsymbol{\xi})^T + \mathbf{I} \right\rangle_{Y^0}, \end{cases} \tag{5.4.8}$$

where $\boldsymbol{\xi}$ solves the following *cell problem* written in general form:

$$\begin{cases} \mathrm{Pe}_{loc}\mathbf{v}\cdot\nabla_{\mathbf{y}}\xi_i - \nabla_{\mathbf{y}}\cdot\big(\boldsymbol{\mathcal{D}}\left[\nabla_{\mathbf{y}}\xi_i + \mathbf{e}_i\right]\big) = \mathrm{Pe}_{loc}\{\langle\bar{\mathbf{v}}_0\rangle_{Y^0} - \bar{\mathbf{v}}_0\}\cdot\mathbf{e}_i & \text{in } Y^0, \\ -\mathbf{n}\cdot\big(\boldsymbol{\mathcal{D}}\left[\nabla_{\mathbf{y}}\xi_i + \mathbf{e}_i\right]\big) = 0 & \text{on } \partial\Sigma^0, \\ \xi_i \text{ is } Y-\text{periodic, and } \langle\xi_i\rangle_{Y^0} = 0, \end{cases} \tag{5.4.9}$$

where $\boldsymbol{\mathcal{D}} \in \{\boldsymbol{\mathcal{D}}_s, \delta\boldsymbol{\mathcal{D}}_b\}$. The Danckwerts boundary conditions at Γ_L are

$$\begin{cases} H_s(\mathbf{x},\bar{\mathcal{S}},\bar{\mathcal{B}}) &= \mathbf{n}\cdot(\mathrm{Pe}\langle\bar{\mathbf{v}}_0\rangle_{Y^0}\bar{\mathcal{S}_i}), \\ H_b(\mathbf{x},\bar{\mathcal{S}},\bar{\mathcal{B}}) &= \mathbf{n}\cdot([\mathrm{Pe}\langle\bar{\mathbf{v}}_0\rangle_{Y^0} + \mathbb{D}^{\mathrm{ch}}\big(\mathrm{Pe}_b\chi(\bar{\mathcal{S}})\nabla\bar{\mathcal{S}}\big)]\bar{\mathcal{B}_i}), \end{cases} \tag{5.4.10}$$

where $\bar{\mathcal{S}}_i = \langle\hat{s}_i\rangle$ and $\bar{\mathcal{B}}_i = \langle\hat{b}_i\rangle$, such that

$$\hat{s}_i = \mathbb{1}_{[0,L_{x_2}/2]}, \quad \text{and} \quad \hat{b}_i = \mathbb{1}_{[-L_{x_2}/2,0]}. \tag{5.4.11}$$

The dimensionless outlet boundary conditions, Γ_R, follow:

$$\begin{cases} H_s(\mathbf{x},\bar{\mathcal{S}},\bar{\mathcal{B}}) &= \mathbf{n}\cdot(\mathrm{Pe}\langle\bar{\mathbf{v}}_0\rangle_{Y^0}\bar{\mathcal{S}}), \\ H_b(\mathbf{x},\bar{\mathcal{S}},\bar{\mathcal{B}}) &= \mathbf{n}\cdot([\mathrm{Pe}\langle\bar{\mathbf{v}}_0\rangle_{Y^0} + \mathbb{D}^{\mathrm{ch}}\big(\mathrm{Pe}_b\chi(\bar{\mathcal{S}})\nabla\bar{\mathcal{S}}\big)]\bar{\mathcal{B}}). \end{cases} \tag{5.4.12}$$

We apply a no-flux condition at $\Gamma_T \cup \Gamma_B$ and zero initial concentrations for the two species to close the effective model. The depth-averaged model homogenisation gives the following dispersion tensors:

$$\mathbb{D}_s^{\mathrm{dis},ij} = \mathbb{D}_\perp^{\mathrm{dis}}\delta_{ij} + (\mathbb{D}_\parallel^{\mathrm{dis}} - \mathbb{D}_\perp^{\mathrm{dis}})\frac{u_i u_j}{|\mathbf{u}|^2}, \tag{5.4.13a}$$

$$\mathbb{D}_b^{\mathrm{dis},ij} = \mathbb{D}_\perp^{\mathrm{dis}}\delta_{ij} + (\mathbb{D}_\parallel^{\mathrm{dis}} - \mathbb{D}_\perp^{\mathrm{dis}})\frac{u_i u_j}{|\mathbf{u}|^2}, \tag{5.4.13b}$$

where δ_{ij} is the Kronecker delta and $\mathbf{u} = \mathrm{Pe}\langle\bar{\mathbf{v}}_{\mathbf{0}}\rangle_{Y^0}$.

5.4.2 The Classical Homogenised Keller-Segel Model

In past studies involving T-sensors, the classical 2D model was applied when studying the mass transport of passive Brownian particles. The convention is justified for T-sensors with a small aspect ratio, since the axial velocity ($x_1x_2 - plane$) becomes uniform [94]. Thus, the effects of the parabolic flow in the shallow depth over the transport of passive Brownian particles can be neglected [94, 68]. Furthermore, the flow velocity is described using the 2D Stokes flow, and the domain is reduced to two dimensions. The classical model is described in Section 3.6 of Chapter 3 and can be retrieved from the depth-averaged model in (5.4.1). For the ease of the reader, we

present the above classical model,

$$\begin{cases} \dfrac{\partial \mathcal{S}}{\partial t} = \nabla \cdot \Big(\mathbf{D}^{\mathrm{dis}} \nabla \mathcal{S} - \mathrm{Pe} \mathcal{V} \mathcal{S} \Big) - \dfrac{\mathrm{Da}}{Y} \dfrac{\mathcal{S}}{\mathcal{S} + \kappa_s} \mathcal{B} & \text{in } [0,T] \times \Omega, \\ \dfrac{\partial \mathcal{S}}{\partial t} = \nabla \cdot \Big(\bar{\mathbf{D}}^{\mathrm{dis}} \nabla \mathcal{B} - \big[\mathrm{Pe} \mathcal{V} + \mathrm{Pe}_b \big\{ \mathbf{D}^{\mathrm{ch}} \chi(\mathcal{S}) \nabla \mathcal{S} \big\} \big] \mathcal{B} \Big) & \\ \qquad + \mathrm{Da} \dfrac{\mathcal{S}}{\mathcal{S} + \kappa_s} \left(1 - \dfrac{\mathcal{B}}{\kappa_c} \right) \mathcal{B} - \kappa_b \mathcal{B} & \text{in } [0,T] \times \Omega. \end{cases} \tag{5.4.14}$$

The dispersion tensors is defined as:

$$\begin{cases} \mathbf{D}^{\mathrm{dis}} &= \Big\langle \big[(\nabla_{\mathbf{y}} \boldsymbol{\xi})^T + \mathbf{I} \big] - \mathrm{Pe}_{loc} \big[\mathbf{v}_0 \otimes \boldsymbol{\xi} \big] \Big\rangle_{Y^0}, \\ \bar{\mathbf{D}}^{\mathrm{dis}} &= \Big\langle \delta \big[(\nabla_{\mathbf{y}} \boldsymbol{\xi}^\delta)^T + \mathbf{I} \big] - \mathrm{Pe}_{loc} \big[\mathbf{v}_0 \otimes \boldsymbol{\xi}^\delta \big] \Big\rangle_{Y^0}, \\ \mathbf{D}^{\mathrm{ch}} &= \Big\langle (\nabla_{\mathbf{y}} \boldsymbol{\xi})^T + \mathbf{I} \Big\rangle_{Y^0}, \end{cases} \tag{5.4.15}$$

where $\boldsymbol{\xi}(\mathbf{y}) = (\xi_1, \xi_2)^T$ is the solution of the cell-problem

$$\begin{cases} \mathrm{Pe}_{loc} \mathbf{v}_0 \cdot \nabla_{\mathbf{y}} \xi_i - \nabla_{\mathbf{y}} \cdot [\nabla_{\mathbf{y}} \xi_i + \mathbf{e}_i] = \mathrm{Pe}_{loc} \{ \langle \mathbf{v}_0 \rangle_{Y^0} - \mathbf{v}_0 \} \cdot \mathbf{e}_i & \text{in } Y^0, \\ -\mathbf{n} \cdot [\nabla_{\mathbf{y}} \xi_i + \mathbf{e}_i] = 0 & \text{on } \partial \Sigma^0, \\ \xi_i \text{ is } Y - \text{periodic, and } \langle \xi_i \rangle_{Y^0} = 0, \end{cases} \tag{5.4.16}$$

The Danckwerts boundary conditions at Γ_L are

$$\begin{cases} H_s(\mathbf{x}, \mathcal{S}, \mathcal{B}) &= \mathbf{n} \cdot (\mathrm{Pe} \langle \mathbf{v}_0 \rangle_{Y^0} \mathcal{S}_i), \\ H_b(\mathbf{x}, \mathcal{S}, \mathcal{B}) &= \mathbf{n} \cdot ([\mathrm{Pe} \langle \mathbf{v}_0 \rangle_{Y^0} + \mathbf{D}^{\mathrm{ch}} \big(\mathrm{Pe}_b \chi(\mathcal{S}) \nabla \mathcal{S} \big)] \mathcal{B}_i), \end{cases} \tag{5.4.17}$$

where $\mathcal{S}_i = \langle \hat{s}_i \rangle$ and $\mathcal{B}_i = \langle \hat{b}_i \rangle$, such that

$$\hat{s}_i = \mathbb{1}_{[0, L_{x_2}/2]}, \quad \text{and} \quad \hat{b}_i = \mathbb{1}_{[-L_{x_2}/2, 0]}. \tag{5.4.18}$$

The dimensionless outlet boundary conditions, Γ_R, follow:

$$\begin{cases} H_s(\mathbf{x}, \mathcal{S}, \mathcal{B}) &= \mathbf{n} \cdot (\mathrm{Pe} \langle \mathbf{v}_0 \rangle_{Y^0} \mathcal{S}), \\ H_b(\mathbf{x}, \mathcal{S}, \mathcal{B}) &= \mathbf{n} \cdot ([\mathrm{Pe} \langle \mathbf{v}_0 \rangle_{Y^0} + \mathbb{D}^{\mathrm{ch}} \big(\mathrm{Pe}_b \chi(\mathcal{S}) \nabla \mathcal{S} \big)] \mathcal{B}). \end{cases} \tag{5.4.19}$$

We apply a no-flux condition at $\Gamma_T \cup \Gamma_B$ and zero initial concentrations for the two species to close the effective model. The classical model homogenisation gives the following dispersion tensors:

$$D_s^{\mathrm{dis},ij} = D_\perp^{\mathrm{dis}} \delta_{ij} + (D_\parallel^{\mathrm{dis}} - D_\perp^{\mathrm{dis}}) \frac{u_i u_j}{|\mathbf{u}|^2}, \tag{5.4.20a}$$

$$D_b^{\mathrm{dis},ij} = D_\perp^{\mathrm{dis}} \delta_{ij} + (D_\parallel^{\mathrm{dis}} - D_\perp^{\mathrm{dis}}) \frac{u_i u_j}{|\mathbf{u}|^2}, \tag{5.4.20b}$$

where δ_{ij} is the Kronecker delta and $\mathbf{u} = \mathrm{Pe} \langle \mathbf{v_0} \rangle_{Y^0}$.

5.5 Numerical Investigations

All numerical simulations were obtained using COMSOL Multiphysics™(version 5.3a) using a default element type and solver. In each simulation step, we conducted a mesh refinement procedure to verify that the obtained data were independent of the computational elements for all simulations.

Remark 5.2. *For all simulations assuming both chemotactic sensitivity functions defined in Eqs.*(3.4.50)*, the effective model provided the same results. Furthermore, the time-stepping simulations at a steady state gave the same results when simulating the stationary model.*

5.5.1 Effective Dispersion Tensors

In this section, the simulation results are obtained assuming the classical effective model described in Section 5.4.2. The effective tensors for the bacterial population and the tracer (fluorescein) were obtained by solving the *cell problem* in (5.4.16) defined on the periodic unit cell shown in Figure 5.4. The zero order flow approximation in (5.4.16) is derived by upscaling the 2D Stokes equation in porous media, as demonstrated in Section 3.2. Note that the simulations showed that dispersion tensors in Eqs.(5.4.15) to be diagonal.

The log-log plots of two dispersion components computed using a range of values of the Péclet number, $\mathrm{Pe} = 1 - 6 \times 10^4$. As expected, the dispersion tensors are decomposed into the sum of a diffusive term and mechanical dispersion term; thus, the log-log plots reveal that the mechanical term does not kick in when the Péclet number values define diffusion-advective regimes. The plots demonstrate that when $\mathrm{Pe} < \mathcal{O}(\varepsilon^{-1})$, we obtain isotropic diffusion tensors,

$$\mathbf{D}^{\mathrm{dis}} = D^h \mathbf{I}. \tag{5.5.1}$$

The mechanical effects of the flow start when the Péclet number reaches $\mathcal{O}(\varepsilon^{-1})$. For that order, we obtain two diagonal dispersion tensors with longitudinal and transverse components. The tensors are expressed in Eq.(5.4.20). The transverse dispersion is visualised by the eigenvector perpendicular to the flow (x_2-direction), whereas the longitudinal dispersion is visualised by the eigenvector describing the dispersions in the direction of the flow (x_1-direction). At the order ε^{-1}, the two eigenvalue plots $D_{\perp}^{\mathrm{dis}}$ and $D_{\parallel}^{\mathrm{dis}}$ initially appear to follow power law behaviour. As the flow velocity increases, the transverse eigenvalue overtakes the longitudinal eigenvalue. However, when the value of the Péclet number reaches ε^{-2}, the transverse eigenvector reaches an inflexion point and plateaus from the initial power law growth, whereas the longitudinal dispersion continues following power law behaviour.

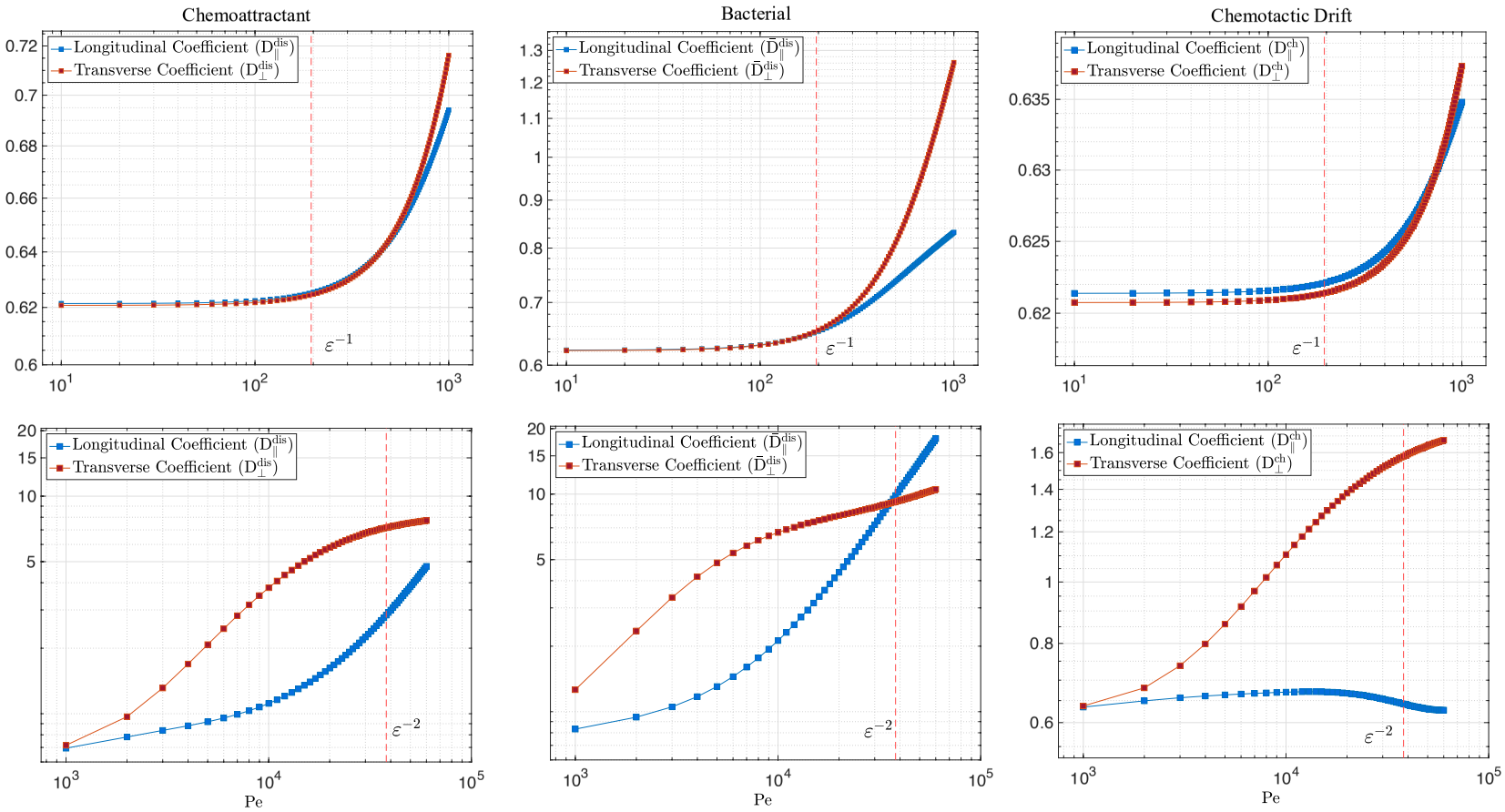


Figure 5.5: *Log-log plots for eigenvalues of the dispersion tensors for the chemoattractant, bacteria ($D^{*\star} = D_b^*$) and the chemotactic drift ($\varepsilon^{-1} = 195$). The vertical lines mark the orders ε^{-1} and ε^{-2}. The effective tensors were obtained by solving* (5.4.16) *defined on the periodic unit cell shown in Figure 5.4. While the zero order flow approximation in* (5.4.16) *is derived from the homogenisation of the 2D Stokes equation in porous media, as demonstrated in Section 3.2.*

The behaviour of two hydrodynamic dispersion eigenvalues, illustrated in Figure 5.5, agrees with the behaviour of the experimental results from Daneyko et al. [52] using a similar microstructure. In the log-log plots of the chemotactic tensor of the transverse eigenvalue $D_{\perp}^{\mathrm{ch}}$ and the longitudinal eigenvalue $D_{\parallel}^{\mathrm{ch}}$, the variation between the two eigenvalues is quite small in comparison. Both eigenvalues remain close to each other for all Pe_{loc}, resulting from computing the chemoattractant tensor $\mathbf{D}^{ch}$ without the effect of mechanical dispersion. Including the classical Taylor dispersion of the chemoattractant and bacterial suspension generated by the shallow channel geometry would not change the general effective tensor behaviour in Figure 5.5.

In conclusion, according to the plots in Figure 5.5, we expect an enhanced transport in the transverse direction of the flow for both species. Thus, the pore structure enhances the mixing in the main channel of the T-sensor. However, the chemotactic tensor experiences small variations in its two eigenvalues; thus, the chemotactic drift enhancement depends on the mixing efficiency between the two species. Mixing in the T-sensor occurs at the interface between the two injected species.

5.5.2 Effective Mixing Boundary Layer

The mixing efficiency of T-sensor is often measured by the width of the mixing boundary layer between two streams. The mixing boundary layer is a transition zone between two streams characterised by a large concentration gradient. An increase in the width of the mixing zone indicates efficient mixing across the interface. To uncover the effect of the porous microstructures on the mixing boundary layer, we consider the single species model describing the tracer and microbial tests. The simulations of the non-chemotactic tests are achieved by letting: $\delta = 1$ and $\chi_0 = 0$ in the bacteria equation. In Figure 5.6, we plotted the spatial distribution for the chemoattractant concentrations and chemoattractant gradient in the main channel. In the plots, the mixing layer of the concentration and the chemotactic gradient plume broaden at the channel centreline: $x_2^* = 0$. The effectiveness of the mixing process in the main channel is correlated with the broadening of the propagated concentration in the axial direction, following a normal distribution [204, 173, 192]. At a transect located at x_1^*, the concentration $C = C^*/C_i^*$ reads as follows:

$$F(x_2^*) = C = \frac{1}{2}\left[1 - \mathrm{erf}\left(\frac{x_2^*}{\sigma^*\sqrt{2}}\right)\right]. \tag{5.5.2}$$

The standard deviation detected at time t^* asymptotically approaches

$$\sigma^* = \sqrt{D^* t^*}. \tag{5.5.3}$$

Assuming a steady-state system, by replacing t^* with the diffusion time, $T^* = x_1^*/V^*$, we arrive at the following theoretical estimation of the boundary layer width:

$$\delta^*(x_1^*) = \sqrt{\frac{x_1^* D^*}{V^*}}. \tag{5.5.4}$$

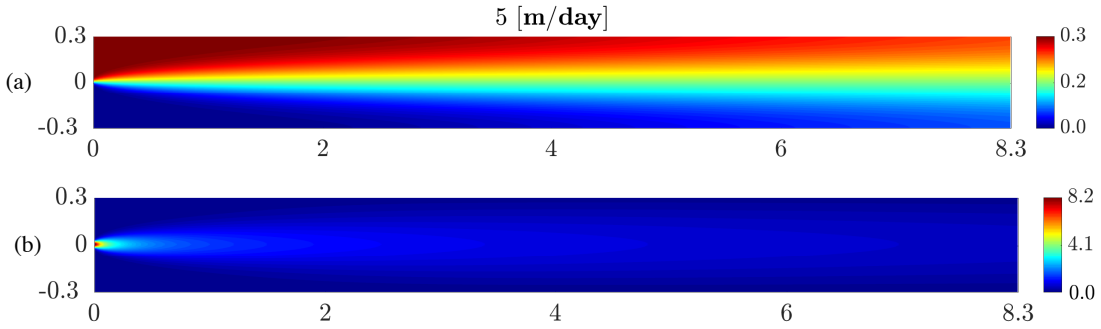


Figure 5.6: *Numerical results of the homogenised model in the 2D domain: (a) dimensional spatial distribution of the chemoattractant concentration $\mathcal{S}^*$ under different flow velocities and (b) spatial concentration of the chemoattractant gradient* $\|\nabla^*\mathcal{S}^*\| = \sqrt{\left(\partial\mathcal{S}^*/\partial x_1^*\right)^2 + \left(\partial\mathcal{S}^*/\partial x_2^*\right)^2}$. *The plots were obtained by solving* (5.4.16) *defined on the periodic unit cell shown in Figure 5.4. The zero order flow approximation in* (5.4.16) *is derived by upscaling the 2D Stokes equation in porous media, as demonstrated in Section 3.2.*

The broadening of the mixing zone down the channel is generated by cross-stream flux rates, whereas translational diffusion is absent. Similarly, in the porous T-sensor, the dispersion in the transverse direction is critical in enhancing the mixing process, whereas the longitudinal dispersion is absent [1, 52]. Thus, we write Eq. (5.5.2) using the homogenisation results as follows:

$$\mathcal{F}_{\text{eff}}(x_2^*) = \mathcal{C}_{\text{eff}} = \frac{1}{2}\left[1 - \text{erf}\left(\frac{x_2^*}{\sigma_{\text{eff}}^*\sqrt{2}}\right)\right]. \tag{5.5.5}$$

Thus, the effective theoretical boundary layer is estimated by

$$\delta_{\text{eff}}^*(x_1^*) = \sqrt{\frac{x_1^* D^* D_\perp^{\text{dis}}}{V^*}}. \tag{5.5.6}$$

Finally, we write Eq.(5.5.4) and Eq. (5.5.6) in dimensionless form at transect $x_2(i) = i\varepsilon$ (for $i = 1, \cdots N$), respectively, as follows:

$$\delta(i) = \sqrt{i\varepsilon \text{Pe}^{-1}}, \tag{5.5.7}$$

$$\delta_{\text{eff}}(i) = \sqrt{i\varepsilon \text{Pe}_\perp^{-1}}, \tag{5.5.8}$$

where $\text{Pe}_\perp = (L_{x_1^*} V^*)/(D^* D_\perp^{\text{dis}})$. The exact width of the effective boundary layer is equal the full width at half maximum (FWHM) of the Gaussian function (see Figure 5.7 for more details).

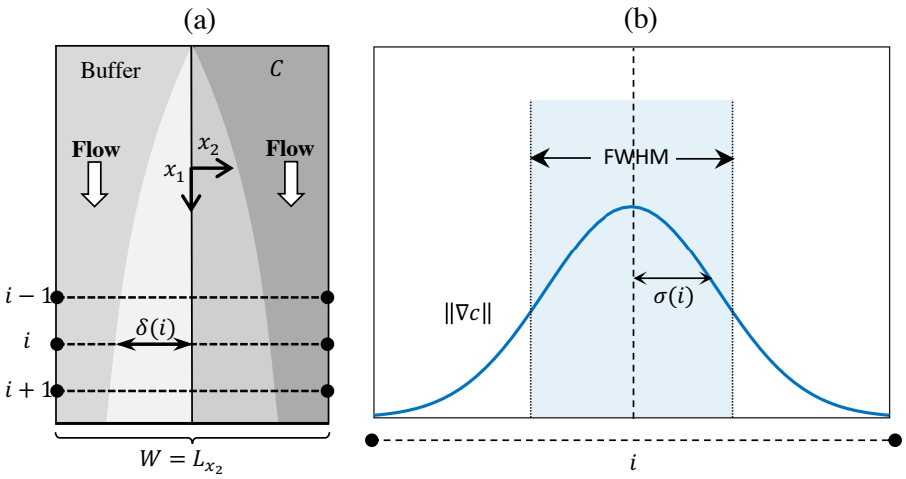


Figure 5.7: *(a) Illustration of the non-dimensional mixing boundary layer. (b) Full width at half maximum of the Gaussian probability density curve* FWHM*. Using direct numerical simulations, we computed* FWHM *using a MATLAB function [143] (*$(\text{FWHM}) = 2\sqrt{2\ln 2}\,\sigma \sim 2.355\sigma$*).*

As expected, the broadening of the mixing layer is enhanced in the porous microstructure (see Figure 5.8). The increase in transverse dispersion increases the boundary layer widths. However, Figure 5.8 reveals that the broadening of the exact mixing layer reaches a limit, then plateaus. This result can be explained formally by the fact that, in such cases, the exact boundary layer reaches a saturation level near the boundaries not accounted for in Eq.(5.5.8) [90]. Interestingly, as the flow velocity increases to $V^* = V^*_{avg} = 20$ [m/day], the exact mixing layer does not saturate, which may predict hindered mixing by the flow.

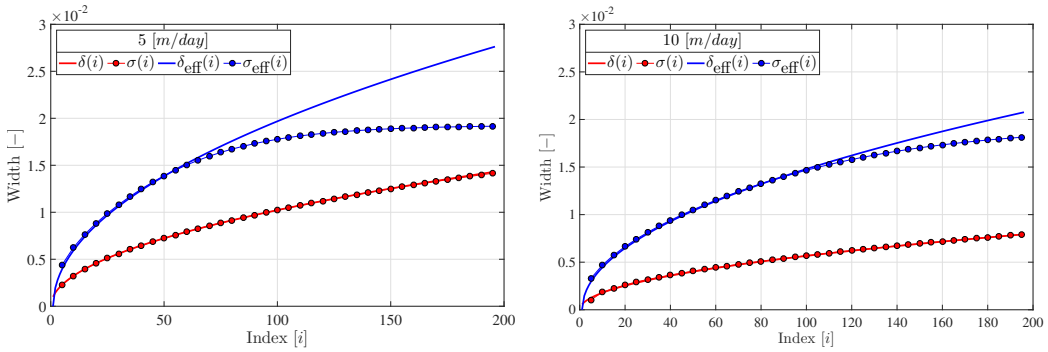
5.6 Comparison Against Experimental Data

In this section we test the effective model predictions against the data in Long and Ford [122] and the simulation results of the upscaled model in Porter et al. [157]. We aim to test the validity of upscaled model and provide more insight regarding the transport of bacterial population in such experiments.

5.6.1 Testing the Classical Homogenised Model

Traditionally, the linear velocity measurements reported in Long and Ford [122] refer to the superficial velocities obtained by estimating the permeability of porous media

(a) $V^*_{avg} = 5\ [m/day]$ (b) $V^*_{avg} = 10\ [m/day]$



(c) $V^*_{avg} = 20\ [m/day]$

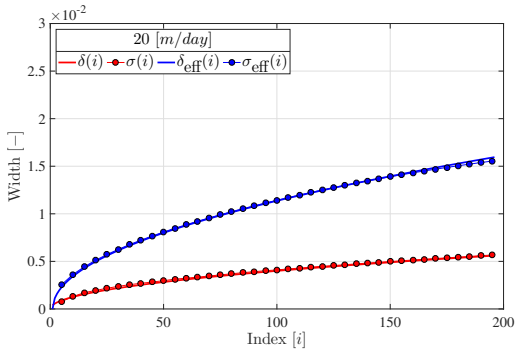


Figure 5.8: *Plots of the boundary layer width at transient locations represented with indices $i = 2 \cdots 195$, such that $x_1(i) \leftarrow i$. Here we are solving* (5.4.16) *defined on the periodic unit cell shown in Figure 5.4. where the zero order flow approximation in* (5.4.16) *is derived by upscaling the 2D Stokes equation in porous media, as demonstrated in Section 3.2. Red curves denote the width of boundary layers computed assuming the original model defined in a 2D non-porous domain, whereas blue curves denote boundary layers using the homogenised model.*

using the Carman-Kozeny equation [180, 165, 56, 174, 92]. In the context of asymptotic homogenisation, the superficial (Darcy velocity) and the interstitial (mean pore velocity) linear velocities are related as follows:

$$\underbrace{\langle \mathbf{v}_0^* \rangle_{Y^0}}_{\substack{\text{interstitial} \\ \text{velocity}}} = \phi^{-1} \underbrace{\langle \mathbf{v}_0^* \rangle}_{\substack{\text{superficial} \\ \text{velocity}}}, \tag{5.6.1}$$

where $\phi = 0.4$. It is worth noting that it has been shown that the experimentally estimated permeability is not the same as the permeability obtained using upscaling methods [193, 174]. However, since any detailed informations regarding the pressure drop and volumetric flow rates are inaccessible, we set the provided experimental readings of the linear velocities as the characteristic flow at the inlet and the outlet

in Eq.(5.2.9). For comparison reasons, we consider the reported linear flow velocities in (5.1.3) to represent both the superficial velocity, $\langle \mathbf{v}_0^* \rangle_{Y^0} = V_{avg}^*$ and interstitial linear velocity, $\langle \mathbf{v}_0^* \rangle_{Y^0} = \phi^{-1} V_{avg}^*$.

Figure 5.9 displays the simulation results for the tracer data, while Figure 5.10 shows the results for the bacterial controlled data. The simulation for $\langle \mathbf{v}_0^* \rangle_{Y^0} = \phi^{-1} V_{avg}^*$ and $\langle \mathbf{v}_0^* \rangle_{Y^0} = V_{avg}^*$, are almost the same. For the chemotactic data test, when setting $\langle \mathbf{v}_0^* \rangle_{Y^0} = \phi^{-1} V_{avg}^*$, the classical model provided better predictions for $V_{avg}^* = 10,\ 20$ [m/day]; however, it failed to improve the predictions of the density peak location and height for $V_{avg}^* = 5$ [m/day], as seen in Figure 5.11. The results of the upscaled model developed using the volume averaging method in Porter et al. [157] were equivalent to the homogenised classical model if we set $\langle \mathbf{v}_0^* \rangle_{Y^0} = V_{avg}^*$, as shown in Figure 5.11. By looking at the chemotactic test data alone, we can conclude that an increase in the average pore water velocity makes chemotactic transverse migration less likely. Porter et al. [157] claim that their effective chemotactic model without chemotactic drift fits the data better when the average flow is greater than 20 [m/day]. However, based on our simulations, $\langle \mathbf{v}_0^* \rangle_{Y^0} = \phi^{-1} V_{avg}^*$, gave a better fit of the data for flow velocities starting from 10 [m/day], as seen in Figure 5.11.

So far, we have seen that the classical model developed using the asymptotic homogenisation method and the upscaled model developed using volume averaging gave similar predictions for the same mean pore flow. However, it is important to note that the two upscaled models are distinct. The volume averaging method considers the dispersion effects of the chemotactic velocity in each periodic subdomain. Therefore, the resulting upscaled model depends on the simulation results at each of the 4700 subdomains since the chemoattractant gradient values change in space and time. However, according to simulations conducted by Porter et al. [157], the chemotactic drift averaged zero in most subdomains, except for a small region near the entrance characterised by steep gradients, as illustrated in Figure 5.6. Therefore, the computed chemotactic dispersion at each subdomain had no significant influence on the overall distribution of the bacterial density. However, using the asymptotic homogenisation method, we established that the chemotactic drift role only appears globally before applying the procedure. Thus, simulating the effective model is less expensive. Lastly, the identical simulation results of the two upscaled models indicate the robustness of the two upscaling methods. Furthermore, it serves as numerical validation for the effective model in Section 3.6 of Chapter 3.

5.6.2 Testing the Homogenised Depth-Averaged Model

In general, in T-sensor devices, the diffusion appears in the transverse direction of the flow [93, 41, 129]. Thus, any change in the longitude component has no effect. Therefore, when we imposed the classical longitude dispersion the simulation results of the classical homogenised model shown in Figures 5.9, 5.10, and 5.11 remained unchanged (simulation results are not shown). Thus, any discrepancies be-

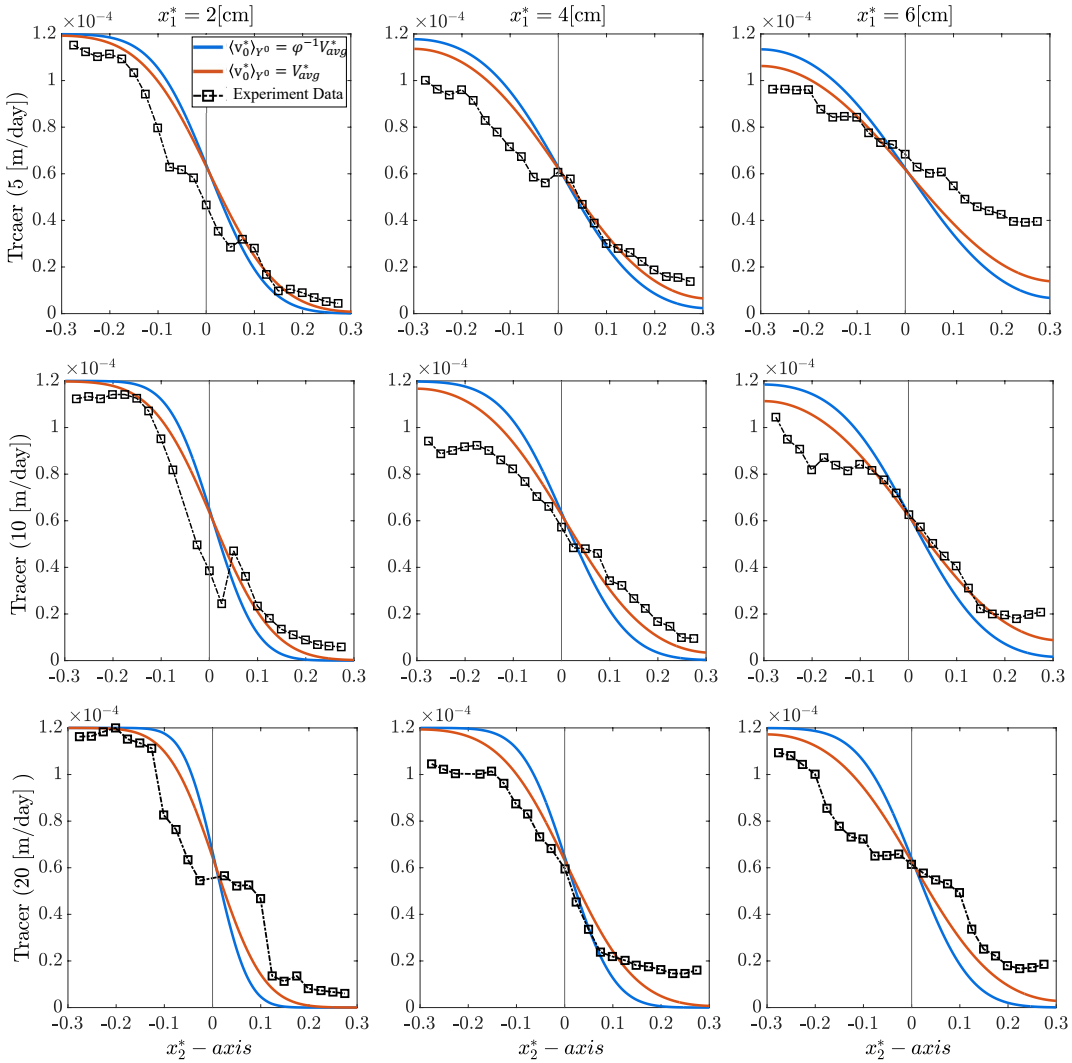


Figure 5.9: *Plots with the predicted tracer profiles using the homogenised classical model in* (5.4.14)-(5.4.19) *modified to consider the transport of the tracer alone. The profiles were plotted against the experimental data from Long and Ford [122]. In these simulations we assumed both the superficial velocity,* $\langle \mathbf{v}_0^* \rangle_{Y^0} = V_{avg}^*$*, and interstitial linear velocity,* $\langle \mathbf{v}_0^* \rangle_{Y^0} = \phi^{-1} V_{avg}^*$.

tween the depth-averaged and classical homogenised models are attributable to the differences between local depth-averaged and the classical Darcy flow models at the local scale. The effect of the local flow appears when computing the dispersion tensors in Eqs.(5.4.8) associated with the cell problems in Eqs.(5.4.9).

In Figure 5.12, we notice some improvement in the tracer concentrations using the depth-averaged homogenised model, especially for $V_{avg}^* = 20$ [m/day]. Interestingly,

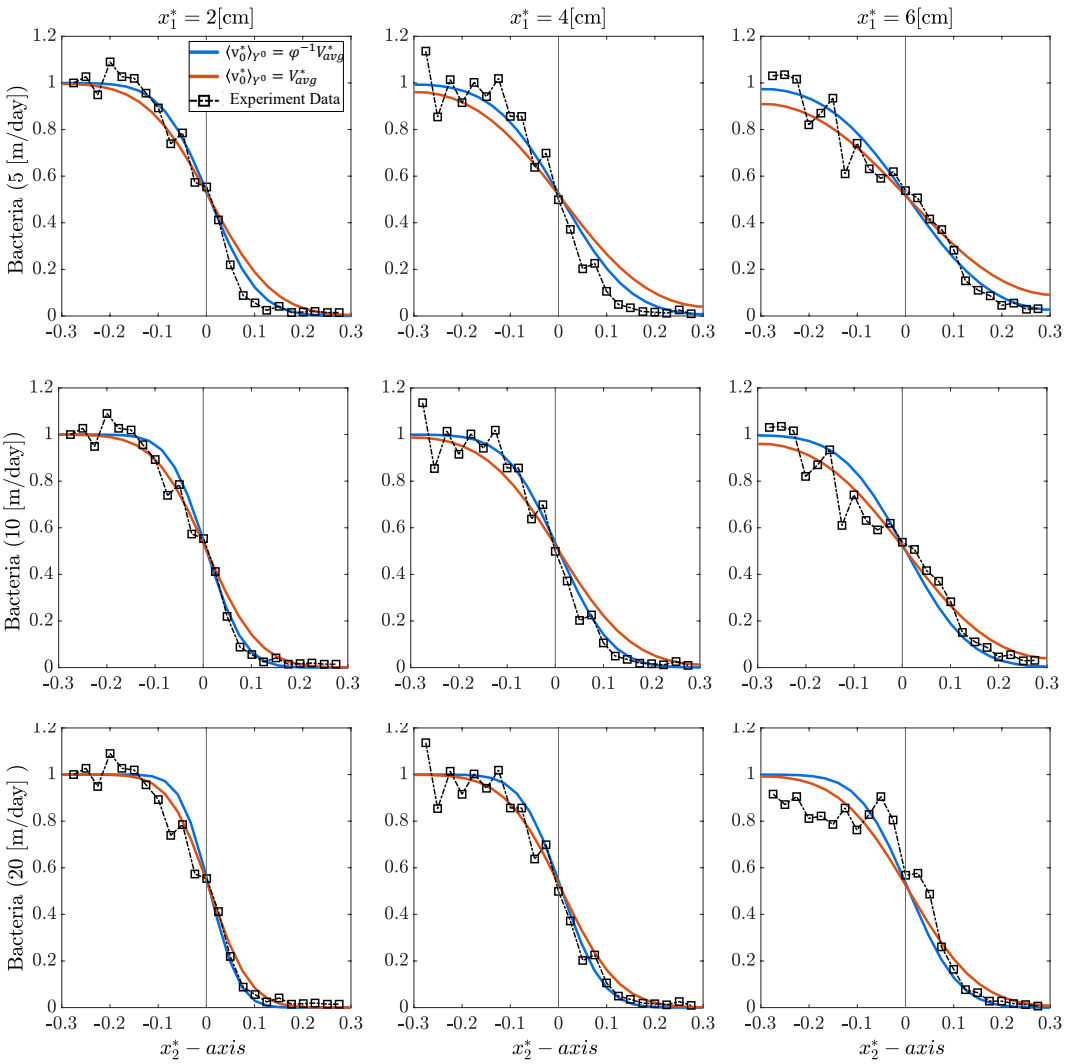


Figure 5.10: *Plots with the predicted bacteria profiles for the non-chemotactic test (control test) using the classical model in* (5.4.14)-(5.4.19) *modified to consider the transport of the bacteria alone. The bacterial density was scaled by the initial injected density and plotted against the experimental data from Long and Ford [122]. As in Figure 5.9, we assumed both the superficial velocity,* $\langle \mathbf{v}_0^* \rangle_{Y^0} = V_{avg}^*$*, and interstitial linear velocity,* $\langle \mathbf{v}_0^* \rangle_{Y^0} = \phi^{-1} V_{avg}^*$*.*

when using the depth-averaged model, the bacterial densities gave worse predictions as the density curves became flatter with increased flow velocities, as shown in Figure 5.13. Furthermore, as seen in Figure 5.14, the depth-averaged homogenised model fails to generate any chemotactic transverse migration when compared to the classical

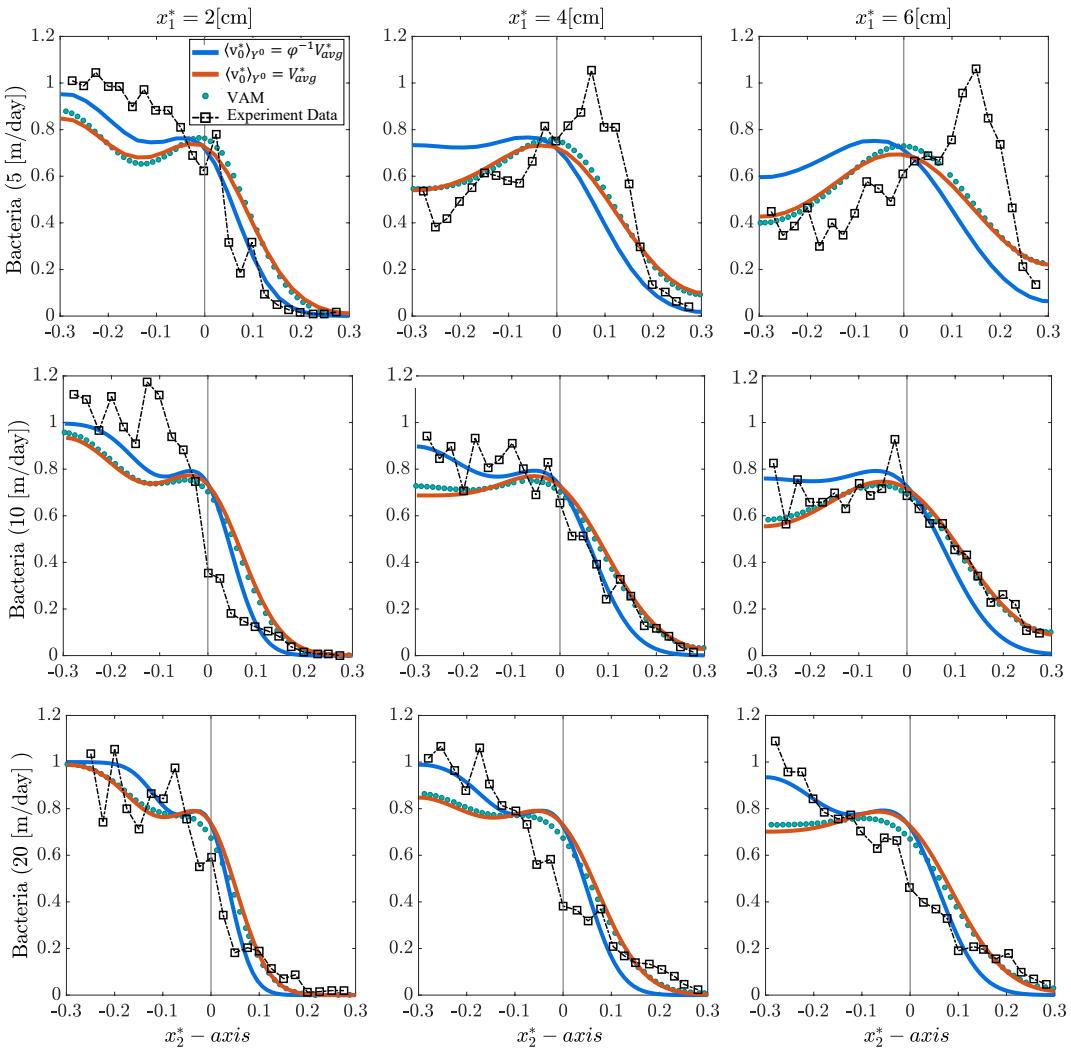


Figure 5.11: *Plots of the predicted chemotactic bacterial population profiles using the classical model in* (5.4.14)-(5.4.19)*, the bacterial density was scaled by the initial injected density and plotted against the experimental data from Long and Ford [122]. As before, in the simulations we assumed both the superficial velocity,* $\langle \mathbf{v}_0^* \rangle_{Y^0} = V_{avg}^*$*, and interstitial linear velocity,* $\langle \mathbf{v}_0^* \rangle_{Y^0} = \phi^{-1} V_{avg}^*$*.*

model. Therefore, we deduce that when using the depth-average model the chemotactic drift plays no role in the transport of the chemotactic bacteria population.

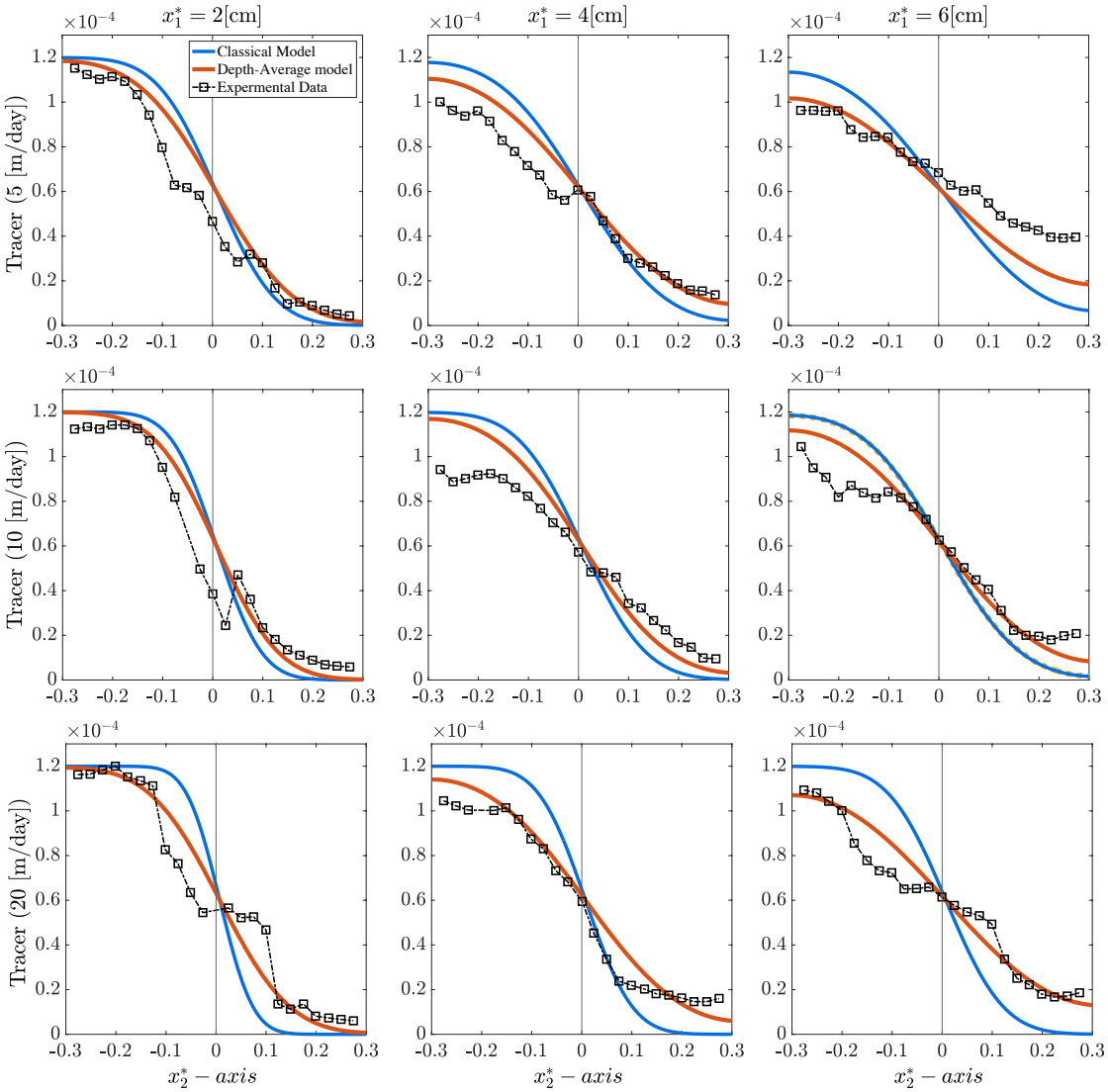


Figure 5.12: *Plots comparing the predicted tracer profiles obtained from simulating the homogenised classical model in* (5.4.14)-(5.4.19) *and the depth-averaged model in* (5.4.7)-(5.4.12) *after being modified to account for the tracer transport only. The tracer profiles are plotted against the experimental tracer data from Long and Ford [122] while assuming* $\langle \mathbf{v}_0^* \rangle_{Y^0} = \langle \bar{\mathbf{v}}_0^* \rangle_{Y^0} = \phi^{-1} V_{avg}^*$.

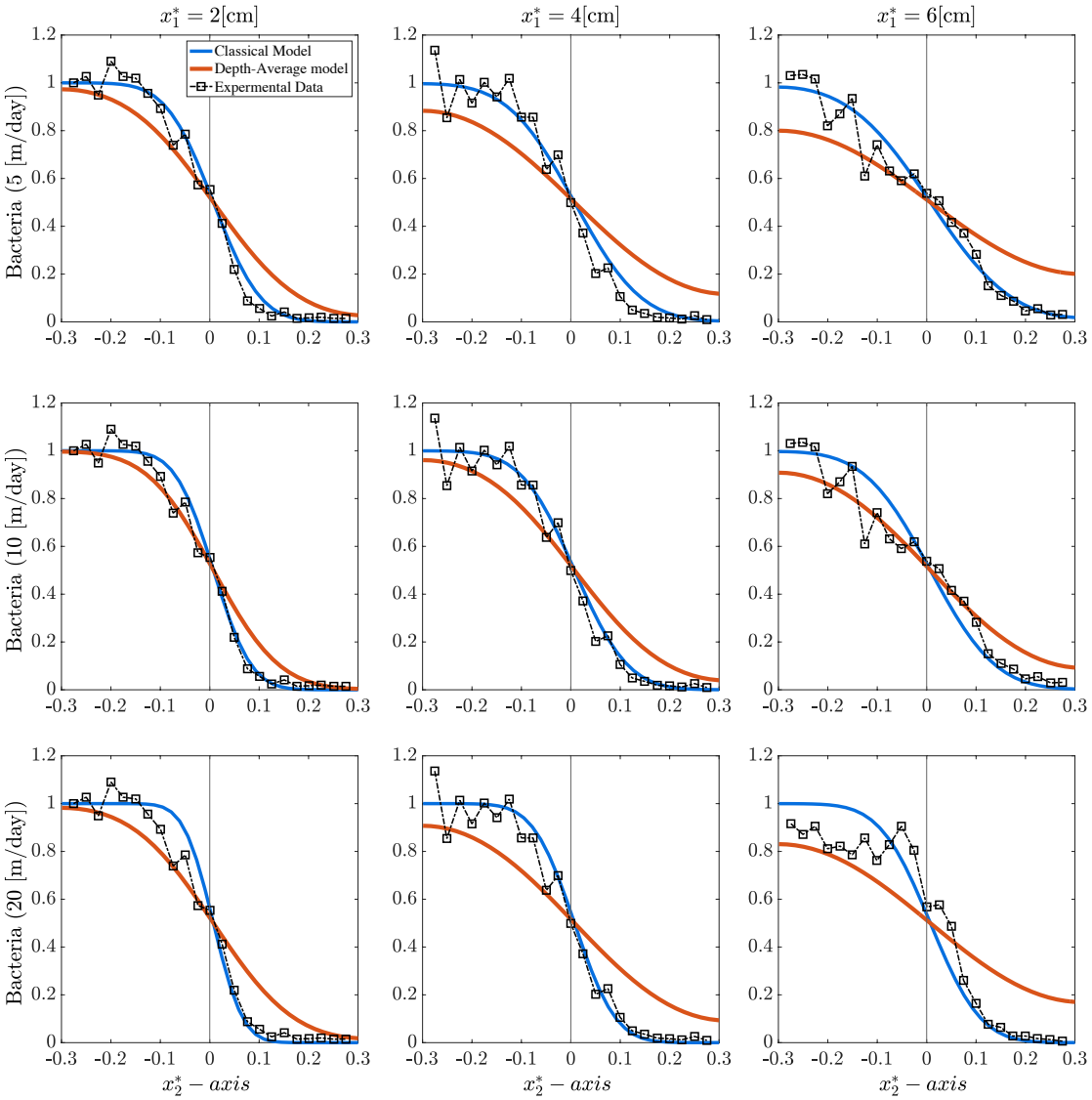


Figure 5.13: *Repeated tests comparing the predicted control profiles against the experimental control data from Long and Ford [122]. Here we conducted simulations of the classical model in* (5.4.14)-(5.4.19) *and the depth-averaged model in* (5.4.7)-(5.4.12) *after being modified to account for the transport of the bacterial density in the control test only. In the simulations we assumed that* $\langle \mathbf{v}_0^* \rangle_{Y^0} = \langle \bar{\mathbf{v}}_0^* \rangle_{Y^0} = \phi^{-1} V_{avg}^*$.

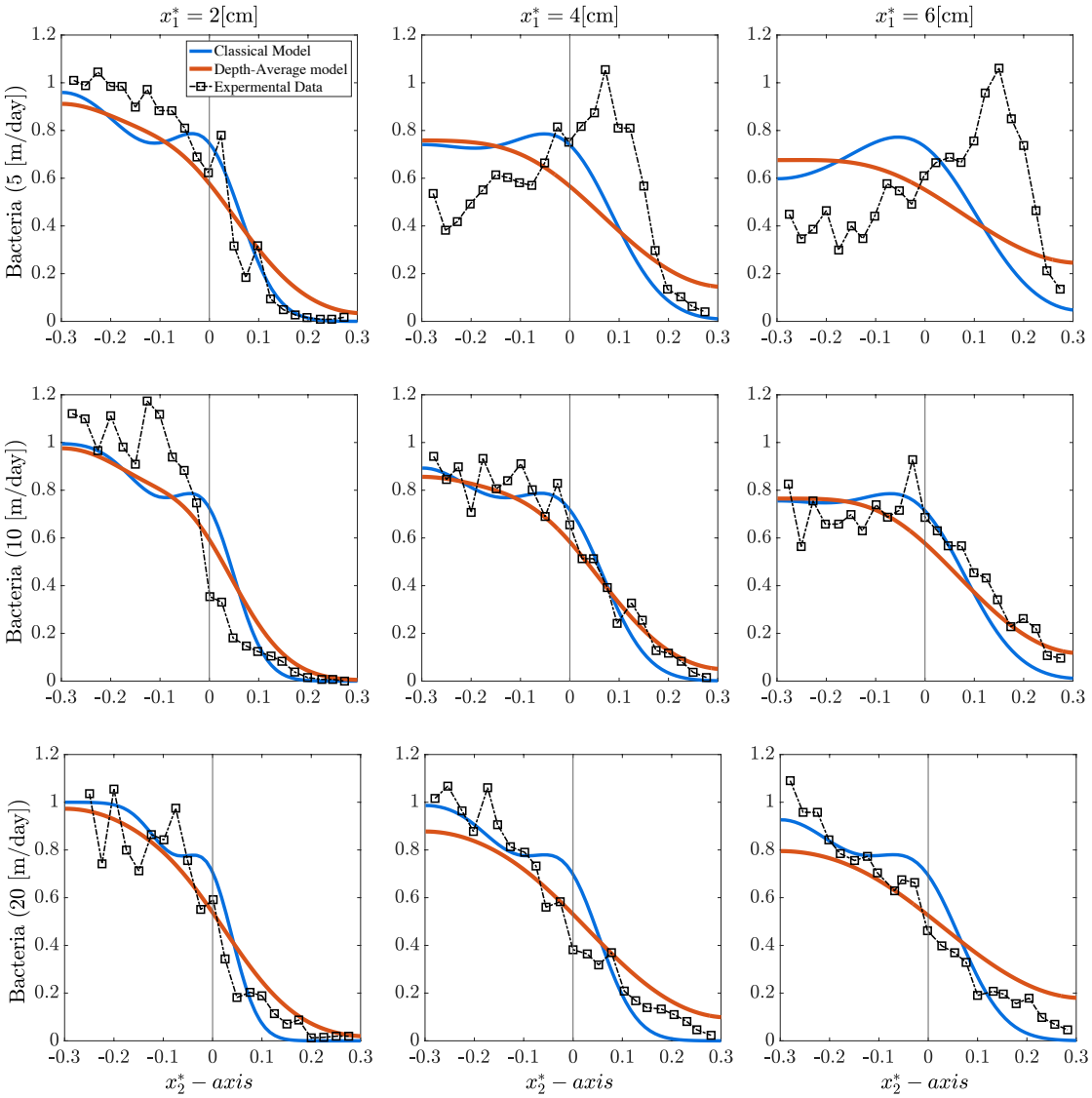


Figure 5.14: *Plots comparing the chemotactic test data from Long and Ford [122] against the predictions obtained from the simulations of the classical model in* (5.4.14)-(5.4.19) *and the depth-averaged model in* (5.4.7)-(5.4.12). *Here we are assuming* $\langle \mathbf{v}_0^* \rangle_{Y^0} = \langle \bar{\mathbf{v}}_0^* \rangle_{Y^0} = \phi^{-1} V_{avg}^*$.

5.7 Discussion and Conclusions

This chapter investigated the performance and accuracy of the homogenised Keller-Segel model in flow-based microfluidic devices. First, we expressed the Stokes flow and the classical Keller-Segel model in the main channel. Then, we proposed two approaches to express the transport model in two dimensions (the classical and depth-averaged models). The simulation results of the homogenised classical Keller-Segel model were identical to the results using the upscaled model developed using the volume averaging method, which reinforces the claim regarding the robustness of the two upscaled models. We claim that the identical simulation results are a numerical validation of the proposed upscaled model using asymptotic homogenisation. Furthermore, we argued that using asymptotic homogenisation gives a much simpler model that is easier to simulate.

Following that, we conducted two numerical studies. In the first study, we computed the effective dispersivities associated with the classical effective model and verified that the dispersion tensor's behaviour agrees with behaviour of the experimentally computed tensors with similar microstructure. Then, we used the tensors to investigate and analyse the effect of the microstructure on enhancing the mixing zone. We compared the effective models with the experimental data in the second numerical study. In the non-chemotactic model, the simulations provided better predictions for the passive tracer data with the depth-averaged model. However, the classical model presented a better fit for the bacterial control test. The trend continued when simulating for the chemotactic test data. Overall, the depth-average model failed to fit the chemotactic test data. The inconsistency between the predictions suggests that the suspended bacterial population no longer behaves as a passive tracer. We provide a general discussion concerning these inconsistencies below.

The most important point we want to address concerns the application of the classical Taylor dispersion theory to the bacterial motility. Note that, when developing the depth-averaged model, we followed the suggestions in the study of Chu et al. [47] to justify applying the classical Taylor dispersivities as in the case for diffusiophoretic. However, the simulations results were not in favour of the generalisation suggested in Chu et al. [47]. One reason is that although diffusiophoresis colloid transport model is similar to the Keller-Segel model where the chemotactic velocity is replaced with

$$\chi(s^*)\nabla^* s^* := \Gamma_p \nabla^* \log s^*, \tag{5.7.1}$$

where Γ_p denotes the diffusiophoretic mobility of the suspended colloidal particles [18, 19, 47], the size of the particles is much smaller ($0.1 - 10$ [nm]). In general, large colloidal particles carried by the flow are sterically excluded from the region of slow fluid motion near the walls. Therefore, larger solutes actually move faster than smaller solutes [53]. In fact, as we have mentioned in the Chapter 1, Peng and Brady [154] showed that classical Taylor dispersion is applicable only when $\mathrm{Kn}_H \ll 1$. This is not the case for the microfluidic device in Long and Ford [122] where $\mathrm{Kn}_H > 1$.

Therefore, the Keller-Segel model in VTPM in Section 5.2.3 is not well defined, since the bacteria motility at the pore scale is no longer diffusive. Moreover, the swimming behaviour of bacterial changes near the wall when $\mathrm{Kn}_H \ll 1$ depending on the flow velocity values [154].

Chapter 6

Conclusions

This chapter will conclude the thesis by summarising the most significant findings and connecting those findings to the main objectives of the research. In addition, it will explain the study's limitations and provide future directions that could be pursued by subsequent research.

6.1 Review of the Thesis

This thesis addresses the chemotactic transport of bacteria suspension in a saturated porous medium under different flow conditions. The body of this thesis was motivated by several experimental studies investigating the role of chemotaxis in enhancing the removal of contaminants in subsurface environments. We organised the chapters to serve two aims: the first concerns describing the mathematical model in a porous medium; the second concerns performing different numerical investigations of theoretical and experimental case studies. The investigations aimed to validate the effective model we derived by comparing the predicted results of the effective model with direct simulations of the Keller-Segel model in porous media or using experimental data. In Chapter 2, we proposed a classical Keller-Segel model that incorporated confinement, unidirectional flows and metabolic rates. We started with a discussion about the validity of defining a continuum model at the pore scale. It follows that assuming a weak porosity domain is sufficient to ensure theoretical validity of the continuum model in a porous microstructure. More simplified assumptions were introduced to limit the chemotactic mechanism to the aqueous phase. In Chapter 3, we applied the asymptotic homogenisation procedure by first scaling the different processes according to their effects on mass flow at the microscopic scale. We argued, using dimensionless analysis, that the chemotactic velocity and metabolic rate processes effects on the mass transport appear only at the global scale. The only limiting cases affecting the mass transport are related to the flow strength, and thus, we have three effective regimes: the diffusion, the advection-diffusion and the

advection-dispersion transport regimes. The homogenisation procedure revealed that the chemotactic drift is scaled according to the diffusion time scale of the substrate (chemoattractant) effective tensor. Compared to the upscaled Keller-Segel model obtained using volume averaging methods in Valdés-Parada et al. [195], the effective models developed using asymptotic homogenisation are of a simpler form. Moreover, we included metabolic terms not considered in Valdés-Parada et al. [195].

Next we used the homogenised Keller-Segel model to conduct several numerical investigations concerning two case studies. The first case study, investigated in Chapter 4, concerns travelling chemotactic bands in porous media under different flow regimes. The validation method is achieved by comparing between the simulation results of the exact model defined on a simple microstructure and the homogenised model. In addition, we used the effective model to illustrate the effect of the interplay of growth and chemotactic drift on the travelling wave speed. Starting with the effective model defined in an immobile aqueous phase, the simulation results of the homogenised model were in excellent agreement with those of the exact model. Thus showing that our earlier arguments of a non-dominant impact of the metabolic rates and chemotactic drifts at the pore scale were justified. When we included the weak advective flows, we observed a Galilean transformation of the same bands as in the immobile phase. Therefore, the validation of the advection-diffusion regime followed from the validation argument of the stagnant flow simulations. However, in the case of the advection-dispersion regime, we were not able to provide any numerical validation due to the numerical instability of the unsteady system.

The second case study, investigated in Chapter 5, involved a microfluidic device. The device fabricated by Long and Ford [122] was one of the earliest studies which attempted to elucidate the interplay between flow and chemotactic drift in porous media. The confined geometry, in particular, the shallow depth, departed from the geometry assumed in Chapter 2. Therefore, we proposed two approaches, the first was to follow Porter et al. [157] and ignore the dispersion effects caused by the shallow depth, the second approach was to introduce the classical Taylor dispersivities, as suggested by Chu et al. [47], into the Keller-Segel model before homogenisation. The simulation results of the first approach were identical to those found in Porter et al. [157], and thus provided a form of a numerical validation to the homogenised model. The second approach showed much improvement in the homogenised model predictions for the tracer test data than those for bacterial controlled test data. We took these observations as an indication that the bacterial population does not always follow the classical Taylor dispersivity as also suggested by Dehkharghani et al. [57] and Peng and Brady [154]. Furthermore, despite applying the classical Taylor dispersivity theory to the chemoattractant equation, the simulation results showed an improvement for higher flow velocities, but failed to capture the experimental data for slower flow velocity. We concluded that applying the classical Keller-Segel model is problematic due to the difficulties caused by the shallow channel depth on the swimming behaviour of the suspended bacterial population.

6.2 Future Work

There are several potential expansions of the current study, which can roughly be divided into four categories: model validation, experimental studies, simulations, and extension. Below we briefly discuss the different possible extensions of the current study.

Throughout this thesis, we validated the predictions of the models derived in Chapter 2 using full-scale simulations or experiments. Given the limited availability of experimental data, it was more fruitful to pursue numerical validation against direct numerical solutions. Thus, to complete the numerical validation, we are exploring some numerical simulations concerning the direct simulations of the travelling wave solution for the unsteady system concerning the dominant advective regime [198, 211, 177, 207]. The results in this thesis lend a novel quantitative understanding of the impact of chemotactic transport in subsurface environments. In Chapter 5, we aimed to demonstrate the potential of our upscaled mathematical models in designing future experimental studies that take into consideration the impact of confined flows. As in Walsh and Saar [198], our study demonstrated that bacterial chemotaxis is better studied in a static medium. The effect of wall shear rates should be included for the flow-stopped microfluidic devices, either by increasing the channel depth to include the classical Taylor dispersion, or by accurately including the modified Taylor dispersion and effective microbial velocities as reported in Dehkharghani et al. [57] and Peng and Brady [154].

Furthermore, the simulations using the multi-relaxation lattice-Boltzmann method in Yan and Hilpert [211] and Yan et al. [212] can be repeated using the derived upscaled parameters in our thesis and, thus, enhance our understanding of the effect of the large differences in diffusivity time scales of the different species on the chemotactic wave shape in dominant advective regimes. Furthermore, more sophisticated homogenisation techniques can benefit from our results, where in situ substrate gradient measurements can be implemented to the upscaled Keller-Segel model owing to the insight of chemotactic drift responses in a porous medium. Finally, the possibilities for model extension are vast. For example, in a static medium, the model can be extended to include cell-cell interaction and clogging effects, while in weak and strong flows, the retardation impact on the transport model and the effect of the different flow velocities on the measurements of the retardation factors could be included (see Dentz et al. [60]). Note that the models derived in this thesis can naturally be adopted for diffusiophoretic colloids or any other biased movement of particles.

Bibliography

[1] R. C. Acharya, A. J. Valocchi, C. J. Werth, and T. W. Willingham. Pore-scale simulation of dispersion and reaction along a transverse mixing zone in two-dimensional porous media. *Water Resources Research*, 43(10):W10435, 2007.

[2] J. Adler. Chemotaxis in bacteria. *Science*, 153(3737):708–716, 1966.

[3] J. Adler. A method for measuring chemotaxis and use of the method to determine optimum conditions for chemotaxis by escherichia coli. *Microbiology*, 74 (1):77–91, 1973.

[4] J. Adler, G. L. Hazelbauer, and M. Dahl. Chemotaxis toward sugars in escherichia coli. *Journal of Bacteriology*, 115(3):824–847, 1973.

[5] T. Ahmed and R. Stocker. Experimental verification of the behavioral foundation of bacterial transport parameters using microfluidics. *Biophysical Journal*, 95(9):4481–4493, 2008.

[6] M. Alexander. *Biodegradation and bioremediation*. Academic Press, San Diego, 1999.

[7] G. Alexandre, S. Greer-Phillips, and I. B. Zhulin. Ecological role of energy taxis in microorganisms. *FEMS Microbiology Reviews*, 28(1):113–126, 2004.

[8] G. Allaire. Homogenization and two-scale convergence. *SIAM Journal on Mathematical Analysis*, 23(6):1482–1518, 1992.

[9] G. Allaire and K. El Ganaoui. Homogenization of a conductive and radiative heat transfer problem. *Multiscale Modeling & Simulation*, 7(3):1148–1170, 2009.

[10] G. Allaire and Z. Habibi. Homogenization of a conductive, convective, and radiative heat transfer problem in a heterogeneous domain. *SIAM Journal on Mathematical Analysis*, 45(3):1136–1178, 2013.

[11] G. Allaire, E. Bonnetier, G. Francfort, and F. Jouve. Shape optimization by the homogenization method. *Numerische Mathematik*, 76(1):27–68, 1997.

[12] G. Allaire, R. Brizzi, A. Mikelić, and A. Piatnitski. Two-scale expansion with drift approach to the taylor dispersion for reactive transport through porous media. *Chemical Engineering Science*, 65(7):2292–2300, 2010.

[13] G. Allaire, A. Mikelić, and A. Piatnitski. Homogenization approach to the dispersion theory for reactive transport through porous media. *SIAM Journal on Mathematical Analysis*, 42(1):125–144, 2010.

[14] W. M. Alley, T. E. Reilly, and O. L. Franke. *Sustainability of ground-water resources*. U.S. Geological Survey Circular, 1186, 1999.

[15] A. Almqvist, J. Fabricius, T. S. Lundström, and P. Wall. Flow in thin domains with a microstructure: Lubrication and thin porous media. In *AIP Conference Proceedings*. AIP Publishing LLC 020172, 2017.

[16] W. Alt. Biased random walk models for chemotaxis and related diffusion approximations. *Journal of Mathematical Biology*, 9(2):147–177, 1980.

[17] D. B. Amchin, J. A. Ott, T. Bhattacharjee, and S. S. Datta. Influence of confinement on the spreading of bacterial populations. *PLOS Computational Biology*, 18(5):e1010063, 2022.

[18] J. T. Ault, P. B. Warren, S. Shin, and H. A. Stone. Diffusiophoresis in one-dimensional solute gradients. *Soft Matter*, 13(47):9015–9023, 2017.

[19] J. T. Ault, S. Shin, and H. A. Stone. Diffusiophoresis in narrow channel flows. *Journal of Fluid Mechanics*, 854:420–448, 2018.

[20] J. Auriault. Heterogeneous medium. is an equivalent macroscopic description possible? *International Journal of Engineering Science*, 29(7):785–795, 1991.

[21] J.-L. Auriault and P. Adler. Taylor dispersion in porous media: Analysis by multiple scale expansions. *Advances in Water Resources*, 18(4):217–226, 1995.

[22] M. Auset and A. A. Keller. Pore-scale processes that control dispersion of colloids in saturated porous media. *Water Resources Research*, 40(3):W03503, 2004. doi: https://doi.org/10.1029/2003WR002800. URL `https://agupubs.onlinelibrary.wiley.com/doi/abs/10.1029/2003WR002800`.

[23] J. W. Barton and R. M. Ford. Determination of effective transport coefficients for bacterial migration in sand columns. *Applied and Environmental Microbiology*, 61(9):3329–3335, 1995.

[24] J. W. Barton and R. M. Ford. Mathematical model for characterization of bacterial migration through sand cores. *Biotechnology and Bioengineering*, 53 (5):487–496, 1997.

[25] T. Baumann and C. J. Werth. Visualization and modeling of polystyrol colloid transport in a silicon micromodel. *Vadose Zone Journal*, 3(2):434–443, 2004.

[26] J. Bear. *Dynamics of fluids in porous media*. Dover Publications, Inc, New York, NY, USA, 1972.

[27] J. Bear and Y. Bachmat. *Introduction to modeling of transport phenomena in porous media*. Springer Netherlands, 1990.

[28] D. A. Beard. Taylor dispersion of a solute in a microfluidic channel. *Journal of Applied Physics*, 89(8):4667–4669, 2001.

[29] R. Bearon and A. Hazel. The trapping in high-shear regions of slender bacteria undergoing chemotaxis in a channel. *Journal of Fluid Mechanics*, 771:R3, 2015.

[30] A. Bensoussan, J.-L. Lions, G. Papanicolaou, and T. Caughey. Asymptotic analysis of periodic structures. *Journal of Applied Mechanics*, 46(2):477–477, 1979.

[31] H. Berg and D. Brown. Chemotaxis in escherichia coli analyzed by three-dimensional tracking. In *Chemotaxis: Its Biology and Biochemistry*, volume 19, pages 55–78. Karger Publishers, 1974.

[32] H. C. Berg. Chemotaxis in bacteria. *Annual Review of Biophysics and Bioengineering*, 4(1):119–136, 1975.

[33] A. P. Berke, L. Turner, H. C. Berg, and E. Lauga. Hydrodynamic attraction of swimming microorganisms by surfaces. *Physical Review Letters*, 101(3):038102, 2008.

[34] T. Bhattacharjee and S. S. Datta. Bacterial hopping and trapping in porous media. *Nature Communications*, 10(1):1–9, 2019.

[35] T. Bhattacharjee and S. S. Datta. Bacterial hopping and trapping in porous media. *Nature Communications*, 10(1):2075, 2019.

[36] T. Bhattacharjee, D. B. Amchin, J. A. Ott, F. Kratz, and S. S. Datta. Chemotactic migration of bacteria in porous media. *Biophysical Journal*, 120(16): 3483–3497, 2021.

[37] T. Bhattacharjee, D. B. Amchin, R. Alert, J. A. Ott, and S. S. Datta. Chemotactic smoothing of collective migration. *Elife*, 11:e71226, 2022.

[38] J. P. Boon. Theoretical models for bacterial motion and chemotaxis. *Advances in Chemical Physics*, 29:169–190, 2009.

[39] A. Bourgeat, M. Jurak, and A. Piatnitski. Averaging a transport equation with small diffusion and oscillating velocity. *Mathematical Methods in the Applied Sciences*, 26(2):95–117, 2003.

[40] D. A. Brown and H. C. Berg. Temporal stimulation of chemotaxis in *Escherichia coli*. *Proceedings of the National Academy of Sciences*, 71(4):1388–1392, 1974.

[41] H. Bruus. *Theoretical microfluidics*, volume 18. Oxford University Press, Oxford, 2008.

[42] D. Button. Kinetics of nutrient-limited transport and microbial growth. *Microbiological Reviews*, 49(3):270–297, 1985.

[43] T. A. Camesano and B. E. Logan. Influence of fluid velocity and cell concentration on the transport of motile and nonmotile bacteria in porous media. *Environmental Science & Technology*, 32(11):1699–1708, 1998.

[44] K. C. Chen, P. T. Cummings, and R. M. Ford. Perturbation expansion of Alt's cell balance equations reduces to Segel's one-dimensional equations for shallow chemoattractant gradients. *SIAM Journal on Applied Mathematics*, 59 (1):35–57, 1998.

[45] K. C. Chen, R. M. Ford, and P. T. Cummings. Mathematical models for motile bacterial transport in cylindrical tubes. *Journal of Theoretical Biology*, 195(4): 481–504, 1998.

[46] S. Chilukuri, C. H. Collins, and P. T. Underhill. Impact of external flow on the dynamics of swimming microorganisms near surfaces. *Journal of Physics: Condensed Matter*, 26(11):115101, 2014.

[47] H. C. Chu, S. Garoff, R. D. Tilton, and A. S. Khair. Macrotransport theory for diffusiophoretic colloids and chemotactic microorganisms. *Journal of Fluid Mechanics*, 917, 2021.

[48] D. Clausznitzer, O. Oleksiuk, L. Løvdok, V. Sourjik, and R. G. Endres. Chemotactic response and adaptation dynamics in escherichia coli. *PLoS computational biology*, 6(5):e1000784, 2010.

[49] Committee on Ground Water Cleanup Alternatives. *Alternatives for ground water cleanup*. National Academies Press, Washington, D.C, 1994.

[50] J. Cremer, T. Honda, Y. Tang, J. Wong-Ng, M. Vergassola, and T. Hwa. Chemotaxis as a navigation strategy to boost range expansion. *Nature*, 575 (7784):658–663, 2019.

[51] F. Dahlquist, P. Lovely, and D. Koshland. Quantitative analysis of bacterial migration in chemotaxis. *Nature New Biology*, 236(65):120–123, 1972.

[52] A. Daneyko, D. Hlushkou, S. Khirevich, and U. Tallarek. From random sphere packings to regular pillar arrays: analysis of transverse dispersion. *Journal of Chromatography A*, 1257:98–115, 2012.

[53] S. Datta and S. Ghosal. Characterizing dispersion in microfluidic channels. *Lab on a Chip*, 9(17):2537–2550, 2009.

[54] P. de Anna, A. A. Pahlavan, Y. Yawata, R. Stocker, and R. Juanes. Chemotaxis under flow disorder shapes microbial dispersion in porous media. *Nature Physics*, 17(1):68–73, 2021.

[55] A. J. De Kerchove and M. Elimelech. Calcium and magnesium cations enhance the adhesion of motile and nonmotile pseudomonas aeruginosa on alginate films. *Langmuir*, 24(7):3392–3399, 2008.

[56] M. De Pra, W. De Malsche, G. Desmet, P. J. Schoenmakers, and W. T. Kok. Pillar-structured microchannels for on-chip liquid chromatography: Evaluation of the permeability and separation performance. *Journal of Separation Science*, 30(10):1453–1460, 2007.

[57] A. Dehkharghani, N. Waisbord, J. Dunkel, and J. S. Guasto. Bacterial scattering in microfluidic crystal flows reveals giant active Taylor–Aris dispersion. *Proceedings of the National Academy of Sciences*, 116(23):11119–11124, 2019.

[58] A. Dehkharghani, N. Waisbord, and J. S. Guasto. Self-transport of swimming bacteria is impaired by porous microstructure. *Communications Physics*, 6(1): 18, 2023.

[59] J. Delgado. A critical review of dispersion in packed beds. *Heat and Mass Transfer*, 42(4):279–310, 2006.

[60] M. Dentz, A. Creppy, C. Douarche, E. Clément, and H. Auradou. Dispersion of motile bacteria in a porous medium. *arXiv preprint arXiv:2201.04628*, 2022.

[61] G. Desmet and G. V. Baron. Chromatographic explanation for the side-wall induced band broadening in pressure-driven and shear-driven flows through channels with a high aspect-ratio rectangular cross-section. *Journal of Chromatography A*, 946(1-2):51–58, 2002.

[62] M. R. Doshi, P. M. Daiya, and W. N. Gill. Three dimensional laminar dispersion in open and closed rectangular conduits. *Chemical Engineering Science*, 33(7): 795–804, 1978.

[63] K. Drescher, J. Dunkel, L. H. Cisneros, S. Ganguly, and R. E. Goldstein. Fluid dynamics and noise in bacterial cell–cell and cell–surface scattering. *Proceedings of the National Academy of Sciences*, 108(27):10940–10945, 2011.

[64] K. J. Duffy and R. M. Ford. Turn angle and run time distributions characterize swimming behavior for *Pseudomonas putida*. *Journal of Bacteriology*, 179(4): 1428–1430, 1997.

[65] K. J. Duffy, P. T. Cummings, and R. M. Ford. Random walk calculations for bacterial migration in porous media. *Biophysical Journal*, 68(3):800–806, 1995.

[66] K. J. Duffy, R. M. Ford, and P. T. Cummings. Residence time calculation for chemotactic bacteria within porous media. *Biophysical Journal*, 73(6):2930–2936, 1997.

[67] H. J. Dupin and P. L. McCarty. Impact of colony morphologies and disinfection on biological clogging in porous media. *Environmental Science & Technology*, 34(8):1513–1520, 2000.

[68] D. Dutta, A. Ramachandran, and D. T. Leighton. Effect of channel geometry on solute dispersion in pressure-driven microfluidic systems. *Microfluidics and Nanofluidics*, 2(4):275–290, 2006.

[69] M. D. Egbert, X. E. Barandiaran, and E. A. Di Paolo. A minimal model of metabolism-based chemotaxis. *PLoS Computational Biology*, 6(12):e1001004, 2010.

[70] L. C. Evans. *Partial differential equations*. American Mathematical Society, Providence, 1998.

[71] B. Ezhilan and D. Saintillan. Transport of a dilute active suspension in pressure-driven channel flow. *Journal of Fluid Mechanics*, 777:482–522, 2015.

[72] J. Fabricius, J. G. I. Hellström, T. S. Lundström, E. Miroshnikova, and P. Wall. Darcy's law for flow in a periodic thin porous medium confined between two parallel plates. *Transport in Porous Media*, 115(3):473–493, 2016.

[73] J. Fabricius, E. Miroshnikova, and P. Wall. Homogenization of the Stokes equation with mixed boundary condition in a porous medium. *Cogent Mathematics*, 4(1):1327502, 2017.

[74] S. Fan and R. G. Endres. A minimal model for metabolism-dependent chemotaxis in *Rhodobacter sphaeroides*. *Interface Focus*, 4(6):20140002, 2014.

[75] N. Figueroa-Morales, G. L. Mino, A. Rivera, R. Caballero, E. Clément, E. Altshuler, and A. Lindner. Living on the edge: transfer and traffic of *E. coli* in a confined flow. *Soft Matter*, 11(31):6284–6293, 2015.

[76] R. M. Ford and P. T. Cummings. On the relationship between cell balance equations for chemotactic cell populations. *SIAM Journal on Applied Mathematics*, 52(5):1426–1441, 1992.

[77] R. M. Ford and R. W. Harvey. Role of chemotaxis in the transport of bacteria through saturated porous media. *Advances in Water Resources*, 30(6-7):1608–1617, 2007.

[78] R. M. Ford and D. A. Lauffenburger. Measurement of bacterial random motility and chemotaxis coefficients: II. Application of single-cell-based mathematical model. *Biotechnology and Bioengineering*, 37(7):661–672, 1991.

[79] R. M. Ford and D. A. Lauffenburger. Analysis of chemotactic bacterial distributions in population migration assays using a mathematical model applicable to steep or shallow attractant gradients. *Bulletin of Mathematical Biology*, 53 (5):721–749, 1991.

[80] R. M. Ford, B. R. Phillips, J. A. Quinn, and D. A. Lauffenburger. Measurement of bacterial random motility and chemotaxis coefficients: I. Stopped-flow diffusion chamber assay. *Biotechnology and Bioengineering*, 37(7):647–660, 1991.

[81] A. Fowler. *Mathematical geoscience*. Springer, London, 2011.

[82] X. Fu, S. Kato, J. Long, H. H. Mattingly, C. He, D. C. Vural, S. W. Zucker, and T. Emonet. Spatial self-organization resolves conflicts between individuality and collective migration. *Nature Communications*, 9(1):1–12, 2018.

[83] C. L. Gaol, L. Ganzer, S. Mukherjee, and H. Alkan. Investigation of clogging in porous media induced by microorganisms using a microfluidic application. *Environmental Science: Water Research & Technology*, 7(2):441–454, 2021.

[84] T. B. Gatski and J.-P. Bonnet. Chapter 4 - experimental measurement and analysis strategies. In T. B. Gatski and J.-P. Bonnet, editors, *Compressibility, Turbulence and High Speed Flow (Second Edition)*, pages 79–116. Academic Press, Oxford, 2013.

[85] A. C. Grimm and C. S. Harwood. Chemotaxis of *Pseudomonas* spp. to the polyaromatic hydrocarbon naphthalene. *Applied and Environmental Microbiology*, 63(10):4111–4115, 1997.

[86] C. S. Harwood, R. E. Parales, and M. Dispensa. Chemotaxis of *Pseudomonas putida* toward chlorinated benzoates. *Applied and Environmental Microbiology*, 56(5):1501–1503, 1990.

[87] M. Hassanpourfard, Z. Nikakhtari, R. Ghosh, S. Das, T. Thundat, Y. Liu, and A. Kumar. Bacterial floc mediated rapid streamer formation in creeping flows. *Scientific Reports*, 5(1):1–12, 2015.

[88] U. Hornung. *Homogenization and porous media*, volume 6. Springer New York, NY, 1996.

[89] D. Huizenga and D. M. Smith. Knudsen diffusion in random assemblages of uniform spheres. *AIChE Journal*, 32(1):1–6, 1986.

[90] R. F. Ismagilov, A. D. Stroock, P. J. Kenis, G. Whitesides, and H. A. Stone. Experimental and theoretical scaling laws for transverse diffusive broadening in two-phase laminar flows in microchannels. *Applied Physics Letters*, 76(17): 2376–2378, 2000.

[91] H.-H. Jeong. Recent developments in bacterial chemotaxis analysis based on the microfluidic system. *SLAS TECHNOLOGY: Translating Life Sciences Innovation*, 26(2):159–164, 2021.

[92] V. A. S. Júnior, A. F. S. Júnior, T. A. Simões, and G. P. Oliveira. Poiseuille-number-based Kozeny–Carman model for computation of pore shape factors on arbitrary cross sections. *Transport in Porous Media*, 138(1):99–131, 2021.

[93] A. E. Kamholz and P. Yager. Molecular diffusive scaling laws in pressure-driven microfluidic channels: deviation from one-dimensional Einstein approximations. *Sensors and Actuators B: Chemical*, 82(1):117–121, 2002.

[94] A. E. Kamholz, E. A. Schilling, and P. Yager. Optical measurement of transverse molecular diffusion in a microchannel. *Biophysical Journal*, 80(4):1967–1972, 2001.

[95] F. Kargi. Re-interpretation of the logistic equation for batch microbial growth in relation to monod kinetics. *Letters in Applied Microbiology*, 48(4):398–401, 2009.

[96] T. Kaya and H. Koser. Direct upstream motility in *Escherichia coli*. *Biophysical Journal*, 102(7):1514–1523, 2012.

[97] E. F. Keller and G. M. Odell. Necessary and sufficient conditions for chemotactic bands. *Mathematical Biosciences*, 27(3-4):309–317, 1975.

[98] E. F. Keller and L. A. Segel. Initiation of slime mold aggregation viewed as an instability. *Journal of Theoretical Biology*, 26(3):399–415, 1970.

[99] E. F. Keller and L. A. Segel. Traveling bands of chemotactic bacteria: a theoretical analysis. *Journal of Theoretical Biology*, 30(2):235–248, 1971.

[100] E. F. Keller and L. A. Segel. Model for chemotaxis. *Journal of Theoretical Biology*, 30(2):225–234, 1971.

[101] J. B. Keller. Effective behavior of heterogeneous media. In U. Landman, editor, *Statistical mechanics and statistical methods in theory and application*, pages 631–644. Springer US, New York, NY, 1977.

[102] J. B. Keller. Darcy's law for flow in porous media and the two-space method. In R. L. Sternberg, editor, *Nonlinear partial differential equations in engineering and applied science*, pages 429–443. Routledge, 1980.

[103] C. Kennedy and R. Aris. Traveling waves in a simple population model involving growth and death. *Bulletin of Mathematical Biology*, 42(3):397–429, 1980.

[104] F. I. Khan, T. Husain, and R. Hejazi. An overview and analysis of site remediation technologies. *Journal of Environmental Management*, 71(2):95–122, 2004.

[105] T. Krell, J. Lacal, J. A. Reyes-Darias, C. Jimenez-Sanchez, R. Sungthong, and J. J. Ortega-Calvo. Bioavailability of pollutants and chemotaxis. *Current Opinion in Biotechnology*, 24(3):451–456, 2013.

[106] V. R. Krishnamurthi, N. Harris, A. Rogers, M. Zou, and Y. Wang. Interactions of *E. coli* with cylindrical micro-pillars of different geometric modifications. *Colloids and Surfaces B: Biointerfaces*, 209:112190, 2022.

[107] K. Kusy and R. M. Ford. Monte Carlo simulations derived from direct observations of individual bacteria inform macroscopic migration models at granular porous media interfaces. *Environmental Science & Technology*, 41(18):6403–6409, 2007.

[108] K. Kusy and R. M. Ford. Surface association of motile bacteria at granular porous media interfaces. *Environmental Science & Technology*, 43(10):3712–3719, 2009.

[109] J. Lacal, F. Muñoz-Martínez, J.-A. Reyes-Darías, E. Duque, M. Matilla, A. Segura, J.-J. O. Calvo, C. Jímenez-Sánchez, T. Krell, and J. L. Ramos. Bacterial chemotaxis towards aromatic hydrocarbons in *Pseudomonas*. *Environmental Microbiology*, 13(7):1733–1744, 2011.

[110] M. P. Lanfranconi, H. M. Alvarez, and C. A. Studdert. A strain isolated from gas oil-contaminated soil displays chemotaxis towards gas oil and hexadecane. *Environmental Microbiology*, 5(10):1002–1008, 2003.

[111] L. M. Lanning and R. M. Ford. Glass micromodel study of bacterial dispersion in spatially periodic porous networks. *Biotechnology and Bioengineering*, 78(5): 556–566, 2002.

[112] L. M. Lanning, R. M. Ford, and T. Long. Bacterial chemotaxis transverse to axial flow in a microfluidic channel. *Biotechnology and Bioengineering*, 100(4): 653–663, 2008.

[113] I. R. Lapidus and R. Schiller. A model for traveling bands of chemotactic bacteria. *Biophysical Journal*, 22(1):1–13, 1978.

[114] D. Lauffenburger, C. R. Kennedy, and R. Aris. Traveling bands of chemotactic bacteria in the context of population growth. *Bulletin of Mathematical Biology*, 46(1):19–40, 1984.

[115] D. A. Lauffenburger. Quantitative studies of bacterial chemotaxis and microbial population dynamics. *Microbial Ecology*, 22(1):175–185, 1991.

[116] P. Lewus and R. M. Ford. Quantification of random motility and chemotaxis bacterial transport coefficients using individual-cell and population-scale assays. *Biotechnology and Bioengineering*, 75(3):292–304, 2001.

[117] N. A. Licata, B. Mohari, C. Fuqua, and S. Setayeshgar. Diffusion of bacterial cells in porous media. *Biophysical Journal*, 110(1):247–257, 2016.

[118] J.-L. Lions. *Some methods in the mathematical analysis of systems and their control*. Beijing, Science Press, 1981.

[119] J. Liu and R. M. Ford. Idling time of swimming bacteria near particulate surfaces contributes to apparent adsorption coefficients at the macroscopic scale under static conditions. *Environmental Science & Technology*, 43(23):8874–8880, 2009.

[120] J. Liu, R. M. Ford, and J. A. Smith. Idling time of motile bacteria contributes to retardation and dispersion in sand porous medium. *Environmental Science & Technology*, 45(9):3945–3951, 2011.

[121] Z. Liu, K. Zhang, and X. Cheng. Rheology of bacterial suspensions under confinement. *Rheologica Acta*, 58(8):439–451, 2019.

[122] T. Long and R. M. Ford. Enhanced transverse migration of bacteria by chemotaxis in a porous t-sensor. *Environmental Science & Technology*, 43(5):1546–1552, 2009.

[123] W. Long and M. Hilpert. Analytical solutions for bacterial energy taxis (chemotaxis): Traveling bacterial bands. *Advances in Water Resources*, 30(11):2262–2270, 2007.

[124] W. Long and M. Hilpert. Analytical solutions for bacterial energy taxis (chemotaxis): Traveling bacterial bands. *Advances in Water Resources*, 30(11):2262–2270, 2007.

[125] W. Long and M. Hilpert. Lattice-Boltzmann modeling of contaminant degradation by chemotactic bacteria: Exploring the formation and movement of bacterial bands. *Water Resources Research*, 44(9):W09415, 2008.

[126] P. S. Lovely and F. Dahlquist. Statistical measures of bacterial motility and chemotaxis. *Journal of Theoretical Biology*, 50(2):477–496, 1975.

[127] N. Lu, T. Bevard, A. Massoudieh, C. Zhang, A. C. Dohnalkova, J. L. Zilles, and T. H. Nguyen. Flagella-mediated differences in deposition dynamics for *Azotobacter vinelandii* in porous media. *Environmental Science & Technology*, 47(10):5162–5170, 2013.

[128] D. M. Mackay and J. A. Cherry. Groundwater contamination: Pump-and-treat remediation. *Environmental Science & Technology*, 23(6):630–636, 1989.

[129] A. Manz, G. Simone, J. S. O'Connor, and P. Neuzil. *Microfluidics and Lab-on-a-Chip*. Royal Society of Chemistry, London, 2020.

[130] R. B. Marx and M. D. Aitken. Bacterial chemotaxis enhances naphthalene degradation in a heterogeneous aqueous system. *Environmental Science & Technology*, 34(16):3379–3383, 2000.

[131] J. W. McClaine and R. M. Ford. Characterizing the adhesion of motile and nonmotile *Escherichia coli* to a glass surface using a parallel-plate flow chamber. *Biotechnology and Bioengineering*, 78(2):179–189, 2002.

[132] C. Mei and J.-L. Auriault. The effect of weak inertia on flow through a porous medium. *Journal of Fluid Mechanics*, 222:647–663, 1991.

[133] C. C. Mei. Method of homogenization applied to dispersion in porous media. *Transport in Porous Media*, 9(3):261–274, 1992.

[134] R. Mesibov and J. Adler. Chemotaxis toward amino acids in *Escherichia coli*. *Journal of Bacteriology*, 112(1):315–326, 1972.

[135] R. N. Moghaddam and M. Jamiolahmady. Slip flow in porous media. *Fuel*, 173: 298–310, 2016.

[136] R. Mok, J. Dunkel, and V. Kantsler. Geometric control of bacterial surface accumulation. *Physical Review E*, 99(5):052607, 2019.

[137] M. Molaei, M. Barry, R. Stocker, and J. Sheng. Failed escape: solid surfaces prevent tumbling of *Escherichia coli*. *Physical Review Letters*, 113(6):068103, 2014.

[138] J. A. Moore-Ott, S. Chiu, D. B. Amchin, T. Bhattacharjee, and S. S. Datta. A biophysical threshold for biofilm formation. *Elife*, 11:e76380, 2022.

[139] M. Nagel and F. Gallaire. Boundary elements method for microfluidic two-phase flows in shallow channels. *Computers & Fluids*, 107:272–284, 2015.

[140] M. Nagel, P.-T. Brun, H. Berthet, A. Lindner, F. Gallaire, and C. Duprat. Oscillations of confined fibres transported in microchannels. *Journal of Fluid Mechanics*, 835:444–470, 2018.

[141] A. V. Narla, J. Cremer, and T. Hwa. A traveling-wave solution for bacterial chemotaxis with growth. *Proceedings of the National Academy of Sciences*, 118 (48):e2105138118, 2021.

[142] National Research Council and others. *Alternatives for managing the nation's complex contaminated groundwater sites*. National Academies Press, 2013.

[143] T. O'Haver. peakfit.m (https://www.mathworks.com/matlabcentral/fileexchange/23611-peakfit-m), matlab central file exchange. 2021.

[144] M. S. Olson, R. M. Ford, J. A. Smith, and E. J. Fernandez. Quantification of bacterial chemotaxis in porous media using magnetic resonance imaging. *Environmental Science & Technology*, 38(14):3864–3870, 2004.

[145] M. S. Olson, R. M. Ford, J. A. Smith, and E. J. Fernandez. Analysis of column tortuosity for mncl2 and bacterial diffusion using magnetic resonance imaging. *Environmental Science & Technology*, 39(1):149–154, 2005.

[146] M. S. Olson, R. M. Ford, J. A. Smith, and E. J. Fernandez. Mathematical modeling of chemotactic bacterial transport through a two-dimensional heterogeneous porous medium. *Bioremediation Journal*, 10(1-2):13–23, 2006.

[147] J. Ortega-Calvo, A. Marchenko, A. Vorobyov, and R. Borovick. Chemotaxis in polycyclic aromatic hydrocarbon-degrading bacteria isolated from coal-tar-and oil-polluted rhizospheres. *FEMS Microbiology Ecology*, 44(3):373–381, 2003.

[148] T. Pak, L. F. d. L. Luz Jr, T. Tosco, G. S. R. Costa, P. R. R. Rosa, and N. L. Archilha. Pore-scale investigation of the use of reactive nanoparticles for in situ remediation of contaminated groundwater source. *Proceedings of the National Academy of Sciences*, 117(24):13366–13373, 2020.

[149] G. Pandey and R. K. Jain. Bacterial chemotaxis toward environmental pollutants: role in bioremediation. *Applied and Environmental Microbiology*, 68(12): 5789–5795, 2002.

[150] I. Pankratova and A. Piatnitski. Homogenization of convection-diffusion equation in infinite cylinder. *Networks & Heterogeneous Media*, 6(1):111–126, 2011.

[151] R. E. Parales. Nitrobenzoates and aminobenzoates are chemoattractants for *Pseudomonas* strains. *Applied and Environmental Microbiology*, 70(1):285–292, 2004.

[152] R. E. Parales, J. L. Ditty, and C. S. Harwood. Toluene-degrading bacteria are chemotactic towards the environmental pollutants benzene, toluene, and trichloroethylene. *Applied and Environmental Microbiology*, 66(9):4098–4104, 2000.

[153] J. A. Pedit, R. B. Marx, C. T. Miller, and M. D. Aitken. Quantitative analysis of experiments on bacterial chemotaxis to naphthalene. *Biotechnology and Bioengineering*, 78(6):626–634, 2002.

[154] Z. Peng and J. F. Brady. Upstream swimming and Taylor dispersion of active brownian particles. *Physical Review Fluids*, 5(7):073102, 2020.

[155] F. Phillips and M. Castro. 5.15 - groundwater dating and residence-time measurements. In H. D. Holland and K. K. Turekian, editors, *Treatise on Geochemistry*, pages 451–497. Pergamon, Oxford, 2003.

[156] M. Popa, I. Mamaliga, S. Petrescu, and E. T. I. Tudose. Axial dispersion study in fixed bed columns. *Rev. Chim*, 66:668–672, 2015.

[157] M. L. Porter, F. J. Valdés-Parada, and B. D. Wood. Multiscale modeling of chemotaxis in homogeneous porous media. *Water Resources Research*, 47(6): W06518, 2011.

[158] S. Pradeep and P. E. Arratia. Bacteria: To biofilm or not to biofilm. *Elife*, 11: e80891, 2022.

[159] S. Pradhan, I. Shaik, R. Lagraauw, and P. Bikkina. A semi-experimental procedure for the estimation of permeability of microfluidic pore network. *MethodsX*, 6:704–713, 2019.

[160] H. M. Quinn. A reconciliation of packed column permeability data: Column permeability as a function of particle porosity. *Journal of Materials*, 2014:1–22, 2014.

[161] H. H. Ramaiah. *Homogenization of complex flows in porous media and applications*. Phd thesis, École Polytechnique, Palaiseau, France, 2013.

[162] B. E. Rapp. *Microfluidics: modeling, mechanics and mathematics*. Micro and Nano Technologies. Elsevier Science, Netherlands, 2022.

[163] S. A. Reinecke and B. E. Sleep. Knudsen diffusion, gas permeability, and water content in an unconsolidated porous medium. *Water Resources Research*, 38 (12):16/1–15, 2002.

[164] P. Reynolds, P. Sharma, G. Jenneman, and M. McInerney. Mechanisms of microbial movement in subsurface materials. *Applied and Environmental Microbiology*, 55(9):2280–2286, 1989.

[165] J. Richardson, J. Harker, and J. Backhurst. Chapter 4 - flow of fluids through granular beds and packed columns. In J. Richardson, J. Harker, and J. Backhurst, editors, *Chemical Engineering (Fifth Edition)*, Chemical Engineering Series, pages 191–236. Butterworth-Heinemann, Oxford, 2002.

[166] M. A. Rivero, R. T. Tranquillo, H. M. Buettner, and D. A. Lauffenburger. Transport models for chemotactic cell populations based on individual cell behavior. *Chemical Engineering Science*, 44(12):2881–2897, 1989.

[167] C. J. Roush, C. M. Lastoskie, and R. M. Worden. Denitrification and chemotaxis of *Pseudomonas Stutzeri* KC in porous media. *Journal of Environmental Science and Health Part A*, 41(6):967–983, 2006.

[168] P. Royer. Advection–diffusion in porous media with low scale separation: Modelling via higher-order asymptotic homogenisation. *Transport in Porous Media*, 128(2):511–551, 2019.

[169] V. Y. Rudyak, V. M. Aniskin, A. A. Maslov, A. V. Minakov, and S. G. Mironov. *Micro-and Nanoflows: Modeling and Experiments*, volume 118 of *Fluid Mechanics and Its Applications*. Springer Cham, 2018.

[170] S. Sakanoue. Integration of logistic and kinetics equations of population growth. *Ecological Modelling*, 261:93–97, 2013.

[171] S. K. Samanta, B. Bhushan, A. Chauhan, and R. K. Jain. Chemotaxis of a *Ralstonia* sp. SJ98 toward different nitroaromatic compounds and their degradation. *Biochemical and Biophysical Research Communications*, 269(1):117–123, 2000.

[172] E. Sánchez-Palencia. *Non-homogeneous media and vibration theory*, volume 127 of *Lecture Notes in Physics*. Springer-Verlag, New York, 1980.

[173] F. Schaumburg, R. Urteaga, P. A. Kler, and C. L. Berli. Design keys for paper-based concentration gradient generators. *Journal of Chromatography A*, 1561: 83–91, 2018.

[174] R. Schulz, N. Ray, S. Zech, A. Rupp, and P. Knabner. Beyond Kozeny–Carman: predicting the permeability in porous media. *Transport in Porous Media*, 130 (2):487–512, 2019.

[175] L. A. Segel. A theoretical study of receptor mechanisms in bacterial chemotaxis. *SIAM Journal on Applied Mathematics*, 32(3):653–665, 1977.

[176] P. K. Sharma, M. J. McInerney, and R. Knapp. In situ growth and activity and modes of penetration of *Escherichia coli* in unconsolidated porous materials. *Applied and Environmental Microbiology*, 59(11):3686–3694, 1993.

[177] W. Shen, C. Zhang, and J. Zhang. Relaxation method for unsteady convection–diffusion equations. *Computers & Mathematics with Applications*, 61(4):908–920, 2011.

[178] J. L. Sherwood, J. C. Sung, R. M. Ford, E. J. Fernandez, J. E. Maneval, and J. A. Smith. Analysis of bacterial random motility in a porous medium using magnetic resonance imaging and immunomagnetic labeling. *Environmental Science & Technology*, 37(4):781–785, 2003.

[179] R. Shipley, G. Jones, R. Dyson, B. Sengers, C. Bailey, C. Catt, C. Please, and J. Malda. Design criteria for a printed tissue engineering construct: a mathematical homogenization approach. *Journal of Theoretical Biology*, 259 (3):489–502, 2009.

[180] R. Singh and M. S. Olson. Transverse mixing enhancement due to bacterial random motility in porous microfluidic devices. *Environmental Science & Technology*, 45(20):8780–8787, 2011.

[181] L. W. Sinton, M. L. Mackenzie, N. Karki, R. R. Braithwaite, C. H. Hall, and M. J. Flintoft. Transport of *Escherichia coli* and F-RNA bacteriophages in a 5 m column of saturated pea gravel. *Journal of Contaminant Hydrology*, 117 (1-4):71–81, 2010.

[182] U. Sommer. A comparison of the droop and the Monod models of nutrient limited growth applied to natural populations of phytoplankton. *Functional Ecology*, 6:535–544, 1991.

[183] H. Song, Y. Wang, and K. Pant. Three-dimensional analytical model for pressure-driven cross-stream diffusion in microchannels with arbitrary aspect ratios. In *International Conference on Micro/Nanoscale Heat Transfer*, pages 27–37. American Society of Mechanical Engineers, 2012. `https://doi.org/10.1115/MNHMT2012-75134`.

[184] P. A. Spiro, J. S. Parkinson, and H. G. Othmer. A model of excitation and adaptation in bacterial chemotaxis. *Proceedings of the National Academy of Sciences*, 94(14):7263–7268, 1997.

[185] H. A. Stone. Introduction to fluid dynamics for microfluidic flows. In H. Lee, R. M. Westervelt, and D. Ham, editors, *CMOS Biotechnology*, pages 5–30. Springer US, Boston, MA, 2007.

[186] H. A. Stone, A. D. Stroock, and A. Ajdari. Engineering flows in small devices: microfluidics toward a lab-on-a-chip. *Annu. Rev. Fluid Mech.*, 36:381–411, 2004.

[187] P. J. Sturman, P. S. Stewart, A. B. Cunningham, E. J. Bouwer, and J. H. Wolfram. Engineering scale-up of in situ bioremediation processes: a review. *Journal of Contaminant Hydrology*, 19(3):171–203, 1995.

[188] B. L. Taylor and I. B. Zhulin. In search of higher energy: metabolism-dependent behaviour in bacteria. *Molecular Microbiology*, 28(4):683–690, 1998.

[189] B. L. Taylor, I. B. Zhulin, and M. S. Johnson. Aerotaxis and other energy-sensing behavior in bacteria. *Annual Reviews in Microbiology*, 53(1):103–128, 1999.

[190] G. I. Taylor. Dispersion of soluble matter in solvent flowing slowly through a tube. *Proceedings of the Royal Society of London. Series A. Mathematical and Physical Sciences*, 219(1137):186–203, 1953.

[191] N. Tufenkji and M. B. Emelko. Fate and transport of microbial contaminants in groundwater. In J. Nriagu, editor, *Encyclopedia of Environmental Health*, pages 715–726. Elsevier, Amsterdam, 2011.

[192] R. Urteaga, E. Elizalde, and C. L. Berli. Transverse solute dispersion in microfluidic paper-based analytical devices (μpads). *Analyst*, 143(10):2259–2266, 2018.

[193] F. J. Valdes-Parada, J. A. Ochoa-Tapia, and J. Alvarez-Ramirez. Validity of the permeability Carman–Kozeny equation: a volume averaging approach. *Physica A: Statistical Mechanics and its Applications*, 388(6):789–798, 2009.

[194] F. J. Valdés-Parada, M. L. Porter, K. Narayanaswamy, R. M. Ford, and B. D. Wood. Upscaling microbial chemotaxis in porous media. *Advances in Water Resources*, 32(9):1413–1428, 2009.

[195] F. J. Valdés-Parada, M. L. Porter, K. Narayanaswamy, R. M. Ford, and B. D. Wood. Upscaling microbial chemotaxis in porous media. *Advances in Water Resources*, 32(9):1413–1428, 2009.

[196] P. Velasco-Casal, L. Y. Wick, and J.-J. Ortega-Calvo. Chemoeffectors decrease the deposition of chemotactic bacteria during transport in porous media. *Environmental Science & Technology*, 42(4):1131–1137, 2008.

[197] M. Vigeant and R. M. Ford. Interactions between motile *Escherichia coli* and glass in media with various ionic strengths, as observed with a three-dimensional-tracking microscope. *Applied and Environmental Microbiology*, 63 (9):3474–3479, 1997.

[198] S. D. Walsh and M. O. Saar. Macroscale lattice-Boltzmann methods for low Péclet number solute and heat transport in heterogeneous porous media. *Water Resources Research*, 46(7):W07517, 2010. https://doi.org/10.1029/2009WR007895.

[199] M. Wang and R. M. Ford. Transverse bacterial migration induced by chemotaxis in a packed column with structured physical heterogeneity. *Environmental Science & Technology*, 43(15):5921–5927, 2009.

[200] M. Wang and R. M. Ford. Quantitative analysis of transverse bacterial migration induced by chemotaxis in a packed column with structured physical heterogeneity. *Environmental Science & Technology*, 44(2):780–786, 2010.

[201] M. Wang, R. M. Ford, and R. W. Harvey. Coupled effect of chemotaxis and growth on microbial distributions in organic-amended aquifer sediments: Observations from laboratory and field studies. *Environmental Science & Technology*, 42(10):3556–3562, 2008.

[202] R. Watteaux, R. Stocker, and J. R. Taylor. Sensitivity of the rate of nutrient uptake by chemotactic bacteria to physical and biological parameters in a turbulent environment. *Journal of Theoretical Biology*, 387:120–135, 2015. https://doi.org/10.1016/j.jtbi.2015.08.006.

[203] S. Whitaker. *The method of volume averaging*, volume 13 of *Theory and Applications of Transport in Porous Media*. Springer Dordrecht, Netherlands, 1998.

[204] M. S. Williams, K. J. Longmuir, and P. Yager. A practical guide to the staggered herringbone mixer. *Lab on a Chip*, 8(7):1121–1129, 2008.

[205] M. E. Witt, M. J. Dybas, R. M. Worden, and C. S. Criddle. Motility-enhanced bioremediation of carbon tetrachloride-contaminated aquifer sediments. *Environmental Science & Technology*, 33(17):2958–2964, 1999.

[206] J. Wong-Ng, A. Celani, and M. Vergassola. Exploring the function of bacterial chemotaxis. *Current Opinion in Microbiology*, 45:16–21, 2018.

[207] B. Wongsaijai, N. Sukantamala, and K. Poochinapan. A mass-conservative higher-order ADI method for solving unsteady convection–diffusion equations. *Advances in Difference Equations*, 2020(1):1–24, 2020.

[208] M. Wu, J. W. Roberts, S. Kim, D. L. Koch, and M. P. DeLisa. Collective bacterial dynamics revealed using a three-dimensional population-scale defocused particle tracking technique. *Applied and Environmental Microbiology*, 72(7): 4987–4994, 2006.

[209] X. Xu, Z. Li, and A. Nehorai. Finite element simulations of hydrodynamic trapping in microfluidic particle-trap array systems. *Biomicrofluidics*, 7(5): 054108, 2013.

[210] C. Xue, H. J. Hwang, K. J. Painter, and R. Erban. Travelling waves in hyperbolic chemotaxis equations. *Bulletin of Mathematical Biology*, 73(8):1695–1733, 2011.

[211] Z. Yan and M. Hilpert. A multiple-relaxation-time lattice-Boltzmann model for bacterial chemotaxis: effects of initial concentration, diffusion, and hydrodynamic dispersion on traveling bacterial bands. *Bulletin of Mathematical Biology*, 76(10):2449–2475, 2014.

[212] Z. Yan, E. J. Bouwer, and M. Hilpert. Coupled effects of chemotaxis and growth on traveling bacterial waves. *Journal of Contaminant Hydrology*, 164:138–152, 2014.

[213] Y. Yang, A. M. Pollard, C. Höfler, G. Poschet, M. Wirtz, R. Hell, and V. Sourjik. Relation between chemotaxis and consumption of amino acids in bacteria. *Molecular Microbiology*, 96(6):1272–1282, 2015.

[214] J. Yuan, R. W. Branch, B. G. Hosu, and H. C. Berg. Adaptation at the output of the chemotaxis signalling pathway. *Nature*, 484(7393):233–236, 2012.

[215] L. Y. Zaval'skii, A. Marchenko, and R. Borovik. The study of bacterial chemotaxis to naphthalene. *Microbiology*, 72(3):363–368, 2003.

[216] H. Zhong, G. Liu, Y. Jiang, J. Yang, Y. Liu, X. Yang, Z. Liu, and G. Zeng. Transport of bacteria in porous media and its enhancement by surfactants for bioaugmentation: a review. *Biotechnology Advances*, 35(4):490–504, 2017.

[217] J. Zhou, S. Tian, K. Yang, Z. Dong, and J. Cai. Chapter eleven - enhanced gas recovery technologies aimed at exploiting captured carbon dioxide. In D. A. Wood and J. Cai, editors, *Sustainable Natural Gas Reservoir and Production Engineering*, volume 1 of *The Fundamentals and Sustainable Advances in Natural Gas Science and Engineering*, pages 305–347. Gulf Professional Publishing, 2022.

.